Yanez Lopez, Maria (2015) Detecting neuroinflammation with molecular MRI. PhD thesis, University of Nottingham.

Radiological Sciences
Division of Clinical Neuroscience, School of Medicine
Queen’s Medical Center

Detecting neuroinflammation with molecular MRI

by Maria Yanez Lopez

Thesis submitted to the University of Nottingham

for the degree of Doctor of Philosophy

Supervisors: Dr Henryk Faas, Professor Dorothee Auer

Internal Assessor: Professor Alan Perkins

May 2015

Contents

Abstract

The work in this thesis is focused on the study of neuroinflammation with molecular magnetic resonance imaging (MRI) methods. Neuroinflammation is a response of the central nervous system to pathological insult and it is present in many neurological disorders, such as Alzheimer's disease. Being able to image neuroinflammation non-invasively with MRI techniques would have an important clinical value for diagnosis and assessment of therapy effectiveness. The aim of this work is to develop and validate an MR biomarker of neuroinflammation using MR Spectroscopy (MRS) and chemical exchange saturation transfer imaging (CEST). First, intravenous administration of lipopolysaccharide (LPS) is used as a mild inflammatory stimulus in wild type mice and in a mouse model of Alzheimer's disease (AD). Elevated levels of the osmolyte myo-inositol, measured with MRS and microglia activation are found in AD mice after LPS administration. Due to the inherent low spatial resolution of MRS, a CEST MRI method is developed next. A myo-inositol CEST protocol is optimised, using Matlab simulations based on the Bloch-McConnell equations for a three pool model, in order to maximize the contrast and to estimate the amount of signal that can be expected *in vivo*. *In vitro* and *in vivo* tests are presented and a fast CEST sequence is developed, while the experimental difficulties and limitations of the technique are discussed. A CEST protocol is finally applied to evaluate the metabolite response to an LPS inflammatory challenge using MRS and histology as validation. A correlation is described between CEST and MRS myo-inositol levels, as well as between CEST and microglia concentration (Iba1 immunostaining), which highlight the potential of CEST as a non-invasive *in vivo* neuroinflammatory biomarker.

Declaration

I declare that this thesis is my own work based on research that was undertaken during my study in the Department of Radiological Sciences, School of Medicine, the University of Nottingham. Dr Henryk Faas and Dr Marie-Christine Pardon performed many of the experiments for the MRS LPS study, as detailed in chapter 3, and they have been the main contribution in the study designs and data interpretation from a biological point of view. Histological experiments and analysis detailed in chapter 3 were performed by colleagues Alessandra Agostini, Felicity Easton and others. I was responsible for all MR sequence programming, protocol optimisation (including Matlab simulations and *in vitro* experiments), data post-processing and analysis, with contributions from others being acknowledged in the thesis. The MR experiments in chapter 5 and the pilot experiments in chapter 3, together with a small part of the experiments in the full study (n=5 animals) were performed by me. Finally, animal work, including surgery, immunohistochemistry procedures and analysis mentioned in chapter 5 were also performed by me.

Acknowledgments

I would like to take this opportunity to thank all the people who have helped me during my studies.

First, I would like to express my deep and sincere gratitude to my supervisor, Dr Henryk Faas, for his continuous support, constructive comments, and important guidance, which have had a remarkable influence on my entire thesis and future career. I also wish to express my warm sincere thanks to Dr. Marie-Christine Pardon, who always made me feel welcome in her lab and whose personal collaboration and guidance were critical throughout this work. I warmly thank Professor Dorothee Auer, Professor Alan Perkins and Dr Paul Morgan, for their constructive criticism and excellent advice and comments during my studies.

I want to thank Dr Malcolm Prior and Bryan Morris for their help with MR technical issues and their patience. I am deeply thankful to past and present members of my research group: Ryan Bendell, Alex Taylor, Gaelle Ardito, Felicity Easton and Ryan Hegarty, for their contributions and support during these past three plus years. I would like to thank Alessandra Agostini and other members in Dr. Marie-Christine Pardon's group for all their help and support. Thanks also to all my colleagues from Radiological Sciences, who made my time at the department enjoyable and memorable.

I would also like to thank all my flatmates and friends in Nottingham (Philippine, Sanaa, Diane and Christine), who made the cold temperatures bearable and introduced me to new hobbies. Last, but not least, I want to thank my family and friends from Galicia:

Gracias a mis padres por apoyarme y haberme ayudado tanto a llegar hasta aquí. Gracias a mis amigos, en especial Sara, Jorge, Amanda, Aitor y Martín, por estar siempre ahí a pesar de la distancia. Y finalmente, gracias a Brais, por acompañarme todos estos años y confiar siempre en mí.

Introduction

The aim of this thesis is to develop and validate an MR biomarker of neuroinflammation in a mouse model of Alzheimer's disease, using MR Spectroscopy (MRS) and chemical exchange saturation transfer imaging. Neuroinflammation is a response of the central nervous system to a pathological insult and it plays an important role in a wide range of neurological disorders, such as neurodegenerative diseases (Alzheimer's disease, Huntington's disease or amyotrophic lateral sclerosis) and inflammatory disorders like multiple sclerosis and stroke. Molecular imaging is the discipline dealing with the characterization, measurement and visualization of the biological pathways at the cellular/molecular level. Being able to image neuroinflammation non-invasively with molecular magnetic resonance (MR) techniques would provide clinicians with an invaluable tool for early diagnosis of these disorders, assessment of progress disease and of therapy effectiveness.

In vivo MR Spectroscopy is a robust tool, which can be applied to measure key metabolites of neuroinflammation, but suffers from poor spatial resolution in order to gain an understanding of such a dynamic process. Not affected by this limitation, chemical exchange saturation transfer is a molecular MRI contrast mechanism, which benefits from ultra high magnetic fields and can provide metabolite specific contrast in the form of high resolution images.

The main challenges to attain these objectives are finding the right quantitative molecular biomarker, having a robust neuroinflammatory model with which to test the hypothesis and finally, the development and validation of a reproducible *in vivo* CEST protocol. The aim of this work was therefore to establish a robust *in vivo* CEST protocol and then apply this method in the context of neuroinflammation. For that, a neuroinflammatory stimulus will be used, together with a control method (MRS) and validation (histology), to find out where the contrast is coming from.

Chapter 1 introduces basic NMR concepts, starting from the quantum mechanics of nuclear magnetization and a description of macroscopic NMR theory and techniques. Building on these basic principles, magnetic resonance spectroscopy (MRS) and chemical exchange saturation transfer (CEST), which are the main techniques used in this work, are then discussed in detail.

Chapter 2 presents the concept of neuroinflammation and the processes involved, followed by a review of the state of-the-art of molecular imaging methods for monitoring neuroinflammation, which identifies the need for novel non-invasive quantitative molecular biomarkers.

Chapter 3 describes the detection of the early metabolic response to a mild inflammatory stimulus (lipopolysaccharide administration, LPS) with MR Spectroscopy. In a pilot study, the intensity and time course of the response was evaluated, in a series of *in vivo* experiments. Then, a full study, including wild type mice and an Alzheimer's disease (AD) mouse model, where the neuroinflammatory response is expected to be amplified, together with histological techniques for validation. The aim of this chapter is to evaluate metabolite changes with a established technique such as MRS and a particular focus on the glial marker myo-inositol, considered as a good candidate for an *in vivo* non-invasive neuroinflammatory biomarker.

Chapter 4 starts with a review of theoretical aspects of CEST. The rest of the chapter describes the work performed in order to optimise a CEST experiment: first, computer simulations based on a two or three compartment exchange are presented and compared with *in vitro* data from phantoms containing CEST metabolites. This chapter is focused on optimising CEST parameters, in order to maximize the contrast for *in vivo* experiments and to gain a better understanding of the CEST process and the associated practical problems.

Chapter 5 builds on the CEST optimization work from chapter 4 to develop an optimised *in vivo* chemical exchange saturation transfer protocol at 9.4 T. The computer simulations from chapter 4 are used for optimising the *in vivo* CEST contrast. Fast MRI readout techniques are evaluated for robustness and reproducibility to acquire CEST images, and the animal setup is optimised to minimise motion and B_0 inhomogeneities. Finally, following from chapter 3, a 9.4 T *in vivo* CEST study is presented, investigating the response to a mild inflammatory stimulus (LPS) of AD mice and controls, with MRS and histology for validation.

Chapter 6 summarizes the main findings obtained in this work, the limitations of the experiments, potential clinical applications/translation and discusses possible future steps for the project.

CHAPTER 1

Nuclear magnetic resonance review

1.1 Introduction

Nuclear Magnetic Resonance (NMR) is the study of the magnetic properties of the nuclei, first described by Bloch and Purcell in 1946. By measuring the electromagnetic energy absorption of a nucleus when placed in an external static magnetic field, information about its internal structure and quantum properties can be revealed. The non-invasive nature of the method makes it ideally suitable for studying the structure of living tissues, with techniques such as *in vivo* magnetic resonance spectroscopy (MRS) and *in vivo* magnetic resonance imaging (MRI) [1].

This chapter introduces the basic NMR principles. The quantum mechanics of nuclear magnetization are briefly considered (1.2.1), followed by a description of macroscopic NMR theory and techniques. Magnetic resonance spectroscopy (MRS) is discussed in detail in section 1.3, continuing with a short introduction to magnetic resonance imaging (MRI, 1.4) and a more detailed review of chemical exchange saturation transfer (CEST, 1.5).

1.2 Nuclear magnetic resonance, NMR

1.2.1 Nucleus in a static magnetic field

Orbital angular momentum Any object with a rotational motion around an specific point has a property called angular momentum, a conserved vector defined $\vec{L} = \vec{r} \times \vec{p} = \vec{r} \times m\vec{v}$. Therefore, electrons spinning around a nucleus will have a non zero angular momentum, whose amplitude and direction are quantized in the quantum mechanical description:

$$L = (h/2\pi)\sqrt{l(l+1)} \qquad (1.2.1)$$

$\hat{z}$ component:

$$L_z = (h/2\pi)m_l \tag{1.2.2}$$

with m_l being a set of $2l+1$ values, between $-l$ and $+l$. Therefore, a particle with a orbital angular momentum l can have any of these $2l+1$ sublevels, which are degenerate (have the same energy) in the absence of an external electromagnetic field.

If we now consider an atom from a classical point of view, the electrons rotating around the nucleus create a current, which gives raise to a magnetic field and therefore has a magnetic moment. Both orbital magnetic moment and orbital angular momentum are related by the gyromagnetic ratio γ_l, which is specific for each nucleus [2].

Spin angular momentum Spin is an intrinsic property of the elementary particles. As a type of angular momentum, its quantum mechanical description is as follows

$$s = \sqrt{s(s+1)}h \tag{1.2.3}$$

$$s_z = m_s h \tag{1.2.4}$$

with m_s being a set of $2s+1$ values, between $-s$ and $+s$ (sublevels). Spin is also related to a spin magnetic moment by the gyromagnetic ratio γ_s.

Total angular momentum The general quantum mechanical form of the coupling of both spin and orbital angular momentum for an elementary particle is:

$$j = \sqrt{j(j+1)}h; j = l+/-s \tag{1.2.5}$$

$$j_z = m_j h \tag{1.2.6}$$

again with m_j being a set of $2j+1$ values (sublevels), between $-j$ and $+j$. An angular momentum has an associate magnetic moment $\vec{\mu}$, in this case $\vec{\mu}_j = \gamma\vec{I}$

Total angular momentum of a nucleus: nuclear spin Nuclei are often considered as single entities with total angular momentum $\vec{I}$ (also misleadingly called nuclear spin), taking into account the total angular momentum of all the protons and neutrons forming the nucleus. This is the expression of the related magnetic moment $\vec{\mu}$, $\vec{\mu} = \gamma\vec{I}$, making it clear that as nuclear spin is quantized, so is the magnetic moment. Moreover, if a nucleus has a zero nuclear spin, its magnetic moment is also zero, thus not presenting any of the properties outlined next.

Now an external static magnetic field, $\vec{B}_0$, is introduced in the picture. In the absence of an external electromagnetic field the $2I+1$ nuclear spin states have the same energy, but when one is introduced the degeneracy is lifted. This phenomenon is called the Zeeman effect.

$$E_Z = -\vec{\mu} \times \vec{B}_0 \tag{1.2.7}$$

By taking $\vec{B_0}$ as a constant magnetic field in the $\vec{z}$ direction, that is, $\vec{B_0} = B_0\hat{k}$, the expression 1.2.7 becomes:

$$E_Z = -\mu_z B_0 = -\gamma m_I \hbar B_0 \tag{1.2.8}$$

All of these energy states are within the ground state of a nucleus and the energetic differences among them are much smaller than the one between the ground state and the first excited state. The energy gap between two Zeeman states (assuming I is 1/2) is:

$$\Delta E_Z = -(\frac{1}{2}\gamma\hbar B_0 + \frac{1}{2}\gamma\hbar B_0) = \gamma\hbar B_0 \tag{1.2.9}$$

In order to observe a transition from one level to the other, the amount of energy ΔE_Z would have to be supplied to the nucleus. This can be achieved with electromagnetic radiation of the appropriate frequency, called the Larmor frequency or resonance frequency, ω_L :

$$\gamma\hbar B_0 = \hbar\omega \tag{1.2.10}$$

$$\omega_L = \gamma B_0 \tag{1.2.11}$$

If the external electromagnetic field introduced is very strong (orders of magnitude higher than the ones produced in NMR), the effect it produces is called the Paschen-Back effect, widely studied in astrophysics [3]. The term "very strong field" is relative, since the field strength required depends on the particular energetic transition being considered. A strong field is one that induces Zeeman splitting comparable with or greater than the multiplet splitting of energy levels. In this limiting case, the spin and orbital angular momenta align independently with $\vec{B_0}$, a total angular momentum $\vec{J}$ is not defined and the splitting of the energy levels follows different selection rules.

1.2.2 Precession

When an external static magnetic field, $\vec{B_0}$, is applied to a nucleus, its magnetic moment experiences a torque $\vec{\tau}$ trying to align it to the main magnetic field $\vec{B_0}$.

$$\vec{\tau} = \vec{\mu} \times \vec{B_0} \tag{1.2.12}$$

From the definition of torque,

$$\vec{\tau} = \frac{d\vec{I}}{dt} \tag{1.2.13}$$

and since $\vec{\mu} = \gamma\vec{I}$, then

$$\frac{d\vec{\mu}}{dt} = \gamma\vec{\mu} \times \vec{B_0} \tag{1.2.14}$$

Assuming that $\vec{B_0}$ is a constant magnetic field in the z direction, $\vec{B_0} = B_0\hat{k}$, the magnetic moment of a nucleus in presence of an external static magnetic field precesses around the $\vec{z}$ axis with a quantized angle, a fixed amplitude and a fixed frequency depending on the magnitude of $\vec{B_0}$, the Larmor frequency.

$$\omega_L = -\gamma B_0 \tag{1.2.15}$$

The Larmor frequency is also the one corresponding to the energy increment between the different Zeeman levels of a specific isotope. In order to determine its value (and consequently identify the nucleus being studied), an oscillating electromagnetic field, i.e.. $\vec{B_1(t)} = B_{1max}cos(w_L t)$, can be applied to the nucleus. In NMR, they are frequently called radiofrequency fields, as they oscillate in the same frequency range as the radio waves (MHz).

1.2.3 Bloch equations

When there is not a single nucleus but a macroscopic sample, it is useful to consider the total magnetic moment of the sample, the magnetization

$$\vec{M} = \sum_{i=1}^{N} \mu_i \tag{1.2.16}$$

which is initially assumed to be pointing towards the z axis.

$$\vec{M} = M_0 \hat{z} \tag{1.2.17}$$

The introductions of the static magnetic field $\vec{B_0}$ and the oscillating electromagnetic field $\vec{B_1}$ will induce changes in both the magnitude and direction of $\vec{M}$. Bloch equations are the macroscopic equivalent of equation 1.2.14:

$$\frac{d\vec{M}}{dt} = \gamma(\vec{M} \times \vec{B(t)}) \tag{1.2.18}$$

$$\text{where } \left.\begin{array}{l} \vec{B(t)} = \vec{B_0} + \vec{B_1(t)} \\ \vec{M} = M_0\hat{z} \\ \vec{B_0} = B_0\hat{z} \\ \vec{B_1} = (B_1x, B_1y, 0) \end{array}\right\} \Rightarrow \frac{d\vec{M}}{dt} = \gamma \begin{vmatrix} \hat{i} & \hat{j} & \hat{k} \\ 0 & 0 & M_0 \\ B_1x & B_1y & B_0 \end{vmatrix}$$

An easy way of simplifying these equations consists of the introduction of a rotating frame of reference, rotating around the z axis with the Larmor frequency. Consequently, $\vec{M}$ is only affected by $\vec{B_0}$ and equation 1.2.18 is reduced to:

$$\frac{d\vec{M}}{dt} = \gamma(\vec{M} \times \vec{B_1(t)}) \tag{1.2.19}$$

The axis of the rotating frame of reference are represented by x', y' and z.

1.2.4 Excitation

Excitation results from applying a radiofrequency pulse $\vec{B_1}$ to the system, producing a precession of the magnetization $\vec{M}$ around the axis of $\vec{B_1}$. This can be illustrated using the Bloch equations. If the RF field is applied in the x' direction, then:

$$\frac{d\vec{M}}{dt} = \begin{pmatrix} 0 & 0 & 0 \\ 0 & 0 & \gamma B_1 x' \\ 0 & \gamma B_1 x' & 0 \end{pmatrix} \begin{pmatrix} M'_x \\ M'_y \\ M_z \end{pmatrix} = \begin{pmatrix} 0 \\ \gamma B_1 x' M_z \\ -\gamma B_1 x' M'_y \end{pmatrix} \tag{1.2.20}$$

$$\frac{d^2 M'_y}{dt^2} = \gamma B_1 x' \frac{dM_z}{dt} = -\gamma^2 B_1 x'^2 M'_y M'_y = Asin(\gamma B_1 x' t) + Bcos(\gamma B_1 x' t) \tag{1.2.21}$$

where A and B are complex constants depending on boundary conditions. If $M'_y = M'_y(0)$ and $M_z = M_z(0)$ when t=0, then $A = M_z(0)$ and $B = M'_y(0)$. Also as $\vec{B} = \vec{B_1 x'}$, $\gamma B_1 x' = w$. Therefore:

$$\left.\begin{array}{l} \vec{M'_x}(t) = M'_x(0)\vec{M'_y}(t) = M_z(0)sin(wt) + M'_y(0)cos(wt) \\ \vec{M_z}(t) = M_z(0)cos(wt) - M'_y(0)sin(wt) \end{array}\right\} \tag{1.2.22}$$

and in matrix form

$$\begin{pmatrix} M'_x \\ M'_y \\ M_z \end{pmatrix} = \begin{pmatrix} 1 & 0 & 0 \\ 0 & cos(wt) & sin(wt) \\ 0 & -sin(wt) & cos(wt) \end{pmatrix} \begin{pmatrix} M'_x(0) \\ M'_y(0) \\ M_z(0) \end{pmatrix} \tag{1.2.23}$$

or

$$\begin{pmatrix} M'_x \\ M'_y \\ M_z \end{pmatrix} = R \begin{pmatrix} M'_x(0) \\ M'_y(0) \\ M_z(0) \end{pmatrix} \tag{1.2.24}$$

The matrix R corresponds to the rotation around the x axis.

1.2.5 Relaxation

During the excitation process, the sample absorbs electromagnetic energy and its magnetization rotates towards the xy plane, called the transverse plane (while the plane parallel to $\vec{B_0}$ and $\vec{M(0)}$ is known as the longitudinal plane). The rotation angle $\theta = \omega t$ depends on the duration and frequency of the $\vec{B_1}$ pulse, and once $\vec{B_1}$ is turned off, $\vec{M}$ returns to its original state, a process called relaxation. That change in $\vec{M}$ is the responsible for the NMR signal as it induces an electromotive force (oscillating at the Larmor frequency) in a detector coil, which registers the signal. Once $\vec{M}$ has returned to its initial position along the z axis, the NMR signal ends. This signal is called free induction decay (fid).

Relaxation involves two different processes: On one hand, after switching off $\vec{B_1}$ the individual spins in the sample gradually release the energy absorbed during the excitation and return to the less energetic state (parallel to the static magnetic field). This is called longitudinal relaxation, as the longitudinal component of the magnetization (M_z) is the one undergoing a change, recovering up to its initial value $\vec{M}_0$, in an exponential manner ruled by time constant T_1:

$$\frac{d\vec{M_z}(t)}{dt} = -\frac{\vec{M_z}(t) - \vec{M}_0}{T_1} \tag{1.2.25}$$

On the other hand, the spins in the sample precess in the transverse plane after excitation, initially with the same phase (coherence) which is lost with time due to mutual interactions (some of them start precessing faster and others slower) in what is known as transverse relaxation (being the so called transverse components of the magnetization vector M'_x and M'_y). Transverse relaxation is an exponential decay, governed by the time constant T_2.

$$\frac{d\vec{M_T}(t)}{dt} = -\frac{\vec{M_T}(t)}{T_2} \tag{1.2.26}$$

Another factor causing transverse relaxation is the imperfect homogeneity of $\vec{B}_0$ and its effect on the different spins. When both phenomena are taken into consideration, the time constant is then T_2*.

Longitudinal relaxation and transverse relaxation can be expressed as part of the Bloch equation. Their effects on the different magnetization vector components are illustrated in Figure 1.1:

$$\frac{d\vec{M}}{dt} = \gamma \begin{pmatrix} 0 & 0 & -B_1y' \\ 0 & 0 & B_1x' \\ B_1y' & -B_1x' & 0 \end{pmatrix} \begin{pmatrix} M'_x \\ M'_y \\ M_z \end{pmatrix} + \begin{pmatrix} -\frac{1}{T_2} & 0 & 0 \\ 0 & -\frac{1}{T_2} & 0 \\ 0 & 0 & -\frac{1}{T_1} \end{pmatrix} \begin{pmatrix} M'_x \\ M'_y \\ M_z \end{pmatrix} + \begin{pmatrix} 0 \\ 0 \\ \frac{M_0}{T_1} \end{pmatrix} \tag{1.2.27}$$

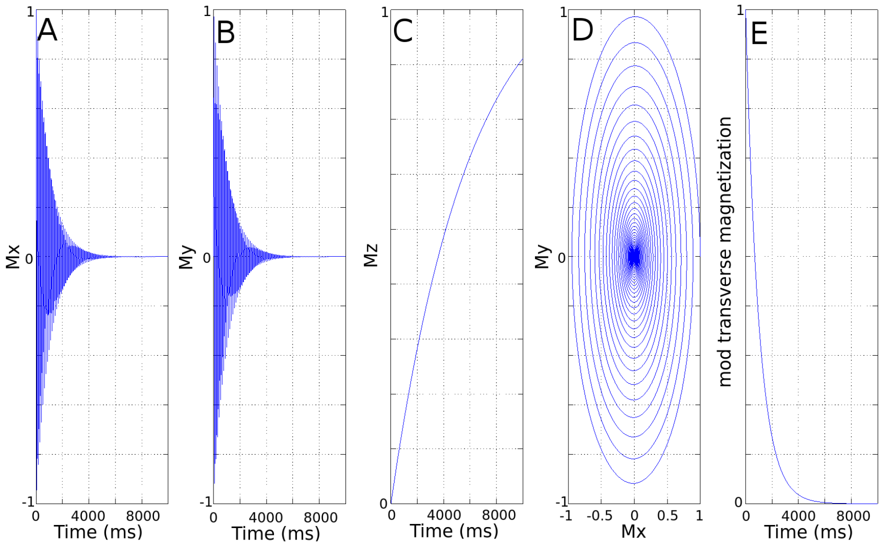

Figure 1.1: Relaxation effects and magnetization vector components: A) M_x decay over time, due to transverse relaxation (T_2). **B)** M_y decay with time, due to transverse relaxation (T_2) **C)** M_z recovery with time, due to longitudinal relaxation (T_1) **D)** M_x and M_y decay exponentially with the same time constant (T_2) **E)** $\sqrt{{M_x}^2 + {M_y}^2}$ decay with time due to transverse relaxation (T_2). This magnitude corresponds to the signal measured in a NMR experiment. T_1 of 600 ms, $T_2 = 100$ ms

1.2.6 Echo formation

A spin echo results from the refocusing of the magnetization of excited spins by another electromagnetic pulse (of ideally 180°). The reason for using such a refocusing pulse in an NMR experiment is that it is much easier to measure the signal of the echo than to measure the free induction decay (fid). Another advantage of this technique is that it provides some shielding against $\vec{B}_0$ inhomogeneity due to the refocusing pulse (transverse relaxation is therefore T_2 dependent, with T_2* effects removed).

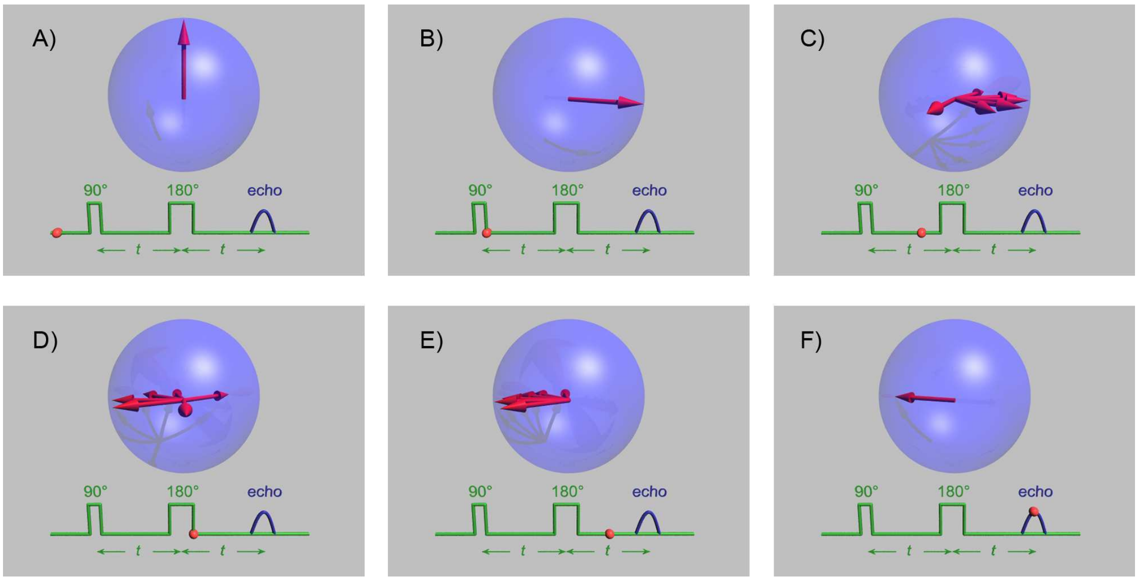

Figure 1.2: Echo formation, from [4]:

A) In the rotating plane, the net magnetization (red arrow) is aligned parallel to the main magnetic field B_0, lying along the z axis. **B)** A 90 ° excitation pulse flips the magnetization to the transverse plane xy (perfect pulses are assumed). **C)** After the 90 ° excitation pulse, the newcomer spins in the transverse plane start to dephase, due to B_0 local inhomogeneities, thus losing coherence and complicating a measure of the signal just then (fast decay). **D)** A 180 ° pulse is applied, which effectively corrects for the dephasing of the spins which will recover coherence and consequently produce the strongest signal (an echo) at twice the time between both pulses, usually called echo time (TE, **E) to F)**) .

1.2.7 Fourier transformation

The Fourier transform is a mathematical operation that extracts the frequency spectrum of a signal. Therefore, an oscillating signal at only one frequency will have a Fourier transform with one single peak at that frequency [1]; if it is a composite signal made up by several oscillations at different frequencies, the Fourier Transform will be a mathematical representation of that spectrum [5]. The operation going from the time domain (original signal) to the frequency domain (resulting frequency spectrum) is called Fourier Transform (FT) and the opposite one, Inverse Fourier Transform (IFT) [6].

$$FT[g(t)] = G(k) = \int_{0}^{\infty} g(t)e^{-2\pi ikt}\,\mathrm{d}t \qquad IFT[G(k)] = g(t) = \int_{-\infty}^{\infty} G(k)e^{+2\pi ikt}\,\mathrm{d}k \quad (1.2.28)$$

Equation 1.2.28 refers to the continuous FT and IFT, but in an NMR experiment the signal is sampled at discrete times resulting in a sum of multiple delta functions, with an algorithm called FFT (fast Fourier Transform [7]).

1.3 Magnetic resonance spectroscopy (MRS)

NMR spectroscopy is a non-invasive technique that uses nuclear magnetic resonance to characterize the internal structure of matter. NMR sensitivity depends on the gyromagnetic ratio and the external magnetic field (see equation 1.2.11). The gyromagnetic ratio γ is specific for each nuclei and it sets ^1H NMR spectroscopy as the most common MRS technique, since ^1H has the second highest γ (being tritium the first) and with added advantages such as its high abundance. Other spectroscopy techniques include nuclei such as ^{13}C(carbon 13), ^{31}P(phosphorus 31), ^{19}F(fluorine 19), ^{23}Na(sodium 23) or ^{39}K(potassium 39) [8].

1.3.1 Chemical shift

One important concept towards investigating the structure of a molecule is that of the chemical shift, which accounts for the different resonant frequencies the same nucleus can have depending on its position in a molecule. This phenomenon is caused by a varying degree of electronic shielding of the nuclei depending on its chemical environment. By applying a Fourier transform to the NMR signal of a sample, its frequency spectrum can be obtained.

---

[1] The symmetry property dictates that for real-valued time functions, the Fourier transform is conjugate symmetric, F(-ω) = F*(ω) and hence, only the transform of positive ω values is needed for such a function. Therefore, a periodic function like sin(x), will contain transformed peaks in not one, but two places (positive and negative frequency components).

Chemical shifts are usually not measured in Hz, since this would depend on the scanner field strength B_0. Instead they are expressed as the distance to a reference frequency in ppm (parts per million). The chemical shift of the singlet tetramethylsilaneis (TMS) is the accepted internal standard for calibrating chemical shift for ^1H MRS. TMS is assigned as 0 ppm and all other chemical shifts are determined relative to it.

1.3.2 J coupling

NMR sensitivity depends on the gyromagnetic ratio and the external magnetic field (equation 1.2.11). Hence, it can be improved by increasing the magnetic field $\vec{B}_0$ (high-resolution NMR spectra). As a consequence, the peaks can be seen to be split into smaller ones, caused by the phenomenon called scalar or J-coupling, an interaction between a nuclear spin indirectly influencing one another through hyperfine interactions with local electrons. J coupling is field independent and it provides information on the structure of molecules, allowing compound identification. Dipolar couplings, where two nuclear spins directly influence each other are prevalent in liquids, but cancel out due to rapid molecular tumblings.

1.3.3 Single volume localization and chemical shift displacement artifact

In an ^1H MRS experiment, the signal comes from all protons in the sample. For an *in vitro* experiment with a uniform sample this is not a problem, but in an *in vivo* experiment the situation is different: without the use of volume localization, tissue and magnetic field heterogeneity will produce a non specific and broad signal.

Once a region of interest (ROI) is established, volume localization removes unwanted signals coming from outside the ROI, therefore creating a more meaningful metabolite signature for the region studied. Also, it produces narrower spectral lines, with more uniform excitation, since B_0 and B_1 homogeneity improve when reducing the ROI.

The most common localization methods use a frequency selective radio-frequency (RF) pulse in the presence of a magnetic field gradient to choose a voxel. Adding a magnetic field gradient $\vec{G}$ yields:

$$B(\vec{r}) = B_0 + \vec{r}\vec{G} \tag{1.3.1}$$

$$\omega(\vec{r}) = \gamma B(\vec{r}) = \gamma B_0 + \gamma \vec{r}\vec{G} \tag{1.3.2}$$

where γ is the gyromagnetic ratio and ω the frequency. Assuming $\vec{G}$ is a gradient applied in the $\vec{x}$ direction,

$$\omega(x) = \gamma B_0 + \gamma x G_x = \omega_0 + \gamma x G_x \tag{1.3.3}$$

and looking at the position x,

$$x = \frac{\omega(x) - \omega_0}{\gamma G_x} \tag{1.3.4}$$

This results in a chemical shift displacement or spatial displacement between species with different chemical shifts. Chemical shift ($\Delta\omega$) is the resonant frequency of a particular nucleus compared with the water frequency, it depends on the gyromagnetic ratio, the main magnetic field and more importantly, on the chemical environment of the nucleus.

$$\Delta x = \frac{\Delta\omega}{\gamma G_x} \tag{1.3.5}$$

From this equation, it is apparent that the chemical shift displacement increases with high fields for an equal gradient strength. For example, the chemical shift water-lipids at 4 T is around 580 Hz, while at 9.4 T is 1360 Hz. This could mean a displacement of around one mm in a 2x2x2 mm voxel (PRESS sequence, 7 T). Therefore, tissue heterogeneity must be taken into account for example to avoid lipid contamination in a voxel in the brain from lipids from outside the skull.

1.3.4 Shimming

High magnetic field homogeneity is required to clearly discriminate between close metabolic resonances in a MRS spectrum. Shim coils generate currents that can minimise the inhomogeneity of the main magnetic field $\vec{B_0}$ for a sample. A linear expansion of spherical harmonic functions is used to describe the distribution of the magnetic field $\vec{B_0}$, with the typical shim coil setup allowing to correct up to the second order:

$$\vec{B_0} = \sum_{n=0}^{\infty} \sum_{m=0}^{n} C_{nm} \left(\frac{r}{a}\right)^n P_{nm}(cos\theta)[m(\phi - \psi_{nm})] \tag{1.3.6}$$

where a is the average bore radius, r the sample position, and C_{nm} and ψ_{nm} are constants. Shimming is performed either manually or using automated methods:

Manual shim requires manually altering the currents in each shim coil until the desired homogeneity is achieved, which can be a challenging task for *in vivo* applications.

Automatic shimming methods:

Magnetic field map based shimming After defining the region of interest to be optimised, the coefficients of the linear expansion of spherical harmonics for the $\vec{B_0}$ distribution in that region are calculated and the shims are adjusted accordingly. The $\vec{B_0}$ distribution is obtained from a gradient echo based field map.

Projection based shimming The $\vec{B_0}$ distribution is portrayed by measuring the field along a limited number of linear projections. Methods like FASTMAP (fast automatic shimming technique by mapping along projections) are quick and efficient for regions of interest with a simple geometry.

1.3.5 Water suppression

Water is the most abundant tissue molecule containing protons, resonating at around 4.7 ppm. *In vivo*, due to the low concentration of all the other proton-containing metabolites compared with free water, the water peak dominates the spectrum and water suppression is necessary to accurately detect the rest of metabolites. There are a range of protocols to achieve a specific suppression of the water resonance in a spectrum; the two most common are:

CHESS Chemical shift selective water suppression (CHESS) consists of a RF selective saturation pulse on the water frequency followed by a magnetic field gradient dephasing all the coherences in the water protons, prior to excitation. This is usually repeated a few times, due to imperfect suppression caused by B_0 and B_1 inhomogeneities. This protocol does not disturb the magnetization in the area of interest, though it requires a fast readout sequence afterwards, since the magnetization of the suppressed water will recover with T_1.

VAPOR Variable pulse powers and optimized relaxation delays (VAPOR) combines the CHESS approach with T_1 water suppression (using optimised delays between the pulses that exploit the T_1 differences between the water and other metabolites) and it is mostly used for *in vivo* applications.

1.3.6 MRS sequences: PRESS, STEAM, LASER

PRESS Point Resolved Spectroscopy (PRESS) is a double spin echo technique, with two 180° refocusing pulses after a single 90° excitation pulse (all slice-selective). Sequence details are shown in Figure 1.3. Crusher gradients around the 180° refocusing pulses ensure the dephasing of the signal from outside the desired volume.

STEAM Stimulated Echo Acquisition Mode (STEAM) uses three 90° pulses, Figure 1.4 (instead of 90° 180° 180° for PRESS).

Advantages of STEAM are the short echo times that can be achieved (a few ms, allowing for more metabolites visualization), but it has a lower SNR than PRESS, since half of the signal is lost in the creation of the stimulated echo (the second 90° pulse only flips half of the transverse magnetization to the longitudinal axis, the other half being dephased by crushers).

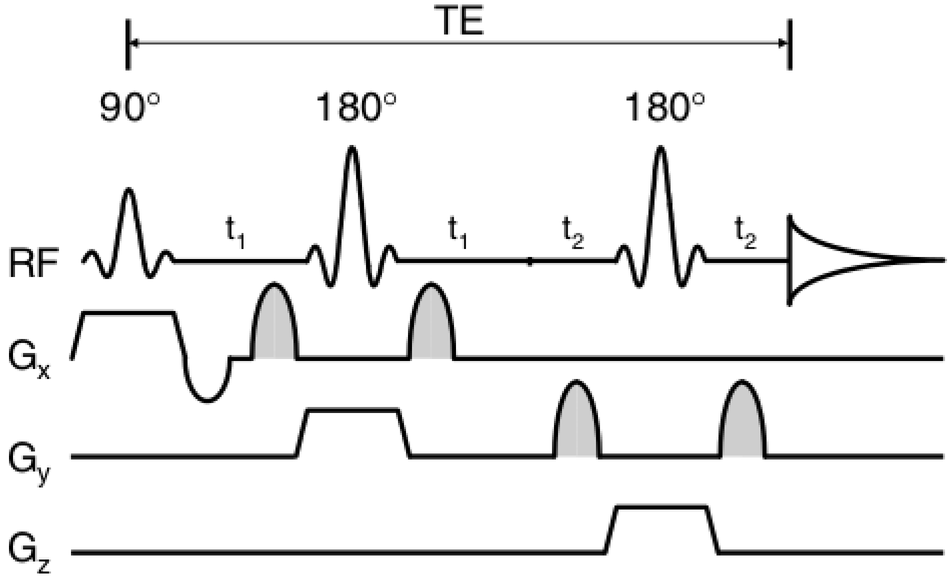

Figure 1.3: PRESS pulse sequence, from de Graaf [8]: The 90° pulse flips the spins to the xy plane and the first 180° pulse creates an echo at time $2t_1$. After a t_2 delay, a second 180° pulse refocuses the signal again, creating an echo at $2t_1 + 2t_2$, the TE of the sequence. The signal from the final echo is coming from the intersection of the three planes selected by the three pulses, thus defining a volume.

LASER Localization by Adiabatic Selective Refocusing (LASER) uses adiabatic excitation and refocusing pulses. The advantage of this method is that it is insensitive to B_1 variations (adiabatic) and produces defined excitation profiles at high fields (also minimizing chemical shift displacement), since refocusing adiabatic pulses have a much higher bandwidth compared to the pulses used in PRESS or STEAM [9]. A disadvantage is the longer TE required, due to the many pulses used for refocusing.

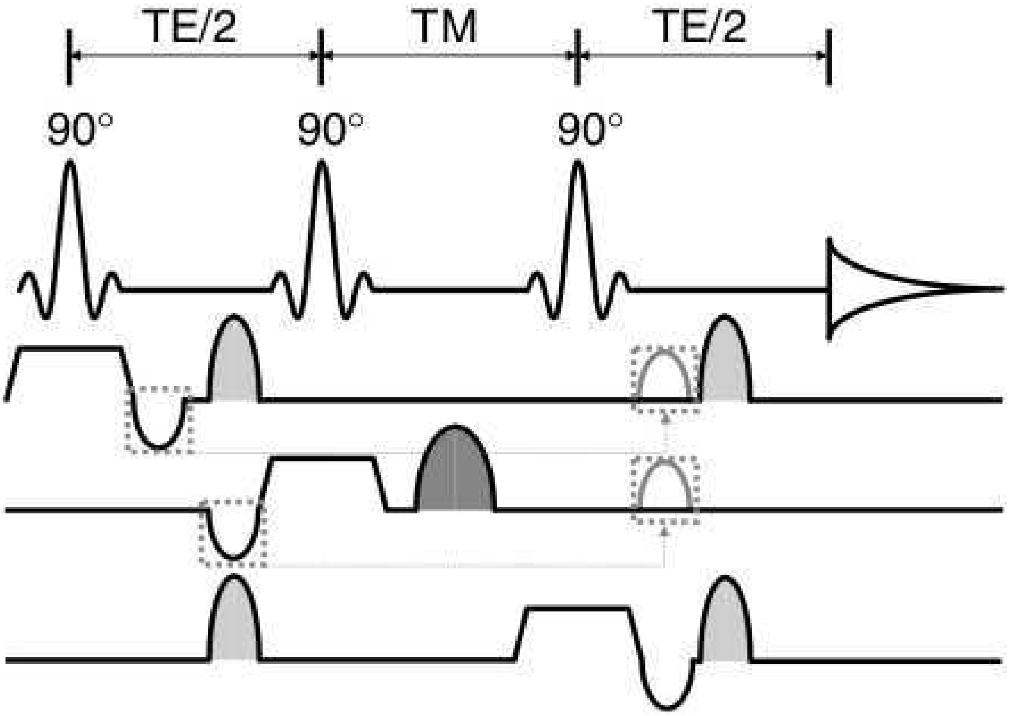

Figure 1.4: STEAM pulse sequence, from de Graaf [8]: This kind of sequences generates four spin echoes: from the first pulse and the second (at TE), from the first pulse and the third (at $TE + 2TM$), from the second and the third (at $\frac{TE}{2} + 2TM$), from all three (at 2TM, equivalent to the PRESS echo) and one stimulated echo (at $TE + TM$). This final echo is the one STEAM uses, and therefore all the others are suppressed via gradient crushers.

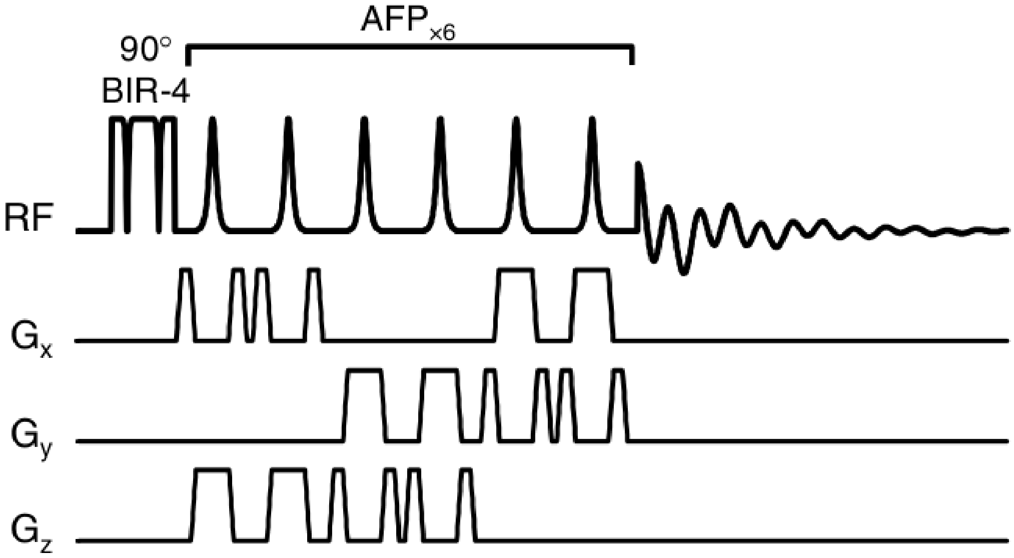

Figure 1.5: LASER pulse sequence, from de Graaf [8]: A non-selective adiabatic pulse (B_1 insensitive rotation composite pulse, BIR-4) performs the excitation of the whole sample, followed by three pairs of adiabatic full passage (AFP) refocusing pulses, defining the volume of interest. Signals from outside are removed with crusher gradients around the AFP pulses.

1.3.7 Postprocessing

Eddy current correction Faraday's law of induction establishes that changing magnetic fields induce electric currents in conductors. Rapidly switching the gradients in a localised MRS sequence creates eddy currents, which produces asymmetric resonances in an MRS spectrum. A simple way of removing residual eddy currents is by acquiring a reference scan without water suppression with the same parameters, and later using it to correct the suppressed spectrum. This is equivalent to performing a first order phase correction in the dataset.

Phase correction and frequency alignment The signal to noise (SN) of an MRS spectrum can be improved by increasing the number of averages, although there is a trade-off between SN and acquisition time. Individually acquiring spectra in small groups can be useful when there are movement artifacts over a long *in vivo* experiment, since macroscopic motion can lead to a loss in signal due to phase cancellations in the spectra summation, which can be avoided by prior individual phase correction.

In a similar fashion, individual/small groups frequency alignment will produce narrower spectral widths and reduce artifacts in the final spectrum in the presence of motion or frequency drift.

1.3.8 Metabolite quantification

In a ^1H MRS spectrum, there is an overlap between the MRS peaks of the metabolites. Therefore, even if a metabolite concentration is directly proportional to the total area under its peak(s), it is often difficult to discern the individual peaks. MRS metabolite quantification can be achieved with the LCmodel [10]. This software performs an automatic fit of an *in vivo* spectrum based on a model of linear combinations of *in vitro* individual metabolites (the basis file, containing simulations or real spectra taken with the same sequence and magnetic field strength). The analysis provides metabolite concentrations and their uncertainties, in the form of estimated standard deviations (Cramér-Rao bounds). A free software alternative is TARQUIN (Totally Automatic Robust Quantitation in NMR [11]).

Metabolite concentrations are usually expressed through ratios to another peak in the MRS spectrum, conventionally total creatine or choline, since these are assumed to be generally stable in *in vivo* tissue. In order to get absolute values, in units such as millimoles per kilogram wet weight, there are several strategies:

External reference A phantom of known properties can be positioned inside the coil, together with the subject and a reference spectrum is acquired, to establish a direct comparison.

Replacement method This method consists of replacing the subject with a phantom simulating the same characteristics and then take a calibration measurement using the same parameters (matching the previous coil load).

Water signal reference The water signal can be used as an internal reference, by taking a spectrum without water suppression as a reference, with the rest of the parameters identical.

In most cases, T_1 and T_2 values are required, together with postprocessing corrections [12], involving segmentation of the grey/white matter areas in each voxel and accounting for partial volume effects arising from different amounts of specific tissue types in the voxel, such as cerebrospinal fluid [13].

When the usual approach is not enough to detect a particular metabolite of interest due to low concentration or strong overlapping, spectral editing can be used, meaning that special sequences are designed aiming to record only the target and eliminate the other metabolites from the spectrum (commonly used for GABA, glutamine, lactate [12]).

1.4 Magnetic resonance imaging (MRI)

MRS provides information about the composition of a sample and the structure of the molecules contained in it, but it lacks information about the spatial distribution of those molecules. In order to obtain spatial resolution, the magnetic resonance imaging (MRI) approach consists of having the external magnetic field vary with the position in the sample. This spatial dependence, which is automatically translated to the Larmor frequency (see equation 1.2.11) and therefore to specific nuclei is achieved with the use of magnetic field gradients, resulting in the formation of an image [14, 15].

Magnetic field gradients break the uniformity of the external magnetic field $\vec{B_0}$ making its strength vary over space: $\vec{B(r)}$.

$$\vec{B(r)} = \vec{B_0} + \vec{r}\vec{G} \tag{1.4.1}$$

with $\vec{G}$ taking the form (for example) of a linear magnetic field gradient, that is, $\vec{B}$ changing linearly with position $\vec{r}$,

$$\vec{G} = \frac{d\vec{B}}{d\vec{r}} \rightarrow \left.\begin{aligned} G_x &= \frac{dB_x}{dx} \\ G_y &= \frac{dB_y}{dy} \\ G_z &= \frac{dB_z}{dz} \end{aligned}\right\} \tag{1.4.2}$$

The introduction of magnetic field gradients provide an alternative to the spin echo sequence. A gradient echo sequence is faster than spin echo due to the absence of the refocusing pulse and the fact that the flip angle of the excitation pulse is usually less than 90 degrees, so it requires less time to recover, ready for the next excitation. Instead of refocusing pulses, gradients produce the echo, dephasing and rephasing the spins. It is more susceptible to artifacts caused by inhomogeneities and magnetic susceptibility variations than spin echo sequences.

There are a number of properties of spins which can lead to contrast in MRI images. The most basic are:

Relaxation As has been said in section 1.2.5, relaxation consists of two different processes. Longitudinal relaxation refers to the longitudinal component of the magnetization M_z recovering up to its initial value M_0, following equation 1.2.25, whose solution is

$$M_z(t) = M_0(1 - e^{\frac{-t}{T_1}}) \tag{1.4.3}$$

Transverse relaxation is the loss of transverse magnetization caused by the loss of coherence of the spins (equation 1.2.26) in a exponential decay

$$M_{xy}(t) = M_0 e^{\frac{-t}{T_2}} \tag{1.4.4}$$

The constants governing the recovery of the longitudinal magnetization T_1 and the decay of the transversal magnetization T_2 can be used as a source of contrast for MRI, since they are properties of the tissue being imaged.

One way of getting T_1 contrast in an image is using a simple inversion recovery pulse sequence: a 180° pulse followed by a spin echo acquisition. During the period following the first 180° pulse (called inversion time, TI), all the spins with different T_1 recover at different rates, as can be seen in the simulation in Figure 1.6. In there, Mz_1 and Mz_2 (longitudinal magnetizations of nuclei with $T1_1$ and $T1_2$ respectively) start to differ at the beginning during TI and will end up having different contrast in the final image if the repetition time (TR) is chosen appropriately.

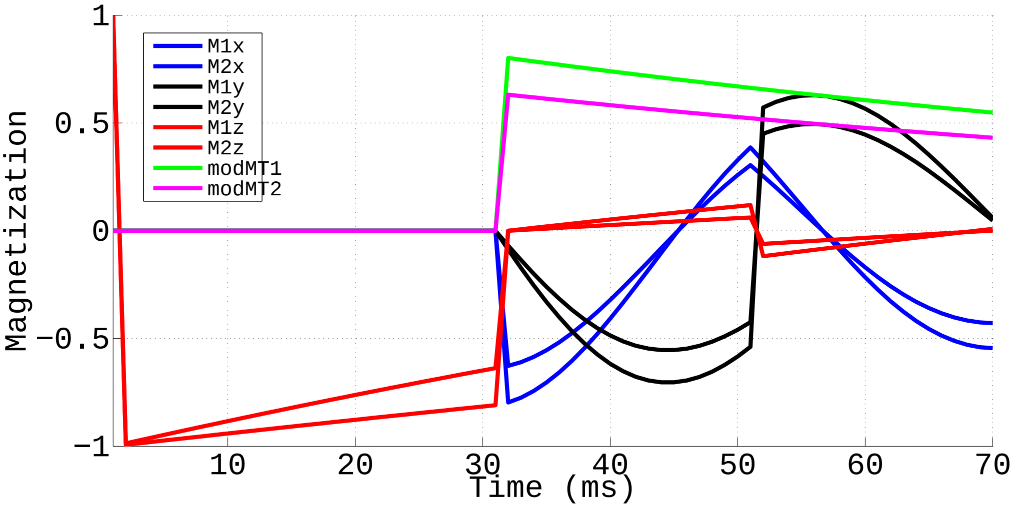

Figure 1.6: Simulation of T_1 contrast Inversion recovery sequence, two nuclei. $T1_1 = 300$ ms,$T1_2 = 150$ ms, TI = 30 ms, TE = 70 ms. In blue, M_x of compounds 1 and 2 and in black, M_y of compounds 1 and 2. In red, M_z components, while the NMR signal (modulus of transverse magnetization) is represented in green and fuchsia colour. The difference between these last two lines provides the T_1 contrast.

A simulation of a T_2 weighted experiment can be seen in Figure 1.7, using a spin echo signal.

Proton density Proton density imaging is the modality where the contrast in an image depends on the number of protons per voxel, which again it is different between diverse tissue types. If proton density is the contrast being sought, T_1 and T_2 contrast should be minimised, by chosen a long TR (protons fully relaxed) and a short TE value (minimal signal decay before acquisition).

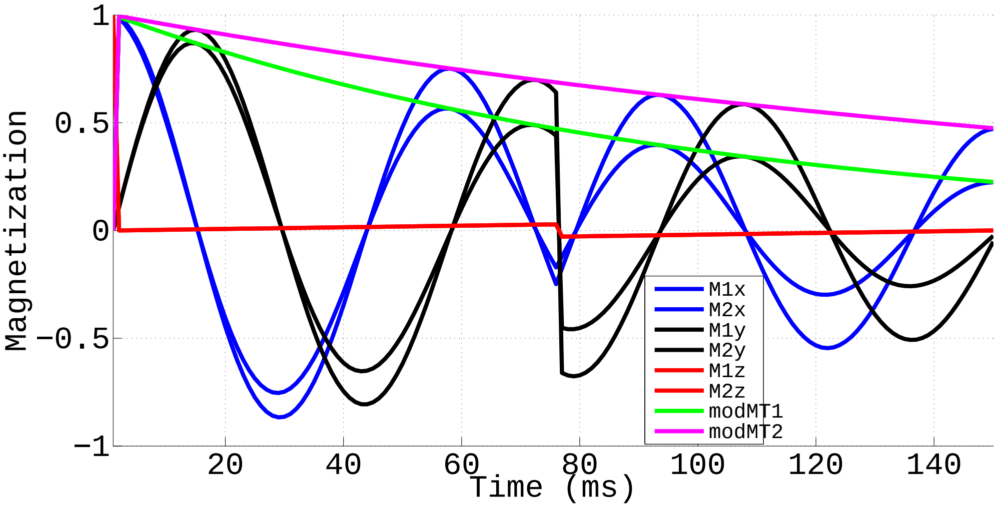

Figure 1.7: Simulation of T_2 contrast Spin echo sequence, two nuclei. $T2_1 = 100$ ms,$T2_2 = 200$ ms, TE = 150 ms. In blue, M_x of compounds 1 and 2 and in black, M_y of compounds 1 and 2. In red, M_z components, while the NMR signal (modulus of transverse magnetization) is represented in green and fuchsia colour. The difference between these last two lines provides the T_2 contrast.

1.5 Chemical exchange saturation transfer (CEST) review: techniques and applications

Ward et al. [16] were the first to indirectly observe a low-concentration labile metabolite using magnetic resonance imaging (MRI) through the exchange of its protons with those of the solvent water in a solution. They did so by applying a frequency selective saturation pulse to the labile protons and measuring the signal loss being transferred to the water, naming the process Chemical Exchange Saturation Transfer (CEST).

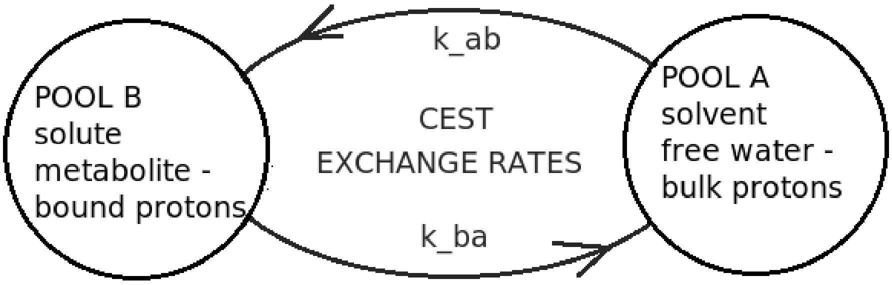

Figure 1.8: CEST exchange rates diagram: k_{ba} represents the exchange rate constant between pool B (solute, bound protons) and pool A (solvent, free protons), while k_{ab} represents the back exchange.

Chemical exchange has been studied in many different nuclei: ^{1}H, ^{31}P,^{19}F, ^{13}C, ^{129}Xe, however most of the CEST literature focuses on the chemical exchange of protons, i.e.

$$AH + B \Leftrightarrow A + BH \tag{1.5.1}$$

where A is pure water and B a metabolite containing groups with exchangeable protons (such as hydroxyl, amine, amide and imino groups). Chemical exchange is the origin of the CEST contrast and depends on parameters such as the exchange rate between water and labile protons (k_{ex}), the difference in their Larmor frequencies, the populations of the exchangeable protons, water T_1, T_2 and magnetic field strength [17].

This contrast can be transferred to MR in different ways, although saturation transfer was the first used and still dominates the CEST literature (even being part of the nomenclature).

1.5.1 Physical principles of the saturation transfer process

In a system consisting of a free water pool (pool A) and a metabolite pool with exchanging protons (the bound water pool, pool B), both pools have an inherent magnetization. The magnetization vector, or total magnetic moment of a sample is defined as:

$$\vec{M} = \sum_{i=1}^{N} \mu_i \tag{1.5.2}$$

where $\vec{\mu}_i$ represents the magnetic moment of nucleus i and N is the number of nuclei.

In the absence of any magnetic field all the spins are randomly orientated and the net magnetization will be zero. But when the ^1H protons are subjected to an external magnetic field ($\vec{B_0}$), their spins align either parallel or antiparallel to the field. Since the parallel alignment is the lowest energy state of the two, it will be filled with a higher probability, following Boltzmann's Law and therefore creating a net magnetization $\vec{M}$ parallel to $\vec{B_0}$. This situation can be observed in the left part of Figure 1.9 (from Sherry and Woods [18]), for both the bound and the free protons, assuming that $\vec{B_0}$ is parallel to the z axis.

If an electromagnetic RF pulse $\vec{B_1}$ is applied to pool B ($|\vec{B_1}| << |\vec{B_0}|$) providing the spins with enough energy as to equilibrate the population of both energy levels, $\vec{M}$ becomes zero like in the absence of any magnetic field. This is called called saturation of pool B, and it is illustrated in the center of Figure 1.9.

Protons are exchanged all the time in this system at a rate k (exchange rate of the reaction: k_{ab}, from the solvent to the solute, and k_{ba}, from the solute to the solvent, see Figure 1.8), and now that both pools have a different magnetization they produce a visible effect: the saturated protons from pool B travel to pool A, which gradually becomes saturated, and the non-saturated protons from pool A go to pool B to be saturated and continue the cycle. Consequently, the water magnetization and therefore the MRI signal becomes attenuated, as in the right part of

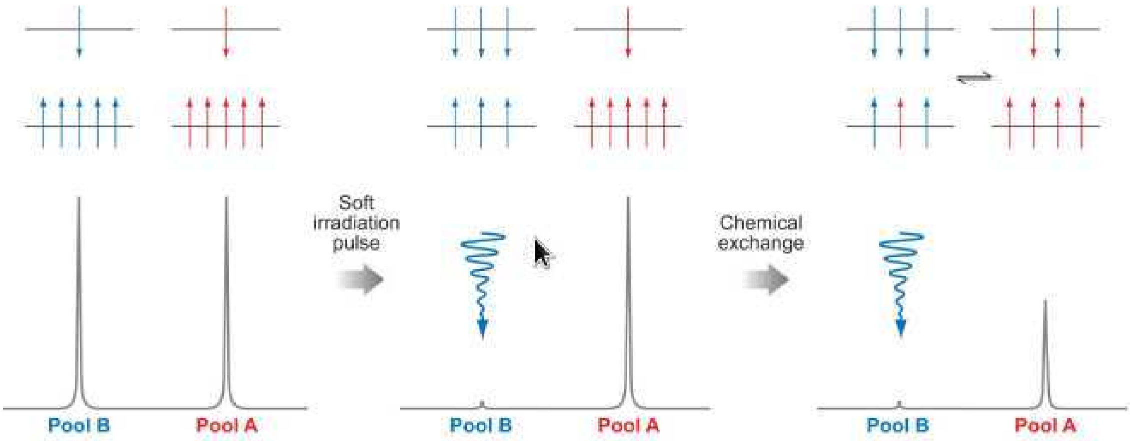

Figure 1.9: CEST contrast, from Sherry and Woods [18]
A) Most of the spins forming the magnetization of pool A (free protons) and pool B (solute protons) are aligned parallel to the main magnetic field (z axis). **B)** An electromagnetic RF pulse applied to pool B gives enough energy to equilibrate the spin levels (saturation). **C)** The saturation of pool B is transferred to pool A by chemical exchange, producing an attenuation of the water signal proportional to pool B concentration.

Figure 1.9.
A complete saturation of the bound pool is difficult to achieve for saturation times shorter than five times T_1, specially with fast exchange rates and so a partial saturation is obtained instead in most cases [19].

Other alternative possibilities for exchange transfer involve the use of label-transfer modules (LTM) for inversion, dephasing or frequency encoding (FLEX method [20]).

1.5.2 CEST, MT and NOE

Chemical exchange saturation transfer is considered to be part of magnetization transfer (MT), which has several different pathways, shown in Table 1.1.

Dipolar-dipolar interactions can be also called “conventional MT”, and have been known since as early as 1978 [21]. They arise from the presence of a macromolecular pool, which is not detected in a normal MRI experiment due to the short T_2 (around 10 μs) of its tightly bound protons, but can affect the magnetization of the free water pool through exchange processes. As can be seen in Figure 1.10, the absorption lineshape of the macromolecular protons is of the order of kHz, so any off-resonance RF pulse acting in that range will saturate these protons, which is why it is impossible to entirely separate CEST and conventional MT contrast [22] with this method.

Traditionally, the conventional MT effects were assumed to be symmetric around the water

Name	Description
Chemical exchange, CEST	Chemical exchange between exchangeable protons (-OH, -NH_2, -NH, -COOH, -SH...)
Dipolar coupling or Conventional MT	Interactions between: -Immobile protons from the macromolecule solid phase. -Bound protons on the hydrated molecular surface. -Free water protons.

Table 1.1: Magnetization transfer pathways

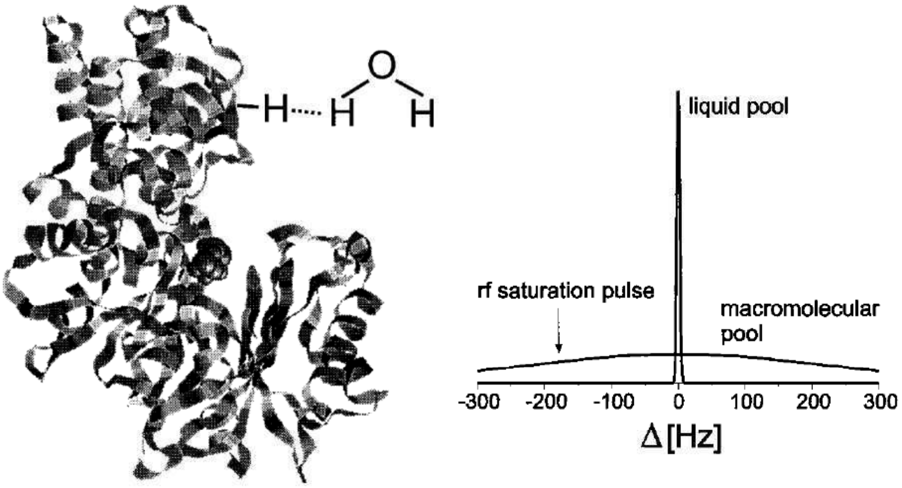

Figure 1.10: Conventional magnetization transfer, from Henkelman et al. [23]

Left Magnetization transfer between tightly bound protons (macromolecular pool) and free protons in the surface layer (liquid pool). **Right** Broad absorption lineshape of macromolecular protons, around 1-50 kHz, which will get saturated by any RF CEST pulse applied at those frequencies.

peak in the Z spectrum, hence making CEST the only source of asymmetry in it, calculated just by subtracting both sides of the Z spectrum (analysis first made in 1998, by Guivel-Scharen et al. [24]). However, older [25] and recent [26] findings showed that MT effects are in fact asymmetric, or symmetric but shifted with respect to the water peak [27].

The Nuclear Overhauser Effect (NOE) is the transfer of nuclear spin polarization from one nuclear spin population to another via dipole-dipole cross-relaxation. Overhauser predicted in 1953 the enhancement of nuclear spin polarization in metals upon saturation of the electron spins [28], and the nuclear equivalent was described by Solomon in 1956 [29].

CEST studies at ultra-high magnetic fields have reported additional upfield magnetization transfer effects at about 0-5 ppm in the proton spectrum or -5 to 0 ppm in the Z spectrum. These effects have been attributed to NOE enhancements from aliphatic and olefinic protons. If signals originating from non-exchangeable protons appear in a CEST experiment, this suggests the existence of a transfer mechanism to water. However, the nature of the mechanism producing the observed NOE upfield, and how it affects the quantification of CEST contrast is still not clear [30]. Ling et al., Jin et al. attributed it to direct through-space dipolar transfer [31, 32], while van Zijl and Yadav proposed a relay mechanism via exchangeable protons [19].

1.5.3 CEST sequences: prepulses and readouts

A typical basic setup for a CEST experiment is shown in Figure 1.11: the offset irradiation partially saturating the exchanging protons of a metabolite ("presaturation module"), followed by an "imaging module", to look at the effect suffered by the main water peak due to the chemical exchange of the saturated protons. There are two main types of presaturation modules:

Continuous wave prepulse : The simplest and easiest to optimise, it consists of a long (a few seconds) low-powered rectangular off-resonance pulse with a constant pulse power. Right before the imaging module, a crusher gradient spoils the residual transverse magnetization, so as to avoid any unwanted echoes appearing during the imaging module. The CEST experiments using this approach are called CW-CEST. They can entail a high power deposition (high specific absorption rate, SAR), which makes them unsuitable for most clinical MRI scanners. The term CW refers to the use of one RF channel dedicated to the continuous RF pulse and another one to the imaging module [34], but it is often used to describe an approximation, or pseudo-CW approach. In this setup, a single RF channel is available and the rectangular long prepulse is turned off right before the imaging module, which should be as short as possible to avoid losing too much CEST contrast (which decays with T_1).

Train of shaped prepulses : Repeated off resonance shaped pulses with high power but short

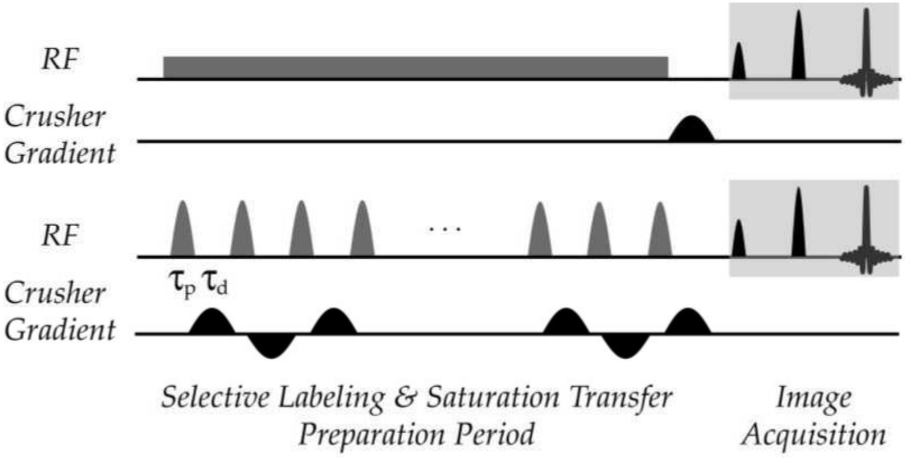

Figure 1.11: CEST presaturation schemes, from Sun et al. [33]
Top CW CEST: Long low-powered hard pulse (seconds) **Bottom** Pulsed CEST: train of high-powered short shaped pulses (milliseconds each) separated by even shorter delays.

width, spaced by shorter intervals can build up and maintain a saturation steady state, in what is called a pulsed CEST experiment (see Figure 1.11, from Sun et al. [33]). As before, random crusher gradients after each prepulse spoil the residual transverse magnetization, to avoid echoes due to transverse coherence [34]. The average $\vec{B}_1$ power can be higher than in the CW-CEST case (less SAR), but ω_1 is no longer constant and new parameters have to be considered when optimising the sequence, such as the duration of the prepulses, the shape and the delay between them. Standard pulse shapes are Gaussian (the most used [33–36]), Hanning-windowed Gaussian [22], sinc-gauss [37] or Fermi [38].

If the presaturation pulse were to be applied before every line of k space, a full CEST experiment would be quite long, therefore fast imaging readouts are predominant for CEST studies in order to improve temporal resolution. Sequences such as EPI [39–42], RARE [43, 44], FLASH [45] or FISP [46–49] are commonly used.

1.5.4 Representing the CEST contrast

Metabolites can be identified through their CEST effect, normally represented in a Z spectrum, which is a graph that shows the dependence between the intensity of the water signal and the frequency ω of the $\vec{B}_1$ field. Assuming a two pool system (water and a single CEST species), the water signal (normalised to the one observed without saturation) is measured throughout a range of $\vec{B}_1$ frequencies, therefore having an almost constant value over the entire spectrum with a big inflexion at the water frequency (set by default at 0 ppm), and a smaller one at the CEST metabolite frequency, see Figure 1.12 (from Sherry and Woods [18]).

$$Zspectrum = \frac{M_{sat}}{M_0} \tag{1.5.3}$$

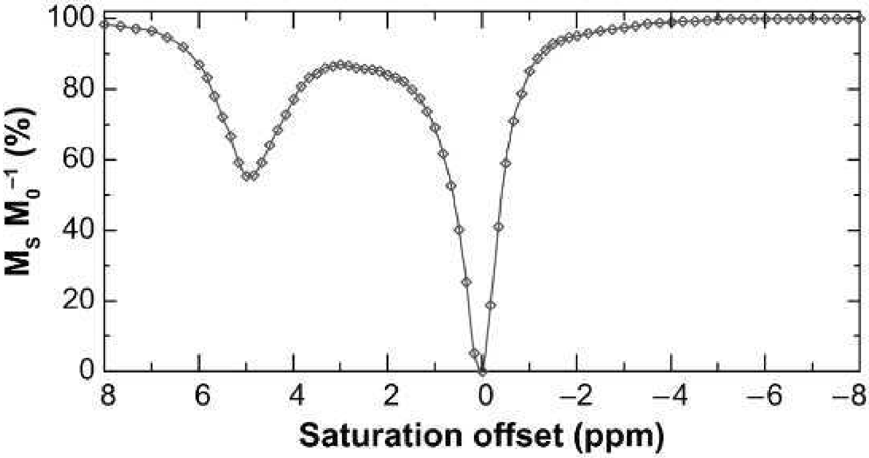

Figure 1.12: Example of an *in vitro* Z spectrum, barbituric acid, from Sherry and Woods [18]

The water frequency is at 0 ppm and the barbituric acid exchanging protons resonate at about 5 ppm. There are no other contributions in this phantom.

CEST techniques require the condition of slow exchange regime, or slow to intermediate regime in order to selectively saturate the solute protons [19]:

$$k_{ba} \leq \Delta\omega \tag{1.5.4}$$

where k_{ba} is the exchange rate from the bound protons to the free water and $\Delta\omega$ is the chemical shift ($\Delta\omega = \omega_{water} - \omega_{bound\ protons}$) [50]. Therefore, CEST benefits from high fields: the frequency separation is increased and there is a reduced interference of direct water saturation.

The *in vivo* Z spectrum contains many more features: direct saturation or spillover is still present at 0 ppm (its shape determined by B_1, T_1 and T_2 relaxations), while the broad MT resonance determines the baseline, amine and amide CEST effects can be found at 2 ppm and 3.5 ppm respectively [52], accompanied by visible Nuclear Overhauser Effects (NOE) mediated effects in the aliphatic range (see Figure 1.13). Several molecules containing hydroxyl groups have CEST effects in the 0-1.5 ppm region [31, 43, 53, 54], but they are not separate peaks from the water, which makes them harder to identify.

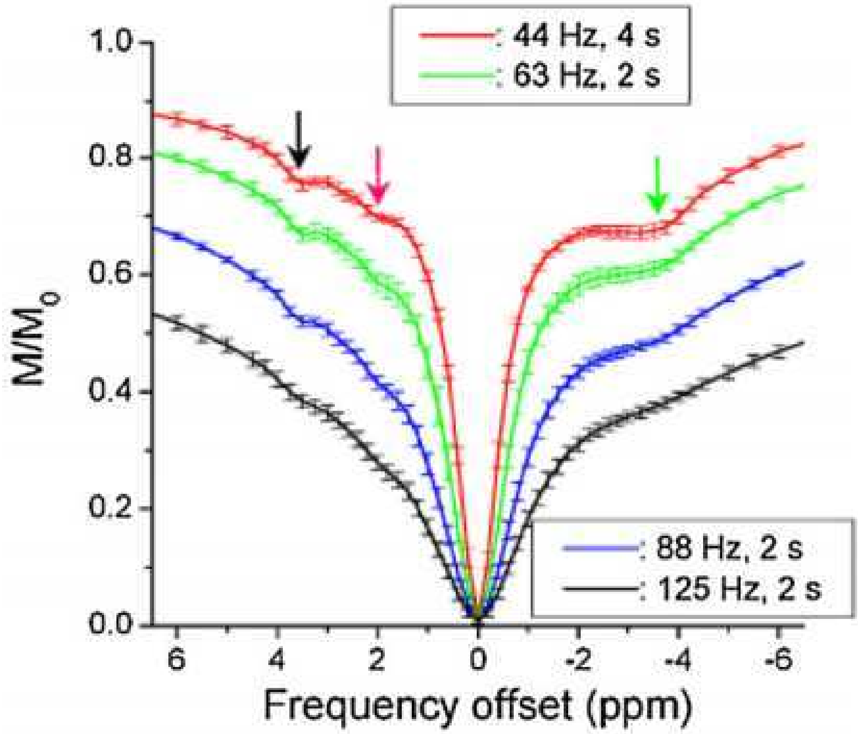

Figure 1.13: Example of an *in vivo* Z spectrum, rat cortex, from Jin and Kim [51]
The water frequency is at 0 ppm. There are visible amine and amide CEST contributions at 2 ppm (red arrow) and 3.5 ppm (black arrow) respectively, together with NOE mediated effects (green arrow) and a broad MT asymmetric effect.

1.5.4.1 MTRasym

In order to avoid spillover, which may dilute the CEST effect, an asymmetry analysis is often applied [19], taken from the Magnetization Transfer literature:

$$\text{CEST effect} = MTR_{asym}(\Delta\omega) = MTR(\Delta\omega) - MTR(-\Delta\omega) = \frac{M_{sat}(-\Delta\omega)}{M_0} - \frac{M_{sat}(\Delta\omega)}{M_0} \quad (1.5.5)$$

An assumption of the MTRasym metric is that the conventional magnetization transfer effects are also symmetric around the water peak, which is just an approximation. Other metrics and analysis methods have been recently developed to overcome the limitations of the traditional MTRasym, while novel acquisition techniques exist to separate MT from CEST, but are outside of the scope of this review (SAFARI [55], uMT [56], FLEX [20], LOVARS [57], CERT [58, 59]).

1.5.4.2 Other metrics and analysis methods

Inverse metric Eliminates spillover and macromolecular magnetization transfer effects (unwanted T_2 and MT contributions) making it more CEST specific, but it requires the system to have reached steady state or near steady state. [60, 61].

$$MTR_{Rex}(\Delta\omega) = \frac{1}{MTR(\Delta\omega)} - \frac{1}{MTR(-\Delta\omega)} \quad (1.5.6)$$

Model based analysis: multiple Lorentz pool fitting First proposed by Zaiss et al. [62], it is a fast and semi-quantitative analysis method that decomposes the CEST spectrum into a sum of Lorentzian shapes (with parameters such as amplitude A, width ω and frequency offset Δ, see equation 1.5.7). The number of Lorentzian pools can vary according to the application [63], but they often represent amide, amine, aliphatic peaks, MT, direct saturation or if applicable, paramagnetic CEST compounds [47]. This method, based on the weak saturation pulse approximation (more details in section 4.2.2), relies on enough SNR and sampling points [62].

$$signal(\Delta) = 1 - \sum_{i=1}^{n} A_i = (1 + (\frac{\Delta - \Delta_{oi}}{0.5 * \omega_i})^2)^{-1} \quad (1.5.7)$$

Model based analysis: MT Conventional magnetization transfer effects (MT) can be included in the the Bloch equations via a 3-pool model: water pool, bound pool, macromolecular pool, just by adding more coupled equations [64], similar to the situation when there is more than one CEST agent [65], more details in section 4.2.3. An assumption made in this case is the null proton exchange between bound pool and macromolecular pool (negligible compared to exchange with water, because of the small concentrations of those two pools). Using this kind of model for fitting a CEST experiment -which as has been said before, is always inherently also an MT experiment-, is an involved but more robust alternative to the use of the asymmetry analysis (equation (1.5.5) [22]). The number of pools for these analysis methods generally depends on the application, in approximation of an ideal n-pool model.

Model based analysis: APTR* Similarly, this approach relies on a three pool model fitting of CEST data, using the modified Bloch equations for chemical exchange, with pools for water, amide and asymmetric MT effects ($MT + NOE$). However, the objective of this method is to obtain a so called pure APT contrast (APTR*), which can be isolated from the other effects offering more robust results than the traditional MTRasym metric [66].

1.5.5 CEST applications

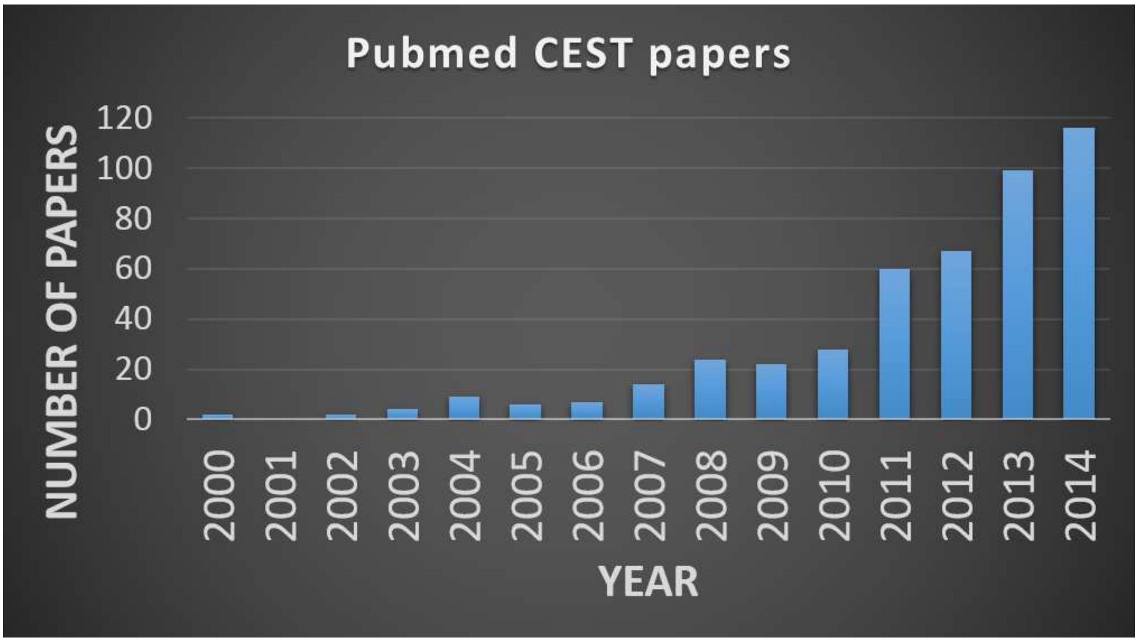

Figure 1.14: Published Pubmed CEST papers, 2000-2014. The search included the terms "CEST" and "Chemical exchange saturation transfer".

The CEST body of work has been constantly growing since the field started about fifteen years ago (Figure 1.14), with new agents, techniques and applications. A CEST contrast agent is a substance used to enhance the contrast of specific molecules in the body in CEST MRI imaging and can be endogenous (from inside the organism) or exogenous (from outside the organism). CEST agents are also often classified in three groups: diamagnetic CEST agents (diaCEST), paramagnetic exogenous CEST agents (paraCEST) and hyperpolarized CEST (hyperCEST). HyperCEST [67–84] uses xenon (hyperpolarised to increase detectability) as the solvent instead of water and cryptophane cages to create the chemical shift.

DiaCEST and paraCEST agents have very different frequency offsets referred to the water peak (0 ppm): a range of 0-7 ppm for diaCEST compounds and from -800 ppm to +800 ppm for paraCEST, which allows for imaging of faster exchanging species with more selective irradiation (see reviews in [85–87]).

As CEST contrast agents, endogenous diamagnetic substances have important advantages. They are non-invasive and readily available in the organism, but can be affected by low specificity and SNR. In table 1.2 several amide, amine and hydroxyl CEST metabolites are listed, together with reported *in vivo* applications (clinical and preclinical). Even though chemical shifts vary depending on the proton site in a molecule, an unequivocal assignation of CEST peaks in the Z spectrum to metabolites *in vivo* is normally not possible, due to many overlapping contributions. However, knowledge of the CEST contributors in a specific tissue and their properties (exchange rates, chemical shifts, T_1, T_2), can be used to establish a correlation between apparent CEST effects and metabolites [52].

Endogenous CEST groups	***In vivo* CEST metabolite reports**	***In vivo* applications**
Amines -NH_2 (2 ppm)	Creatine (CreCEST, 1.9 ppm) [88–91] Amine proton exchange (APEX, 2.5 ppm) [32, 92] Glutamate (GluCEST, 3 ppm) [93–98]	Muscle energetics Ischaemia Neuropsychiatric disorders
Amides -NH (3.5 ppm)	Amide proton transfer (APT) [26, 33, 59, 61, 66, 99–118] Glycosaminoglycans NH (3.5 ppm) (gagCEST) [31]	Cancer, stroke
Hydroxyls -OH (0.6-1.5 ppm)	Glycogen (GlycoCEST) [54] Glycosaminoglycans OH (1-2 ppm) (gagCEST) [31, 119–122] myo-inositol (MICEST, 0.6 ppm) [53, 123] Glucose (GlucoCEST) [43, 124, 125]	Glycogen metabolism Osteoarthritis Neurological disorders Cancer metabolism

Table 1.2: Endogenous CEST

The CEST effect is mainly determined by the exchange rate and the concentration of the labile protons relative to those of the water protons. Therefore, amide proton transfer (APT) is by far the most studied endogenous CEST contrast, due to the very low exchange rate (around 30 Hz) and relatively high concentration, which permits imaging at clinical fields (3 T). One of the applications makes use of the sensitivity to pH changes (the exchange rate k of a CEST metabolite is a function of temperature, pH and buffer properties of the solution [126]), to evaluate ischemic tissue [26, 66, 99, 108, 117], while others map the amide proton content in order to identify tumours [105, 110, 113, 116], even grading them [118]. However, APT contrast is affected by MT asymmetry and other contributions, which need to be isolated and understood [61, 114].

On the other end, hydroxyl groups can have from 500 Hz to more than 10000 Hz exchange rate, and they also suffer from small chemical shifts (0-1.5 ppm), which requires the use of high field scanners (>7 T or equal) to try to meet the slow to intermediate regime condition. Moreover, direct water saturation effects reduce their CEST sensitivity, and limit the saturation power that can be applied. Even so, molecules containing hydroxyl groups have been imaged with CEST MRI:
Glycosaminoglycans CEST imaging in cartilage (gagCEST) has the potential to be a biomarker of osteoarthritis [31, 119–122, 127–133]. *In vivo* imaging of glucose (glucoCEST) has been used to identify and characterise tumours, which have an upregulated glucose metabolism [43, 124, 125]. Finally, myo-inositol CEST (MICEST) has been proposed as a glial marker, with a study in a mouse model of Alzheimer's disease showing higher MICEST contrast than controls [123].

Amine groups have also been described as endogenous CEST contrast: for example the CEST effect of neurotransmitter glutamate has been studied in preclinical stroke models (pH effect), Alzheimer's disease mouse model [94], normal human brain [93, 95] and spinal chord [96].

NOE mediated signal can be detected in the aliphatic range in the Z spectrum, and although often considered a confounder for CEST effects (APT), it can provide complementary contrast and information, with an identical acquisition process [31, 59, 61, 111, 114, 134–138].

1.5.6 Postprocessing

B_0 inhomogeneity

The asymmetry analysis performed to remove the effects of direct water saturation (equation (1.5.5)) requires knowledge of the water frequency in every voxel. This information can be obtained in different ways: one possibility is to extract it from the Z spectrum, by interpolation of the signal close to 0 ppm and then to look for the offset of maximum saturation. This type of analysis will be compromised when there is too much asymmetry near the water peak (due to closely resonating CEST metabolites) or if the peak is too broad (strong RF power) [139].

Another possibility is the acquisition of an independent measurement of B_0, such as the acquisition of a gradient echo phase map to obtain a B_0 map [140] and use it to correct the CEST map. However, this method only provides a relative measure of the center frequency in a voxel. Also, a map acquired in this way would have to be co-registered if the sequence used is not identical.

To avoid these problems, there is the water saturation shift referencing (WASSR) [141] method: WASSR consists of the correction of B_0 inhomogeneities using a pure direct saturation image. Such an image is acquired using minimal B_1 prepulse power and duration, in order to minimise any CEST or MT contributions to the contrast. Thus, an absolute value for the frequency shift (the deviation from a conventional absolute water frequency, 0 ppm) is obtained for every voxel. A maximum symmetry algorithm is normally used, but there are other alternatives such as Lorentzian fitting [142]. Afterwards, the CEST image is corrected on a voxel-by-voxel basis. The WASSR sampling requires less offsets than a Z spectrum (around 16), but it still takes longer than a conventional B_0 map. One advantage, however, is its higher specificity to the related CEST experiment, since both CEST and WASSR images are taken using the same protocol [141]. A situation where WASSR performs well is when there is an overlap between the CEST and the water peaks, causing an asymmetric broadening at the center of the Z spectrum, which complicates the direct determination of the water frequency resonance.

Improving the CEST contrast

After obtaining a B_0/WASSR map, the Z spectrum is interpolated and shifted to center it around 0 ppm. Interpolation methods can be a simple spline method, or a polynomial fitting [101]. Algorithms can be applied to smooth noisy Z spectra [143] and the voxels with low SNR can be filtered out [45, 144] to avoid interpolation errors. Integral maps [145], combining information from a range of frequencies, can be calculated after B_0 correction in order to improve SNR, compared with the CEST map at a single frequency. Finally, alternative procedures such as multiple pool Lorentzian fitting or model based fitting can be applied instead of MTRasym (see section 1.5.4.2).

1.5.7 Advantages and disadvantages of CEST

CEST allows the observation of very low concentrated metabolites (mM range), even in some cases, metabolites which are not observed in the correspondent NMR spectrum [54] under physiological conditions. Therefore, it overcomes the lack in sensitivity of traditional MRI compared with PET or optical methods [19]. Moreover, diaCEST uses endogenous diamagnetic substances to obtain MRI contrast, thus avoiding the inherent toxicity of many paramagnetic exogenous agents [146]. CEST contrast can also be switched on and off and no expensive specific equipment is required. Finally, the CEST contrast benefits from higher fields: the separation of exchangeable protons from water (Δw) is proportional to the magnetic field strength. A larger Δw will allow the use of CEST agents with faster exchange rates and still adhere to the slow to moderate exchange rate regime ($\Delta \mathrm{w} \geq k_{ba}$). Moreover, longer T_1 relaxation times at higher fields will slow down the recovery from saturation, ensuring a larger contrast [139].

CEST images can be prone to artifacts, since they are vulnerable to B_0 and B_1 artifacts, especially at high fields. However, the main disadvantage of CEST over other molecular imaging techniques is the complexity of identifying the source of signal *in vivo*: for diaCEST many metabolites have overlapping signals in the 0-4 ppm range, with further contributions from traditional MT, NOE and spillover effects, which require careful interpretation and analysis.

CHAPTER 2

Molecular imaging methods for neuroinflammation review

2.1 Introduction

This chapter introduces the pathological process of neuroinflammation and highlights its clinical importance in neurological disorders. The current available imaging methods are reviewed and their advantages and shortcomings discussed. The chapter is divided in two main parts: in section 2.2 neuroinflammation and the processes involved are presented, while section 2.3 contains an overview of the *in vivo* molecular imaging methods and its applications related to monitoring neuroinflammation, with special emphasis in magnetic resonance methods (section 2.4).

The aim of this chapter is to examine the need for new non-invasive biomarkers for neuroinflammation.

2.2 Neuroinflammation

Neuroinflammation is the cascade of events that constitutes the chronic response of the central nervous system (CNS) to a pathological insult [147], involving factors such as activation of microglia and astroglia, in addition to expression of proinflammatory cytokines and chemokines. If the initial inflammatory response (acute inflammation) fails to identify and suppress the source of the problem, a chronic process may begin with further damage [148].

Neuroinflammation plays an important role in a wide range of disorders: neurodegenerative diseases (Alzheimer's disease, Parkinson's disease, Huntington's disease or amyotrophic lateral sclerosis [147]), stroke and inflammatory disorders such as multiple sclerosis, by contributing to processes of neuronal dysfunction, injury and loss, therefore conducing to disease progression.

However, its role is still poorly understood, due to the many other underlying processes taking place.

Imaging neuroinflammation using a quantitative molecular biomarker would have a strong clinical relevance for earlier detection and treatment monitoring [149].

2.2.1 Cytokines

Cytokines are small proteins that are relevant in cell signalling, as they can affect the behaviour of other cells. Pro-inflammatory cytokines such as interleukin (IL)-1 and tumour necrosis factor alpha (TNF-α) promote systemic inflammation. They initiate the cascade of inflammatory mediators by targeting the endothelium, promoting chemokine (small cytokines) release. There is a balance established between pro-inflammatory and anti-inflammatory cytokines. Anti-inflammatory cytokines block or suppress the activity of proinflammatory cytokines and chemokines. Examples include IL-4, IL-10, IL-13, and transforming growth factor TGF-β [150].

2.2.2 Cellular markers

One of the recognized signs of neuroinflammation is microglia activation [151]. Microglia, a type of glial cell (10% to 20% of glial cells in the human brain) are the resident macrophages of the CNS and have two different phenotypes: in their resting state, during which microglial cells have a highly ramified form, with long branches and a small cellular body, they constantly sample their surroundings watching for changes in the environment (bacteria, virus, damaged or anomalous structures, etc) and performing cleanup duties. Microglia undergo activation as a response to an anomalous situation [153], leading to multiplication, recruitment to the site of injury, morphological changes and release of a range of substances: pro-inflammatory neurotoxic mediators and anti-inflammatory compounds (TNFα, IL-6 and IL-1β). Morphologically, they adopt a more macrophage-like form, with thicker processes and a denser core. Activated microglia can at the same time have a neurotoxic behaviour (removing the damaged cells, secreting pro-inflammatory signals) and neuroprotective role (tissue repair and regeneration), promoting the reconstruction of the cerebral tissue [154]. This dual nature leads to tissue damage related to microglia activation, which together with the limited regenerative ability of the CNS makes an uncontrolled neuroinflammation response a dangerous event [155].

The microglia phenotype is regulated by soluble factors and cellular interactions. Microglia responds to stimulus such as blood brain barrier disruption (exposure to fibrinogen mechanism), neurotransmitter alterations (for example glutamate excess, either resulting from increased release from neurons or reduced clearance from astrocytes), damaged cells (with presence of

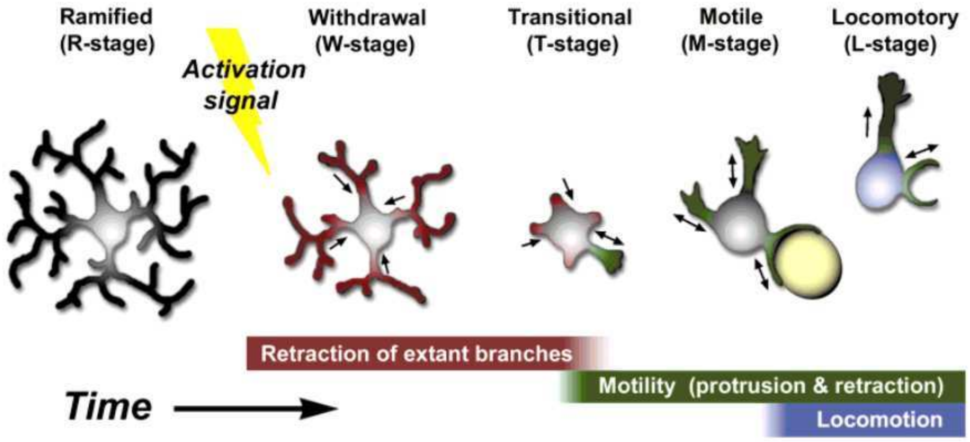

Figure 2.1: Microglia activation, model of morphological changes, from [152]
From left to right: Microglia undergoes activation from a resting state, with a small cell soma and numerous thin branched processes, to an activated form (with thicker and shorter branches, plus denser cellular bodies.

extracellular ATP) or loss of neuronal input (peripheral nerve injury) [156].

Other CNS intrinsic and blood-borne cells are also involved in the neuroinflammatory process: Pro-inflammatory cytokines segregated by activated microglia (such as TNF-α) can promote generation of new oligodendrocytes [157], impair the integrity of the brain blood barrier (BBB) or signal directly to astrocytes, lymphocytes and macrophages to regulate their function [158]. Neuronal activity can also be indirectly affected by these interactions. If alterations in the BBB take place during the neuroinflammatory process, this can lead to infiltration in the CNS of T cells, B cells, macrophages and leukocytes.

Another type of glial cells, NG2-positive oligodendrocyte progenitor cells (NG2-OPCs) can proliferate and migrate towards an injury [159], or replace lost oligodendrocytes in inflammatory situations [160]. Also present in the CNS, neural stem cells can generate different cell types which will join in the neuroinflammatory response [161]. In the context of severe damage, endothelia and endothelial progenitors [162], together with fibroblast-related cells [163] contribute to tissue replacement. Leukocytes functions include phagocytosis, debris removal [164] and can even be directly involved in tissue repair [165].

The heterogeneity of the participating agents and varied responses have led to a new terminology. "Reactive gliosis" refers to microglia, astroglia and NG2-OPCs. This term is used in substitution of the previously defined "resting" and "activated" states. Glial cells in the healthy CNS are not resting, but continually monitoring the local microenvironment, involved in a constant dynamic surveillance (microglia) or in synapse interactions (astrocytes). On the other hand, "activated" seems to imply a sort of binary switch, that goes against the reality of the existence of multiple glial responses to different anomalous stimulus (see Figure 2.2), which are varied in quality and intensity [166].

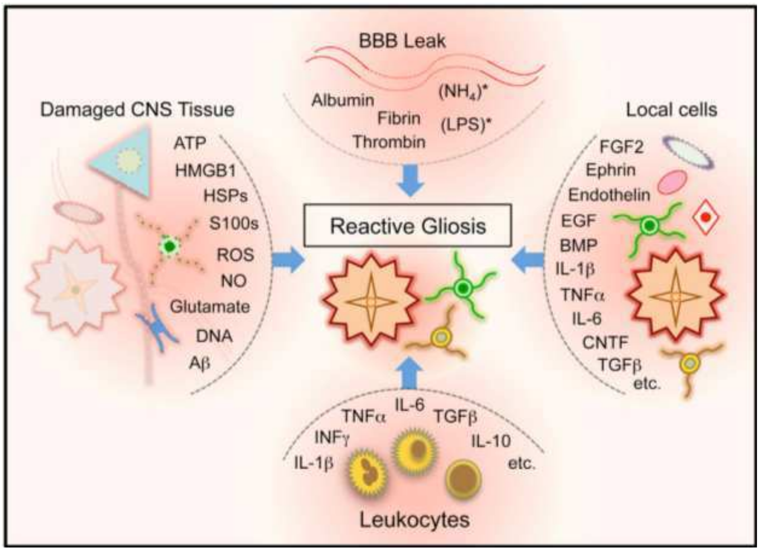

Figure 2.2: Multicellular and multimolecular regulation of reactive gliosis, from Burda and Sofroniew [166]: Reactive gliosis can be induced and regulated by a wide range of molecular signals, coming from varied CNS intrinsic and extrinsic sources.

The gold-standard method to study microglia and other cells involved in the neuroinflammatory response is immunohistochemistry.

2.2.3 Immunohistochemistry

Immunohistochemistry (IHC) is a method that can detect antigens in cells of a biological tissue making use of the specific binding antibody-antigen. Antibodies (Ab, or immunoglobulin, Ig) are glycoproteins whose function is to identify and label foreign substances in the body. They do so by reacting to a unique part of the target or antigen (from ANTIbody GENerator), and binding to it.

Antibodies suitable for neuroinflammatory processes in a biological tissue used in this work are:

Iba1 Ionized calcium-binding adapter molecule: Specifically expressed in microglia cells in the brain, its expression is upregulated during activation, although it binds to both activated and non activated states. An example can be seen in Figure 2.3 [167], where a mouse has received a systemic injection of LPS. A clear difference can be observed between the activated microglia on the right and the resting one in the controls (left).

More specific antibodies for activated microglia are, for example, CD68 (marker of active phagocytosis) and CD11b, a marker for activation/recruitment of both microglia and macrophages [168].

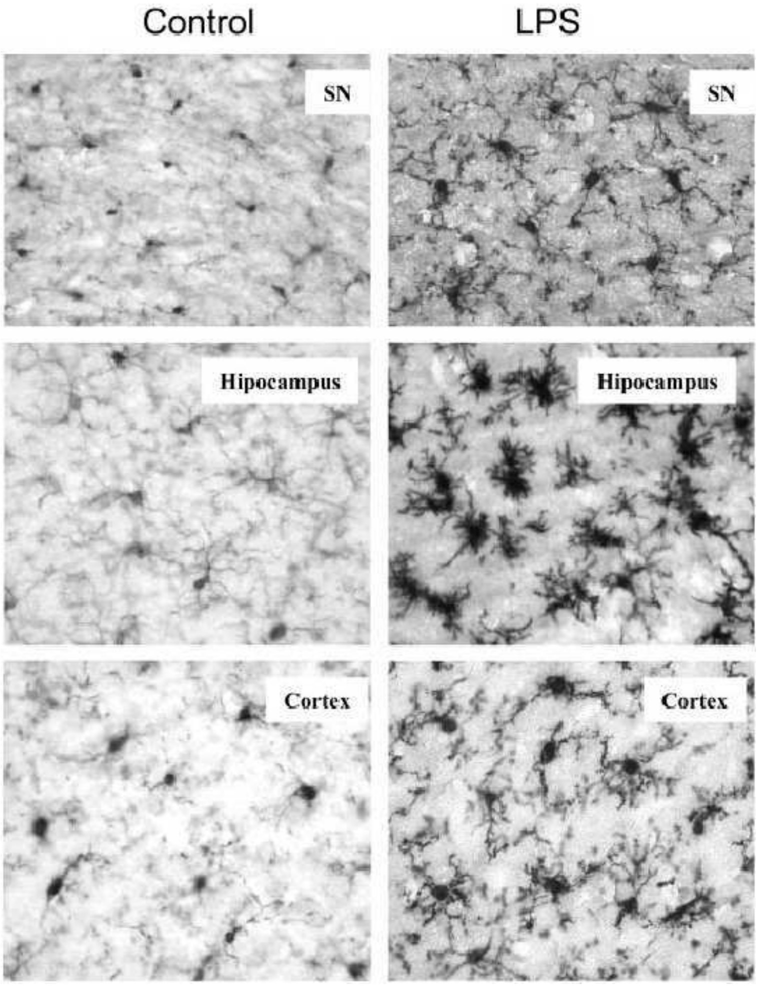

Figure 2.3: Iba1 immunostaining of three different regions of a mouse brain [167]: substantia nigra (SN) on top, hippocampus in the middle and cortex at the bottom row. The right column tissues have received a systemic injection of LPS, and the left column are the equivalent controls. Higher concentration of microglial cells, which have also shortened their ramifications and grown thicker bodies (signs of activation) can be seen on the right column, especially in the hippocampus region.

GFAP Glial fibrillary acidic protein: Expressed by several CNS cells, in particular, astrocytes. High abundance of GFAP stained astrocytes suggests presence of astrogliosis or reactive astrocytes [169].

Immunohistochemistry has been historically important to identify the agents involved in neuroinflammation, especially microglia, providing insights into functional and structural characteristics [153]. Therefore, although an invasive technique, histochemistry is the gold standard for validation of new techniques, but only provides a static picture of the complex neuroinflammatory process, without any dynamic information of the reactions taking place.

2.2.4 Innate and adaptive immune system in neuroinflammation

The innate or non-specific immune system comprises the cells and mechanisms that provide generic and immediate defence against infection. In neuroinflammation, microglia are the resident innate immune cells, responsible for the early response towards an anomalous stimulus, active in the recruitment of immune cells to sites of infection, via cytokine release [170]. Other innate immune cells from outside the CNS can also be involved, with phagocytic cells such as macrophages and neutrophils infiltrating the CNS when the BBB integrity is impaired.

The adaptive or acquired immune system is the responsible for creating immunological memory after an initial response to a specific pathogen, leading to an enhanced response to future encounters with the same pathogen. Antigens, defined in section 2.2.3, are substances that elicit the adaptive immune response, which is carried out by lymphocytes. Microglia can regulate both the innate and adaptive system, indirectly facilitating the entry in the CNS of T and B cells [171].

2.2.5 Myo-inositol as a molecular marker of neuroinflammation

The osmolyte myo-inositol is considered a putative glial marker since it is primarily present in glial cells. It has been proposed as a marker for microglial activation [172, 173], with two possible mechanisms: first, since myo-inositol is found in a much higher concentration in glial cells than neurons, during activation, the proliferation and migration of microglia in a specific area will have as a result the increase the myo-inositol content in the region. A second argument considers the fact that myo-inositol functions as an osmolyte maintaining glial cell volumes. Since activated glia have enlarged cell volumes, they tend to have elevated levels of myo-inositol [174]. However, the physiological mechanism has not been properly described and evidence is usually centered about myo-inositol levels increasing in several neuroinflammatory disorders (see section 2.3.2.1).

2.2.6 Lipopolysaccharide administration as a neuroinflammatory stimulus

Lipopolysaccharide (LPS) is a bacterial endotoxin. Once in the brain, it binds to the Toll-like receptor 4 (TLR4), predominantly expressed in microglia in the CNS, as an agonist [175], stimulating cytokines (IL-1β and TNFα) and chemokines release and inducing neuroinflammation, with microglia and astrocyte activation. LPS administration, either central or peripheral, is considered a neuroinflammatory model and has been widely used as a neuroinflammatory stimulus [176]. There are several mechanisms postulated as to how peripheral LPS induces its effects on the brain. One of the most common is that it does it directly, by crossing the brain blood barrier (BBB) [177], but other authors support different indirect processes: stimulation of afferent nerves [178], release of particles with BBB crossing capabilities [179], acting at circumventricular organs [180] or altering BBB permeabilities and functions [181]. A study by Banks and Robinson concluded that brain uptake of circulating LPS was very limited and therefore, most effects of peripherally administered LPS were likely mediated through LPS receptors located outside the BBB [182].

LPS effects have been studied with different readouts: behavioural (reduced locomotor activity and food burrowing [183, 184]), TSPO PET [185–188], optical [189, 190] and MRI: superparamagnetic iron oxide cell tracking [191, 192] and MRS (see detailed review in 3.2), often accompanied by histological verification (reactive gliosis).

2.3 *In vivo* molecular imaging methods review

Molecular imaging is the discipline dealing with the characterization, measurement and visualization of the biological pathways at the cellular/molecular level. It has been outlined as the "noninvasive, quantitative, and repetitive imaging of targeted macromolecules and biological processes in living organisms" [193]. In contrast with anatomical imaging (which shows the consequences of the molecular changes), molecular imaging can provide information of a disease onset, allowing earlier detection and treatment monitoring [194].

2.3.1 Nuclear imaging: Positron emission tomography, PET

PET is a nuclear imaging technique requiring a radioactive isotope (tracer) with a short half-life able to bind specifically to the biomolecular target. Once the tracer is introduced in the body and enough time for binding has passed, the imaging process begins:
the radioactive isotope undergoes positive beta decay, releasing a positron. The positron travels through the tissue, its kinetic energy decreasing until annihilation occurs (usually, no more than 1 mm away from the tracer/biomolecule compound). Annihilation is the interaction of

an electron and a positron resulting in their destruction and in the emission of two gamma rays (at exactly 180° from the centre of mass frame). This phenomenon is the one detected by the PET scanner, which is typically made of a torus of scintillators. These scintillators together with photomultipliers (PMTs) or avalanche photodiodes detect and amplify the gamma rays. Any pair arriving at two opposite scintillators within a predetermined time window may be called coincident and will trigger the recording of an event. From a large number of events, the original distribution of the tracers (and consequently, of the biomolecules) can be reconstructed using mathematical models, providing an image.

In neuroimaging, the tracer is introduced intravenously and needs to be able to cross (at least partially) the brain blood barrier (BBB).

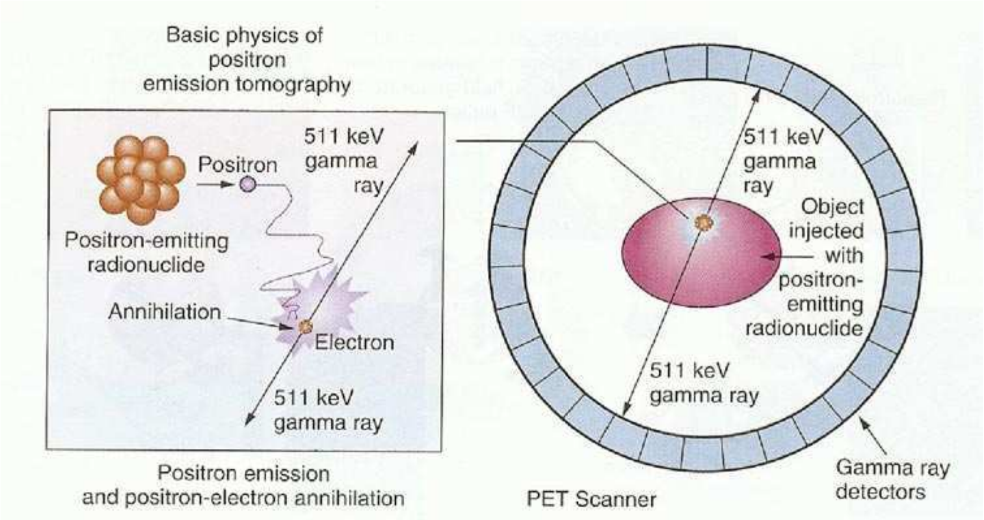

Figure 2.4: PET process, from http://www.cellsighttech.com/technology/pet.html
Inside a PET scanner, a radionuclide injected in a system undergoes positive beta decay, releasing a positron, which then finds an electron resulting in the annihilation of both. Two gamma rays at exactly 180° from the centre of mass frame are emitted in opposing directions and are recorded by the PET scanner detectors.

2.3.1.1 Applications of PET in imaging neuroinflammation

The following binding targets provide relevant information in the context of neuroinflammation:

Translocator protein, TSPO

The peripheral benzodiazepine receptor (PBR), known as the translocator protein 18-kDA (TSPO) can be found mostly in the outer membrane of the mitocondria, and its expression in microglia, macrophages, lymphocytes, neutrophiles and astrocytes increases during inflammation [195]. Therefore it is considered as an *in vivo* marker of neuroinflammation [196] and it has been used extensively in humans. The most common PET tracer for

TSPO is the isoquinoline carboxamide PK 11195, ^{11}C labelled. Clinical research applications include Alzheimer's disease, were a correlation was found between ^{11}CPK 11195 binding and cognitive scores [197], and increased binding in AD patients vs controls in certain brain areas [198]. Similarly, increased binding has also been observed in FTLD (frontotemporal lobar degeneration, [199]). Studies with ^{11}CPK 11195 in Parkinson disease report conflicting evidence about the existence of a correlation with disease severity [200–202]. In multiple sclerosis patients, a study by Banati et al. [203] shows that ^{11}CPK 11195 PET can delineate areas affected by disease activity, while Thiel et al. [204] reports a correlation with clinical outcome in stroke.

Other viable tracers are ^{11}C PBR28, ^{18}F FEAC, ^{18}F-DPA-714 (a review of the alternatives can be found here [205]), while novel ones are continuously being developed and tested, see Figure 2.5 [188].

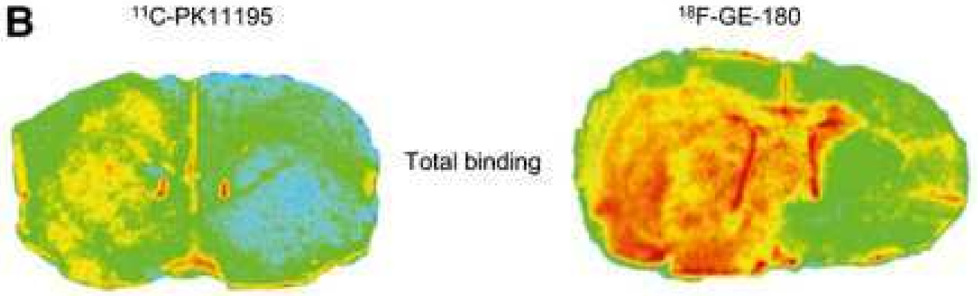

Figure 2.5: Comparison of two PET tracers binding for TSPO in a rat brain, from [188]
LPS intracerebral administration (10 μg) induced neuroinflammation on the left hand side of the brain. **Left:** ^{11}C-PK11195 **Right:**^{18}F-GE-180

Type 2 Cannabinoid Receptor (CB_2R)

The type 2 cannabinoid receptor (CB_2R) is part of the human endocannabinoid system, participating in central and peripheral inflammatory processes. In particular, it is upregulated by activated microglia, and appropriately labelled ligands can be used to image its distribution using PET, such as ^{11}C-A-836339 [187] (preclinical study, lipopolysaccharide neuroinflammatory stimulus injected mice showed an increased uptake in all brain areas) and ^{11}C-NE40 [206] (clinical feasibility study, novel tracer tested in healthy subjects for the first time, to investigate biodistribution and radiation dosimetry).

Inflammatory cytokines, COX-2

Cyclooxygenase (COX) is a integral membrane glycoprotein. The isoform COX-2 is rapidly expressed in several cell types in inflammatory conditions [207], and preclinical PET studies have been performed by binding it to ligands such as ^{11}Crofecoxib [208] with inconsistent results.

Glucose metabolism

There is evidence [209] of increased glycolysis in various immune cells participating in the inflammatory response. This can be assessed with the tracer ^{18}FFDG. However, in a neurodegenerative state, glycolysis is reduced [210],[211],[212], limiting the application of this technique for neuroinflammation [149].

Leukocyte infiltration

Alterations in the BBB often take place during the neuroinflammatory process, leading to possible infiltration of plasma components or leukocytes into the CNS. Leukocytes can be labelled by incubation with tracer compounds, followed by *in vivo* delivery for later PET detection once they cross the BBB during inflammation (clinical evidence from multiple sclerosis, ischemic and haemorrhagic stroke and Alzheimer's disease [149]). Confounders may arise due to labelling leakage during the process and unspecific accumulation in the brain [213]. This effect can also be imaged by measuring perfusion across the BBB. Nevertheless, according to [214], BBB disruption is not always permanent and can be transient in some areas, thus not correlating with functional effects, which limits its use as a neuroinflammatory marker.

2.3.1.2 Advantages and disadvantages of PET

The main advantages of PET are its high sensitivity, far superior to MRI or CT: even small amounts of the tracer can be detected with PET [149] and its specificity, with many available tracers binding to particular targets. However, depending on the tracer used, poor signal to noise ratio images can occur due to low tracer-receptor binding affinity, non-specific binding or, for neuroimaging, low brain uptake (in many cases, the tracer can bind to molecules outside of the brain [215]). Another issue is the fact that, due to the positron having travelled a certain distance from its creation (emission site) to its annihilation (detection site), PET resolution is inherently worse than magnetic resonance imaging or computed tomography [149]. But the main disadvantage of PET is the ionizing radiation required: the dose a patient receives has to be carefully watched and repeated PET scannings result in increased risk [216], making it less suitable for longitudinal studies. Moreover, the use of ionizing radiation implies complying with extensive safety regulations and the radioisotope production process time constraints: due to their short lives (^{11}C:20.4 min, ^{18}F:109.8 min), they need to be produced near the facilities in cyclotrons right before any procedure [2].

For neuroinflammation, translocator protein (TSPO) PET is currently considered as the most reliable marker and tracer ^{11}C PK 11195 features predominantly in the literature. However, this tracer has disadvantages such as a low SNR, the short half life of ^{11}C and the absence of a standardized quantitative imaging analysis method: there is not a robust kinetic model to aid in the image interpretation, coupled with the difficulty of finding a reference, an area of the brain with no tracer binding [205]. Because of these reasons, other alternative tracers are currently being studied, less prone to these errors.

2.3.2 Magnetic Resonance Spectroscopy

MR spectroscopy (MRS) is a non-invasive technique that uses nuclear magnetic resonance to characterize the internal structure of matter. Although not an imaging technique, it can be used to monitor neuroinflammation in a predetermined area. A description of the MRS signal, sequences and techniques can be found in chapter 1.

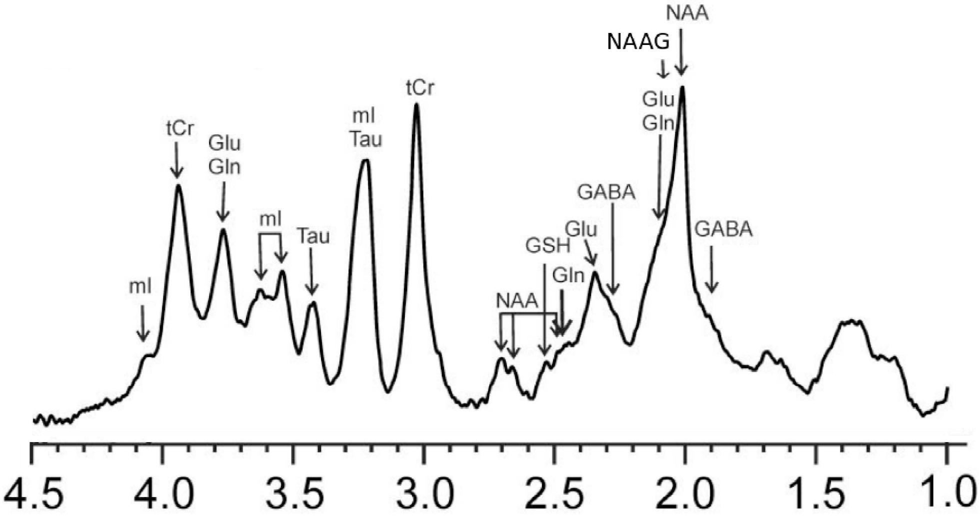

Figure 2.6: Mouse brain ^{1}H NMR spectrum at 9.4 T,, adapted from Braakman et al. [217] Metabolite levels that can be observed include: glutamate (Glu), glutamine (Gln), N-Acetyl Aspartate (NAA), myo-inositol (mI), total creatine (tCr), total choline (tCho), taurine (Tau), GABA, glutathione (GSH), N-acetylaspartylglutamate (NAAG).

2.3.2.1 Applications of MRS in monitoring neuroinflammation

^{1}H and ^{31}P MRS have both been used for neuroinflammatory applications. ^{31}P MRS provides information about energy metabolites (phosphocreatine, ATP), while ^{1}H MRS (covering most of the clinical literature) provides the levels of several metabolites related to glial and neuronal density. Important metabolites that can be measured with MRS are:

N-Acetyl Aspartate, NAA: Since it is only found in the nervous system (almost exclusively in neurons), NAA is considered to be a marker of neuronal density/dysfunction [173], but it is not directly related to neuroinflammation. Activated microglia can release neurotoxic inflammatory mediators, which can provoke a reduction in the NAA peak [174]. Examples include an observed decrease of NAA in several brain areas in patients suffering Alzheimer's disease [218, 219], multiple sclerosis [220], HIV [221] and Hepatitis C [222]. In an MRS spectrum the main NAA resonance corresponds to the peak at 2.01 ppm.

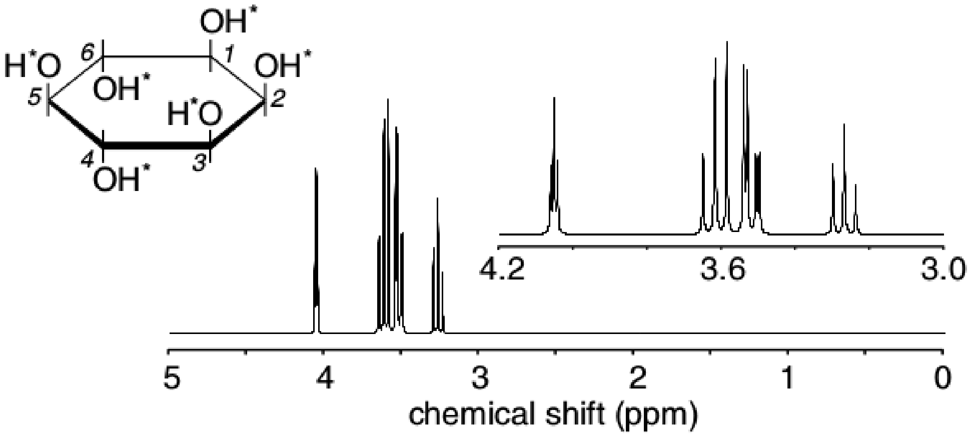

Figure 2.7: Myo-inositol molecule, from de Graaf [8]

Myo-inositol has six NMR protons, producing four groups of MRS resonances

***Myo*-Inositol, Ins:** Myo-inositol has six NMR protons, producing four groups of resonances: a doublet of doublets at 3.52 ppm, and three triplets (at 3.61 ppm, 3.27 ppm and 4.05 ppm).

It has been proposed as a marker for microglial activation [172, 173]. The arguments revolve around the fact that myo-inositol is present in a much higher concentration in glial cells than neurons and they proliferate when activated, leading to an increase in myo-inositol levels. Also, since myo-inositol is an osmolyte maintaining glial cell volumes and activated glia have enlarged volumes, they would have elevated levels of myo-inositol [174].

Clinical examples of increased myo-inositol levels can be found in multiple sclerosis [223], HIV [224], Hepatitis C [222], Down's syndrome [225] and Alzheimer's disease (AD) [218]. This has been interpreted as a sign of gliosis [226], from microglial or astrocytic activation, but ultimately, the mechanism behind these alterations is unclear [227].

Myo-inositol changes have been shown to presage the onset of cognitive decline in conditions with a neuroinflammatory component [228–231]. For example, elevations of myo-inositol levels in Alzheimer's disease have been shown to precede a decrease in NAA levels (sign of neuronal loss or dysfunction) and a full clinical manifestation of the disease [226].

A study by Marjanska et al. reports an increase in myo-inositol levels with age in a preclinical mouse model of Alzheimer's disease (APP-PS1), which is absent in wild-type controls [232], see Figure 2.8. This increase, at around 20 months of age, is attributed to microglial activation in those animals, which may accelerate at that age.

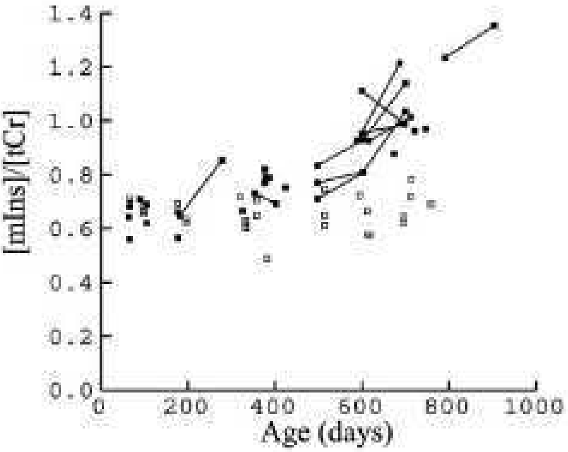

Figure 2.8: Myo-inositol increase with age in a mouse model of Alzheimer's disease (APP-PS1) from Marjanska et al. [232].
On the y axis, the ratios of myo-inositol to total creatine levels, which are used as a reference, while the x axis represents the age of the mice (up to 904 days). The black squares datapoints belong to the transgenic APP-PS1 animals, with the white squares as controls. The solid lines between datapoints represent repeated measurements on the same animals. There is a myo-inositol increase with age in the AD mice, not observed in the controls.

Glutamate, Glu: Glutamate is the primary neurotransmitter involved in excitotoxicity and direct precursor of GABA. It is compartmentalised in pre/post synaptic terminals, astrocytes, and found with minimal concentrations in the extracellular space. A loss of homoeostatic regulation caused by neuroinflammation can lead to increased availability of extracellular glutamate (enhanced astrocytic and activated microglia release [233]). Several *in vitro* studies support this, showing increased glutamate production in activated microglial cells [234, 235]. Furthermore, reduced levels of intracellular glutamate may also reflect decreased reuptake of glutamate from the extracellular space by activated glia (decreased glutamatergic metabolism [236]).

An excessive concentration of extracellular glutamate can cause cell death, which in turn manifests as cognitive impairment. Alterations in glutamate levels produced by changes in glutamatergic regulation are characteristic of many neurodegenerative diseases [237], such as Alzheimer's disease, where reduced MRS ratios have been found in the hippocampus and Parkinson's disease, with reduced levels in the sustantia nigra [174].

As a molecule, glutamate has a complex NMR signal spread over many resonances (see

Figure 2.9), which at low magnetic fields is indistinguishable from the metabolite glutamine (Gln). Therefore, the sum of both (referred as Glx) is often quantified in MRS instead.

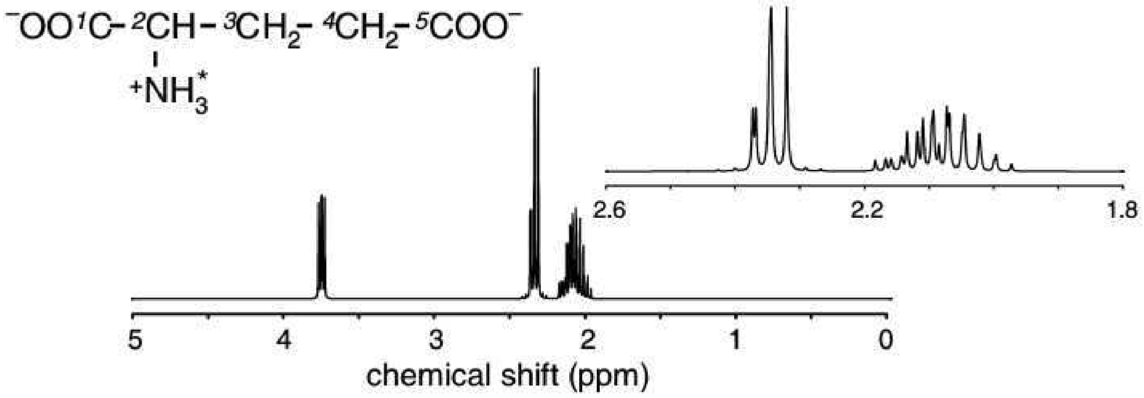

Figure 2.9: Glutamate molecule, from de Graaf [8]

Glutamate has two methylene groups and one methine group, strongly coupled, giving raise to a complex NMR signal, with many low intensity resonances.

Total choline, tCho and total Creatine, tCr: Choline is a marker for cell membrane metabolism and cellular turnover [174]. Its main single resonance at 3.22 ppm is often called total choline and it has contributions from free choline, glycerophosphorylcholine (GPC) and phosphorylcholine (PC) [8]. The peaks at 3.0 ppm and 3.93 ppm correspond to creatine and phosphocreatine (normally referred as total creatine), and are related to the levels of cellular energy metabolites.

However, both choline and creatine can be found in higher concentrations in glial cells than in neurons [172], which may create confusion when interpreting metabolite ratios data in neuroinflammation [12].

γ-Aminobutyric acid, GABA: Main inhibitory neurotransmitter in the CNS, with six NMR protons creating two triplets (3.01 ppm and 2.28 ppm) and a quintet (1.89 ppm). Due to its low abundance (about 1 mM in the human brain) and the overlap of all its resonances with higher concentrated metabolites in the MRS spectrum, its measurement usually requires specialized editing techniques (by isolating its signal from the rest of the spectrum) [238]. Elevated GABA levels have been found in Parkinson's disease patients [239].

The main advantage of MRS over many molecular imaging techniques is the non-invasive nature of the method, together with a robust and clinically accessible technique, as well as the existence of standardized analysis protocols and dedicated software. It can assess *in vivo* levels of relevant metabolites for neuroinflammation such as myo-inositol or glutamate, which often correlate well with clinical variables and neurological disease progression, providing a useful target for monitoring treatment effects [174].

However, special care must be taken for quantification in the context of neuroinflammation. As has been mentioned before, metabolite concentrations are usually expressed through ratios to total creatine or choline, with the assumption that the concentration of that metabolite remains constant (age, condition,etc.). But both choline and creatine are found in higher concentrations in glial cells than in neurons and consequently, they may be elevated in a neuroinflammatory context [172].

Nevertheless, the main disadvantage of MRS when monitoring neuroinflammation is the complex and dynamic nature of the phenomenon, which require a much higher spatial resolution than MRS can offer, in order to gain a thorough understanding [240], even if this can be improved with the use of multivoxel spectroscopy (MRSI) [241]. Time resolution can also be a hurdle, since obtaining a reasonable signal-to-noise ratio (SNR) in a MRS spectrum requires many averages (or bigger voxels, at the expense of spatial resolution), due to the inherent low sensitivity of MR and the very low concentrations of the metabolites of interest in comparison with the water peak (around 100000 times difference [174]). As an example, the parameters used in later chapters for *in vivo* preclinical MRS (mouse brain) required a minimum voxel size of 2x2x2 mm and 512 averages, with an experimental time of around 21 minutes per spectrum (SNR=18).

2.3.3 Optical imaging

Optical imaging refers to imaging techniques using visible, ultraviolet, and infrared light. The source of contrast can be bioluminescence, fluorescence, absorption or reflectance.

2.3.3.1 *In vivo* applications of optical imaging in neuroinflammation

Fluorescence imaging In fluorescence imaging, an external light of appropriate wavelength excites a target fluorescent molecule, which then releases light of a lower energy (longer wavelength) [242]. An example of target molecule is be the green fluorescent protein (GFP), first isolated from a jellyfish by Martin Chalfie, Osamu Shimomura, and Roger Y. Tsien, who were awarded the 2008 Nobel Prize in Chemistry for their discovery.

This protein has to be attached to the target of interest by DNA engineering, which illustrates the complexity of *in vivo* fluorescence microscopy. An example of an *in vivo* application for imaging neuroinflammation is the study by Davalos et al. [243], showing the dynamics of the response of microglial cells (labelled with GFP) to a traumatic brain injury [243], see Figure 2.10.

But if the imaging depth is to be more than a few mm, near infrared fluorescence (NIRF) has to be used: the absorption coefficient of tissue is much lower in the near infrared region (700-900 nm) and therefore, light can penetrate more deeply, to depths of several centimetres. *In vivo* application examples are lymphocyte infiltration in experimental autoimmune encephalomyelitis (EAE, most common animal model for multiple sclerosis) rats [244] or detecting neuroinflammation after cerebral ischaemia [245].

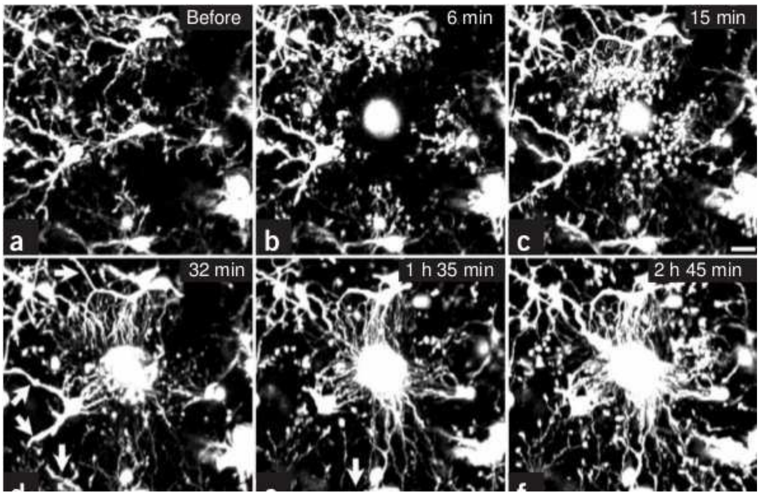

Figure 2.10: *In vivo* fluorescence imaging in a mouse cortex, from Davalos et al. [243]. **A)**Baseline **B)** to **F)** Microglia moving towards injury site, with proliferation and activation, images taken from 6 min to 2 hours 45 min after the lesion (created by a two-photon laser).

Bioluminescence imaging BLI exploits the ability of several non-mammalian organisms to biochemically generate light. An example of this is the firefly: the catalysis of the substract luciferin by the enzyme luciferase in the presence of oxygen, magnesium and ATP releases visible photons. In order to use this natural phenomenon as an imaging tool, genetic engineering (to produce the expression of luciferase genes) is performed on the relevant cells, which are later injected together with the necessary substract and observed. The emission of light is measured quantitatively with a highly sensitive charge-coupled device (CCD) camera, and can be linked to the presence of a promoter of a specific gene [246].

In vivo applications for neuroinflammation are restricted to small animals. They include the use of transgenic mice with a GFAP promoter as condition for the light emission process in several disorders, such as cerebral ischaemia [247], experimental autoimmune encephalomyelitis [248] and intracranial kainic acid injection [249]; other promoters (TLR2, in cerebral ischaemia [250]) or visualization of bone marrow cells differentiating into microglia after infiltration, following intrahippocampal LPS injection [190].

2.3.3.2 Advantages and disadvantages of optical imaging

The main advantage of optical imaging is its high sensitivity (potentially around picomolar [242]), combined with a very low background signal. Other assets are the use of non-ionizing radiation and relatively inexpensive equipment. Specific limitations of *in vivo* fluorescence imaging are the lack of penetration depth in biological tissues (caused by light absorption and scattering which decreases with increasing wavelength). Although NIRF allows for deeper penetrations (several cm), this only enables imaging of subcortical structures in humans. Bioluminescence imaging benefits from the absence of a external light source, but the requirement of luciferase genes and substrate insertions in the subjects cells or whole body clearly restricts its *in vivo* use to animal models.

2.4 Magnetic resonance imaging of neuroinflammation

Magnetic resonance imaging (MRI) has inherent advantages such as the absence of ionizing radiation or the capability of producing high spatial resolution three dimensional images in comparison with nuclear, optical imaging, which makes it ideal for clinical applications [251]. It is however, less sensitive, since the signal is proportional to the population difference of the spins of $^1H/^{19}F$, etc. in two different energy levels, which is very small. A range of MRI techniques are currently being explored for imaging neuroinflammation:

2.4.1 Structural

Structural readouts such as atrophy, vascular malformation or accumulation of extracellular water (edema) can be obtained with MRI [252]. In particular, measuring the brain volume has diagnostic value in neurodegenerative diseases (multiple sclerosis, see review in [253]), since brain atrophy is a sign of neuronal loss. However, by this point, irreversible damage has already occurred in the brain and the disease process is well advanced [153]. Moreover, brain atrophy is not directly related to neuroinflammation.

2.4.2 Superparamagnetic iron oxide nanoparticles

These particles are formed by an iron oxide core (magnetite FE_3O_4 or maghemite γFE_2O_3) and a variable coating. Their terminology is based on the size of the whole particle: superparamagnetic iron oxide nanoparticles (SPIO, 50-180 nm), ultrasmall superparamagnetic iron oxide nanoparticles (USPIO, 10-50 nm, the most common) or very small superparamagnetic iron oxide nanoparticles (VUSPIO, less than 10 nm). Once they are present in a tissue, they can shorten

T_1 (hyperintense T_1 weighted images) and T_2 (hypointense T_2 weighted images) to a greater extent than gadolinium (and with a longer circulating half-life [254]).
Applications for imaging neuroinflammation include for example, tracking macrophage infiltration in the brain in experimental autoimmune encephalomyelitis (EAE) models [1].

In a study by Chin et al., circulating macrophages become labelled before entering the brain due to systemically administrated USPIO [256]. Another application is the observation of EAE lesions with higher sensitivity than gadolinium enhanced MRI [214, 257] (see Figure 2.11) or studying tumour morphology with labelled activated microglia [258]. Monitoring macrophage infiltration with iron oxide particles seems to provide complementary information to measuring BBB integrity with gadolinium and a few preliminary human studies have already used this technique [259]. Limitations of this approach are unspecific labelling [240] and toxicity concerns. The former can be improved with the extraction of the cells, followed by accurate *in vitro* labelling and their posterior reinjection, as opposed to the labelling process taking place in the circulatory system. Confounders such as blood pool effects and bleedings should be taken into account, as they can also produce negative MRI contrast [260].

A more important limitation is that macrophage infiltration is not present in all neuroinflammatory processes, especially not at the onset, since it requires a weakened BBB and does not provide information on the behaviour of the CNS intrinsic immune agents, such as microglia.

---

[1] Experimental autoimmune encephalomyelitis (EAE) is an animal model of brain inflammation. Inflammatory demyelinating disease of the CNS, mostly used with rodents and considered as an animal model of multiple sclerosis (MS), EAE is characterized by T-cell and monocyte infiltration in the CNS, associated with local inflammation. There are two main approaches to induce EAE: the first is based on direct immunization with autoantigen (active EAE). Sensitization to myelin antigens in EAE usually requires an adjuvant (agent that can potentiate an immune reaction). Adjuvants can be synthetic materials or bacterial components with the capacity of activating the innate immune system via pattern recognition receptors, for example CFA (Complete Freund's Adjuvant), Pertussis toxin, Muramyl dipeptide, Lysoleeithin or LPS. The second approach to induction involves the transfer of activated T cells, specific for myelin-associated autoantigens of the CNS (passive EAE) [255].

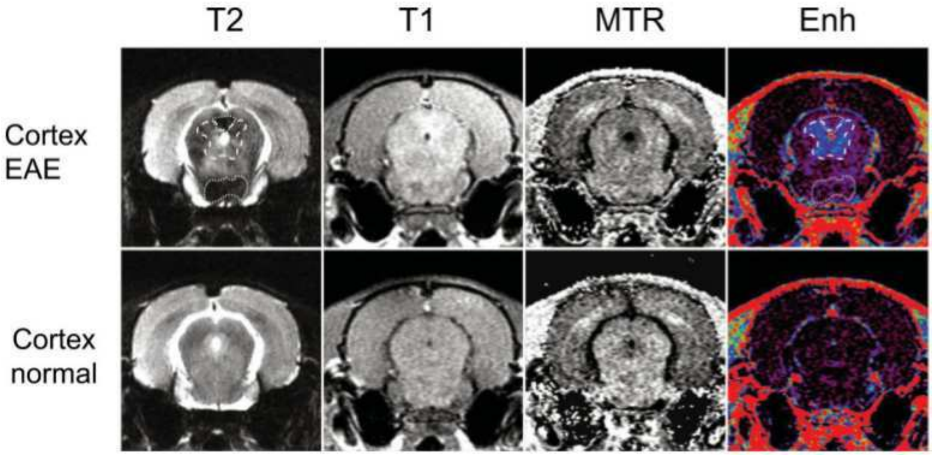

Figure 2.11: USPIO contrast, from Rausch et al. [214].
T_2 and T_1 images (first two columns), compared with MT images (third column) and Gd MRI enhancement (fourth column), in the cortex of a EAE mouse model (top row) and controls (bottom row).

2.4.3 Manganese enhanced MRI, MEMRI

Manganese (Mn^{2+}) provides positive MRI contrast in T_1 weighted images (T_1 shortening). Mn^{2+} acts as a Ca^{2+} agonist in biological systems and is taken up in neurons and glial cells, highlighting areas of intense neuronal activity under normal brain conditions [261]. Only a few studies have proposed MEMRI applications related to neuroinflammation: Wideroe et al. found a morphological correlation between MEMRI enhancement and microglia activation brain areas in rat ischaemia ([262], see Figure 2.12). A similar relation has been reported in cathepsin D-deficient mice [263]. In a recent study, Bade et al. found that inflammation stimulates Mn^{2+} uptake by neurons [264] (mouse model, LPS intracerebral injection).

Excessive exposure to Mn^{2+} leads to central nervous system toxicity, which needs to be taken into account for MEMRI. As for neuroinflammatory applications, MEMRI has specificity limitations, since it is very difficult to distinguish between gliosis and neuronal death/injury, which is not directly related to neuroinflammation [262, 264].

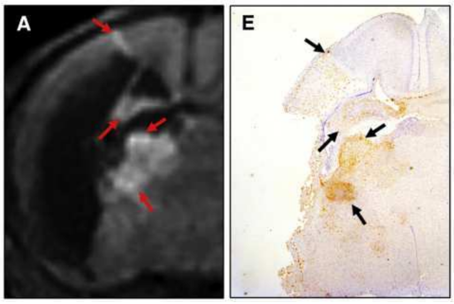

Figure 2.12: MEMRI enhancement in a rat pup suffering from ischaemia, from [262]
Left: MEMRI image. **Right:** Activated microglia (histology, CD68)

2.4.4 Fluorine MRI

The natural, stable, fluorine isotope ^{19}F is MR active, with a resonance frequency which is 94% that of the ^{1}H. It has a magnetic sensitivity similar to the ^{1}H nucleus (83%). The main advantage of ^{19}F MRI is its high specificity, due to the lack of background signal in the organism. There is no endogenous fluorine and therefore, all the signal in a ^{19}F MRI experiment comes from the fluorine injected beforehand in the form of an MRI contrast agent, which however also leads to long experiment times and low signal to noise ratio in the images (low ^{19}F concentration). To satisfy the need for a high concentration of ^{19}F nuclei, perfluorocarbons (PFCs) are often used as contrast agents: these are molecules with a similar structure to organic compounds, with all the hydrogen atoms replaced by fluorine [265].

Inflammation has been visualized using the uptake of PFCs (systemic intravenous injection) by macrophages in the peripheral and central nervous system [260, 266] for example in a model of focal cerebral ischaemia [267]. Another study has employed ^{19}F nanoparticles and a specifically designed probe to overcome low SNR issues [268].

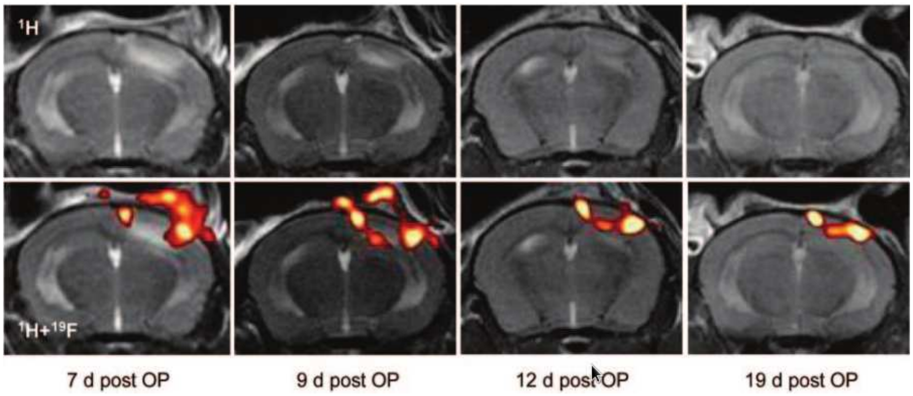

Figure 2.13: PFCs infiltration over time in a ischemic region (macrophages), mouse brain, from Flogel et al. [267].
Top:^{1}H MRI images over time (7 to 19 days after iv PFCs administration). **Bottom:** Correspondent ^{19}F MRI images, which show the macrophage infiltration.

2.4.5 CEST

Chemical exchange saturation transfer (CEST) is another molecular MRI contrast mechanism, described in detail in chapter 1. Endogenous CEST compounds include hydroxyl (OH), amine (NH_2) and amide groups (NH). Furthermore, this contrast can be manipulated during the same acquisition. Compared to MRS, the CEST contrast is much higher for many metabolites, due to the amplification of the signal that takes place through many exchanges in the saturation process [139]. These properties make CEST very different from other magnetic resonance modalities, in terms of specificity and sensitivity, being ideally suitable for molecular imaging. However, very few studies have explored the possibility of imaging *in vivo* neuroinflammatory biomarkers with CEST:

Liu et al. reported CEST measurements 24 hours after intratumoral LPS injections (1 mg/kg, n=4 mice), with no significant differences found in the CEST readout a day after drug administration compared to baseline. The small sample size is related to the fact that the LPS group was just a control to exclude inflammation effects and not the main objective of the study, which was to characterise the infection of tumour-homing bacteria in bacteriolytic cancer therapy using endogenous CEST contrast [269].

Haris et al. has proposed CEST imaging of myo-inositol, MICEST [53] (six OH groups per molecule), as a novel contrast method for glial cells proliferation/activation [123]. Myo-inositol MICEST mapping was performed in a mouse model of Alzheimer's disease (n=5, APP-PS1 mice, see Figure 2.14) and age matched wild type (WT) controls. A 50% higher MICEST contrast was found in AD mice, choosing a region of interest devoid of cerebral spinal fluid). Moreover, higher intensity of GFAP immunostaining was observed in the AD animals compared to controls and MRS data suggested an increase in myo-inositol levels in AD mice, although no direct correlation with MICEST could be established. Finally, it is important to mention that these significant CEST differences between groups (AD and WT) have been described only for 20 month old AD mice, the age of all the animals in the study. Cognitive deficits in spatial learning and memory have been reported in this transgenic mouse model at 7 months, with massive amyloid-β (Aβ) load, disrupted cytoarchitecture and significant neuron loss in the dental gyrus at 17 months [270].

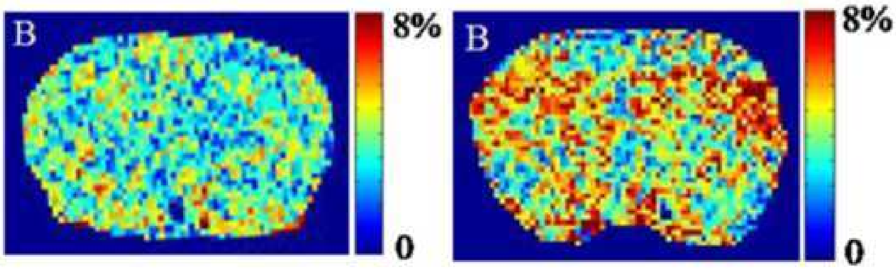

Figure 2.14: MICEST maps, from Haris et al. [123].
Right: brain from a 20 month old AD mouse model (APP-PS1, 50% higher contrast). **Left:** Age matched control.

This group has also reported glutamate measurements using CEST (GluCEST [93]), in the same animals [94], Figure 2.15. The 20 month old AD mice showed a reduction in GluCEST contrast (around 30%) in all brain areas compared with WT controls, while a significant positive correlation was found between GluCEST contrast and glutamate MRS levels ($R^2 = 0.913$). The glutamate changes are however not attributed specifically to neuroinflammation, with only

Alzheimer's disease biochemical changes being mentioned in the discussion.

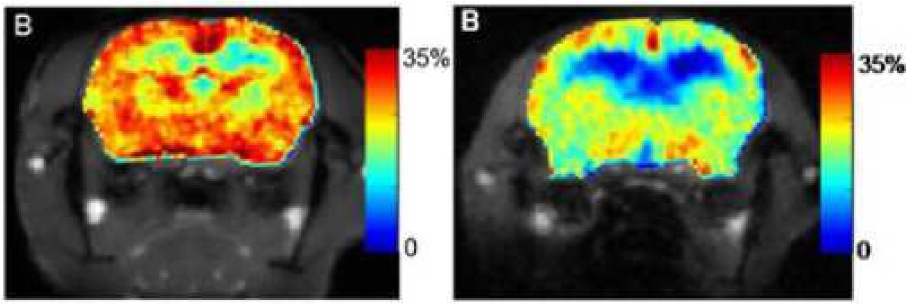

Figure 2.15: GluCEST maps, from Haris et al. [94].
Right: brain from a 20 month old AD mouse model (APP-PS1, 30% reduced contrast). **Left:** Age matched control.

A more recently published study, also involving 20 month old mice, reported a decrease of gluCEST contrast in an animal model of tauopathy (tau transgenic mice with the P301S mutation, PS19) [271]. Glutamate and NAA levels determined with PRESS MRS were lower in the hippocampus of tau mice compared with controls. Reduced gluCEST contrast in the *cornu ammonis* (CA) of the hippocampus and the thalamus were correlated with histological measurements of pathological tau severity, neuron loss and synapse loss. Glutamate changes are again attributed to neurodegeneration and not neuroinflammation.

Increased GlucoCEST accompanied by reduced APT CEST contrast has been recently reported in a mouse model of Alzheimer's disease (rTg4510 mouse), with the same goal of evaluating the degree of neurodegeneration. The *in vivo* glucose uptake was evaluated over time following an intraperitoneal injection of 1 g/kg glucose and was found to be higher in rTg4510 mice compared with controls [272].

Finally, another group has recently reported a 18% GluCEST decrease in a model of selective astrocyte activation (overexpression of the cytokine ciliary neurotrophic factor, CNTF). Lentiviral vector injections (lenti-CNTF) were administered in alternating brain hemispheres for n = 4 rats. The area characterised by GluCEST contrast closely matched the region of astrocyte activation as measured by immunostaining (Vimentin), see Figure 2.16. LASER MRS results showed an increase in myo-inositol (61%) and total choline (33%), accompanied by a decrease in glutamine (-14%), total NAA (-19%), taurine (-9%) and glutamate (-18%) [273].

Technical difficulties of CEST include the overlapping of many metabolites in the CEST signal, the influence of B_0 and B_1 inhomogeneities on the resulting images and the very different models, implementation, postprocessing and analysis strategies that are often used. Some of the CEST studies reported here are not focused on neuroinflammation specifically, but rather on neurodegeneration. However, they are reported for completeness, since the two processes coexist in disorders such as Alzheimer's disease.

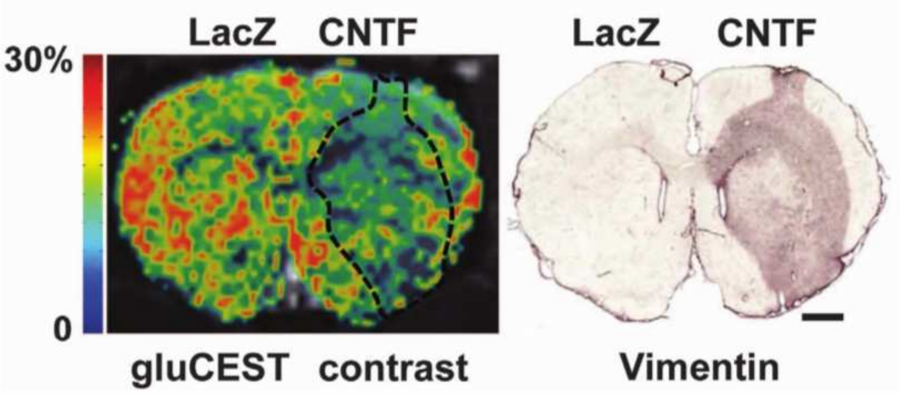

Figure 2.16: GluCEST and immunostaining maps, from Carrillo-de Sauvage et al. [273]. **Left:** GluCEST map (3 ppm) showing a lower gluCEST contrast on the right hemisphere, which has been injected with lenti-CNTF. **Right:** Histology slice: the region stained with vimentin + reactive astrocytes matches the marked area in the gluCEST map.

2.4.6 Discussion

MRI has many advantages over other molecular imaging techniques. It can produce 3D output without the risks associated to ionizing radiation (PET) and with a higher spatial resolution than MRS. Moreover, unlike optical imaging, it is widely used in clinical and preclinical settings. For all these reasons, MRI is the chosen technique to carry out the work in this project, with the objective of developing a quantitative molecular biomarker of neuroinflammation.

Out of all the magnetic resonance techniques mentioned before, MRS and CEST have the advantage of being non-invasive, with the possibility of obtaining biomolecular information without the need of external contrast agents. ^1H MRS can measure potential neuroinflammatory relevant metabolites such as myo-inositol, glutamate, choline and creatine, while myo-inositol and glutamate CEST have been recently developed. The metabolite myo-inositol emerges as a good candidate for the role of non-invasive neuroinflammatory biomarker, related to microglia activation and with a range of clinical and preclinical MRS studies in the literature. Moreover, the spatial resolution limitations associated with MRS can be overcome with CEST. Glutamate is another promising biomarker, related to astrocyte activation, which can also be measured with both MRS and CEST.

However, the only *in vivo* myo-inositol CEST study published so far evaluates a mouse model of Alzheimer's disease at a late stage of development (20 months), when the disease is very advanced and the animals are in a poor state of health. Instead, our aim is to study the early inflammatory response, to try to gain an understanding of the onset of the neuroinflammatory process, which will be very useful for an early diagnosis of neurological disorders. We want to study the metabolite changes (with an emphasis in myo-inositol and glutamate) that are involved at the beginning of the neuroinflammatory cascade, the timeline of these changes and how they relate to microglia and astrocyte activation.

CHAPTER 3

Metabolic response to a LPS challenge in a model of Alzheimer's disease, a MR Spectroscopy study

3.1 Introduction

The overall aim of this chapter is to develop and validate an MR biomarker of neuroinflammation with MR Spectroscopy (MRS) and histology. We want to study the early inflammatory response to a mild inflammatory stimulus (systemic administration of lipopolysaccharides, LPS, introduced in section 2.2.6) in wild type mice and in a mouse model of Alzheimer's disease (AD). The metabolic response to this stimulus will help to understand the early neuroinflammatory processes involved in neurological disorders such as Alzheimer's disease, a concept of capital clinical relevance from a diagnostic point of view.

MR Spectroscopy (MRS) is the monitoring readout, with a capacity to evaluate *in vivo* changes in several key metabolites, such as the glial marker myo-inositol. This osmolyte has been proposed as a marker for microglial activation [172, 173], but the physiological mechanism is not entirely defined (see 2.2.5). Instead, evidence relates mostly to increased myo-inositol levels reported in several neuroinflammatory disorders (clinical studies of Alzheimer's disease [218] and preclinical mouse models [232]).

After a brief review of the MRS studies containing LPS as a neuroinflammatory stimulus published so far (3.2), an MRS pilot study is first presented, to evaluate the intensity and time course of the metabolic response to LPS in wild type mice (3.4). Finally, (in section 3.5), a full study with n=44 mice is introduced, adding histology as validation and including both WT and AD mice genotypes, to assess the influence of a preexistent chronic condition on the neuroinflammatory response.

3.2 MRS studies with LPS as a neuroinflammatory stimulus

Metabolic changes after LPS induced neuroinflammation have been studied with MRS in microglial cell cultures. El Ghazi found an increase in glutamate (67%) and lactate (45%) after 24 hrs exposure to LPS (1 μg/mL) [234]. Lactate, the end product of glycolysis under hypoxic conditions, is normally considered as a potentially toxic metabolic waste product. A few *in vivo* MRS animal studies have also been performed:

Martin-Recuero et al. reported in a conference paper for the first time *in vivo* MRS measurements in wild type mice after an intraperitoneal (ip) LPS injection (5 mg/kg). They found changes in metabolites taurine (Tau), total choline (tCho), glutamate plus glutamine (Glu+Gln) and lactate (Lac), with the first three increasing immediately after injection in the hippocampus region. Another measurement, taken 24 hours later, revealed a significant decrease in Tau and tCho compared to baseline, plus a recovery of the Glu+Gln levels. Three days after injection, they observed an increase in Lac levels (associated to neurotoxicity), accompanied by another increase in tCho levels and a recovery of taurine. The early metabolic changes detected with MRS are attributed to altered osmolyte and phospholipid metabolism, caused by the LPS induced neuroinflammation. MRI measurements were also taken, with T_2 and MT maps showing an increase three days after the LPS administration [274].

Moshkin et al. injected two different ip LPS doses: 50 μg/kg and 500 μg/kg in ICR (imprinting control region) mice. MRS was performed in a voxel in the hippocampus three hours after the LPS administration, with no significant effects for the smaller dose and a increase in N-Acetyl Aspartate (NAA), total choline (tCho) and GABA for the higher dose. The focus of this study was to study the metabolic changes caused by a deficiency of available energy to the brain cells, caused by LPS or 2-deoxy-d-glucose (2DG) [275].

Lodygensky et al. performed an intracerebral LPS injection in the corpus callosum of rats (1 mg/kg) and took MRS measurements 24 hours later. Their results show an increase in lactate (toxicity) and macromolecules, accompanied by an intense microglial activation (evaluated with histology, CD68) due to neuroinflammation [276].

The baseline state of the animal can also be relevant: according to Cunningham et al., in the presence of a chronic disease (such as Alzheimer's disease) microglia are "primed" and will have a bigger response to LPS, producing a stronger inflammatory reaction [184]. But if the LPS dose administered is too high, a condition known as sickness syndrome can be induced, producing symptoms such as anorexia, fever, and lethargy [277], being counterproductive to study any differential effects deriving from initially primed microglia.

These studies provide a picture of the complexity of the processes involved, with the metabolic changes being dose and time dependent. There are no myo-inositol changes reported in any of these three studies, but at least one of them reports microglia activation. This raises questions over how the mechanism of myo-inositol as a glial marker works, both in intensity and time frames. For example, potential interesting questions are if myo-inositol is a marker of microglia activation, then how many glial cells are required to produce an MRS visible change in myo-inositol, in which state of activation should those cells be and at what time during the process does the metabolic changes occur.

3.3 The double transgenic amyloid APPswe/PS1dE9 model

The animals used in this study are APPswe/PS1dE9 mice. Double transgenic, they express two different transgenes: the human gene APP695 containing the Swedish mutation K594N/M595L (Amyloid Precursor Protein, APPswe) and presenilin 1 without exon 9 (PS1dE9) [278].

These mutations lead to a progressive, age-related Aβ neuropathology with amyloid plaques and elevated levels of Aβ [278], which are linked to familial forms of Alzheimer's disease (AD) [279]. The mice develop behavioral phenotypic and pathological features which make them useful as an AD model, such as Aβ plaques (as early as 4 months [280]), surrounded by activated microglia and astrocytes and significant memory deficits at 6 months compared with wild type controls [281].

3.4 Pilot study

3.4.1 Objectives

The aim of this pilot study is to evaluate the early metabolic response to a mild inflammatory stimulus, systemic administration of lipopolysaccharides (LPS), in wild type animals with MR Spectroscopy (MRS). The hypothesis is that MRS metabolic changes and in particular, myo-inositol, will reflect LPS induced transient neuroinflammation in the brain, compared with controls. The chosen LPS dose, 100 μg/kg is lower than all of the previously reported to induce significant changes in *in vivo* animal MRS studies. However, it has been proven to have behavioral effects, such as differences in open-field activity and food burrowing, avoiding sickness syndrome [183]. We are looking to establish a time course for the effects of LPS injection with different MRS time point recordings: immediately after injection, 3-6 hours later and 24 hours later.

3.4.2 Methods

3.4.2.1 Animals

All procedures were approved as required under the UK Animals (Scientific Procedures) Act 1986.

9 male spare mice (B6D2F1) were used in this experiment, with an average weight of 43 g ± 2 g. They had been group housed (2-6 per cage) in specific pathogen free (SPF) conditions, with a 12:12 h light-dark cycle, controlled temperature and humidity conditions, plus free access to food and water. The animals had undergone no previous procedures and appeared to be healthy.

3.4.2.2 Study design

Animals were randomly divided in two treatment groups: control (phosphate buffered saline , PBS, Sigma Aldrich, n=6 mice, five of them reused for the drug group a month later) and drug (lipopolysaccharide, LPS, 100 μg/kg, n=3 (+ 5) mice). They were also separated in different time point measurement groups, as in table 3.1.

n=9 mice total	0-4hrs	3-6hours	24hrs
Treatment: LPS	6	1	1
Treatment: PBS	4	1	1

Table 3.1: Study design: experimental groups classified according to treatment (drug/control) and time point of the measurement (in hours after treatment).

The MRS acquisition was performed in the hippocampus. This is one of the most microglial densely populated areas in the mouse brain [282], therefore expected to be more susceptible to LPS effects. Due to its size (2x2x2 mm), the voxel was also covering part of the thalamus, a situation which provided better shim values than if it was covering part of the cortex.

3.4.2.3 Protocol

A first MR spectroscopy scan (total acquisition time 21 min) was acquired to establish a baseline of brain metabolite levels. Then, approximately one hour later, each animal received an iv administration of either LPS (100 μg/kg) or PBS, delivered over an intravenous catheter attached to a tail vein and connected to a syringe pump, while remaining inside the MRI scanner (t = 0h). To track the metabolic response, MRS spectra were acquired for four hours after drug administration. After the last scan, animals were returned to their cages and a food burrowing test was carried out until 40 hours after injection.

Burrowing is a species-typical task and prior training is not needed. The animals have free access to food and water in their cages, plus an additional food filled glass container inside the cage, which is weighted before and after the test. Burrowing as a behavioral test has been shown to be very sensitive to low-dose endotoxin exposure [283].

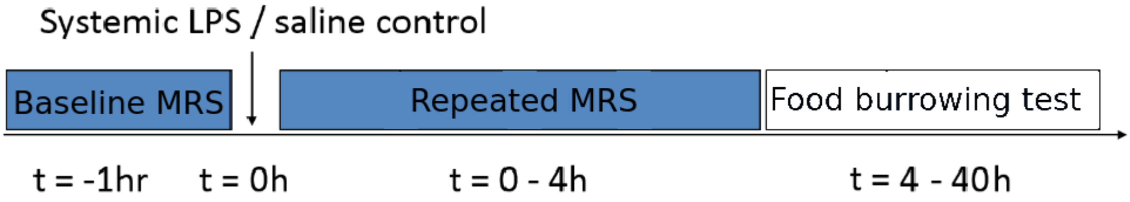

Figure 3.1: Lipopolysaccharide (LPS) MRS pilot experiment protocol. **t=-1h:** induction of anaesthesia, arrangement into the MRI scanner, MRS baseline. **t=0h:** iv administration of the drug/control. **t=0-4h:** MRS acquisitions. **t=4-40h:** Mice recover in their cages, food burrowing test.

3.4.2.4 MRS acquisition and analysis

MR spectroscopy was performed in a horizontal 7 T Bruker system (ParaVision 5.1), using a Point-Resolved Spin echo Sequence (PRESS) sequence: TR/TE = 2500/13 ms, 512 averages, total acquisition time 21 min, 8 dummy scans, 2048 data points, spectral width 4006 Hz. More details about the MR protocol, together with anaesthesia induction and monitoring can be found in the Methods section of the full study (3.5.2).

MRS data was analysed using LCmodel [10] with a simulated PRESS basis file provided by Provencher, with the experimental sequence parameters, without any data postprocessing other than eddy current correction. Inclusion criteria for individual spectra involved rejecting linewidths bigger than 15 Hz. Metabolites consistently within Cramér-Rao bounds < 10% were included in further analysis, i.e. glutamate (Glu), myo-Inositol (Ins), N-acetyl-aspartate (NAA), taurine (Tau), total choline (tCho), total creatine, Glx (Glu + Gln). The quantification of the metabolites was expressed as a ratio to the sum of selected metabolites [284], method which will be discussed further in the following full study. The ratios are expressed as percentages from baseline. The data was separated in groups according to mice treatment, and averages and standard errors were calculated.

MRS data was tested for normality distribution (normal probability plot) and then analysed with a 2-way ANOVA repeated measures mixed model approach using In Vivo Stat software [285], with drug (LPS/control) as a treatment factor, the different time measurements as the repeated factor and baseline levels as covariate. The data was tested for statistically significant differences overall and within groups (5% level). These statistics are hindered by the small sample size and they just aim to illustrate in more detail the pilot data.

3.4.3 Results: time course and MRS response to the LPS challenge

Out of the six animals which received the LPS drug, four had a increase in myo-inositol levels of around 20% (metabolite which has been associated with neuroinflammatory processes [218]), three hours after the injection (no effects at 6 hours or 24 hours). The other two had a indistinguishable response from the controls. This first group of animals has been called "responders" in graph 3.2, while the others are labeled "non responders". A trend for decrease in total choline levels (non significant) over time follows LPS injection, with the first group having a stronger decrease (Figure 3.2B).

Taurine levels showed a significant decrease with time independent of treatment (Figure 3.2C), while the rest of metabolites did not show any significant changes. The food burrowing test did not produce any significant differences between treatments, even when responders/non responders categories were considered.

3.4.4 Discussion

The fact that only 4 out of the 6 LPS animals showed a clear response to the drug might relate to the low LPS dose used or to the unknown degree of neuroinflammation experienced by the mice. The chosen LPS dose, 100 μg/kg has been proven to have behavioral effects, such as differences in open-field activity and food burrowing [183], but histological verification of the degree of inflammation in these animals is desirable for validation and will be incorporated in a subsequent full study. The decrease of taurine levels with time, independent from treatment was an unexpected result from the pilot and will have to wait confirmation from the full study.

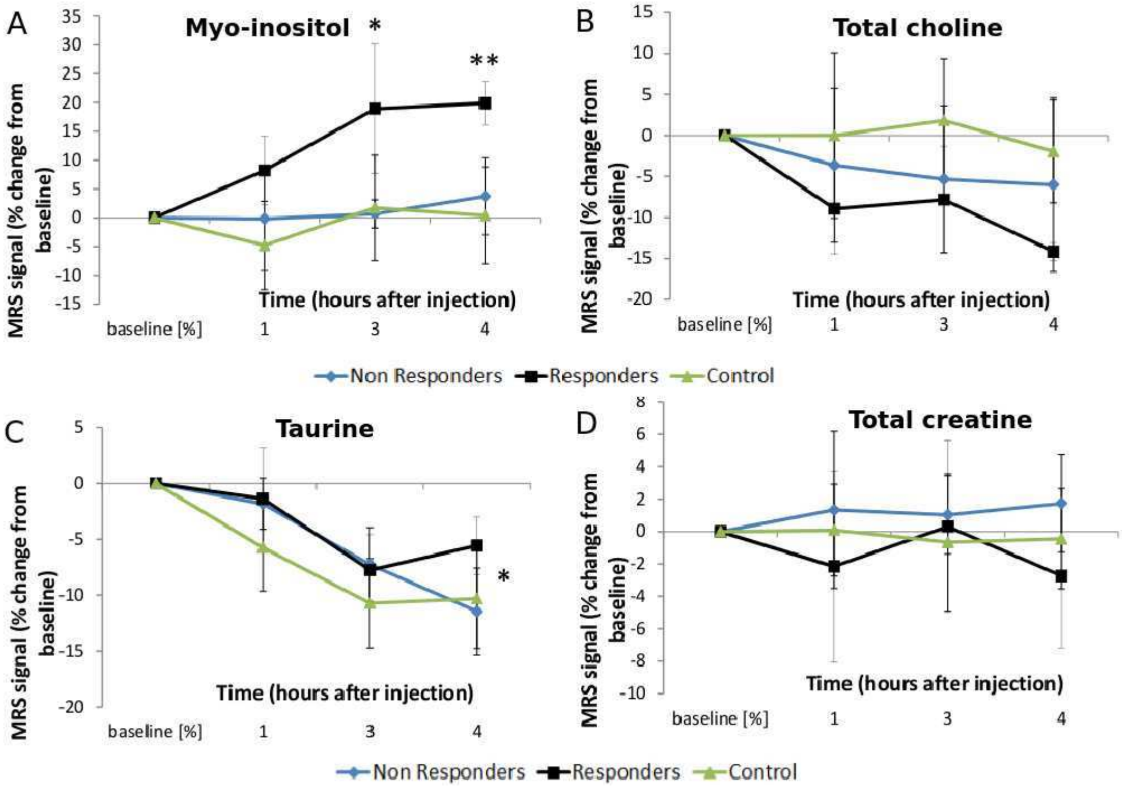

Figure 3.2: Pilot LPS MRS study.

A: percentage change from baseline of myo-inositol MRS ratios over time. The LPS treated animals were divided in two groups: responders (black), with a significant increase at 3 and 4 hours over the other group (non responders, blue). The control mice, PBS treated, are in green. **B:** percentage change from baseline of total choline MRS ratios over time, with the same group division. There is a non significant trend for decrease after the LPS injection, more accentuated in the responders group. **C:** percentage change from baseline of taurine MRS ratios over time (mice divided according to myo-inositol response). Taurine levels show a significant decrease with time independent of treatment. **D:** percentage change from baseline of total creatine MRS ratios over time, with the same group division. There is no change in the creatine levels for any treatment group, which validates its possible use as a reference.

3.5 Metabolic response to a neuroinflammatory challenge in a model of Alzheimer's disease, a MR Spectroscopy study

3.5.1 Objectives

The aim of this full study is to develop and validate an MR biomarker of neuroinflammation, by monitoring with MR Spectroscopy (MRS) the early metabolic response to a mild inflammatory stimulus: systemic administration of LPS.

Building on the pilot study, we hypothesize that MRS metabolic changes and more specifically an increase in myo-inositol levels will reflect LPS induced transient neuroinflammation in the brain. Additionally, we aim to test if the metabolic changes will be more pronounced in animals with a pre-existing chronic brain disorder (mouse model of Alzheimer's disease, AD), compared with controls.

The second objective is the validation of the MRS results using immunohistochemistry to evaluate the degree of microglia activation and reactive astrogliosis as markers of neuroinflammation, which was one of the questions arising from the pilot study results. The ionized calcium-binding adapter molecule (Iba1), expressed in the microglia cells in the brain, is upregulated during activation and the glial fibrillary acidic protein (GFAP) is used to stain reactive astrocytes [169] (more details can be found in section 2.2.3). Our hypothesis is that there is a relationship between myo-inositol MRS changes and microglial activation as seen by histology, with differences between treatment groups and/or mice types.

3.5.2 Methods

3.5.2.1 Animals

All procedures were approved as required under the UK Animals (Scientific Procedures) Act 1986.

44 male mice were used in this experiment, with an average weight of 37 g ± 6 g and an age of 9.2 ± 4 months. Drug and test naive, with no previous procedures, they had been group housed (2-6 per cage) in specific pathogen free (SPF) conditions, with a 12:12 h light-dark cycle, controlled temperature and humidity conditions, plus free access to food and water. As for genotype background, 22 are AD transgenic mice (APPSwe/PS1dE9), 13 are wild type (WT) littermates of the AD and 9 WT C57.

3.5.2.2 Study design

Animals were randomly divided in four groups, with two genotypes: AD transgenic (APPSwe-PS1dE9, n=22 mice) and age-matched wild type controls (WT, n=22 mice) and two different drug treatments: lipopolysaccharide (LPS, 100 μg/kg, n=23 mice) and phosphate buffered saline (PBS, Sigma Aldrich, as control, n=21 mice). The four groups composition can be seen in table 3.2. The chosen sample size is based on a power calculation estimating a 20% myo-inositol increase after LPS (coming from the "responders" mice result from the pilot study, see 3.4). Assuming that the significance level is set at 5% and the sample size is 10, the power of the experiment to detect a biologically relevant 20% change from control is 99% (calculation derived from software In vivo Stat [285]). The total number of animals was then chosen to be n=44, assuming an expecting drop out of around 10 %.

n = 44 mice	AD	WT
Treatment: LPS	12	11
Treatment: PBS	10	11

Table 3.2: Study design; experimental groups. 44 male mice in total, with an average age of 9.2 ± 4 months

The brain region chosen for MRS acquisition was again the hippocampus, due to its high microglial content [282], as well as being one of the most susceptible brain areas to Alzheimer's disease progression [174]. The voxel is also covering part of the thalamus, due to its size (2x2x2 mm) and to avoid the cortical area, more difficult to shim.

3.5.2.3 Protocol

All experimenters were blind to group allocation (genotype or treatment). The first n=5 experiments were performed by me, and the remaining n=39 were performed by Dr Marie-Christine Pardon and Dr Henryk Faas. After animals were anaesthetised and positioned in the imaging system, an iv catheter connected to a syringe pump was introduced in a tail vein, for drug administration inside the scanner. Two MR spectroscopy scans (total acquisition time 42 min) were acquired to establish a baseline of brain metabolite levels. Then, one hour after the first scan, each animal received an iv administration of either lipopolysaccharide (LPS, 100 μg/kg), dissolved in saline solution, or phosphate buffered saline (PBS), delivered through the iv line while remaining inside the MRI scanner. To track the metabolic response, a spectrum was acquired every hour for four hours after drug administration. After the last scan the mice were sacrificed (cervical dislocation) and their brains extracted for histological analysis. The total experiment time was around five hours and a half.

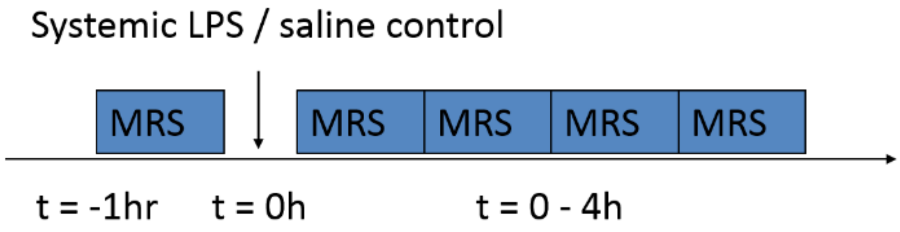

Figure 3.3: Lipopolysaccharide (LPS) MRS experiment protocol.
t=-1h: induction of anaesthesia, arrangement into the MRI scanner, MRS baselines. t=0h: iv administration of the drug/control. t=0-4h: MRS acquisitions, four timepoints.

3.5.2.4 Anaesthesia and monitoring

Mice were anaesthetised with a mixture of oxygen and isoflurane (Isocare, 3% for induction and 1-2% for maintenance). The animals were taken out of the cages, their body weight recorded and then induction was performed inside a plastic box resting on a homeothermic blanket control unit (Harvard Apparatus) outside of the scanner. Immediately after, they were positioned on the custom made scanner holder, tooth bar and ear bars minimizing movement, and the anaesthetic being delivered with a nose cone. Body temperature was monitored using a rectal temperature probe, and in order to keep it stable (around 36.5-37.5 °C), warm water was being constantly pumped through the holder, whose temperature could thus be regulated. The respiration rate was also recorded, using a pressure pad in the chest connected to a small animal unit (SA Instruments, typical respiration rate under anaesthesia: 90-120 breaths/min). An iv catheter connected to a syringe pump was introduced in a tail vein, for drug administration inside the scanner. Eye gel (Lubrithal) was applied in both eyes to avoid desiccation.

3.5.2.5 MRS acquisition

MR recordings were performed with a horizontal 7 T Bruker system (ParaVision 5.1). A volume coil (72 mm outer diameter) was used for excitation and a quadrature mouse brain surface coil for signal detection (Bruker, Karlsruhe, Germany). After tuning and matching, the frequency was adjusted and a global power calibration of the 90° pulse was performed. Three slices in coronal, sagittal, and axial orientations, were acquired with a fast low angle gradient method (FLASH) to check the mouse position and for planning the more detailed subsequent anatomical scans. Any visible position or excessive movement issues were corrected at this stage. For voxel placing, anatomical scans were acquired using a RARE sequence in coronal, sagittal and axial orientation (RARE factor 8, TE 11.8 ms, TR 5 s, matrix size 256 x 256, Field of view FOV 15x20 cm, number of slices 30 slices, slice thickness 0.5 mm). A single voxel of 2x2x2 mm was centered on the right hippocampus and thalamus (see Figure 3.4), this size was chosen during previous experiments because it provides enough signal to noise for quantification and specificity.

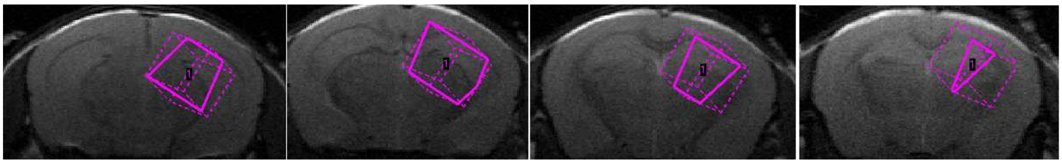

Figure 3.4: Representative MRS voxel:
A representative voxel used for this study, encompassing right hippocampus and thalamus, as seen during the planning stage using a RARE axial image.

Shimming was done first through a global shim (MAPSHIM, Bruker) followed by a local shim of the MRS voxel using FASTMAP. Shim quality was evaluated before every MRS acquisition by measuring the full width half maximum (FWHM) using a PRESS sequence without water suppression, and shims were adjusted if necessary.

Finally, *in vivo* MR spectroscopy was performed using a Point-Resolved Spin echo Sequence (PRESS) sequence: TR/TE = 2500/13 ms, 512 averages, total acquisition time 21 min, 8 dummy scans, 2048 data points, spectral width 4006 Hz. This short echo time was used to maximise the number of metabolites obtained. The water signal (VAPOR, 200 Hz bandwidth) and outer volume were suppressed for improved signal quality. A reference scan without water suppression was also acquired for subsequent eddy current correction, the total acquisition time for one spectrum being 21 minutes and 40 seconds.

To minimise frequency drift, the field-frequency lock was selected (it corrects the main field drift during localized proton MRS). Postprocessing (eddy current correction) was done automatically in Topspin, where the spectra could be visualized right after the acquisition was finished to check for any possible artifacts.

3.5.2.6 Histology

Histology procedures were performed by Alessandra Agostini and others. Mice were humanely killed using an approved (Schedule 1) method (neck dislocation) at approximately four hours after injection, and the brains extracted. Brains were post-fixed in 4% perfluroaldehyde (PFA) and refrigerated for a minimum of 48 hours, then dehydrated by an ascending alcohol series and embedded in paraffin. The paraffin blocks were cut into coronal microtome sections (thickness 7 μm) and those corresponding to a coronal plane around 2 mm posterior to Bregma were drawn up on microscope slides.

These slides were then deparaffined, rehydrated and incubated in citrate buffer, before the staining procedure. Primary antibodies Iba1 and GFAP were used for microglia and astrocytes, respectively. After an appropriate counterstaining procedure, the slides were dehydrated by exposure to various alcohol solutions and to finish, they were slipcovered, avoiding any bubble formation. 20x images were taken with a NanoZoomer 2.0-RS C10730 digital slide scanner (Hamamatsu Photonics K.K. Systems, Japan).

3.5.2.7 Analysis

Analysis of MR spectra and preparation and image analysis of histological slides were carried out blinded to genotype or treatment. MRS analysis was performed by me, while histological data was analysed by Felicity Easton [286].

LCmodel fitting parameters and metabolite quantification references

MRS data was analysed using LCmodel [10] with a simulated PRESS basis file provided by Provencher (sp@lcmodel.CA), with the experimental sequence parameters, without any data postprocessing other than eddy current correction. 17 metabolites are represented in the basis set: alanine (Ala), aspartate (Asp), creatine (Cr), phosphocreatine (PCr), γ-aminobutyric acid (GABA), glucose (Glc), glutamine (Gln), glutamate (Glu), glycerophosphorylcholine (GPC), phosphorylcholine (PCh), glutathione (GSH), myo-inositol (Ins), lactate (Lac), n-acetyl aspartate (NAA), n-acetyl aspartatyl glutamate (NAAG), scyllo-inositol (Scyllo) and taurine (Tau).

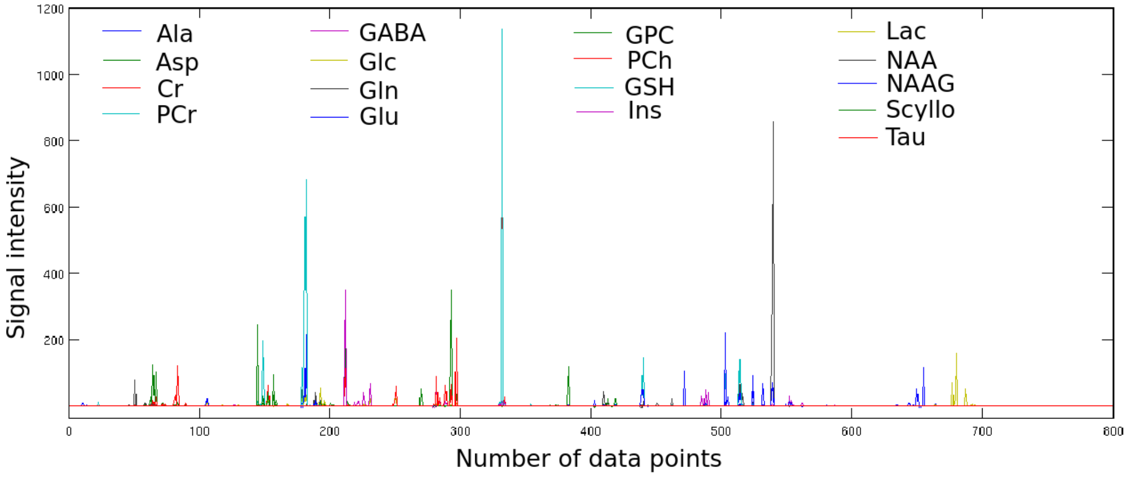

Figure 3.5: Basis file containing 17 metabolite resonances, PRESS sequence

Inclusion criteria for individual spectra involved rejecting linewidths bigger than 15 Hz (one mouse was excluded because of this). Moreover, one of the animals dataset was rejected due to the presence of a brain tumour and three mice were excluded due to an uneven baseline with too many lipid signals, which suggested a misplacement of the voxel (see table 3.3).

Two different sets of fitting parameters were used in the LCmodel software to try to get the best possible fit to the data:

Default parameters These are the most generic parameters, called default control parameters: The window of frequency-domain data that is normally analysed goes from 0.2 ppm to 4 ppm. The parameter NRATIO determines the number of soft constraints applied to the concentration ratios values, with a default value of 12. In this case, because the data is not human data, NRATIO=11 (there are no constraints applied to the taurine/creatine ratio). The preliminary analysis for initial referencing and phasing uses a reduced set of metabolites considered to be the landmarks of the spectrum. The default metabolites are five (parameter NUSE1 =5), including NAA, creatine, glutamate, myo-inositol and GPC (parameter CHUSE1 = "NAA", "Cr", "GPC", "Glu", "Ins").

New parameters The window of frequency-domain data now ranges from 0.5 ppm to 4.1 ppm. This excludes some macromolecules and adds another myo-inositol resonance, close to the water peak. NAA has been removed from the preliminary analysis metabolites: NUSE1 = 4 and CHUSE1 = "Cr", "GPC", "Glu", "Ins". This has been done because NAA was quite low for several datasets, which can compromise the the lineshape assumption based on NAA. The knot spacing for the spline baseline fitting (parameter DKNTMN) has been set to 5, in order to restrict the baseline and make it very flat. This will help prevent possible reproducibility issues caused by large variations in baseline fits [287]. The convolution range (dependent on parameter RFWHM) has been extended (RFWHM = 2.5 from default value 1.8), to obtain a more accurate lineshape estimation. Finally, appropriate values for the zero and first order parameters were introduced as prior phasing information to minimise running time.

Other changes that have also been considered are for example, removing all soft constraints (NRATIO=0), which did not make any significant difference in the results. Also, metabolites GABA and GSH were tentatively removed from the analysis (NOMIT = 2, CHOMIT = "GABA","GSH") to evaluate their influence on the myo-inositol fits. The hypothesis was that maybe both were over-represented in the fits at the expense of myo-inositol, but since that was not the case they were later put back in.

The two different sets of fitting parameters were compared by calculating the residual sum of squares (or RSS). The residual sum of squares is a measure of the amount of error remaining between the regression function (LCmodel fit, in red in Figures 3.6A,B) and the data (raw data, in blue in Figures 3.6A,B). Even when the new set of parameters resulted in more reproducible baselines, the default parameters give the lowest residual sum of squares considering both all the frequency region (Figure 3.6C) and a more myo-inositol specific area, see Figure 3.6D. The chosen myo-inositol range is 3.5 ppm - 3.7 ppm, where the doublet of doublets and the triplet resonances are and the overlap is minor. Therefore, the default LCmodel parameters have been used to analyse the final MRS results in this study.

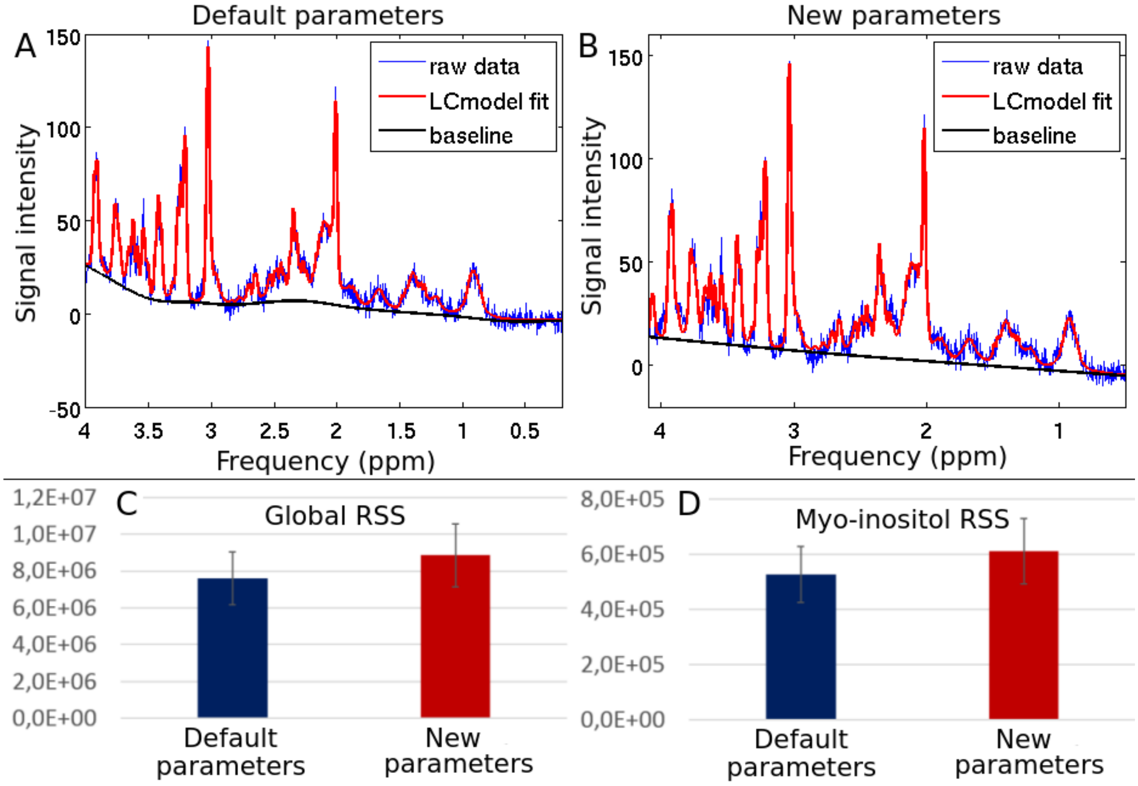

Figure 3.6: LCmodel fitting parameters comparison

A Representative MRS mouse spectrum, analysed with the LCmodel default parameters. Raw data in blue, baseline in black and fitted spectrum in red. **B** Same spectrum analysed with the LCmodel new parameters. Notice the flat baseline achieved with these parameters. **C** Average residual sum of squares of the whole spectrum with the default parameters (blue) and new parameters (red). **D** Average residual sum of squares of the area of the spectrum corresponding to main myo-inositol resonances: 3.5 ppm - 3.7 ppm. Although this was not statistically significant, the default LCmodel parameters give the lowest residual sum of squares (RSS) both globally and in a more myo-inositol specific frequency range of the spectrum.

Metabolites consistently within Cramér-Rao bounds < 10% were included in further analysis, i.e. glutamate (Glu), myo-Inositol (Ins), N-acetyl-aspartate (NAA), taurine (Tau), total choline (tCho), total creatine, Glx (Glu + Gln). The output values of the LCmodel were then imported to Matlab using a custom made analysis tool (Figure 3.7).

The quantification of the metabolites can be expressed in three ways, using three different references: the water concentration (value taken from the water reference scan, without water suppression), the total creatine concentration (using the metabolite total creatine as a reference)

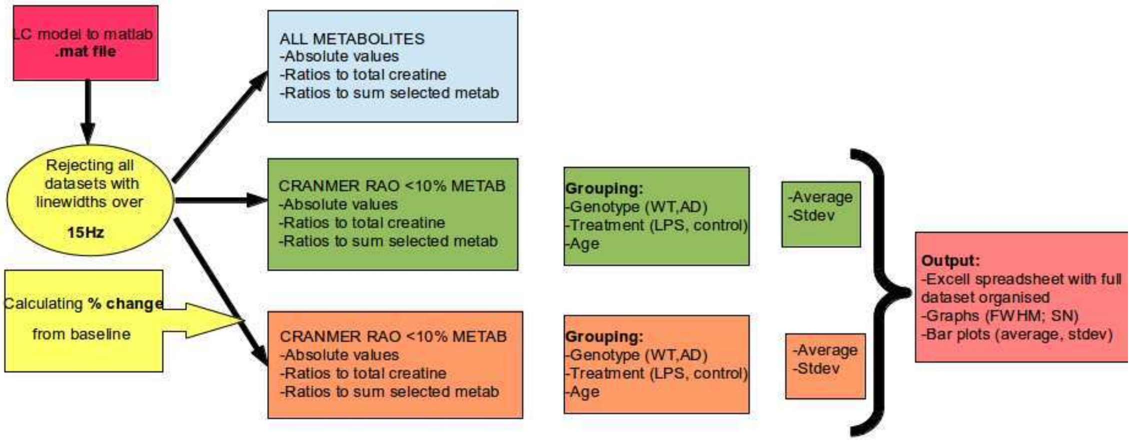

Figure 3.7: MRS tool

This Matlab program imported all the necessary data from LCmodel into Matlab, reading the output files "table", "coord" and "h2o".

or a sum of selected metabolites, by choosing a number of metabolites together as reference [284], as it is a common practice in metabolomics [288]. These metabolites would be the most accurately fitted by the LCmodel, in this case total creatine, total choline, taurine, myo-inositol, NAA and the sum of glutamate and glutamine (Glx). The three references were compared in Figure 3.8: The water content was calculated by importing the water reference file (h2o) from LCmodel into Matlab, extracting the water spectrum, applying automatic phasing corrections and calculating the area under the peak. This process was performed for all six timepoints per animal and the water content is represented in a box plot in Figure 3.8A. The sum of selected metabolites (tCr+tCho+Glx+Ins+Tau+NAA) equivalent distribution over time can be found in Figure 3.8B and the total creatine content in Figure 3.8C. Finally, the reproducibility of the three references is compared in 3.8D, with a bar graph containing the mean standard deviation (expressed as %) of the three methods: 1.5% water content, 3.1% sum of selected metabolites and 3.6% total creatine. In this case, the water content comes out as the best candidate for referencing. However, an experimental mistake during the acquisition of the data has caused the loss of the water reference scans for six animals, which means that the sum of selected metabolites has been the chosen method for normalizing the MRS data in this study.

The MRS ratios have been expressed as percentages from baseline (calculated as the average of the two baseline data points). The data was separated in groups according to mice type and treatment and averages and standard error of the mean were calculated.

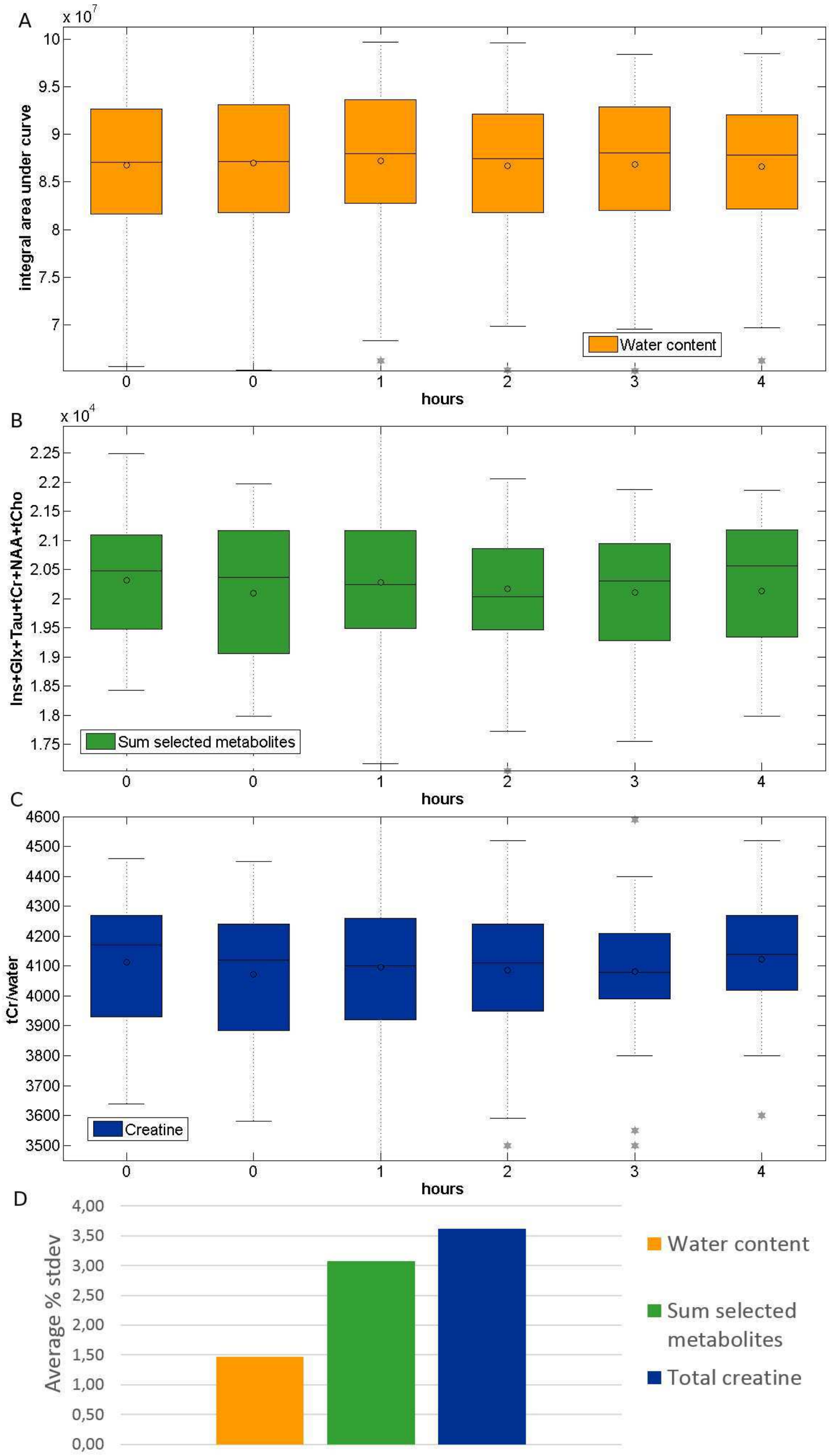

Figure 3.8: MRS metabolite quantification: reference comparison

A: Absolute water content over time. **B:** Sum of selected metabolites (tCr+tCho+Glx+Ins+Tau+NAA) content over time. **C:** Total creatine content over time. **D:** Average standard deviation (expressed as %) of the three references. The reference with the less spread is the water content, followed by the sum of selected metabolites and the total creatine.

n=39 mice total	AD	WT
Treatment: LPS	11	10
Treatment: PBS	9	9

Table 3.3: Data included in MRS analysis

Histology analysis

Histological data was analysed by Felicity Easton, with full details in [286]. Here it follows a summary of the processes involved:

The histology slides were visualized using NDP view 2 software, where region of interests (ROIs) were selected at 30x zoom in the hippocampus: Cornu Ammonis (CA1, CA2, CA3), Dentate Gyrus (DG), Molecular layer (MOL) and Thalamus (THAL). A semi-automatic thresholding was initially performed using ImageJ, the percentage of stained area for every ROI calculated. The results for every treatment group (WT-PBS, WT-LPS, AD-PBS, AD-LPS) were presented, using the averages of all ROIs and individually per each ROI. GFAP staining correlates with reactive astrocytes. However, Iba1 binds to both resting and activated microglia and therefore, a more specific and original method was developed for Iba1 analysis: this method calculates the relative percentage of soma to total cell size (being activated microglia characterized by a bigger soma size, with no branches, opposed to the resting ramified state).

Statistical analysis

MRS statistical analysis was performed using In Vivo Stat [285] and Microsoft Excel 2013. MRS data for a particular metabolite was analysed using a 3-way ANOVA (ANalysis Of VAriance) repeated measures mixed model approach (In Vivo Stat), with drug (LPS/control) and type (AD/WT) as treatment factors, the different time measurements as the repeated factor and baseline levels of the metabolite as covariate. The data was tested beforehand for normality distribution and statistically significant differences overall and within groups (5% level) were detailed. This procedure was performed for myo-inositol, taurine, NAA, glutamate, glutamine, total choline, total creatine, total NAA, GABA, MM09 + Lip 09 and Glu + Gln, in the same dataset. For the histology analysis (done by Felicity Easton, details in [286]), SPSS 2.0 (IBM) and Excel Data Analysis tool pack (Microsoft Excel 2013) were used, with the Mann Whitney-U test for detecting group differences (data not normally distributed).

3.5.3 Results

3.5.3.1 Metabolic response to the LPS challenge

There was a significant myo-inositol increase observed in LPS treated AD mice, in comparison to the AD PBS group (p=0.034) or the wild type LPS group (p=0.030), see Figure 3.9.

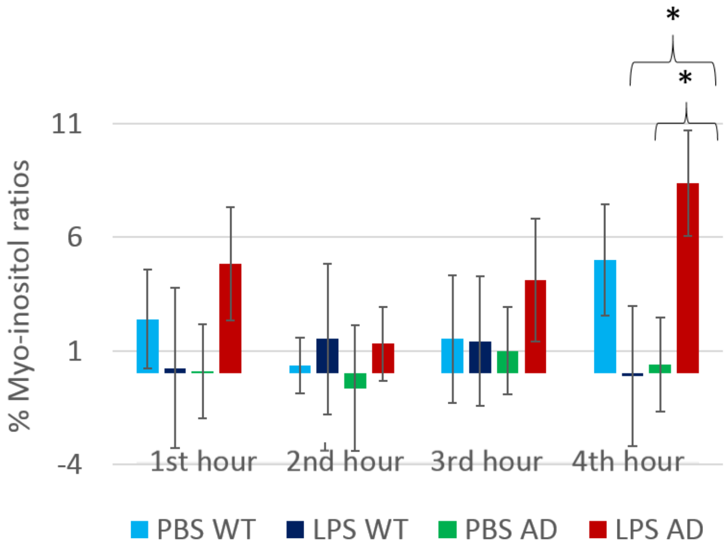

Figure 3.9: Time course of the myo-inositol MRS levels

A: The myo-inositol levels of the LPS treated AD mice increase significantly at four hours, compared with AD controls or with wild-type LPS treated animals (which do not experiment significant changes in their myo-inositol levels compared to the PBS WT). The myo-inositol levels are expressed in percentage change relative to baseline. *p<0.05

As for the rest of metabolites, taurine shows a highly significant overall time effect (p<0.001), together with an interaction treatment/time (p=0.049). Taurine levels decrease with time, a more pronounced effect in AD mice (significant difference between LPS and controls at four hours, p=0.012, Figure 3.10A). Also within the AD group, total creatine levels increase significantly at four hours (p=0.011) with LPS (Figure 3.10B) and finally, NAA decreases significantly in the first hour time point (p=0.046) in the AD-LPS group, compared with AD controls (Figure 3.10C).

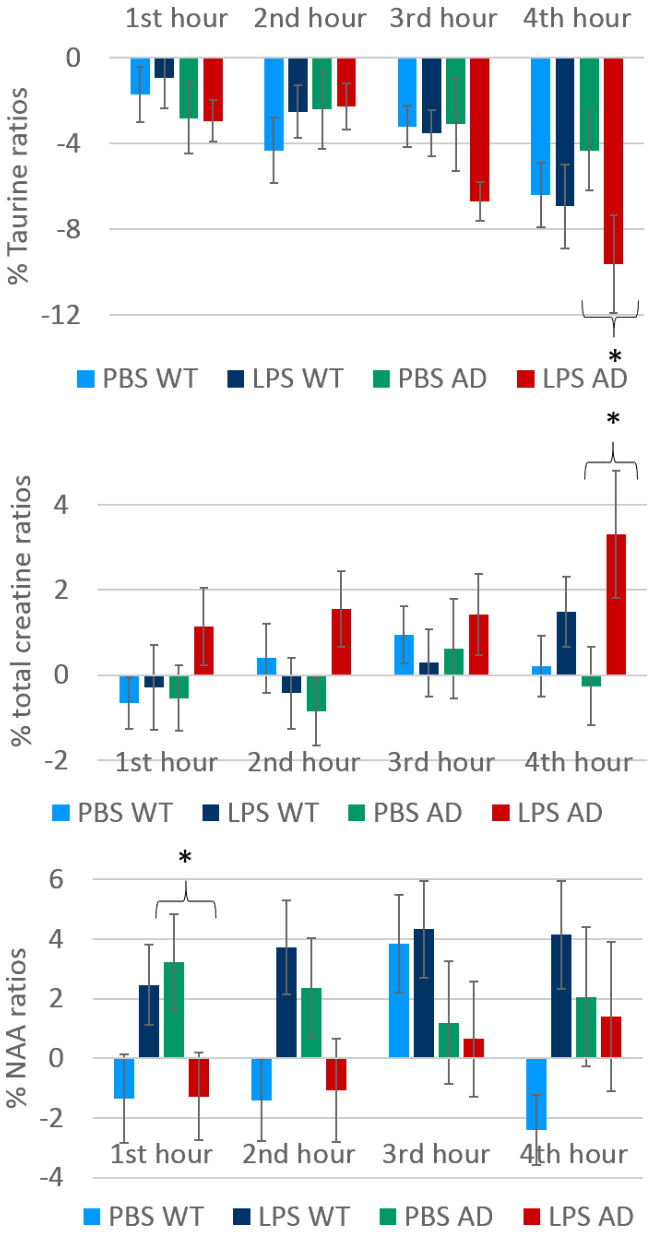

Figure 3.10: Time course of the taurine, total creatine and NAA MRS levels

A: The taurine levels of the LPS treated AD mice decrease significantly at four hours, compared with controls, accompanied by a overall decrease with time independent of drug or genotype. **B:** Total creatine levels increase significantly with LPS at four hours in AD mice, compared with controls. **C:** The NAA levels of the LPS treated AD mice decrease significantly at the first hour, compared with AD controls.

Taurine, total creatine and NAA MRS levels of WT mice do not show significant changes with the drug. *p<0.05

3.5.3.2 Immunohistochemistry results: Iba1 and GFAP staining

The histology results are taken from [286]. The microglial marker Iba1, expressed as average percentage of area stained is higher in LPS treated animals compared with PBS (not distinguishing between genotypes, figure 3.11A). However, when the Iba1 results take into account the soma size as a percentage of total cell pixel count (more specific to activated microglia, which have enlarged soma), the LPS treated animals are again significantly higher, but this time the staining also shows an increase in the AD LPS group compared with WT LPS (figure 3.11B). Finally, the GFAP staining (mean percentage of area stained) differentiates between genotypes (significant increase in AD animals) independent of the drug (figure 3.11C).

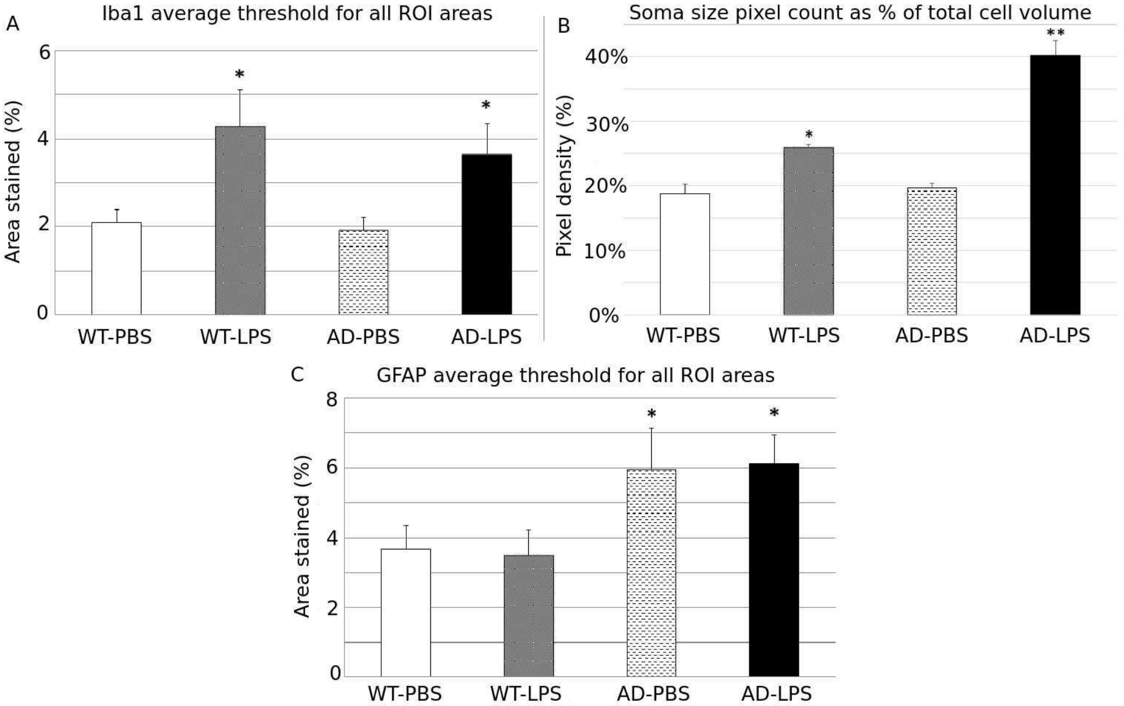

Figure 3.11: From [286]: Analysis of Iba1 and GFAP expression relative to treatment conditions for WT and AD mice.

A: Iba1, mean of percentage of area stained. WT-LPS and AD-LPS groups show a significant increase in percentage area stained relative to corresponding PBS groups. **B:** Iba1, soma size presented as a percentage of total cell pixel count. The soma size as a percentage of total cell pixel count is representative of morphological stage, with significant changes shown between WT-PBS and WT-LPS and AD-PBS and AD-LPS as well as between WT-LPS and AD-LPS. **C:** GFAP, mean of percentage of area stained. AD-PBS and AD-LPS groups show a significant increase in percentage area stained relative to corresponding WT groups. *p<0.05, **p<0.001.

3.5.4 Discussion

Our hypothesis was that MRS metabolic changes and more specifically, an increment in myo-inositol levels will reflect LPS induced transient neuroinflammation in the brain, which will be increased in animals with a pre-existing chronic brain disorder (mouse model of Alzheimer's disease, AD), compared with controls. We found no significant increase overall in myo-inositol levels with LPS for wild-type mice. However, the response in AD mice is indeed stronger, with an increase in myo-inositol four hours after LPS administration (around 10 percent) and this agrees with the hypothesis of microglia being primed in a state of chronic disease, such as Alzheimer's and being more susceptible to insult [289].

The myo-inositol MRS results are supported by histological Iba1 staining: the percentage of stained area analysis reflects a significant increase in the LPS treatment group as compared with the control group, for AD and wild type mice. Since the percentage of stained area highlights both activated and non activated microglia, the more specific measurement of ratios soma size/total cell volume is also considered. Its values are also significantly increased in the LPS treated mice, although differentially higher for AD (around a 100 % increase) than for wild type mice (25 % increase), more in agreement with the myo-inositol MRS values. GFAP results provide further confirmation of this genotype effect, with astrocytes for both AD-PBS and AD-LPS treated groups having around a 60% increased erythrocyte reactivity compared to their WT controls. However, there is no evidence of LPS induced astrogliosis in the model.

Additional metabolic changes include a significant increase in total creatine levels in the LPS AD group compared with controls. Creatine can be found in higher concentrations in glial cells than in neurons [172], which is one of the known pitfalls of using creatine levels as reference in MRS neuroinflammatory studies [12]. This effect would be in agreement with the increased myo-inositol levels observed in the same group.

There is also a significant decrease in taurine levels with time, stronger in LPS AD mice. Martin-Recuero et al. also reports taurine changes over time in a similar *in vivo* MRS experiment after a higher dose LPS administration, with taurine increasing after injection, then decreasing around 24 hours later and finally recovering. These changes are attributed to osmotic alterations [274], since taurine is an osmoregulator. It can also exert neuroprotective actions in neural tissue [290], playing an important role in inflammation associated with oxidative stress (taurine administration with LPS can protect the brain against LPS-induced lipid peroxidation and oxidative stress [291]). This argument is difficult since myo-inositol is also an osmoregulator, but it does not experience the same changes as taurine. Possible effects from the anaesthesia or another part of the experimental setup cannot be excluded.

N-acetyl aspartate (NAA) levels (which are considered a marker of neuronal density/dysfunction, reduced in pathological conditions [173]) significantly decrease in the first hour time point after LPS injection for AD mice, compared with AD controls. However, the high experimental standard error values of NAA measurements (maybe caused by the short echo time MRS PRESS, which maximises macromolecule signals in the NAA frequency range), coupled with the relatively high p value (0.046), raise some doubt over the interpretation of this result. Focusing on statistical limitations of the study, the uneven sample sizes result of data exclusions and specially the small numbers in general limit the reliability and sensitivity of the analysis. Small effects could be present and hiding as non significant, helped by somewhat large statistical errors (with a probable influence of anaesthesia effects). Moreover, some authors [292] are concerned with the use of a single dataset for several statistical tests (or multiple hypothesis testing) creating a risk of false positive results (type I errors). However, no adjustments for multiple tests (or Bonferroni adjustments [293]) are applied to the significance level in this study, since type I errors cannot decrease without inflating type II errors (false negatives) and as Perneger recommends, simply describing what statistical tests have been done and why, and discussing the possible interpretations of each result, helps to reach a reasonable conclusion without the help of Bonferroni adjustments, which should not be used when assessing evidence about specific hypotheses [294].

3.6 Conclusion

Myo-inositol changes, measured with MRS, reflect a mild neuroinflammatory transient state in AD mice, induced by a low dose of LPS and are validated with histology results (Iba1 and GFAP). This neuroinflammatory state is stronger in AD mice than in WT according to Iba1 measurements (soma size method), agreeing with the initial hypothesis of a primed microglial state in the mice with a chronic disease condition [289] compared with wild types. A more specific staining for activated microglia (CD68) could be used in the future to simplify the histology interpretation. There are no significant MRS myo-inositol changes in WT mice, which could be due to the low dose used, although none of the previous *in vivo* MRS LPS studies report changes in myo-inositol in wild type mice [274–276] even at higher LPS doses.

Myo-inositol could be a good candidate for an *in vivo* non-invasive microglial activation biomarker, through its measurement with MR Spectroscopy and could be potentially used to investigate the onset of the neuroinflammatory processes in preclinical models of neurodegenerative diseases, stroke or any other disorder with an inflammatory component, or test anti-inflammatory drugs, in preclinical or clinical settings.

A disadvantage of this approach is the low spatial resolution of MRS to investigate myo-inositol changes throughout the brain in a clinically feasible time, complicating the understanding of such a complex and dynamic phenomenon as neuroinflammation [240]. Therefore, alternative non-invasive MRI techniques would be desirable, such as the possibility of imaging myo-inositol with chemical exchange saturation transfer, which was first applied to characterize advanced stages of AD in a mouse model by [123], and it is further explored in the next chapters (chapter 4 and 5).

CHAPTER 4

Chemical exchange saturation transfer: optimizing a CEST experiment

4.1 Introduction

From the literature review in chapter 2 and the MRS study in chapter 3, glial marker myo-inositol and glutamate emerge as suitable candidates for the global aim of developing an MRI molecular biomarker for neuroinflammation. But myo-inositol contains six OH groups and hydroxyl CEST resonances are affected by direct water saturation effects (because they are very close to the water peak) and B_0 inhomogeneities, especially at the high fields that are required for its measurement. These experimental difficulties, together with the overlap of other similar molecules in the CEST signal are the reason for the work performed in this chapter.

The aim of the CEST simulations is to optimise myo-inositol CEST parameters, in order to maximize the contrast for future *in vivo* experiments and to estimate the amount of myo-inositol CEST contrast that can be expected in the *in vivo* situation.

The aim of the *in vitro* experiments is to gain a better understanding of the CEST process and practical problems associated and to test the accuracy of the simulations, before starting any *in vivo* experiments.

Regarding the structure, section 4.2 contains a CEST simulations literature review (including theory and techniques), while the rest of the chapter details the work performed to optimise a myo-inositol CEST experiment, first with simulations (section 4.3) and then with *in vitro* data (section 4.4).

4.2 Simulating the CEST signal: a review

4.2.1 Bloch-McConnell equations: two pool model

Bloch equations (macroscopic equations describing the total magnetic moment of a sample, the magnetization $\vec{M} = \sum_{i=1}^{N} \mu_i$, in a NMR experiment, see section 1.2.3), can be modified to account for chemical exchange by adding exchange terms (Bloch-McConnell equations [295]). In the simplest case of a two pool model (pool A being bulk water and pool B the bound protons), assuming that $\vec{B}_1$ is applied through the $\vec{y}$ axis, they can be written as [65]:

$$\begin{aligned}
\frac{dM_{xa}}{dt} &= -(\omega_a - \omega)M_{ya} - k_{2a}M_{xa} + C_b M_{zb} \\
\frac{dM_{xb}}{dt} &= -(\omega_b - \omega)M_{yb} - k_{2b}M_{xb} + C_a M_{za} \\
\frac{dM_{ya}}{dt} &= -(\omega_a - \omega)M_{xa} - k_{2a}M_{ya} + C_b M_{yb} - \omega_1 M_{za} \\
\frac{dM_{yb}}{dt} &= -(\omega_b - \omega)M_{xb} - k_{2b}M_{yb} + C_a M_{ya} - \omega_1 M_{zb} \\
\frac{dM_{za}}{dt} &= \frac{M_{0a}}{T_{1a}} - k_{1a}M_{za} + C_b M_{zb} + \omega_1 M_{ya} \\
\frac{dM_{xa}}{dt} &= \frac{M_{0b}}{T_{1b}} - k_{1b}M_{zb} + C_a M_{za} + \omega_1 M_{yb}
\end{aligned} \tag{4.2.1}$$

where

$$k_{1a} = \frac{1}{T_{1a}} + C_a \ ; \quad k_{2a} = \frac{1}{T_{2a}} + C_a \ ; \quad k_{1b} = \frac{1}{T_{1b}} + C_b \ ; \quad k_{2b} = \frac{1}{T_{2b}} + C_b \ ;$$

Here, $C_{a(b)}$ is the transition rate from the spins abandoning pool A(B), $w_1 = 2\pi\vec{B}_1$, ω_a is the resonance frequency of pool A, ω_b is the resonance frequency of pool B, ω is any of frequencies the RF pulse $\vec{B}_1$ is applied at, and $T_{1(2)a(b)}$ are the relaxation times T_1 and T_2 of the spins in pool A and B respectively, without exchange. The group of equations (4.2.1) can be expressed in a more compact matrix form (4.2.2):

$$\begin{pmatrix} \frac{M_{xa}}{dt} \\ \frac{M_{xb}}{dt} \\ \frac{M_{ya}}{dt} \\ \frac{M_{yb}}{dt} \\ \frac{M_{za}}{dt} \\ \frac{M_{zb}}{dt} \end{pmatrix} = \begin{pmatrix} -k_{2a} & C_b & -(\omega_a-\omega) & 0 & 0 & 0 \\ C_a & -k_{2b} & 0 & -(\omega_b-\omega) & 0 & 0 \\ (\omega_a-\omega) & 0 & -k_{2a} & C_b & -\omega_1 & 0 \\ 0 & (\omega_b-\omega) & C_a & -k_{2b} & 0 & -\omega_1 \\ 0 & 0 & -\omega_1 & 0 & -k_{1a} & C_b \\ 0 & 0 & 0 & -\omega_1 & C_a & -k_{1b} \end{pmatrix} \begin{pmatrix} M_{xa} \\ M_{xb} \\ M_{ya} \\ M_{yb} \\ M_{za} \\ M_{zb} \end{pmatrix} + \begin{pmatrix} 0 \\ 0 \\ 0 \\ 0 \\ \frac{M_{0a}}{T_{1a}} \\ \frac{M_{0b}}{T_{1b}} \end{pmatrix} \tag{4.2.2}$$

$$\frac{d\vec{M}}{dt} = A\vec{M} + \vec{B}$$

Many of these parameters can be measured: T_1 and T_2 (with no exchange), M_{0b} (related to the bound pool proton concentration [65]), ω_b (by inspection of the Z spectrum) and finally the exchange rate C_b. C_b can be calculated using this formula (assuming steady state [296]):

$$k = \frac{\text{CEST effect}_{max}}{1-\text{CEST effect}_{max}} \frac{1}{t_{1a}} \tag{4.2.3}$$

The exchange rate depends on temperature, pH and buffer properties. Another possibility is solving the Bloch-McConnell equations (see next section 4.2.2) and fitting to experimental data [22, 65, 296] to get specific parameters (C_b , T_{1a} , T_{1b} , T_{2a} , T_{2b}, ω_b, M_{0b}).

4.2.2 Solving the Bloch-McConnell equations

There are many different ways of solving these equations. Useful approximations to simplify them are for example assuming complete saturation of the spins in pool b. This is the strong pulse approximation [297], which requires only two equations and is equal to having a very strong RF pulse and no direct saturation of the water pool [65]. Another example is the weak pulse approximation, with a very low RF pulse [102], generally applied when ω_1 is small, meaning that there is not going to be direct water saturation. This implies that $(\omega_a - \omega) = \infty$ and the effect of ω_1 in the water pool is neglected leaving only four equations (the x and z magnetizations [102]). The strong and weak approximations can also be combined to create a more general solution [40].

Moreover, the assumption that the exchanging system has reached a steady state is often adopted, in which case the following equation applies:

$$\frac{d\vec{M}}{dt} = 0 \tag{4.2.4}$$

Here, the problem is reduced to solving a number of ordinary coupled equations, which can be done, for example, using Cramer's rule. One problem of this approach is that the solution is only obtained for a specific time (the time where the system reaches steady state), with no information provided about the evolution of the process, or about the state of the system at an earlier stage.

When ω_1 is constant (CW CEST), there is an analytical solution that does not require the assumption of steady state [65, 298]:

$$\vec{M} = e^{At} * (M_0 + A^{-1}\vec{B}) - A^{-1}\vec{B}) \tag{4.2.5}$$

Or in an easier form,

$$\vec{M(t)} = e^{Ct}\vec{M(0)}$$

if equation (4.2.2) is rewritten as:

$$\frac{d\vec{M}}{dt} = C\vec{M} \tag{4.2.6}$$

where the components of the vector $\vec{M(0)}$ are the initial values of the magnetization at t=0, and e^C is the exponential of matrix C. There are many ways of computing the exponential of a matrix [299]: Woessner et al. used the expm1 built-in function from Matlab [65], while Murase and Tanki used the eigenvectors method [298]. This fast method relies on the assumption that ω_1 is constant (CW CEST), but it can be extended to the pulsed CEST case using a discretised approach [22, 36, 300], by dividing the train of shaped pulses in many hard segments and propagating the previous solution through all of them.

Finally, a numerical integration can also be used (for example a fourth-order Runge-Kutta method [301], like the built-in ode45 solver in Matlab). This method can be time consuming, but it is the most rigorous and applies to all experiments (CW and Pulsed CEST), which makes it useful for verification [298].

4.2.3 Bloch-McConnell equations: three pool model

Conventional magnetization transfer (MT) can be included in the the Bloch equations via a 3-pool model (water pool, bound pool, macromolecular pool), just by adding more coupled equations, similar to the situation where there is more than one CEST agent [65]. An assumption made in this case is the null proton exchange between bound pool and macromolecular pool (negligible compared to exchange with water, because of the small concentrations of those two pools). Here are the resulting nine equations in matrix form:

$$\frac{d\vec{M}}{dt} = A\vec{M} + \vec{B} \tag{4.2.7}$$

$$\begin{pmatrix} \frac{M_{xa}}{dt} \\ \frac{M_{xb}}{dt} \\ \frac{M_{xc}}{dt} \\ \frac{M_{ya}}{dt} \\ \frac{M_{yb}}{dt} \\ \frac{M_{yc}}{dt} \\ \frac{M_{za}}{dt} \\ \frac{M_{zb}}{dt} \\ \frac{M_{zc}}{dt} \end{pmatrix} = \begin{pmatrix} -k_{2a} & k_{ba} & k_{ca} & -(\omega_a-\omega) & 0 & 0 & 0 & 0 & 0 \\ k_{ab} & -k_{2b} & 0 & 0 & -(\omega_b-\omega) & 0 & 0 & 0 & 0 \\ k_{ac} & 0 & -k_{2c} & 0 & 0 & -(\omega_c-\omega) & 0 & 0 & 0 \\ (\omega_a-\omega) & 0 & 0 & -k_{2a} & k_{ba} & k_{ca} & -\omega_1 & 0 & 0 \\ 0 & (\omega_b-\omega) & 0 & k_{ab} & -k_{2b} & 0 & 0 & -\omega_1 & 0 \\ 0 & 0 & (\omega_c-\omega) & k_{ac} & 0 & -k_{2c} & 0 & 0 & -\omega_1 \\ 0 & 0 & 0 & (\omega_1) & 0 & 0 & -k_{1a} & k_{ba} & k_{ca} \\ 0 & 0 & 0 & 0 & -\omega_1 & 0 & k_{ab} & -k_{1b} & 0 \\ 0 & 0 & 0 & 0 & 0 & \omega_1 & k_{ac} & 0 & X \end{pmatrix} \begin{pmatrix} M_{xa} \\ M_{xb} \\ M_{xc} \\ M_{ya} \\ M_{yb} \\ M_{yc} \\ M_{za} \\ M_{zb} \\ M_{zc} \end{pmatrix} + \begin{pmatrix} 0 \\ 0 \\ 0 \\ 0 \\ 0 \\ 0 \\ \frac{M_{0a}}{T_{1a}} \\ \frac{M_{0b}}{T_{1b}} \end{pmatrix}$$

$$k_{1(2)a} = \frac{1}{T_{1(2)a}} + k_{ab} + k_{ac}\ ;\quad k_{1(2)b} = \frac{1}{T_{1(2)b}} + k_{ba}\ ;\quad k_{1(2)c} = \frac{1}{T_{1(2)c}} + k_{ca}\ ;\quad X = -k_{1c} - \pi * (\omega_1)^2 * g \tag{4.2.8}$$

g represents the absorption pool for MT, which has been shown to be better described as super Lorentzian in living tissues ([64, 302], see equations 4.2.9 and 4.2.10) and Gaussian in phantom gels ([303], equation 4.2.11):

$$g(\Delta_c, T_{2c}) = \sqrt{\frac{2}{\pi}} \int_0^{\frac{\pi}{2}} \frac{T_{2c}}{3(\cos\theta)^2 - 1} exp(-2(\frac{\Delta_c T_{2c}}{3(\cos\theta)^2 - 1})^2) \sin\theta d\theta \tag{4.2.9}$$

$$g(\Delta_c, T_{2c}) = \sqrt{\frac{2}{\pi}} \int_0^{1} \frac{T_{2c}}{3(u)^2 - 1} exp(-2(\frac{\Delta_c T_{2c}}{3(u)^2 - 1})^2) du \tag{4.2.10}$$

$$g(\Delta_c, T_{2c}) = \sqrt{\frac{2}{\pi}} T_{2c} exp(-(\frac{\Delta_c T_{2c}}{2})^2) \tag{4.2.11}$$

The three pool model equations can be solved analogously as the two pool model ones.

4.2.4 Parameter optimization

The importance of performing CEST simulations arises from the need to optimise the CEST presaturation sequence. The main parameters that the CEST effect depends on are: the RF pulse

$\vec{B}_1$ (number of prepulses, the duration and power/flip angle, delays, shape of the prepulses, etc.), the CEST metabolites concentrations and the relaxation parameters (T_1, T_2) of the pools.

4.2.4.1 CW CEST

The CEST contrast for a specific concentration of a metabolite after a steady-state exchange only depends on one parameter, the $\vec{B}_1$ power or average field, which have the same value, since $\vec{B}_1$ is constant in this case. There is a trade-off between saturation efficiency of the bound pool, with the CEST effect increasing with $\vec{B}_1$ power and spillover effects or direct saturation of the free water pool, since MTRasym decreases with $\vec{B}_1$ power. Therefore, there is an optimal power to maximize the CEST effect (as can be seen in Figure 4.1), which can be proved mathematically by solving the Bloch equations:

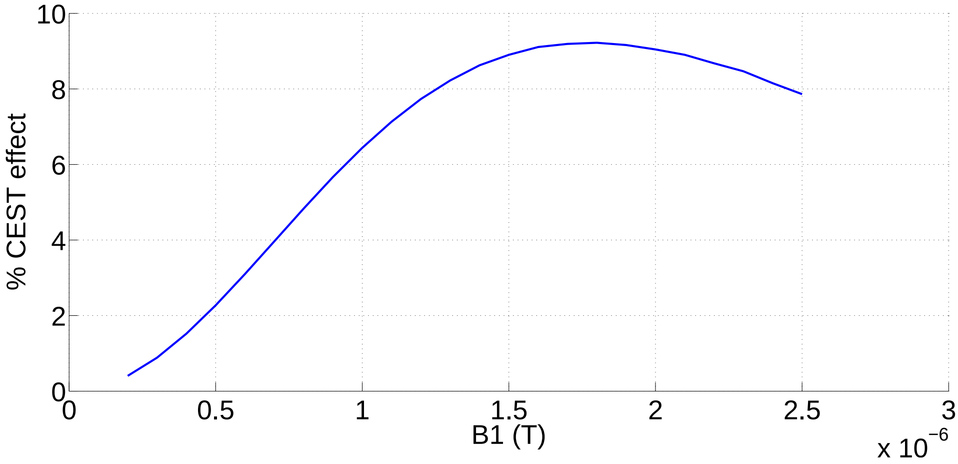

Figure 4.1: Dependence of CW-CEST on B_1 power.

Y axis represents the simulated CEST contrast (MTR_asym) in a CW CEST experiment, while the x axis contains the B_1 power values used, in T. This picture illustrates the existence of an optimal B_1 power. In this particular case, an optimal value of 1.8 μT maximizes the CEST effect (trade off between saturation and spillover effects). Parameters used in this simulation are: Main magnetic field = 7 T, T_2 = 0.9 s, T_1 = 2 s, pool A (water), pool B (myo-inositol, 0.6 ppm, 600 Hz exchange rate), duration of the hard pulse = 5.6 s.

B1 for CW CEST, saturation of bound pool/direct water saturation

Direct water saturation refers to the process of pool A (bulk water) getting saturated as a direct result of the offset RF prepulse and not due to the subsequent chemical exchange. To study its magnitude, a simple case of an offset pulse on a single pool is considered. Using the Bloch equations and assuming steady state ($\frac{dM_x}{dt} = \frac{dM_y}{dt} = \frac{dM_z}{dt} = 0$),

$$\frac{M_x}{T_2} = -(\omega_a - \omega)M_y \tag{4.2.12}$$

$$\frac{dM_y}{T_2} = -(\omega_a - \omega)M_x - \omega_1 M_z \tag{4.2.13}$$

$$\frac{dM_z}{T_1} = \frac{M_0}{T_1} + \omega_1 M_y \tag{4.2.14}$$

Substituting M_x from equation (4.2.12) in equation (4.2.13) and the resulting M_y in (4.2.14), yields:

$$\frac{M_z}{M_0} = \frac{1}{1 + \frac{{w_1}^2 T_1 T_2}{{T_2}^2(\omega_{offresonance} - \omega)^2 + 1}} \tag{4.2.15}$$

Here, the offset pulse is directed at $\omega_{offresonance}$, with a power $B_1 = \frac{\omega_1}{2\pi}$. In order to avoid any direct water saturation, $\frac{M_z}{M_0}$ would have to be 1 and consequently, B_1 = 0. But without an RF pulse, there will be no saturation and no CEST contrast. Focusing now on the situation of the bound protons, the equation describing their magnetization is very similar to (4.2.15), only that for them, the RF pulse is on resonance, $\omega_{offresonance} - \omega = 0$

$$\frac{M_z}{M_0} = \frac{1}{1 + {\omega_1}^2 T_1 T_2} \tag{4.2.16}$$

Here, the situation is the opposite, the bound protons should be as saturated as possible, so ideally, expression (4.2.16) should be 0 and consequently B_1 should be ∞. As it has been proved that increasing B_1 increases the saturation of the bound protons, the only way to avoid having a large direct water saturation as a result of a powerful B_1 would be using a metabolite with a large chemical shift $\omega_{offresonance} - \omega$, which is not possible when dealing with diamagnetic substances.

Other factors for CW CEST

1. *Bound pool proton concentration:* There is a linear increase of the CEST effect with the concentration of the bound protons, due to the existence of more protons exchanging between water and target metabolites. However, this parameter cannot be altered when the targets are endogenous metabolites *in vivo*. Also, this is only true up to a certain concentration (back exchange effect [19]). The following equation applies:

$$\frac{k_{ba}}{k_{ab}} = \frac{M_{0a}}{M_{0b}} \tag{4.2.17}$$

   where k_{ba} is the exchange rate from the bound proton pool to the free protons (water pool), k_{ab} is the back exchange rate from the free protons to the bound protons, and M_{0a} and

M_{0b} are the magnetizations of the bound proton pool and the free proton pool respectively (which are directly proportional to their concentrations).

Phillip Zhe studied the effect of a four-fold increase in bound proton concentration on the optimal B_1 power, finding it negligible [304]. The number of exchangeable protons in a molecule influence the CEST effect the same way as the concentration, the higher number of exchanging protons a molecule has the lower concentration of said molecule is required to achieve the same contrast [19].

2. *Longitudinal and transverse relaxation:* CEST effect is favoured by higher T_1, since the saturation takes longer to relax. This contributes to an enhanced CEST effect with a higher $\vec{B}_0$ (since the longitudinal relaxation constant of the water increases with the main magnetic field [305]). The CEST effect also increases with T_2.
   The optimal B_1 is reduced with increasing T_1, since the saturation has to compete with a slower relaxation and it increases with longer T_2 (sharper water peak causing less spillover).

3. *Chemical shift and chemical exchange rate:*

   The CEST effect is directly proportional to the offset frequency of the bound protons (shown in equation (4.2.15)). Moreover, less influence of spillover at large offsets permits stronger B_1 powers.

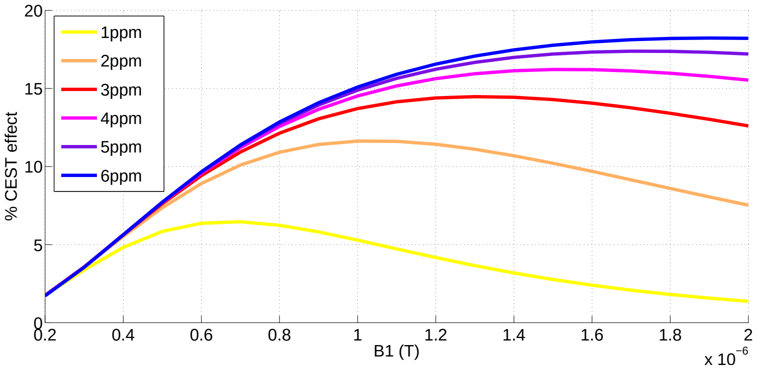

Figure 4.2: Optimal B1 powers for different offsets 1-7 ppm:
Optimal B1 power increases with chemical offset (less spillover effects). Parameters for this two pool model simulation: B_0 = 9.4 T, T_2 = 0.6 s, T_1 = 3 s, 600 Hz exchange rate)

Faster exchanging protons require stronger B_1 powers to be saturated, while the condition of slow regime, or slow to intermediate regime has to be fulfilled, see 1.5.4.

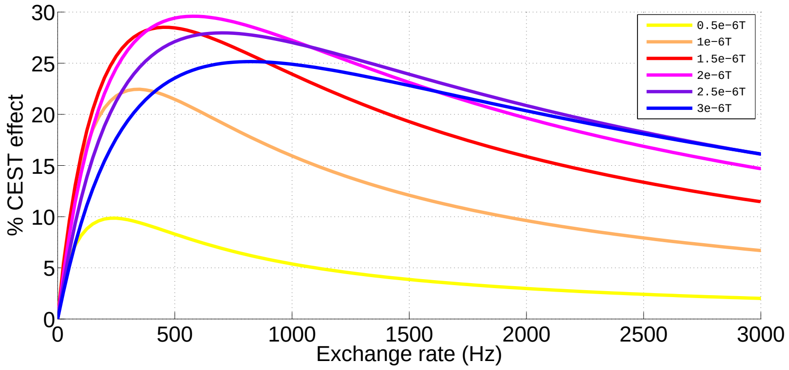

Figure 4.3: CEST effect dependence on exchange rate for different B_1 powers: Slow exchanging protons give raise to higher CEST contrast, with small B_1 powers. Parameters for this two pool model simulation: B_0 = 9.4 T, T_2 = 0.6 s, T_1 = 3 s, chemical offset = 3 ppm

4.2.4.2 Pulsed CEST

Unlike CW CEST, the Pulsed CEST contrast for a specific concentration of a metabolite after a steady-state exchange depends on several parameters, which are under experimental control:

1. *Average irradiation power*

$$B_{avg\ power} = \sqrt{\frac{1}{PTR}\int_0^{PTR} {B_1}^2\,\mathrm{d}t} = \sqrt{\frac{p^2}{dc}}\,\frac{\pi\theta}{180\,\gamma\,p_1\,PTR} \tag{4.2.18}$$

[34] where:

PTR=Pulse train repetition time

$p_1 = \dfrac{\text{average amplitude}}{\text{maximum amplitude}}$ of the RF pulse

$p_2 = \dfrac{\text{average of the square of the amplitude}}{\text{square of the maximum amplitude}}$ of the RF pulse

2. *Average irradiation field amplitude*

$$B_{avg\ field\ amplitude} = \sqrt{\frac{1}{PTR}\int_0^{PTR} B_1\,\mathrm{d}t} = \frac{\pi\theta}{180\,\gamma\,PTR} \tag{4.2.19}$$

[34]

These two values $B_{avg\ power}$ and $B_{avg\ field\ amplitude}$ are a single one in the CW scheme: the RF field $B_{1\mathrm{CW}} = B_{\text{average field amplitude}} = \sqrt{B^2_{\text{average field amplitude}}}$, since there is no variation over time.

3. *Irradiation flip angle,* θ

   This value refers to the application of the pulse on-resonance.

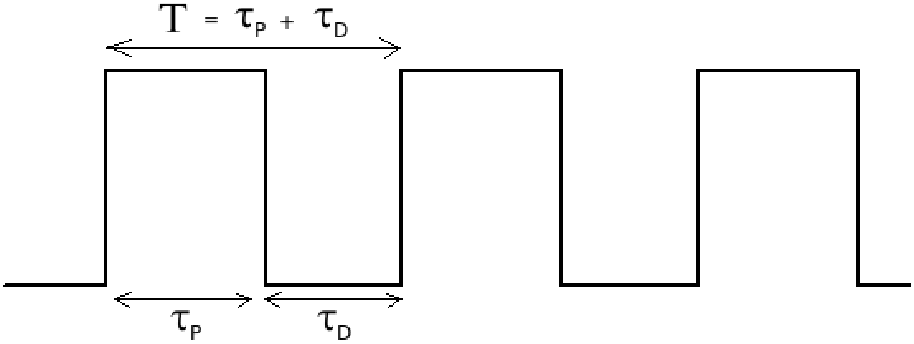

Figure 4.4: Pulse Train parameters:

Pulse train of n=3 prepulses, of T duration (τ_P prepulse + τ_D delay).

4. *Number of prepulses*

   Number of pulses in a pulse train (for example 3 in Figure 4.4)

5. *Duration of the prepulses,* τ_P

6. *Duration of the delays,* τ_D

7. *Duty cycle*

   Duty cycle or dc is defined in general as the ratio of the time when a periodic system is active to the total time. In the case of Figure 4.4, this can be expressed like: $dc = \frac{T}{\tau_P}$

8. *Shape of the prepulses*

   They can be rectangular (Figure 4.4), Gaussian, sinc... (see 1.5.3).

Several studies [33, 34] affirm that the optimal CW **RF power** can be directly translated to a pulsed scheme, providing a similar CEST contrast for exchange rates less than 50 Hz [36]. A smaller CEST contrast will result for faster exchanging species, due to a more inefficiently bound pool saturation and the attenuation during the delays. Besides, the behaviour of the optimal B_1 value for pulsed CEST with frequency offset, bound pool proton concentration and exchange rate seems to match the one of the optimal CW B_1 power (see 4.2.4.1 and [34]). As for the two parameters $B_{avg\ power}$ and $B_{avg\ field\ amplitude}$, Sun et al. studied a linear regression between optimal B_{1CW} and $B_{avg\ amplitude}$ [36], while Zu et al. affirmed that $B_{avg\ power}$ is a "more

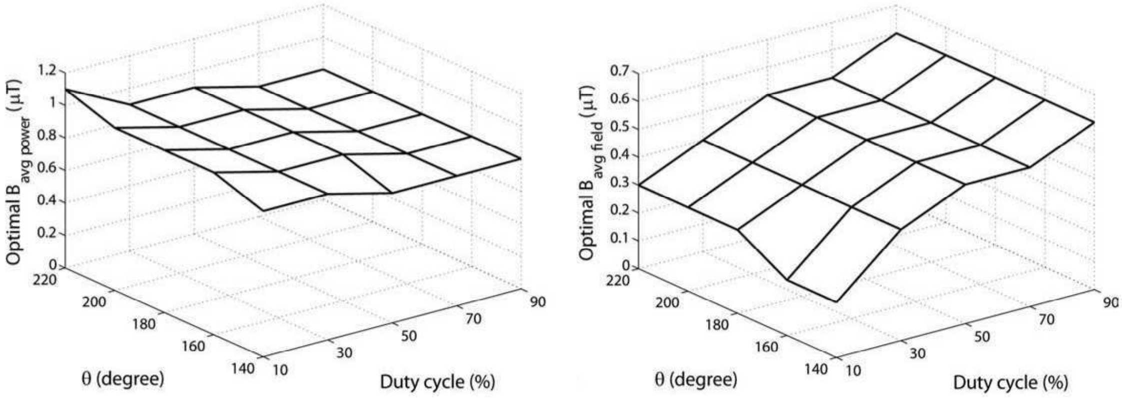

Figure 4.5: $B_{avg\ power}$ **and** $B_{avg\ field\ amplitude}$, from Zu et al. [34]

Experimental $B_{avg\ power}$ (left) and $B_{avg\ field\ amplitude}$ (right) that optimize the pulsed-CEST contrast as a function of flip angle and duty cycle for a creatine and agar phantom.

meaningful sequence metric" [34] than $B_{avg\ field\ amplitude}$, because it is mostly independent from other two parameters, θ and dc (see Figure 4.5).

Furthermore, they checked empirically that the **flip angle** and **duty cycle** are also independent of each other and $B_{avg\ power}$, that is, together they form an orthogonal base for the system. This study results suggest that both dc and θ have optimal values, which are independent of properties like concentration, chemical exchange rate and frequency offset at around 50% and 180° respectively.

An optimal flip angle has been found to be between 180° - 220° for Sun et al. (see Figure 4.6, from [36]) in agreement with Zu et al. [34].

With respect to the **shape of the prepulses**, the only requirement is for their Fourier transform to not have any amplitude close to the water frequency. Their profile is expected to vary smoothly with time and to select appropriately the frequencies in the frequency domain (narrow). Looking at the literature, Gaussian pulses are the ones used in most of the studies [33–36], Sun et al. compared rectangular, Gaussian and sinc pulses with contrasting results: rectangular pulses created a periodic oscillation in the Z spectrum due to the frequency profile of its FT (a sinc) , while the sinc pulses had the disadvantage of higher direct saturation effects compared with the Gaussian pulses [36]. An independent study, from Schmitt et al., arrived at the same conclusion [35].

Some studies have evaluated the influence of the **pulse duration**: Schmitt et al. examined the full width at half minimum (FWHM) of the creatine Z spectra together with the maximum CEST contrast [35]. Their results (Figure 4.7) show a decrease of FWHM with the period T of the prepulses, with the maximum contrast being roughly constant. This broadening of the water peak with shorter pulse duration is also mentioned by Sun et al., and can be explained in terms

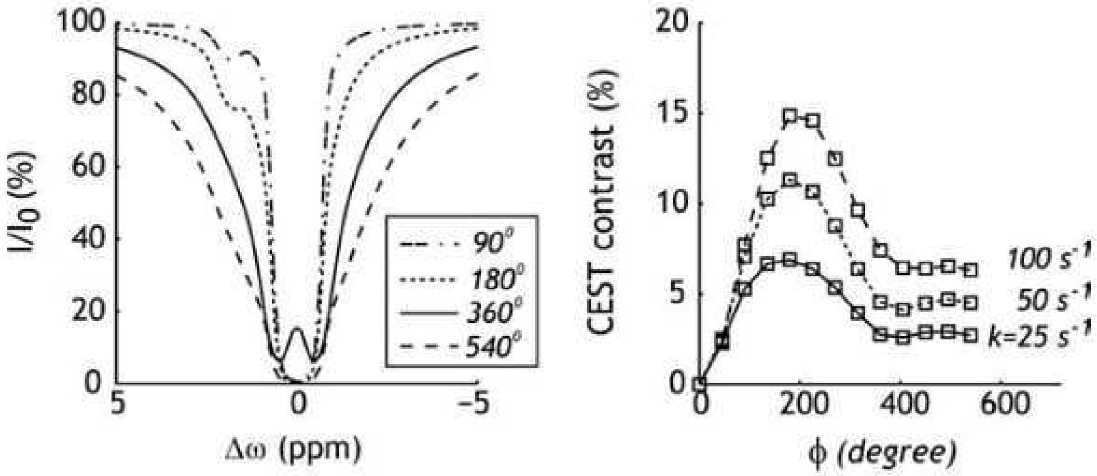

Figure 4.6: Optimal flip angle θ, from Sun et al. [36].

Left: Simulated Z spectra with flip angles of 90° , 180° , 360° and 540°. Exchange rate 50 Hz, chemical shift 1.9 ppm, and pulse duration 15 ms. **Right:** Optimal simulated pulsed-CEST contrast found for flip angles about 180-220°.

of direct saturation. In extreme cases, it can lead to spectral distortions.

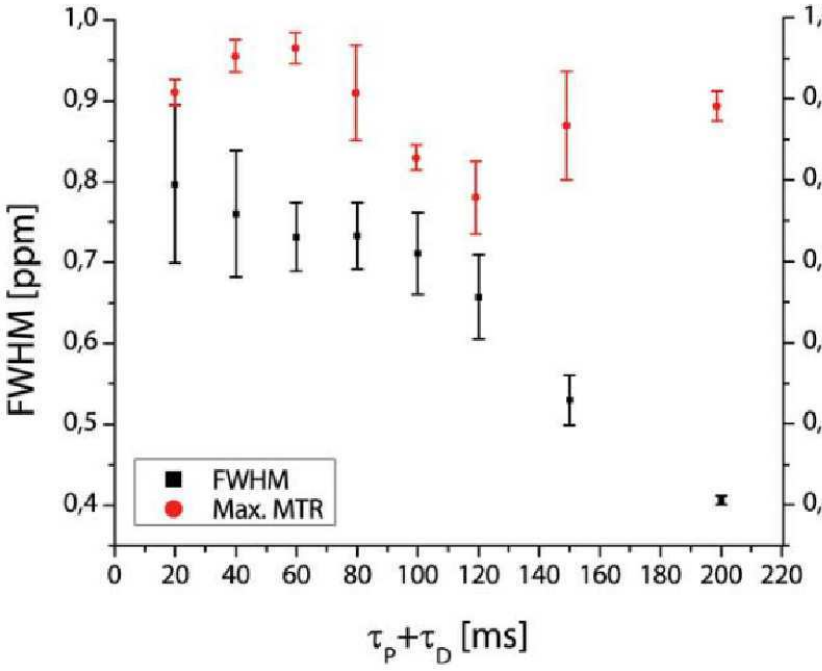

Figure 4.7: Pulse duration and FWHM of Z spectra, from Schmitt et al. [35].

An increase of pulse duration T (τ_P prepulse + τ_D delay) results in a decrease of FWHM of Z spectra for maximum CEST effects. B_0 = 3 T, pulsed CEST (total duration of the saturation pulse train = 2 s), duty cycle = 50% and B_1 = 1 mT, for a 0.05 M creatine phantom at pH 7.4.

4.3 Optimizing a CEST experiment: simulations

4.3.1 Introduction

Simulations are useful to optimise the presaturation parameters of a CEST sequence for a given situation. My aim is to image neuroinflammation, focusing on two key metabolites, myo-inositol and glutamate. The following simulations are focused on optimizing myo-inositol CEST, due to the more complicated nature of the process, compared with imaging glutamate (which resonates further away from the water peak). Moreover, myo-inositol has been revealed as the most relevant biomarker for a mild neuroinflammatory situation, as described in previous results (chapter 3).

Hydroxyl resonances are situated very close to the water peak, and therefore their measurement is made harder by the presence of direct water saturation effects, as well as inhomogeneities of the main B_0 field (even more so since a high B_0 of the order of at least 7 T is required to separate the exchangeable protons from water). Moreover, when studying a particular molecule containing hydroxyl groups, the different competing effects of other similar molecules have to be taken into consideration. Therefore, a careful optimization is crucial for maximizing the *in vivo* myo-inositol contrast.

The main difference in the simulation parameters between the *in vivo* or *in vitro* situation is the value of T_{2a}, the transverse relaxation of the water pool. Living tissue has a T_2 value of around 0.045 s (0.0454 s in the hippocampus, 0.0406 s in the thalamus at 9.4 T [305]), while a phantom made with pure water at the same field will have a T_2 of 0.6 seconds. Haris et al. studied the viability of imaging myo-inositol *in vivo* with phantoms containing distilled water and a range of myo-inositol concentrations (a case where a long T_2 value applies), as well as phantoms containing agarose and myo-inositol (short T_2) [53]. Several studies have exhaustively modelled the CEST effect of amide protons [22, 33–36, 40, 104, 140, 300] and paraCEST agents [64, 306]. My aim is to model the CEST effect of myo-inositol for a better understanding and optimization of the *in vivo* signal. This will involve the study of several cases: long T_2 (distilled water + myo-inositol) and short T_2 (agar gel + myo-inositol) in a two pool model and finally, a three pool model including conventional MT effects. The parameters to be optimized are the presaturation power and duration of the pulse (CW CEST) and the number of prepulses, their power and duration for a pulsed CEST experiment. The ultimate goal is to clarify how much myo-inositol contrast (CEST effect %) can be expected in the *in vivo* situation.

B_0	9.4 T (Agilent preclinical scanner)
T_{1a} (for 9.4T)	**3 s/2.8 s** (water/agar phantom [140]/[34]), **2 s** (mouse hippocampus [305]
T_{2a} (for 9.4T)	**0.6 s** (water phantom), **0.045 s** (mouse hippoc., agar phantom) [34, 305]
T_{1b} (for 9.4T)	**1 s** [140], not relevant for modelling [65]
T_{2b} (for 9.4T)	**0.015 s** [140], not relevant for modelling [65]
T_{1c} (for 9.4T)	**1 s** [33, 140]
T_{2c} (for 9.4T)	**0.000015 s** [34, 140]
Offset frequency b (myo-inositol)	**0.6 ppm** [53]
Offset frequency c (MT pool)	**0 ppm** (agar phantom), **-2.34 ppm** (brain) [307]
Concentration b (myo-inositol)	**10 mM** human hippocampus[308]
Concentration c (MT pool)	**2.1%M0a** [34]
Exchange rate b (myo-inositol)	**600 Hz** [53]
Exchange rate c (MT pool)	**50 Hz** [33]
Frequency sweep range	**+/-2 ppm**

Table 4.1: Parameters to model my CEST experiment

4.3.2 Optimizing a CW CEST experiment: Two pool model

The two pool model is the simplest CEST experiment: pool a, the free pool or water protons and pool b, the bound exchanging protons, six in every myo-inositol molecule (six -OH groups per myo-inositol molecule).

The CW CEST contrast for a specific metabolic concentration only depends on two parameters: B_1 power/average field (same value, since B_1 is constant in this case) and the saturation time, t_{sat}. As for B_1, there is a trade-off between saturation efficiency of the bound pool (CEST effect increases with B_1 power) and spillover effects (direct saturation of the free water pool, also increasing with B_1 power, specially important in hydroxyl CEST). Therefore, there is an optimal power to maximize the CEST effect [33, 40] which can be obtained by solving the Bloch equations. For t_{sat}, it is useful to map the approach of the z magnetization of the system (pool a and pool b) to steady state and thus obtain a relevant time interval for the maximum CEST effect.

4.3.2.1 Two pool model: long T2

Approach to steady state for long T2

Using the parameters above (T_2 being 0.6 s) and a numerical integrator (ode45, Matlab 2013, The Mathworks), a pulse of 1.7 μT is applied to a two pool model system. After solving the six linear differential equations, the magnetization of the free and bound pools is plotted against time and the result is the curve observed in Figures 4.8 and 4.9, the approach to steady state of the system. The bound protons of pool b never get completely saturated with the B_1 used in this simulation, but the higher power required for a full saturation will also increase the direct water saturation effects, thus reducing the CEST effect. This B_1 power has been chosen to maximize the CEST contrast, as will be seen shortly.

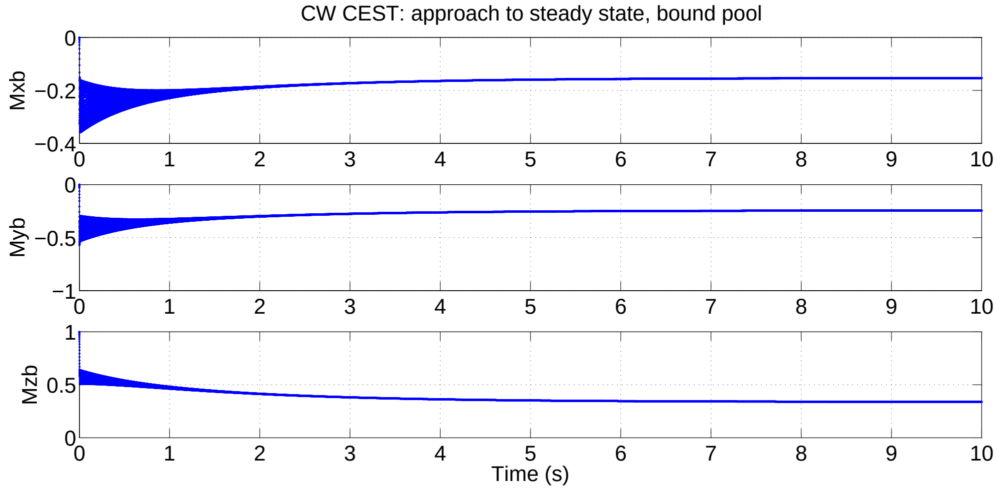

Figure 4.8: Evolution of the magnetization of the myo-inositol protons during a B_1 saturation power of 1.7 μT. From the top, the three graphs represent the x,y (transverse magnetization) and z (longitudinal magnetization) components. None of this variables produces a direct effect in the MRI signal, though the z component exchanges magnetization with the water protons equivalent, the source of signal. The fast exchanging hydroxyl protons never get completely saturated, since the optimum B_1 power they would require is not feasible, due to the large direct water saturation it will cause, hiding the CEST effect at close ppm range.

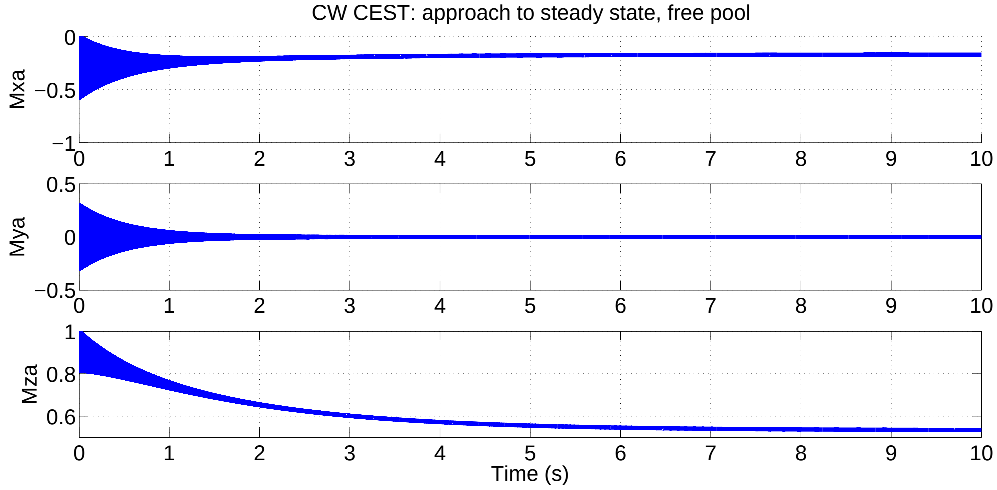

Figure 4.9: Evolution of the magnetization of the water protons during a B_1 saturation power of 1.7 μT. From the top, the three graphs represent the x,y (transverse magnetization) and z (longitudinal magnetization) components. The last one is the source of MRI signal, getting saturated though chemical exchange with the bound protons. The steady state is reached after more than 5 s of continuous saturation.

Optimum CW B1 power and t_{sat} for long T2

Figures 4.8 and 4.9 show the approach to steady state of the system, giving a value between 5 and 10 s for the duration of the saturation pulse. The optimum B_1 for the t_{sat} values in this range have been calculated, and the pair $B_1/\ t_{sat}$providing the highest CEST contrast has been chosen as the optimum. In Figure 4.10 and Figure 4.11, the Z spectrum and CEST effect have been plotted for different 7 s long B_1 powers, showing that the optimum value is 1.7 μT.

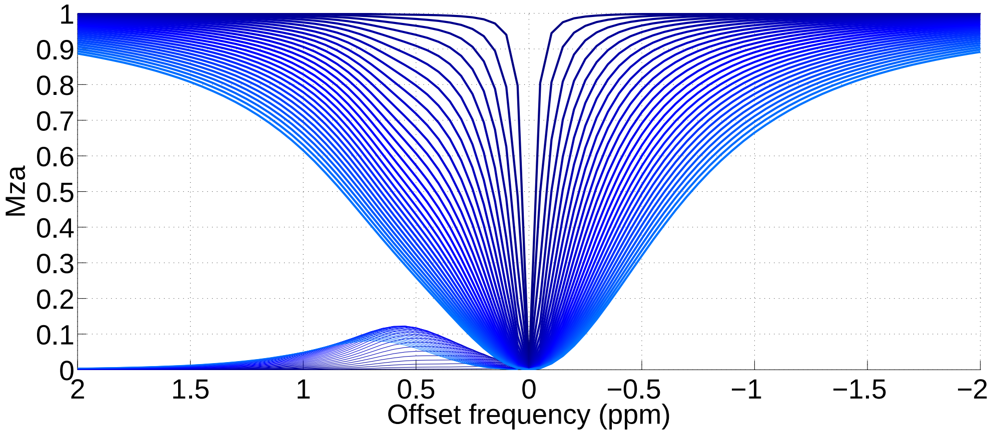

Figure 4.10: Z spectra and MTR_{asym} dependence on B_1 power, for a CW saturation of 7 s. B_1 power range: 0 to 3 μT.

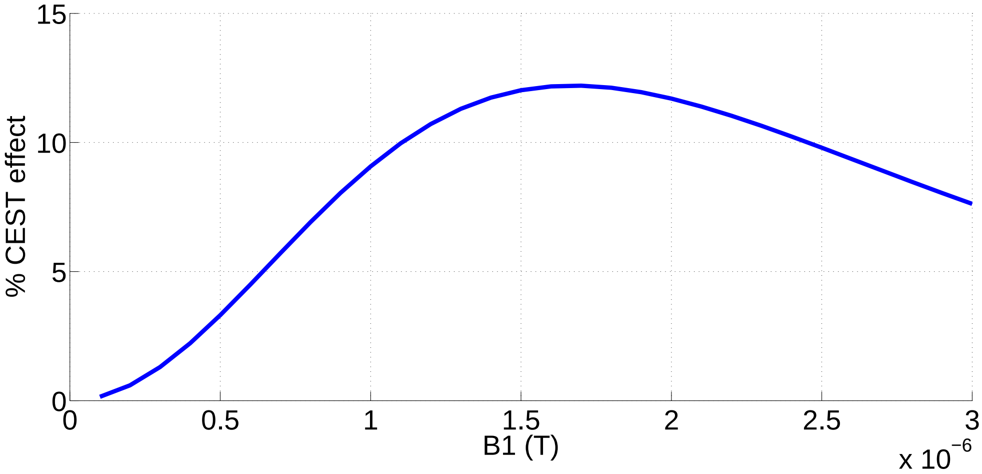

Figure 4.11: % CEST effect dependence on B_1 power, for a CW saturation of 7 s. Like in Figure 4.1, there is a trade off between saturation of the bound protons and spillover effects, with the optimum B_1 value being 1.7 μT.

As for the t_{sat}, Figure 4.12 shows the curve around the optimum value of 6.2 s. In order to avoid getting into a local minimum, several iterations have been performed of this process, choosing the parameters providing the highest CEST contrast.

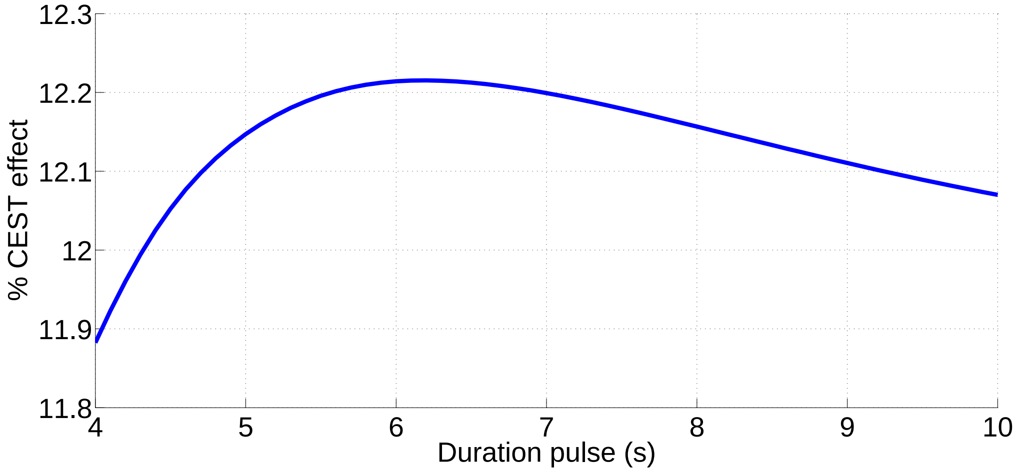

Figure 4.12: % CEST effect dependence on saturation duration, for a B_1 power of 1.7 μT. Although 6.2 s is the optimum value, the curve is quite flat around the maximum (note the scale of the y axis), and therefore choosing a shorter saturation, such as 4 s, will have hardly any impact on the CEST effect, while saving time in the experiment.

CEST effect dependence on concentration for long T2

In Figure 4.13, the simulated CEST effect has been plotted against myo-inositol concentrations of 0-50 mM. The simulations show that CEST effect depends linearly on the concentration at low concentrations, while it becomes non-linear at high concentrations (due to the known process of the back-exchange of saturated protons [309]).

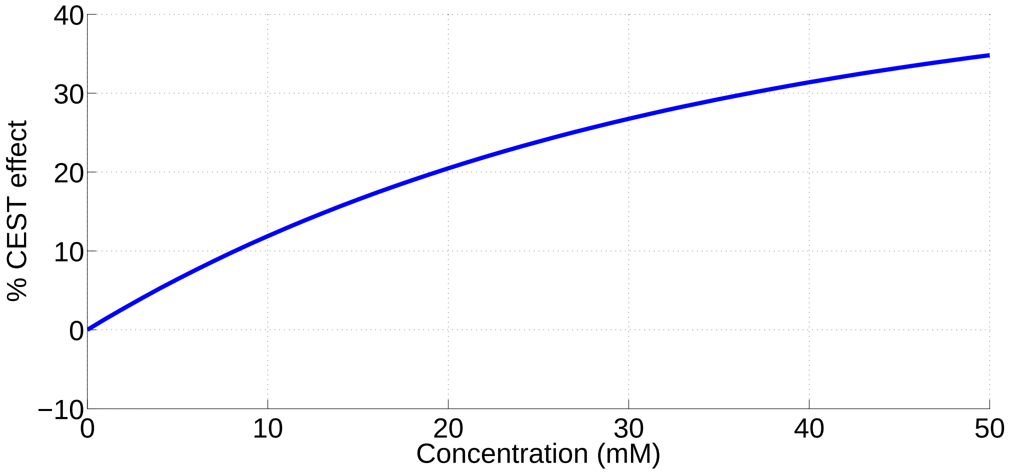

Figure 4.13: CEST effect dependence on myo-inositol concentration: it increases linearly at low concentrations, growing more slowly at higher concentrations. $B_1 = 1.7$ μT, t_{sat}= 4 s

Conclusion

The optimum myo-inositol CEST parameters for a CW experiment using a two pool model with a long T_2 (ie: phantom made of water/saline and myo-inositol) are: t_{sat} = 4 s and B_1 = 1.7 μT, while the expected maximum CEST effect for a 10 mM solution is around 11%.

4.3.2.2 Two pool model: short T2

Approach to steady state for short T2

Looking for a more relevant two pool model for the *in vivo* situation, I now consider a T_2 of 0.045 s, which approximately matches the expected value for *in vivo* brain tissue [305].

Figure 4.14 show the approach to steady state of the system in this case. In comparison with the long T_2 case, the pool b protons achieve less saturation in the steady state, which is reached quicker (2-4 s). An advantage of that will be the reduction in acquisition time of the optimum CW experiment, and a disadvantage, the probable reduction in CEST contrast, which I will be exploring from now on.

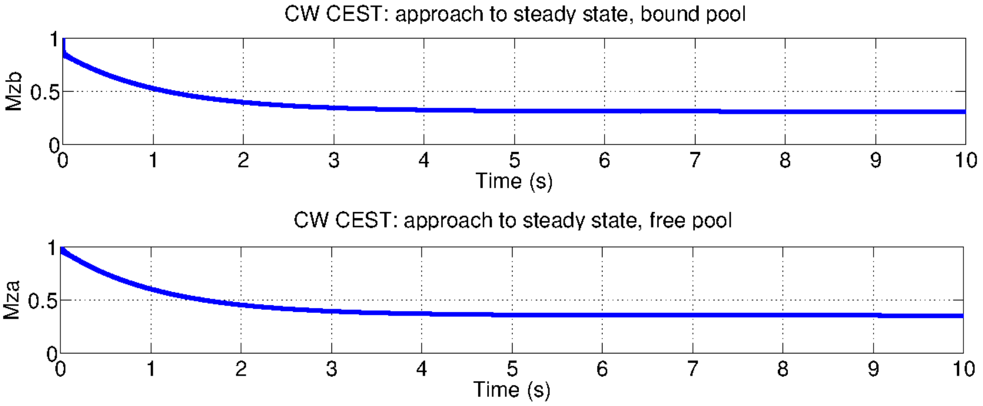

Figure 4.14: Evolution of the magnetization of the myo-inositol and water protons during a B_1 saturation power of 0.9 μT. From the top, the two graphs represent the z (longitudinal magnetization) component of myo-inositol (bound pool) and water (free pool). Since B_1 is smaller than in the long T_2 model, the hydroxyl protons get even less saturated in this case. The bottom graph represents the source of MRI signal, getting saturated though chemical exchange with the bound protons. The steady state is reached faster than in the long T_2 model, but the saturation is smaller (short T_2 model).

Studying the optimum CW B1 power and tsat for short T2

Repeating the previous simulations with the new parameters (and a shorter steady state time), I can calculate the optimum B_1 power and t_{sat} for this case from the graphs below (see Figure 4.15).

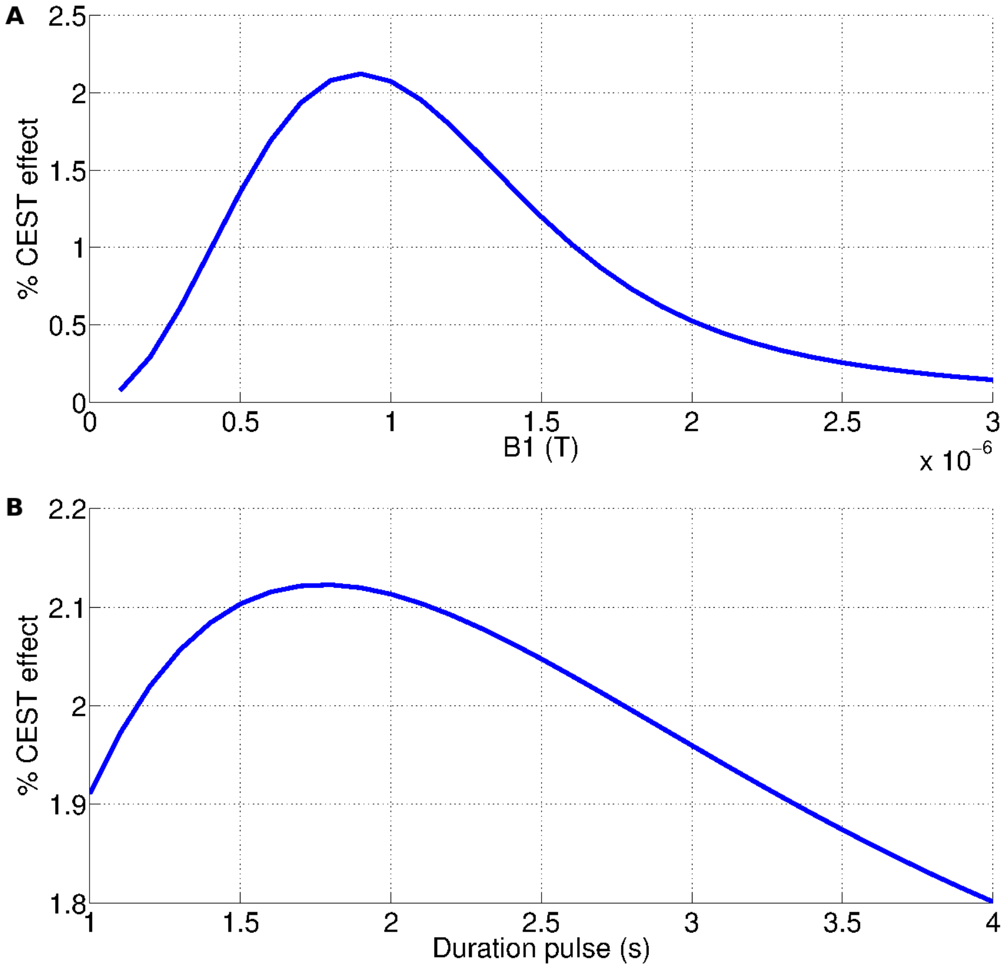

Figure 4.15: % CEST effect dependence on B_1 power and saturation duration, for a CW saturation of 1.8 s.

A: % CEST effect dependence on B_1 power. Again, there is a trade off between saturation of the bound protons and spillover effects, with the optimum B_1 value being 0.9 μT.

B:% CEST effect dependence on saturation duration. 1.8 s is the optimum value.

Studying the CEST effect dependence on concentration for short T2

As before, the simulated Z spectra and CEST effect has been plotted against myo-inositol concentrations of 0-50 mM (Figure 4.16). The CEST effect % is considerably smaller for all concentrations and the linear dependency lasts up to higher concentrations than in the long T_2 case.

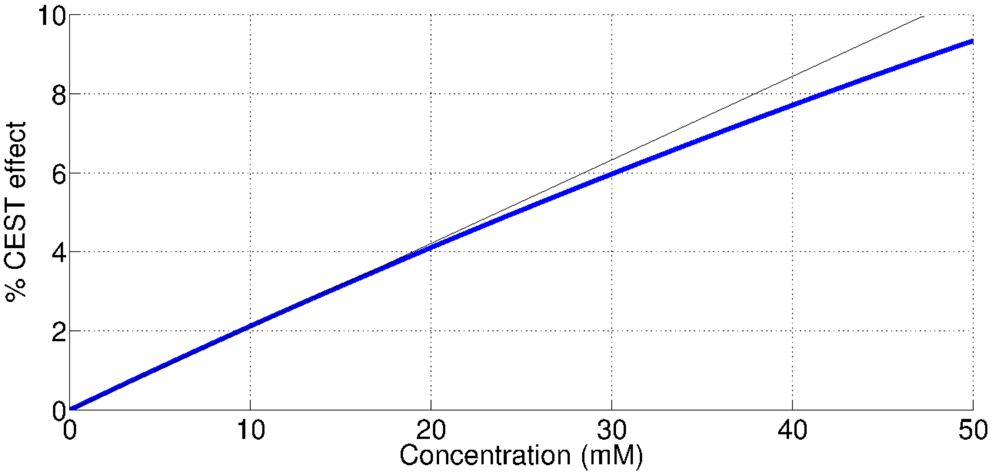

Figure 4.16: CEST effect dependence on myo-inositol concentration: it increases linearly at low concentrations, growing more slowly at higher concentrations. The thin black line shows the linear behaviour at low concentrations. $B_1 = 0.9$ μT, $t_sat =$ 1.8 s

Conclusion

The optimum myo-inositol CEST parameters for a CW experiment using a two pool model with a short T_2 (ie: phantom made of agarose and myo-inositol) are: t_{sat} = 1.8 s and B_1 = 0.9 μT, while the expected maximum CEST effect for a 10 mM solution is around 2%. This value is very small compared with the previous 11% expected for long T_2 values, which showcases the need for simulations in order to understand what to expect in the *in vivo* case, instead of relying on *in vitro* data.

4.3.3 Optimizing a CW CEST experiment: Three pool model

The three pool model adds conventional magnetization transfer effects as a third pool, together with the previous water pool and CEST proton pool. It is a more accurate representation of the *in vivo* situation.

4.3.3.1 Agar phantom

To model the magnetization transfer pool, I first used the parameters of an agar gel phantom (3%): Gaussian absorption line shape (4.2.11), centered at 0 ppm (no asymmetry), a T_2 of 0.045 s and T_1, 2.5 s

The CEST effect has been plotted in Figure 4.17A for different B_1 powers, resulting in an optimum value of 0.9 μT [40], while the optimal saturation time is 1.7 s (4.17B) and the concentration dependence is derived from Figure 4.17C. The optimum values obtained with the three pool model agar simulation are almost the same as the parameters from the short T_2 two pool model, which is a faster and easier method (six equations instead of nine) and would be adequate for this case.

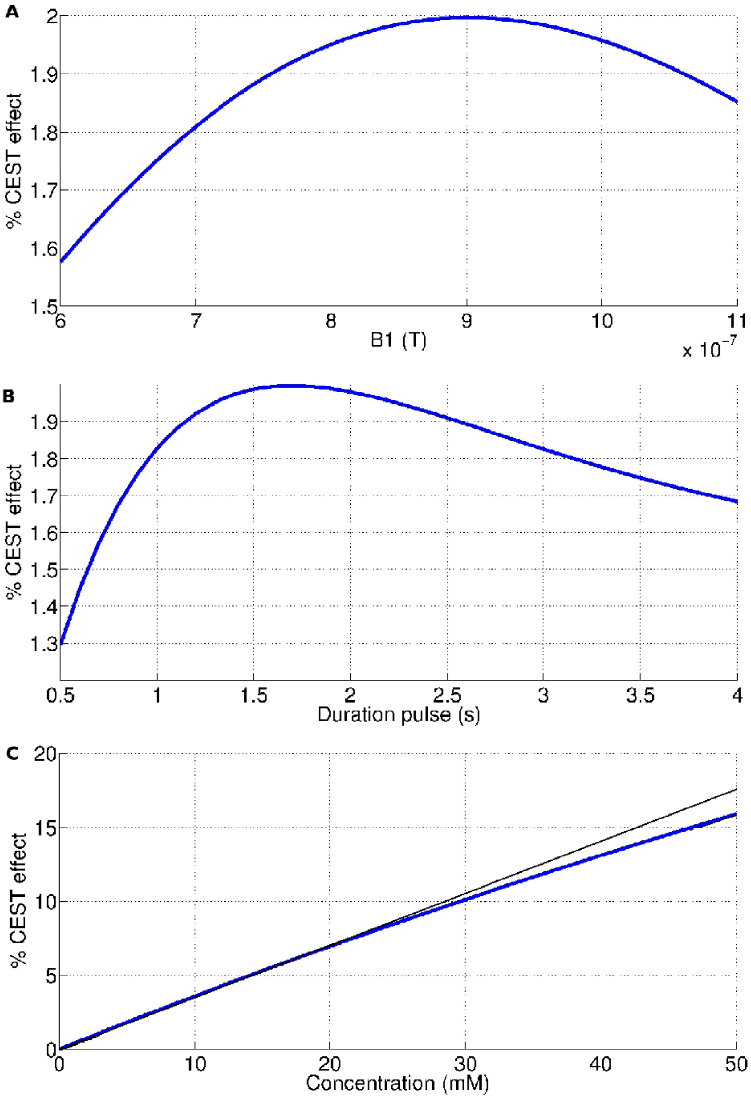

Figure 4.17: 3 pool model, agar phantom

A:% CEST effect dependence on B_1 power, for a CW saturation of 1.7 s. The bound protons saturation/spillover effects equilibrium establishes the optimum B_1 value as 0.9 μT. **B**:% CEST effect dependence on saturation duration, for a B_1 power of 0.9 μT. 1.7 s is the optimum value. **C**:CEST effect dependence on myo-inositol concentration for a 3 % agar phantom. $B_1 = 0.9$ μT, $t_{sat} = 1.7$ s. The thin black line shows the linear behaviour at low concentrations.

4.3.3.2 In vivo MT conditions

In an *in vivo* situation, the asymmetry of the magnetization transfer pool has to be taken into account and a super Lorentzian absorption line shape (see equations 4.2.9 and 4.2.10) centered at -2.34 ppm is more appropriate [307].

In Figure 4.18, the CEST contrast for a range of relevant myo-inositol concentrations (1-12 mM) is presented, showing that the *in vivo* effect will be around 3%. This value approximately matches the myo-inositol *in vitro* data (agar phantoms) from Haris et al. [53].

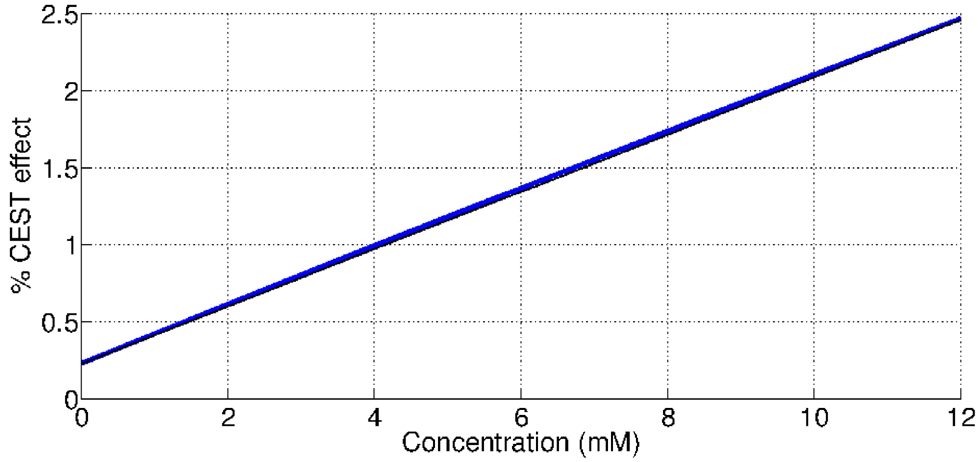

Figure 4.18: CEST effect dependence on myo-inositol concentration for a three pool model (with asymmetric contribution from MT). The thin black line showing linear behaviour is indistinguishable from the blue line. $B_1 = 0.9\ \mu$T, $t_{sat} = 1.7$ s

A hard pulse of 0.9 μT with 1.7 s duration maximizes again the CEST effect for this model (the more closely related to *in vivo* conditions), in line with the short T_2 two pool model results, which has proven to be a very useful approximation for *in vivo* hydroxyl CEST optimization. However, *in vivo* asymmetric magnetization transfer effects will have a significant effect on the CEST contrast for frequency offsets larger than 1 ppm [310], where three pool model simulations will still be relevant (see Figure 4.19).

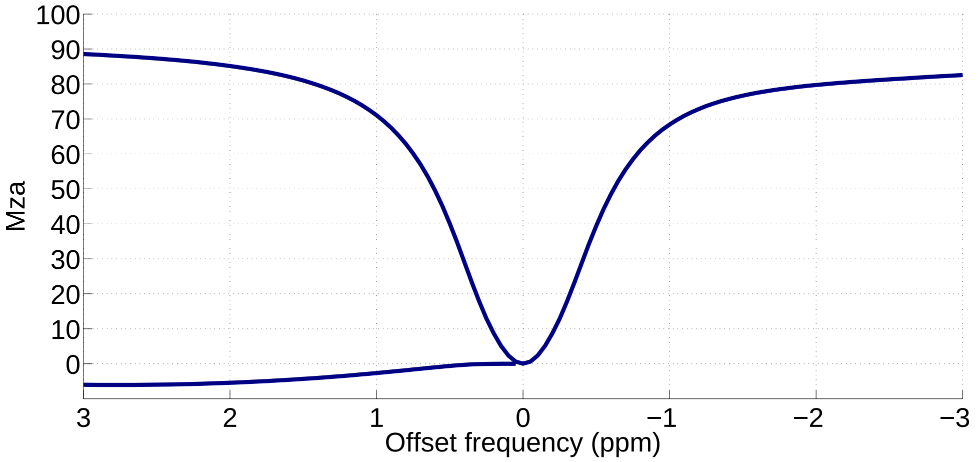

Figure 4.19: MT contribution to the CEST contrast: contrast (measured with MTRasym) created by asymmetric magnetization transfer pool (6% of the concentration of the free pool), in absence of any CEST exchanging metabolites. This effect is responsible for the negative baseline observed in many CEST studies after a certain frequency. Parameters: $B_1 = 0.9\ \mu$T, $t_{sat} = 1.7$ s

4.3.3.3 Myo-inositol CEST parameters in the literature

The first paper published on myo-inositol CEST [53] had a set of water phantoms at pH 7 with different myo-inositol concentrations. In this paper it is mentioned that myo-inositol has a broad peak "centered around 0.6 ppm" and the measured exchange rate is reported to be 600 Hz. The method used to calculate the exchange rate in this study (following [296]) is an approximation, since it is assuming absolute saturation of bound protons and no spillover effects. However, due to the proximity of the myo-inositol pool to the water peak, a low powered saturation pulse has to be used to specifically minimize the direct water saturation, which also causes an incomplete saturation of the myo-inositol protons (as can be seen in the simulations, Figure 4.8). A frequently used alternative to calculate the exchange rate is to perform a fitting of an *in vitro* Z spectrum, but this is specially unreliable in this case, due to the absence of a clear distinctive CEST peak, separated from the water (intermediate-to-fast exchange regime). Instead, we just have an asymmetric broad peak, such as in Figure 4.10. Several sets of parameters can be a reasonable fit to this kind of spectrum, complicating the extraction of a clear exchange rate value, since the other parameters would have to be known within small margins, including the exact chemical shift of the broad myo-inositol peak.

More recently, new CEST approaches other than the conventional saturation transfer experiment have been developed. The FLEX [20] method modulates the water signal by encoding the chemical shift of each proton pool. It has also just has been reported to be very sensitive to chemical exchange based water line broadening, thus making it suitable for studying the parameters of intermediate-to-fast exchange regime protons [311]. Myo-inositol parameters have been estimated to be 1.1 ppm for the chemical offset and 1381 Hz for the exchange rate. These parameters roughly match those obtained from another non standard CEST approach, the spin lock experiment, with a study by Jin and Kim in as early as 2012, predicting myo-inositol parameters to be 0.93 ppm and 1250 Hz [51].

For my optimization procedure, the fact that the myo-inositol resonance frequency is probably further apart from the water peak (around 1 ppm) entails less direct saturation and B_0 artifacts. The 0.5-1 ppm range is suitable for a CEST integral map (described in section 1.5.6) for myo-inositol contrast. However, the exchange rate being faster than 600 Hz would make the myo-inositol protons less saturated than what these simulations assumed. Together with the larger offset, this makes the optimum B_1 power for a maximum CEST contrast slightly higher than 0.9 μT. After redoing the simulations that value is 1.4 μT (for 0.93 ppm, 1250 Hz) or 1.6 μT (for 1.1 ppm, 1381 Hz), with a maximum CEST effect of around 3% (same as before).

4.3.4 Optimizing a Pulsed CEST experiment

A CW approach has been used for all *in vivo* CEST data (see chapter 5), with the presaturation parameters taken from the CW simulations in the previous section. Nevertheless, most of the early *in vitro* CEST data for this project was acquired with a pulsed CEST scheme (see section 4.4.1). The reason behind this is because the fast segmented gradient echo sequence that made possible the use of a long hard pulse was not developed until the beginning of the first *in vivo* experiments (as explained in 5.2), when acquiring a high resolution CEST image in a short amount of time became a priority.

In the initial *in vitro* work, the use of a standard gradient echo sequence meant that the most convenient CEST presaturation scheme was to apply a few short strong pulses before every line of k space, with the saturation building up until the centre of k space was read and the contrast acquired. Full details of the pulsed CEST protocol are in section 4.4.1: four 46 ms Gaussian prepulses per line, with a peak B_1 power of 3 μT. Since the matrix size was 64x64 and the encoding linear, a total of 128 pulses were applied by the time the k space centre was acquired.

4.3.4.1 Gaussian pulse

In order to further characterize the Gaussian pulse, I am going to calculate the equivalent average B_1 power and average B_1 field, as described by Zu et al. [34], using a discretised approach [22, 36, 300] to simulate the pulsed CEST experiment. That is, dividing the train of shaped pulses in many hard segments and propagating the CW analytical solution through all of them. These formulas take into account the discretisation of the Gaussian pulse:

Average B1 field

$$\text{Average } B_1 \text{ field (AF)} = \frac{1}{t}\int_0^t B_1 \,\mathrm{d}t \tag{4.3.1}$$

Separating the Gaussian pulse in discrete hard pulses yields:

$$\text{Average } B_1 \text{ field (AF)} = \sum_i \left(\frac{1}{D} B_1(i) \frac{D}{N}\right) \tag{4.3.2}$$

where N are the number of discrete segments (hard pulses) and D is the pulse duration (s).

Average B1 power

$$\text{Average } B_1 \text{ power (AP)} = \sqrt{\frac{1}{t}\int_0^t (B_1)^2 \,\mathrm{d}t} \tag{4.3.3}$$

Separating the Gaussian pulse in discrete hard pulses yields:

$$\text{Average } B_1 \text{ power (AP)} = \sum_i \left(\sqrt{\frac{1}{D} B_1(i)^2 \frac{D}{N}}\right) \tag{4.3.4}$$

where N is again the number of discrete segments (hard pulses) and D is the pulse duration (s).

Figure 4.20 shows the Gaussian pulse used in the pulsed CEST experiments, with the corresponding B_1 average power and field.

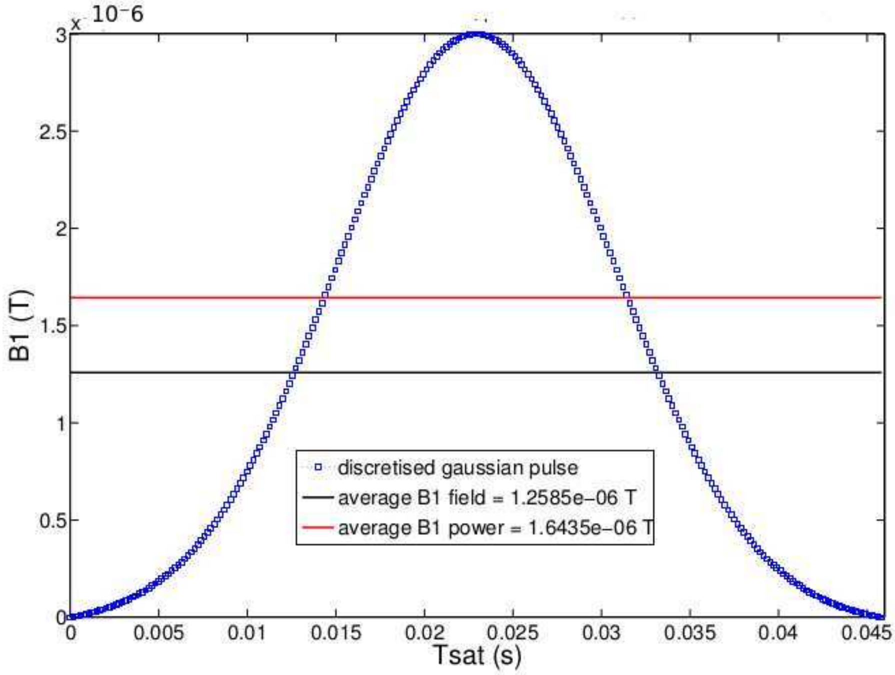

Figure 4.20: Gaussian pulse for pulsed CEST experiments: 46 ms duration, with a peak B_1 power of 3 μT (in blue colour). The red line represents the B_1 average power, 1.64 μT and the black line, the B_1 average field, 1.26 μT

4.3.4.2 Simulations

The parameters used in the simulation include a pulse train of 128 Gaussian pulses with a duration of 46 ms each and no interdelay, a flip angle of 875 degrees, discretised with a minimum of $N = 64$ points. The other parameters needed (i.e. relaxation rates, exchange rate, chemical offset, etc) are the same as in the CW simulations, while the concentration of myo-inositol is 10 mM. More details of the imaging sequence are: TE = 4 ms, TR = 56.43 ms, flip angle = 20 degrees, FOV = 18x18 mm, slice thickness = 1 mm.

First, just to check the simulation accuracy, the discretised pulsed CEST approach is compared with a numerical integration with equivalent parameters (ode45, Matlab, a time consuming but rigorous approach). The results are in Figure 4.21, with good agreement between the two.

Tee et al. compare in their work three different simulations for amine protons (1.9 ppm, 50 Hz): the discretised approach, a CW simulation with a hard pulse power equal to the average B_1 field and another with the average B_1 power. He found that the average B_1 power simplification was a good match for the more computationally expensive discretised Z spectrum, and suggested that it could be a valuable tool for Gaussian pulsed CEST studies and slow exchanging protons [300]. However, myo-inositol does not fit those requirements: the average B_1 field is more adequate as a hard pulse approximation of a Gaussian pulse train than the average B_1 power (see Figure

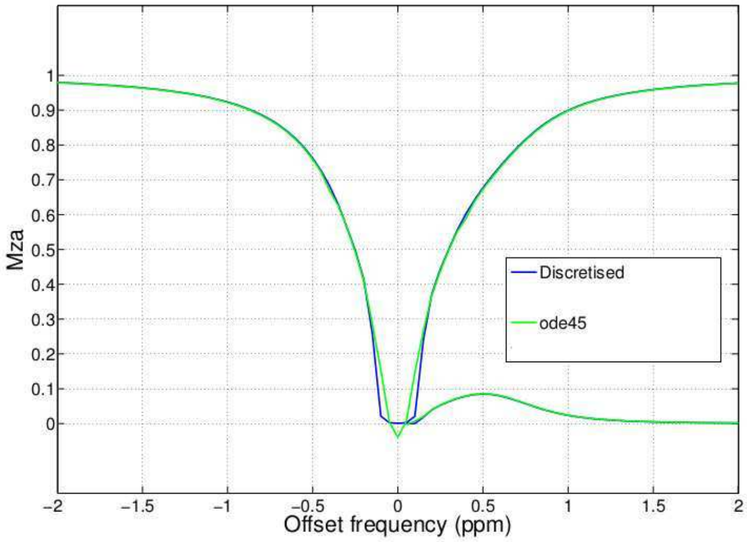

Figure 4.21: Numerical integration and discretised approach: comparison between numerical integration of my Gaussian pulse train (ode45 in built Matlab function, green) and discretised approach (blue), with a quite good overlap everywhere but at the centre of the water peak.

4.22), although the approximation is worse than the amine protons case, which is reproduced in Figure 4.23 together with the original from Tee et al..

In summary, the preferred pulsed CEST simulation method for myo-inositol is the discretised approach. Pulsed CEST parameters used for *in vitro* myo-inositol CEST experiments produce a contrast of around 9 % CEST effect for a myo-inositol concentration of 10 mM (assuming long T_2 pool), which is very similar to the maximum value for the same concentration obtained with the optimized CW CEST myo-inositol simulation (in section 4.3.2.1).

4.3.5 Conclusion

The simulations have provided information about the expected CEST contrast *in vitro* and *in vivo*, using different models with increasing complexity. The simplest case, a two pool model with a long T_2 (ie: phantom made of water and 10 mM myo-inositol) resulted in a maximum CEST effect of around 11% (CW, t_{sat} = 4 s and B_1 = 1.7 μT). The equivalent pulsed CEST experiment produced a contrast of around 9 %, using a train of 128 Gaussian prepulses (with 46 ms duration each, 875 degrees flip angle and 100% duty cycle).

Finally, a model closer to the *in vivo* situation was considered. A two pool model with a short T_2 (ie: phantom made of agarose and 10 mM myo-inositol) yielded a reduced expected maximum CEST effect of around 2% (CW, t_{sat} = 1.8 s and B_1 = 0.9 μT).

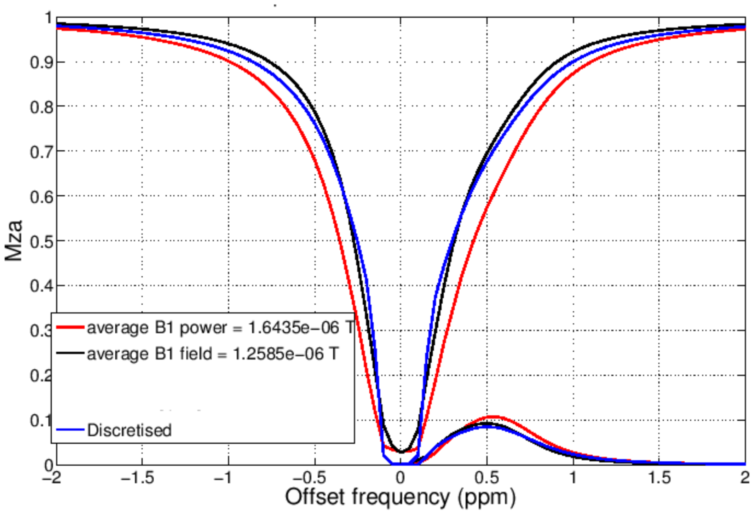

Figure 4.22: Method comparison: comparison between the discretised approach (blue), a CW simulation with a hard pulse power equal to the average B_1 field (black) and another with the average B_1 power (red), all for myo-inositol protons (10 mM, 0.6 ppm, 600 Hz).

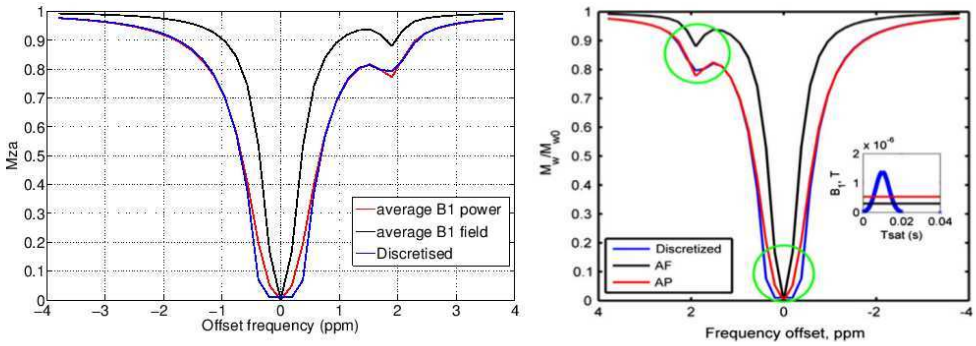

Figure 4.23: Method comparison:

Right: Simulation comparison of the discretised approach, a CW approximation with a hard pulse power equal to the average B_1 field and another with the average B_1 power for amine protons (1.9 ppm, 50 Hz), extracted from Tee et al. [300]. **Left:** replica using my Matlab code.

4.4 Optimizing CEST through *in vitro* experiments

Introduction

Simulations have been useful to optimise the parameters of the CEST sequence and to estimate the CEST contrast in a specific situation. Next, the theory will be experimentally tested and confirmed. The aim of the *in vitro* experiments is to gain a better understanding of the practical problems associated with a CEST experiment, to optimise the imaging protocol and postprocessing, to replicate relevant experiments from the literature and to test the accuracy of the simulations done in the previous section (4.3), before any *in vivo* experiments.

Here is an outline of the protocol for the *in vitro* experiments:

4.4.1 Protocol

Imaging has been performed on a 9.4 T preclinical scanner (Varian, Agilent Technologies), using a volume transmitter coil and a two-channel surface receiver coil. Custom made Matlab code (The Mathworks, 2010) has been used for postprocessing (details in chapter 5).

Shimming Shimming was performed using the FASTMAP protocol, with resulting linewidths of around 6 Hz for individual phantoms.

CEST imaging The CEST imaging sequence used was gradient echo (TE=4 ms, TR=56.43 s, flip angle=20°, 1 mm slice thickness, 64x64 matrix size), with a pulsed CEST presaturation module before every excitation: four Gaussian prepulses (46 ms, 3μT), at variable offsets (between ±2 ppm for myo-inositol, and between ±5 ppm for glutamate or creatine).

Reference image A separate gradient echo image without the prepulse module was taken as a reference.

WASSR image Same as the CEST image, but with 0.1 μT Gaussian prepulses between ±1 ppm.

Postprocessing First, if necessary, the regions of interest (ROIs) are selected and extracted. The image intensity is normalized using the reference and corrected for B_0 inhomogeneities using the WASSR method. Finally, the asymmetry curves are calculated as the signal difference between the positive and negative offsets around the water peak.

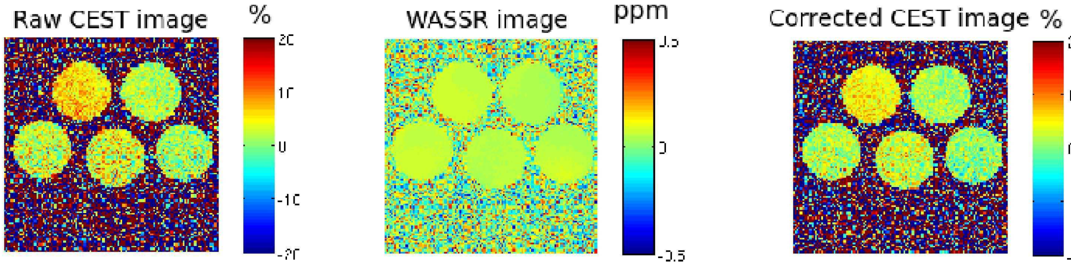

Figure 4.24: CEST image example: Raw image, WASSR map and corrected final CEST image.

4.4.2 Varying metabolite concentration: influence on the CEST effect

Solutions of myo-inositol with increasing concentration (0-12 mM) in saline solution (PBS) and 3% agar myo-inositol phantoms (50 and 100 mM) were prepared at pH 7, before imaging on a 9.4 T MR imager (Varian, Agilent Technologies) using the previously described protocol (4.4.1).

Agar has been used extensively in the literature as a macromolecular short T_2 pool model [302, 303, 312]. After mixing deionized water and myo-inositol to the desired concentration and adjusting the pH of the mixture, agar was added (Sigma Aldrich, 3%) and the solution was heated to the boiling point in a water bath. Finally, the mixture was transferred to a plastic tube and left to rest overnight.

Figure 4.25 shows the CEST effect for the saline myo-inositol solutions, together with the linear relationship between metabolite concentration and CEST effect (experimental data and simulations), while Figure 4.26 shows the CEST effect of the two agar myo-inositol phantoms and the correspondent simulation results.

The saline solution results show a direct proportionality between CEST effect and myo-inositol concentration. Moreover, the values obtained agree with the simulations and also with the literature: Haris et al. has performed a similar experiment (pH 7.4, myo-inositol solutions in PBS: 4, 6 and 10 mM), obtaining CEST effect values of about 4%, 6% and 8% respectively [53].

The agar phantom results are in good agreement with the three pool simulations (free water, myo-inositol, MT). For the magnetization transfer pool, a Gaussian absorption line shape was used to describe the agar phantom and a symmetric MT effect centered around 0 ppm was assumed.

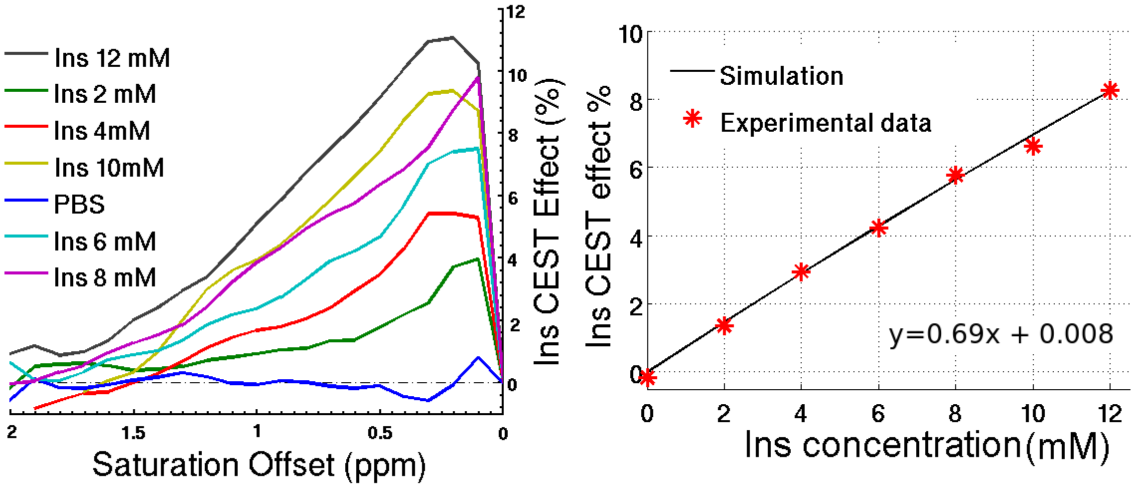

Figure 4.25: CEST effect and metabolite concentration.

Left: CEST effect for all saline myo-inositol solutions (0-12 mM). **Right:** CEST effect linear dependence on myo-inositol concentration, the red asterisks being the experimental data and the solid line the myo-inositol pulsed CEST simulation.

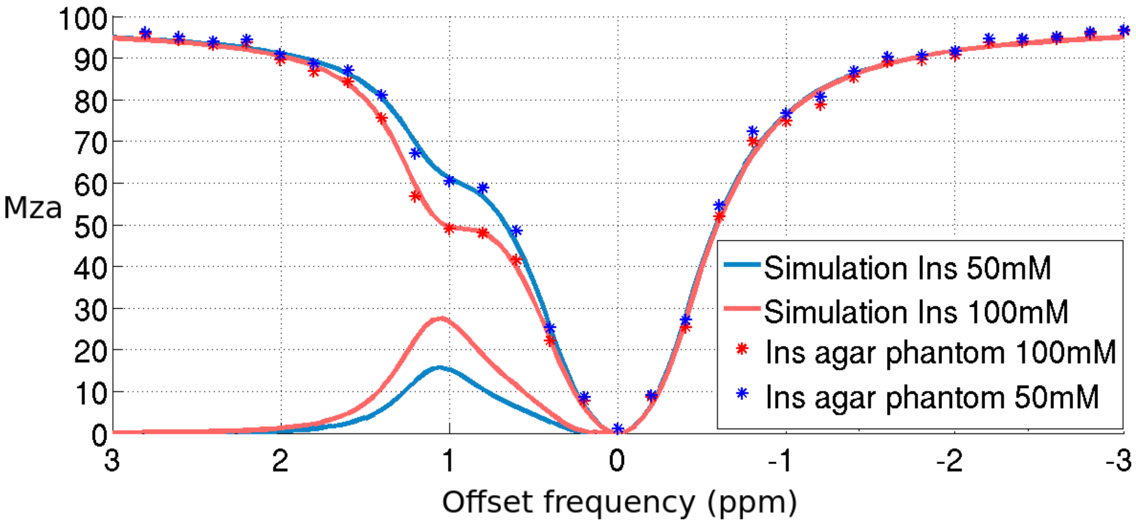

Figure 4.26: CEST effect, agar phantom.

CEST effect and Z spectra are shown for two different myo-inositol concentrations (50 mM, blue and 100 mM, in red), asterisks representing the experimental data points and the solid lines the myo-inositol CEST three pool simulation values. The *in vitro* myo-inositol agar phantom results validate the three pool simulations (free water, myo-inositol, MT).

4.4.3 The complexities of the CEST signal at 0.6 ppm: overlap of different metabolites

One of the questions that the *in vivo* application of CEST raises is specificity, or how many metabolites contribute to the CEST signal obtained in a particular experiment. One of the aims of this project being mapping myo-inositol *in vivo*, which resonates around 0.6 ppm in the Z spectrum, it is important to evaluate which other metabolites give raise to a CEST effect at that particular frequency, thus overlapping with the myo-inositol signal.

Phantoms containing metabolites in biologically relevant concentrations [8] have been prepared in saline (PBS) at pH 7: myo-inositol (Ins, 10 mM), creatine (Cre, 6 mM), glutamate (Glu, 12 mM), glutamine (Gln, 5 mM), taurine (Tau, 6 mM), N-acetyl-aspartate (NAA, 9 mM) and GABA (2 mM). Seven individual phantoms have been prepared, together with three mixed phantoms: Ins-Glu, Ins-Cre, Ins-Glu-Cre.

Figures 4.27 and 4.28 show a subset of contributions to the CEST signal (0-5 ppm) at pH 7 as would appear in a mouse brain.

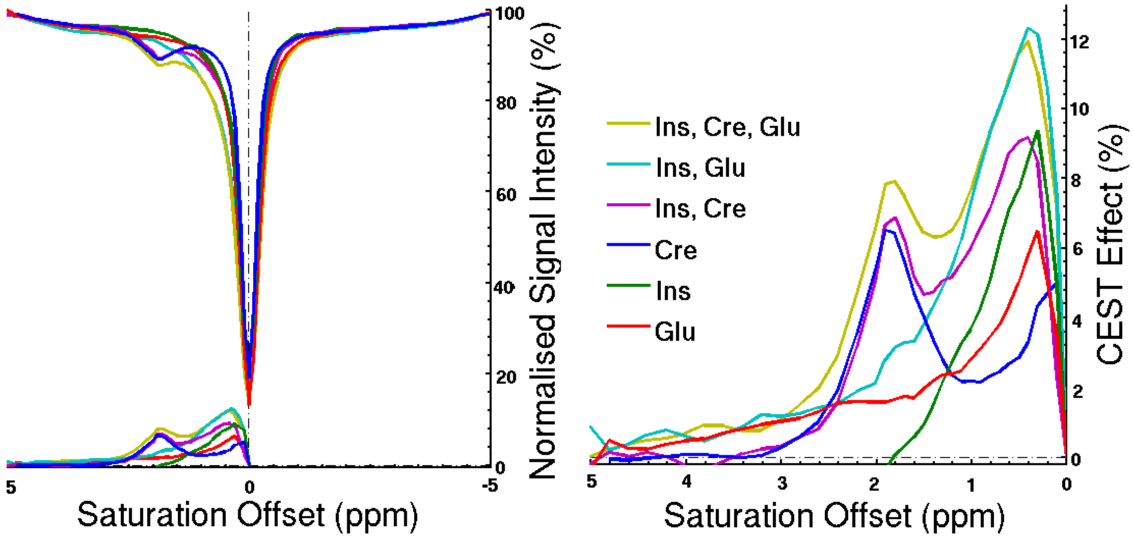

Figure 4.27: Metabolites overlapping with the myo-inositol CEST signal I: *In vitro* Z spectrum (left) and asymmetry spectrum (right) of individual and mixed phantoms: myo-inositol (Ins, 10 mM, green), creatine (Cre, 6 mM, dark blue), glutamate (Glu, 12 mM, red), myo-inositol/creatine (fuchsia), myo-inositol/glutamate (light blue), myo-inositol/creatine/glutamate (yellow). Glutamate and in a lesser extent creatine are examples of metabolites overlapping with myo-inositol at physiological conditions.

In the light of the previous results, different metabolites will contribute to the CEST signal in the 0-5 ppm range, and said contributions have to be examined and discussed in each case. Haris

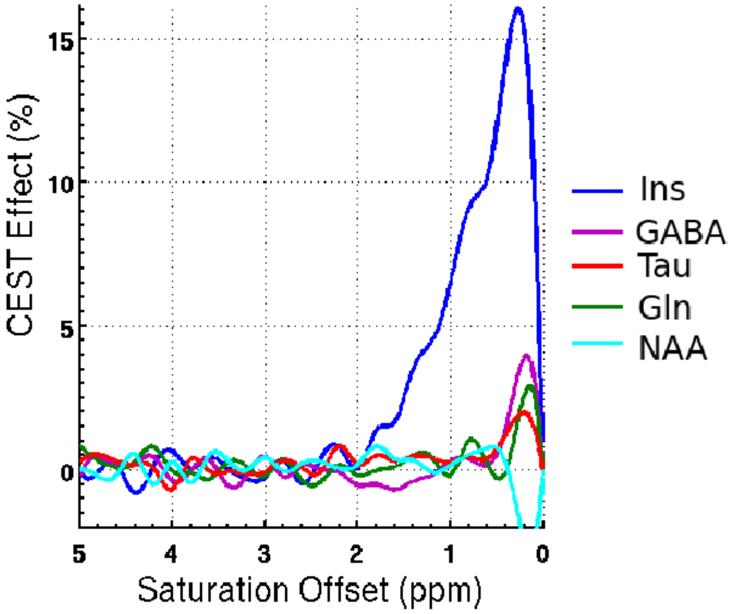

Figure 4.28: Metabolites overlapping with the myo-inositol CEST signal II: *In vitro* CEST asymmetry spectrum of individual phantoms: myo-inositol (Ins, 10 mM, dark blue), glutamine (Gln, 5 mM, green), taurine (Tau, 6 mM, red), N-acetyl-aspartate (NAA, 9 mM, light blue) and GABA (2 mM, fuchsia). These brain metabolites do not overlap with myo-inositol at physiological conditions.

et al. affirms that in his myo-inositol mapping experiment all the contributions from other CEST metabolites are negligible: he states that NAA does not have an observable CEST effect at the physiological pH, and that others like Glu, Cre and GABA show overlapping when not using his optimized sequence [53]. However, Lee et al. concludes that creatine and glutamate produce sizeable contributions to myo-inositol CEST [56], in agreement with the data presented here and with multiple reports of other CEST metabolites containing hydroxyl groups, such as glucose [43]. All the different metabolite contributions (or pools) are directly or indirectly connected and are exchanging magnetization and therefore, the signal observed in a saturation transfer experiment is a nonlinear function of the properties of each pool involved [22]. Consequently, definite relations effect-metabolite do not seem feasible (see 1.5.5), but correlations could be established instead, by validating with other techniques or with a “before/after contrast“ type of experiment. The main limitation in this kind of experiment is the scenario where more than one metabolite is affected since changes in overlapping metabolites could interfere with each other, complicating the interpretation of the CEST contrast.

4.4.4 Buffer solution influence for CEST phantom preparation

The CEST effect is mainly determined by the exchange rate and by the concentration of the labile protons (relative to the water protons), while the exchange rate k of a CEST metabolite is a function of temperature, pH and buffer properties of the solution. The aim of this experiment is to observe the differences between the use of water or phosphate buffered saline (PBS) in *in vitro* CEST experiments. Solutions of 10 mM myo-inositol and 6 mM creatine were prepared in PBS and water at pH 7, before imaging on a 9.4 T MR imager (Varian, Agilent Technologies). The change in solvent produced different results for creatine and myo-inositol: while the CEST effect was significantly suppressed for the creatine solution when prepared in water, it did not vary for myo-inositol, although the centre of the peak was shifted for myo-inositol and remained fixed for creatine (see Figure 4.29).

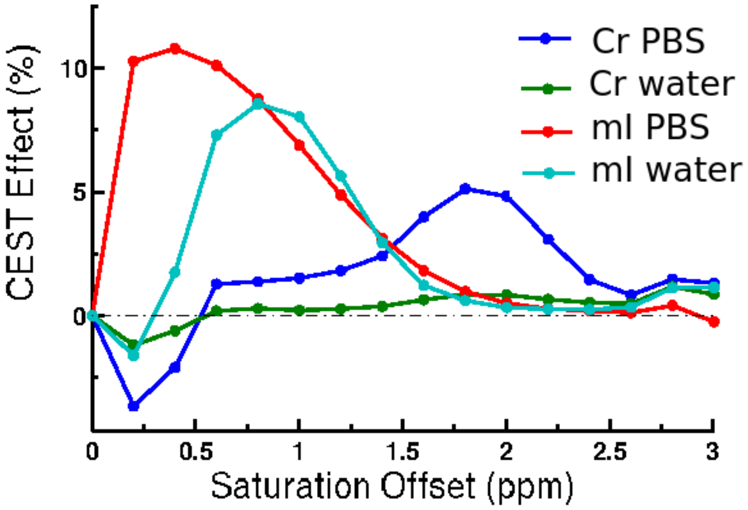

Figure 4.29: CEST effect and buffer solution properties:
CEST effect comparison of 6 mM creatine solutions in water (green) and PBS (dark blue), plus 10 mM myo-inositol solutions in water (light blue) and PBS (red). Different buffer properties raise different CEST effects.

Since the myo-inositol peak is quite broad, and its centre position may vary in different buffer conditions, the integral method [145] could be used for measuring the CEST effect, since it minimizes the errors due to the uncertainty in the position of the peak. Instead of calculating the asymmetry comparing the signal coming from a single resonance frequency on both sides of the water peak ('punctual' approach), the integral approach consists of comparing the areas comprehending a range of frequencies instead, around the supposed CEST maximum and symmetric to the water peak.

4.4.5 Conclusion

A robust *in vitro* CEST protocol has been developed, with a reference image, a CEST array and a WASSR array, to compensate for B_0 inhomogeneities. The MRI sequence for both the CEST and WASSR arrays contains a pulsed CEST approach for presaturation, with a train of 128 Gaussian prepulses and a standard gradient echo readout. However, the time needed for a full experiment (more than 20 min) is not practical for *in vivo* CEST, which requires a faster sequence, developed in chapter 5.

In vitro myo-inositol CEST images have been obtained with this CEST protocol. The *in vitro* results validate the simulations and show the expected linear dependency between concentration and CEST effect. Nevertheless, overlapping of different metabolites in the 0-5 ppm range does not allow the unequivocal identification of myo-inositol in a *in vivo* CEST spectrum. Examples of metabolites contributing to the myo-inositol *in vivo* CEST signal are creatine, glutamate and others containing hydroxyl groups, such as glucose. Therefore, complementary techniques like MRS should be used alongside CEST as validation, to try to establish the source of CEST contrast in a specific challenge.

CHAPTER 5

CEST imaging of neuroinflammation

5.1 Introduction

Chemical exchange saturation transfer (CEST) is a molecular MRI contrast mechanism, in which exchangeable protons are detected indirectly by their effect on the water signal after an off resonance saturation. At higher magnetic fields, the chemical dispersion is larger, which improves the detection and quantification of CEST protons resonating in the proximity of the water peak, by reducing the competing effect of direct water saturation. However, increased B_0 inhomogeneities create artifacts in the Z spectra and CEST images, especially when using gradient echo (GE) readouts, thus reducing the accuracy of the method. A particularly difficult case are metabolites containing hydroxyl groups (OH): their proximity to the water peak makes them more susceptible to both direct water saturation effects and B_0 inhomogeneity artifacts.

The osmolyte myo-inositol, mainly present in glial cells, has been proposed as a marker for microglial activation (part of the neuroinflammatory process), with evidence comprising clinical and preclinical MR Spectroscopy (MRS) studies alike (see section 2.3.2.1). Our own research (chapter 3) shows an increase of myo-inositol MRS levels in a mouse model of Alzheimer's disease (AD) four hours after a systemic injection of lipopolysaccharides (LPS), which is considered a neuroinflammatory model (as described in section 2.2.6 and 2.2.6). This increase was verified with histology (Iba1 staining).

Since myo-inositol also has a CEST effect due to its six hydroxyl groups, the overall objective of this chapter is to evaluate the response to a neuroinflammatory stimulus using CEST, with MRS and histology for verification, in both AD and control mice. CEST has the advantage of a much higher spatial resolution over MRS. A previous study by Haris et al. performed a similar experiment with myo-inositol CEST, MRS and histology, comparing 20-month old AD mice with age matched controls and finding increased contrast in the first group [123]. However, we want to study the early inflammatory response, by injecting in the right hippocampus a low dose of LPS (to avoid sickness syndrome [183]) to young AD mice and age matched controls (3 month old), since this could help to understand the onset of the neuroinflammatory process and would be extremely useful from a diagnostic point of view. The rationale behind using an icv injection instead of a systemic administration of LPS, as in the previous chapter, is to maximise the observed effect in the hippocampus and to be able to use the contralateral side of the brain as control.

This chapter is organized in two parts: the first part, 5.2, explores the challenges of imaging at 9.4 T OH-containing metabolites such as myo-inositol with CEST *in vivo*, in the mouse hippocampus. It continues the CEST optimization that was started in chapter 4, with simulations (section 4.3) and *in vitro* work (section 4.4), with the aim of developing a robust *in vivo* mouse brain CEST methodology at 9.4 T, studying its reproducibility in the 0-3 ppm region.

In the second part of the chapter, 5.3, an *in vivo* study is presented, focused on evaluating the metabolite response to an LPS inflammatory challenge using CEST, MRS and histology.

5.2 CEST *in vivo*: challenges and optimization

In vivo CEST at 9.4 T (Agilent scanner, with software Vnmrj 4.0) requires a fast and robust imaging sequence, together with an appropriate animal holder and careful shimming. The work undertaken to address these issues is detailed in this section:

5.2.1 Animal holder design

A small volume coil (22 mm diameter) creates a more homogeneous magnetic field (good for CEST) compared with the previously used head coil in chapter 3 (72 mm volume transmitter, surface receiver), while keeping the sensitivity required for a mouse brain. For this coil a new animal holder was needed, and several prototypes were designed and built using a 3D printer (by Bryan Morris, Medical Engineering Unit Manager, University of Nottingham), followed by testing. The main issues to overcome are:

Keeping the animal immobilized The small coil diameter (22 mm) and the distance between the edge of the coil and the centre (around 18 mm, which required for part of the animal's body to be inside the coil for an optimal image of the area of interest), did not allow for the use of ear bars, and they also imposed a limitation on the animal size (no more than 30 g weight). On the final model, the animal bites a mouth piece, inside of a nose cone, with two extensible thin rectangular pieces coming up to the cheeks, to reduce breathing artifacts on the images and shimming procedure.

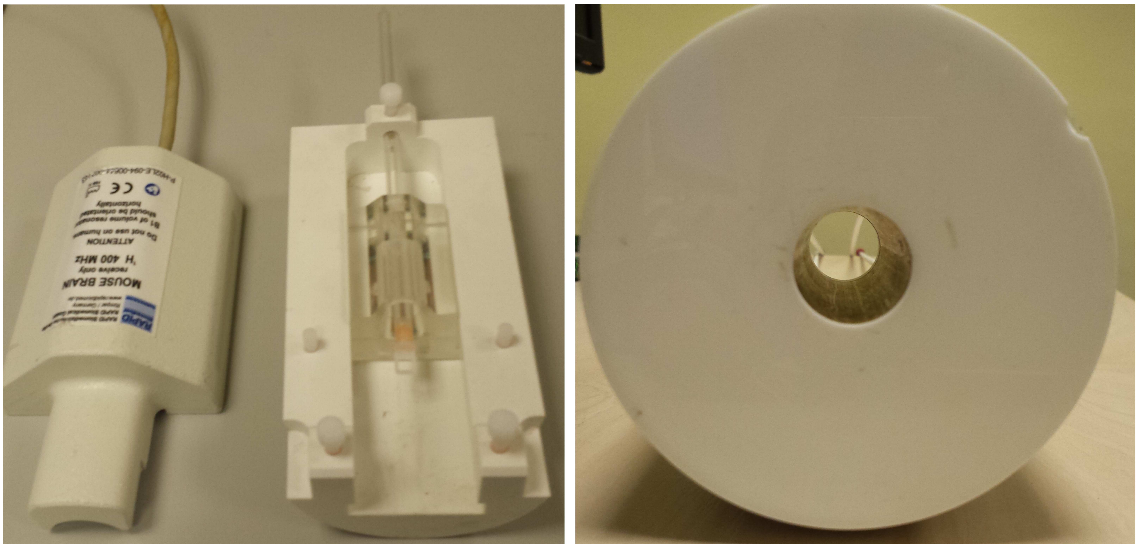

Figure 5.1: Head coil (left) and small volume coil (right), both from Rapid Biomedical.

Maintaining the animal temperature Two separate grids of plastic tubing with circulating warm water were created for this purpose: underneath and over the animal body coming out of the coil. A water bath allowed for temperature control of the water during the scanning.

Scavenging the residual anaesthesia Several holes were made on the nose cone, around the overture made for the mouth piece, so that the excess anaesthesia in there could be absorbed through a scavenger situated at the back of the scanner.

Avoiding shimming artifacts The use of metallic tools to further shape the holder after the 3D printing process caused some shimming artifacts during the testing procedure, which required the creation of a new prototype without these tools.

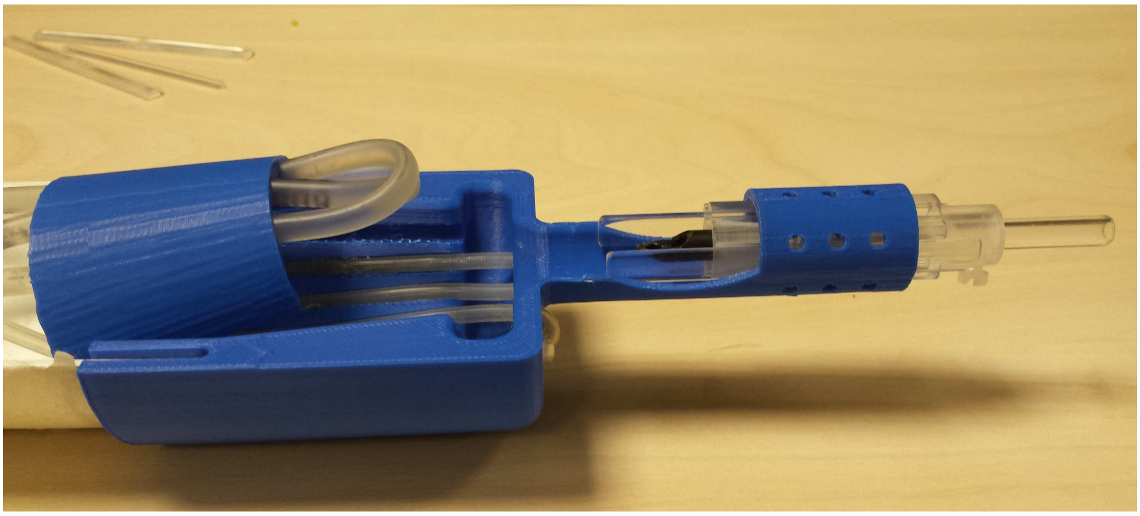

Figure 5.2: Finished animal holder.

5.2.2 CEST sequence development

5.2.2.1 Gradient echo

During the *in vitro* experiments in chapter 4, the CEST sequence consisted of a standard gradient echo single slice readout with linear encoding (20° flip angle, TE = 4 ms, TR = 56.43 ms, FOV = 18x18 mm), with four Gaussian prepulses of 46 ms each (3 μT) and 3 ms delay, applied before every line of k space. The saturation for this sequence starts building up from the first line of k-space until the centre is read, which provides the CEST contrast. Minimal programming was required for this sequence; however, the time for a full CEST experiment (reference, CEST array plus WASSR array) is around 22 min for a 128x128 matrix size.

5.2.2.2 Segmented gradient echo

Looking for higher time resolution for *in vivo* applications, another sequence was developed: a segmented gradient echo single slice with centric encoding (15° flip angle, TE = 1.57 ms, TR = 3.15 ms, 8 dummy scans, FOV = 20x20 mm, 2 mm slice thickness) and a hard prepulse (1.6 s, 0.9 μT) before every segment (two normally used). These values were taken from the CW CEST optimization in chapter 4. Elements of both gems and mprage were used for programming this sequence and the timing of a full CEST experiment was reduced in this way to 10 min, with a similar CEST contrast obtained. The image quality for both sequences, together with simple diagrams can be found in Figure 5.3.

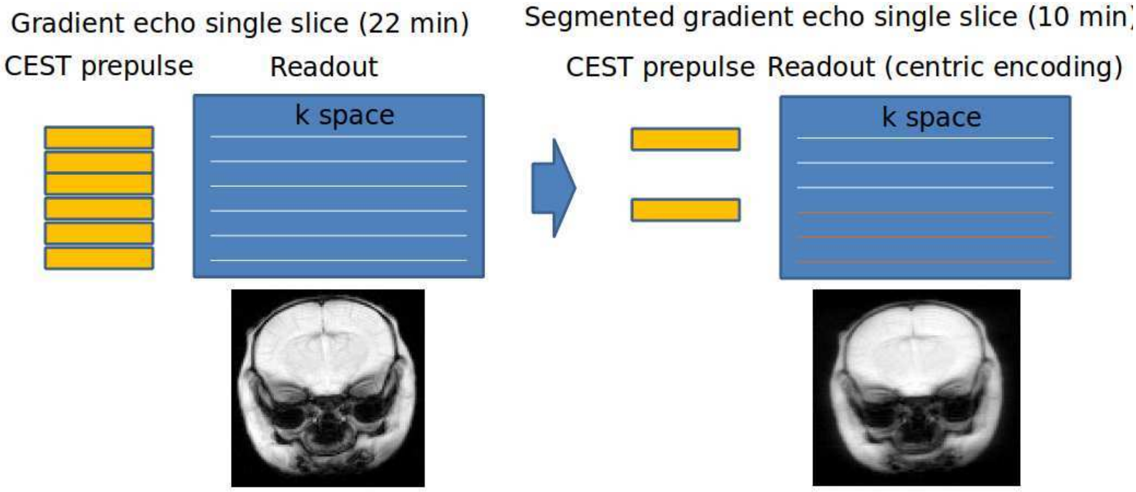

Figure 5.3: Developing a faster CEST sequence:
This diagrams show how the CEST acquisition was shortened, from applying a prepulse in every line of k space (left hand side, conventional gradient echo readout), to only applying the pulse twice for a full image (segmented gradient echo with centric encoding). The image loses definition but not contrast (given by the centre of k space).

5.2.2.3 CINE

After the changes in the pulse sequence had been programmed and tested, the software for the Agilent 9.4 T scanner was updated to a new version, from Vnmrj 3.2 to Vnmrj 4.0, which has several new pulse sequences. CINE, a fast gradient echo sequence is one of them, intended for performing cardiac studies, with options like phase rewinding, RF spoiling, triggering and also segmentation. A centric encoding was implemented for the CINE sequence, and the same CEST prepulse incorporated so that it could be compared with the other one. Both gradient spoiling and RF spoiling were chosen for CINE, alongside with similar TE, TR, number of segments and flip angle parameters (15° flip angle, TE = 1.57 ms, TR = 3.15 ms, 8 dummy scans, FOV = 20x20 mm, 2 mm slice thickness, 2 segments).

5.2.2.4 Reproducibility

To compare the *in vivo* reproducibility of the two segmented gradient echo sequences, CEST measurements (n=4 per each readout) were repeated on a wild type mouse under isoflurane anaesthesia.
CEST experiments were performed on a Varian (Agilent Technologies) preclinical scanner 9.4 T with a transmit/receive volume coil. A continuous wave (CW) saturation scheme (1.6 s hard pulse, 0.9 μT) applied at 31 offsets between ±3 ppm was followed by two different single slice readout imaging modules (128x128 matrix size, 2 mm thickness): segmented gradient spoiled

GE and segmented gradient and RF spoiled GE (CINE), both with centric encoding and 4 min acquisition time. The CW prepulse for the WASSR acquisition was 0.5 s and 0.1 μT, with 35 offsets in ±1 ppm (5 min acquisition time, 9 min for a single experiment).

For the analysis, WASSR frequency shift maps were created using the maximum symmetry algorithm, and the CEST spectra were shifted accordingly, before performing the asymmetry analysis. Three types of CEST maps were obtained from the asymmetry spectra by integrating different regions: 0.4-0.8 ppm (OH1), 1-1.5 ppm (OH2), 1.7-2.3 ppm (NH), Figure 5.4A. ROIs were chosen in the right hippocampus and thalamus to study the variability of the spectra. Standard deviation (SD) maps were calculated for both readouts, and mean and maximum values were obtained (Figure 5.4 B). Mean and SD were calculated for the Z spectra in the two ROIs (see Figure 5.4C).

The CINE readout is the one showing better repeatability, with a lower SD for all three maps (see Figure 5.4B). CEST data is more reproducible the further away from the water peak, with SD(NH,1.7-2.3 ppm) < SD(OH2,1-1.5 ppm) < SD(OH1,0.4-0.8 ppm) for both sequences, as expected since B_0 shifts in the Z spectra affect more severely the closest area to the water peak of the CEST asymmetry curve. Movement is one of the main factors affecting reproducibility.

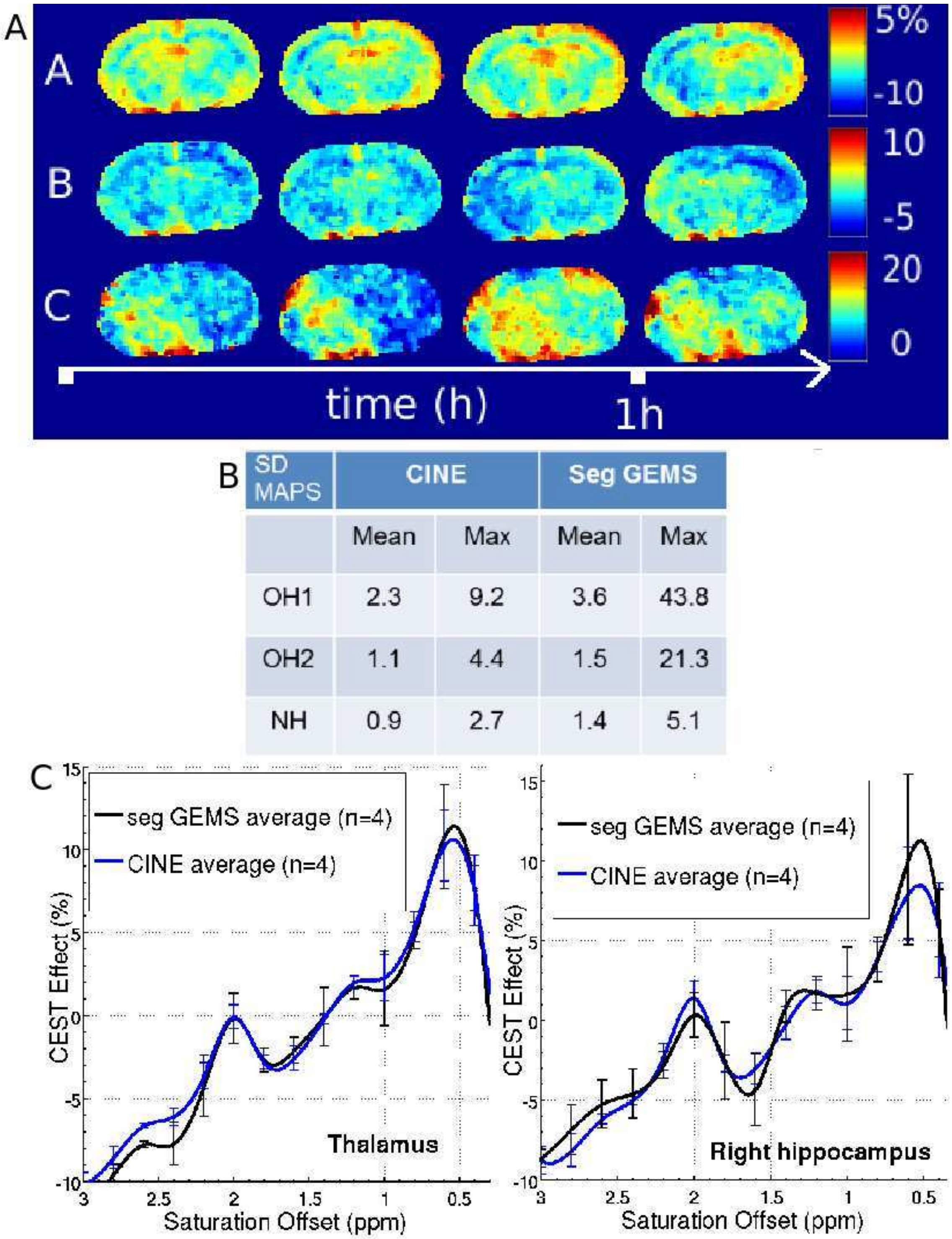

SD MAPS	CINE		Seg GEMS	
	Mean	Max	Mean	Max
OH1	2.3	9.2	3.6	43.8
OH2	1.1	4.4	1.5	21.3
NH	0.9	2.7	1.4	5.1

Figure 5.4: CEST sequence *in vivo* reproducibility: Single slice CEST data from a wild type mouse (n=4 repeated measurements per readout).

A: CINE CEST integral map reproducibility *in vivo*. A) NH 1.7-2.3 ppm, B) OH2 1-1.5 ppm, C) OH1 0.4-0.8 ppm. Comparison of two segmented gradient echo sequences, with **B:** standard deviation map values (%) and **C:** CEST asymmetry spectra. CINE is the more robust readout and CEST data is more reproducible at higher ppm, for both sequences.

5.2.3 Shimming optimization

The field of view (FOV) of the CEST images comprises a 2 mm thick single slice centered in the hippocampus. Several shimming protocols were tested to achieve a B_0 as homogeneous as possible across the brain in that slice, with special emphasis on the hippocampus. Once the mouse was stable in the scanner, the shims were zeroed and a global gradient echo shim (ge3dshim protocol from Vnmrj 4.0) was applied with 4 iterations. Then, a slab was chosen in the shim planner, containing the desired CEST slice, for a further local shim with ge3dshim for up to 4 iterations. If necessary, manual shim was applied after that. The quality of the shim obtained was evaluated by the linewidth measure (between 20 and 35 Hz), in addition to a WASSR image (0 ppm) to observe the water suppression.

The small size of the mouse brain together with high fields and movement complicates the task of shimming [313], even more so in regions of tissue interface changes, such as the cortex and the lower parts of the brain. These susceptibility artifacts caused inhomogeneities in the field maps on those areas, which can compromise the quality of the CEST maps in frequencies close to the water peak (0-1 ppm).

5.2.3.1 Agar caps

In order to reduce these artifacts, a 3% agarose gel [314] was given the shape of a half moon and introduced in a tight fit between the top of the head and the volume coil, before the beginning of the experiment. The caps were made fresh by mixing 20 mL of deionized water with 0.6 g of agar in a small glass beaker. Microwaved until boiling (and put in a hot plate, to remove the bubbles) they were poured into a plastic mould, made of a 2 cm diameter tube sliced in half lengthwise. Once the gel started setting, a second narrower tube was pressed on the top, until the gel was completely solid and could be removed without leaving any residual behind. Finally, a small piece of 1 cm long was cut, with an approximate thickness of 2 mm.

5.2.4 Optimization summary

A new animal holder has been designed and tested for this project, fit for the 22 mm diameter coil and offering proper support and restraint for the mice. Fundamentally, a faster CEST sequence has been developed, based on the CINE sequence (gradient and RF spoiled segmented gradient echo), with centric encoding to capture the maximum CEST contrast and a running time of 10 min for the whole experiment (reference, CEST array and WASSR array). This sequence has proven quite robust, with a higher reproducibility than other alternatives (conventional segmented gradient echo). Finally, the shimming procedure has been evaluated and optimized, since it is one of the key steps to obtain an artifact free myo-inositol CEST image.

Agar caps in between the top of the animal head and the volume coil have been introduced, to reduce the susceptibility changes in areas of tissue interface changes.

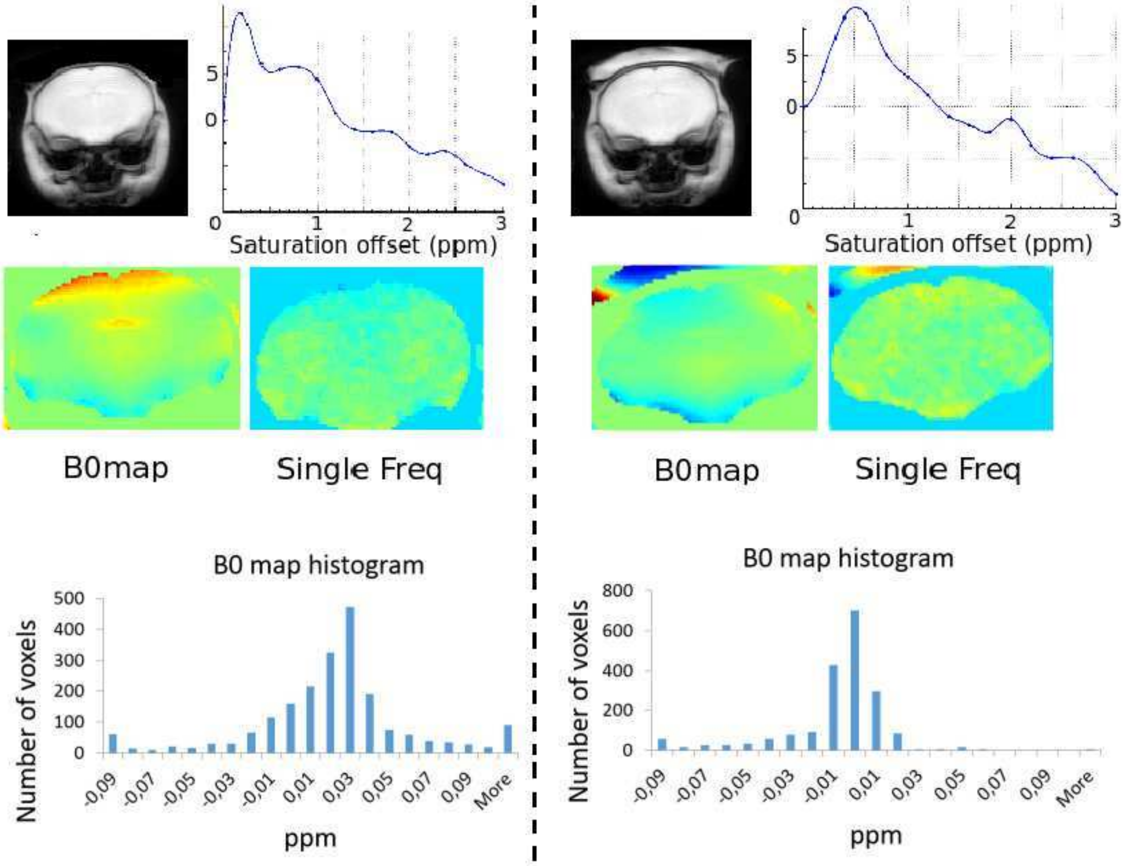

Figure 5.5: *Ex vivo* shimming optimization, agar gel head cap

Left: Anatomical image, B_0 map (WASSR), histogram showing the B_0 map dispersion, 0.6 ppm CEST map and Z spectrum of hippocampus ROI, following shimming procedures. **Right:** Same experiment after the placing of a 3% agarose gel cap on top of the brain, inside the volume coil. Note how the B_0 map homogeneity has improved (less disperse values seen in the histograms), as has the loss of signal in the cortex. Also the Z spectrum in the hippocampus has less artifacts close to the water peak. The B_0 map still shows inhomogeneities in the lower part of the brain (ear canal interface).

5.3 Detecting neuroinflammation with molecular MRI: a preliminary CEST study

5.3.1 Objectives

The aim of this study is to detect with chemical exchange saturation transfer (CEST) the early metabolic response to a mild inflammatory stimulus (hippocampal administration of LPS), using the contralateral side as control. Building on from the MRS study, we hypothesize that LPS induced transient neuroinflammation in the brain will increase myo-inositol levels, especially in animals with a pre-existing chronic brain disorder (mouse model of Alzheimer's disease, AD) and that the myo-inositol change will produce a CEST contrast at 9.4 T. CEST imaging, in particular the detection of metabolites with a resonant frequency close to the water peak (such as hydroxyls) benefits from high magnetic fields, due to the larger chemical dispersion.
The second objective is to validate the CEST contrast with MR Spectroscopy (MRS) and immunohistochemistry (Iba1), to assess the degree of neuroinflammation.

Haris et al. described an increase in myo-inositol CEST for 20-month old AD mice compared with age matched controls [123], with MRS and histology (Iba1) for verification. In contrast, this experiment aims to evaluate the early inflammatory response, to better understand the onset of the process which underlines many neurological disorders.

5.3.2 Methods

5.3.2.1 Animals

All procedures were approved as required under the UK Animals (Scientific Procedures) Act 1986.

28 female mice were used in this experiment, with an average weight of 23.0 ± 1.6g and average age of 3 ± 0.5 months. Drug and test naive, with no previous procedures, they had been group housed (2-6 per cage) in specific pathogen free (SPF) conditions, with a 12:12 h light-dark cycle, controlled temperature and humidity conditions, plus free access to food and water. As for genotype background, 13 are AD transgenic mice (APPSwe/PS1dE9) and 15 are wild type (WT) littermates. Details on the Alzheimer's disease mouse model can be found in chapter 3.

Protocol optimisation was performed with n=11 mice, while n=17 mice were used in a follow up study.

5.3.2.2 LPS CEST study design

Each animal received two unilateral intra-hippocampal injections of 2 μL each: LPS (5 ng/μL, right hippocampus) and phosphate buffered solution as control (PBS, left hippocampus). The brain region chosen for LPS injection was the hippocampus, due to its high microglial content [282], as well as being one of the most susceptible brain areas to Alzheimer's disease progression [174]. CEST and MRS measurements were acquired after LPS/PBS administration and three hours later, the brains were extracted for immunohistochemistry to determine the degree of neuroinflammation and microglial activation (Iba1). The experimenter was blind to group allocation (genotype).

An initial pilot study (over a period of three months) consisted of 11 animals: 4 female AD mice (APPSwe-PS1dE9) and 7 female wild type mice (WT). A second set of animals (n=17: 9 AD, 8 WT) were then used for a study (lasting one month), which started five months after the beginning of the pilot experiments. This study was performed with the previously described protocol, with the addition of a T_2 map acquisition. The T_2 map values were measured to discard the effect of possible T_2 changes caused by neuroinflammation in the CEST contrast. T_2 maps were acquired on a subgroup of 11 animals (5 AD, 6 WT).

The LPS solution was prepared fresh on the day of the first pilot experiment, with the last experiment taking place six months later.

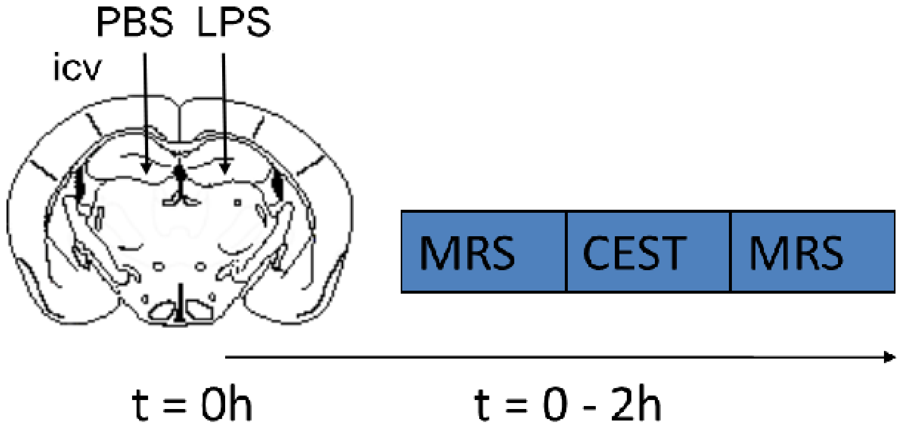

Figure 5.6: LPS CEST protocol:
Coordinates from Bregma of the LPS and PBS injection sites: -2.3 mm front-back, +/-1.5 mm right-left (LPS on the right, PBS on the left), 2 mm depth.

5.3.2.3 Animal surgery, anaesthesia and monitoring

The animals were taken out of the cages, their body weight recorded and then anaesthesia induction was performed inside a plastic box resting on a homeothermic blanket control unit (Harvard

Apparatus) outside of the scanner. Anaesthesia was performed with a mixture of oxygen and isoflurane (Isocare, 3% for induction and 1-2% for maintenance).

The anaesthetised mouse was placed and secured with ear bars in a stereotactic frame in the prone position, lying on top of a warm blanket. Anaesthesia was continuously administered trough a nose cone. A 1 cm-long cut through the skin was made from between the eyes to the back of the head, so that Bregma could be seen clearly. The localization of Bregma was measured, and the coordinates for the injection points calculated. Those coordinates were: -2.3 mm front-back, +/-1.5 mm right-left (LPS on the right, PBS on the left), 2 mm depth. Two perforations were made in the cranium at those positions using a needle attached to the stereotactic arm (Sterile Needle BD Microlance 3).

A 5 μL Neuros Syringe with a removable needle (33 gauge, Hamilton Company) was filled with PBS and positioned in the stereotactic arm and 2 μL were injected in the coordinates to the left of the central line. After that, the same procedure was repeated on the other side, with 2μL of the LPS solution.

Following the surgery, the animals were positioned in the imaging system with a custom made holder (details in section 5.2.1) designed to minimise motion and a circulating water system for body temperature maintenance, monitored using a rectal temperature probe (around 36.5-37.5 degrees Celsius). The respiration rate was also recorded, with a pressure pad in the chest connected to a small animal unit (SA Instruments, typical respiration rate under anaesthesia: 90-120 breaths/min). Eye gel (Lubrithal) was applied in both eyes to avoid desiccation, and an agar gel cap was placed on the animal head to improve shimming results.

5.3.2.4 MRI data acquisition and analysis

MR recordings were performed with a horizontal 9.4 T Agilent system (Vnmrj 4.0 software, Palo Alto, California. A volume coil (22 mm diameter) was used for excitation and signal detection (Rapid Biomedical). After tuning and matching, the frequency was adjusted and a global power calibration of the 90° pulse was performed. A quick gradient echo image on the three planes helped identify any position or excessive movement issues, so that the animal could be repositioned if necessary. To identify the hippocampus and choose an appropriate slice, additional anatomical scans were acquired using a fast spin echo sequence in coronal, sagittal and axial orientation (RARE factor 8, TE 11.8 ms, TR 5 s, matrix size 256 x 256, field of view FOV 15x20 cm, 30 slices, slice thickness 0.5 mm).

CEST

Shimming for CEST was done using the automated procedure ge3dshim, and the linewidth achieved throughout the brain in the slice to be imaged (2 mm thick) was around 20-35 Hz. Manual shims were used when required (more information about shimming in section 5.2.3).
For a CEST experiment, a reference image, a CEST array and a WASSR array were acquired, taking about 10 min in total, all with the same field of view, and with no frequency adjustment in between. The CEST presaturation consisted of a 1.6 s hard pulse (0.9 μT) applied at 40 offsets between ± 4 ppm, followed by single slice segmented GE (CINE) readout (15° flip angle, TE = 1.57 ms, TR = 3.15 ms, 8 dummy scans, FOV = 20x20 mm, 2 mm slice thickness), with a Gaussian excitation pulse and centric encoding, as illustrated in the diagram in Figure 5.7. R represents the number of repetitions (40 images), with S being the number of segments (2) and N the phase encoding steps per segment (64, which makes a total of 128). The acquisition time for the CEST array was 6 min.

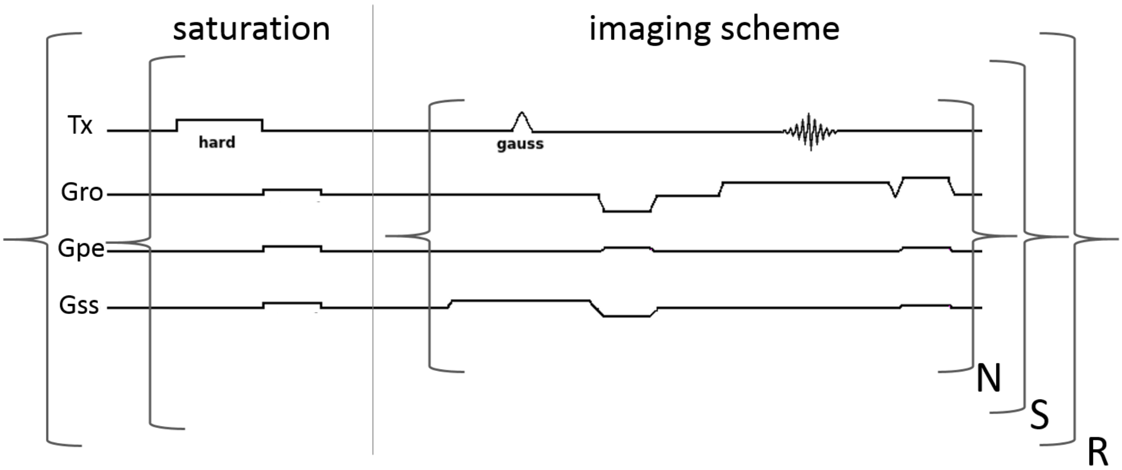

Figure 5.7: Diagram of the CEST sequence.: The saturation consisted of a single hard pulse (1.6 s,0.9 μT). After this pulse, a crusher gradient was applied to spoil the residual transverse magnetization. Following the first saturation module, N=64 lines of k space were acquired with a single slice gradient echo (CINE) imaging scheme. Centric encoding, RF and gradient spoiling were used, with S being the number of segments (2). This process was then repeated for R=40 CEST images (40 offsets between ± 4 ppm). 15° flip angle, TE = 1.57 ms, TR = 3.15 ms, 8 dummy scans, FOV = 20x20 mm, 2 mm slice thickness.

The WASSR array (for B_0 field correction) included a prepulse of 0.5 s and 0.1 μT, with 35 offsets in ± 1 ppm with the same CINE readout (acquisition time 5 min). The reference image was a single CINE acquisition with no prepulses.

CEST analysis

For data analysis, the reference, CEST array and WASSR array images were imported into a custom made CEST tool written in Matlab (see Figure 5.8 for the structure and authors).

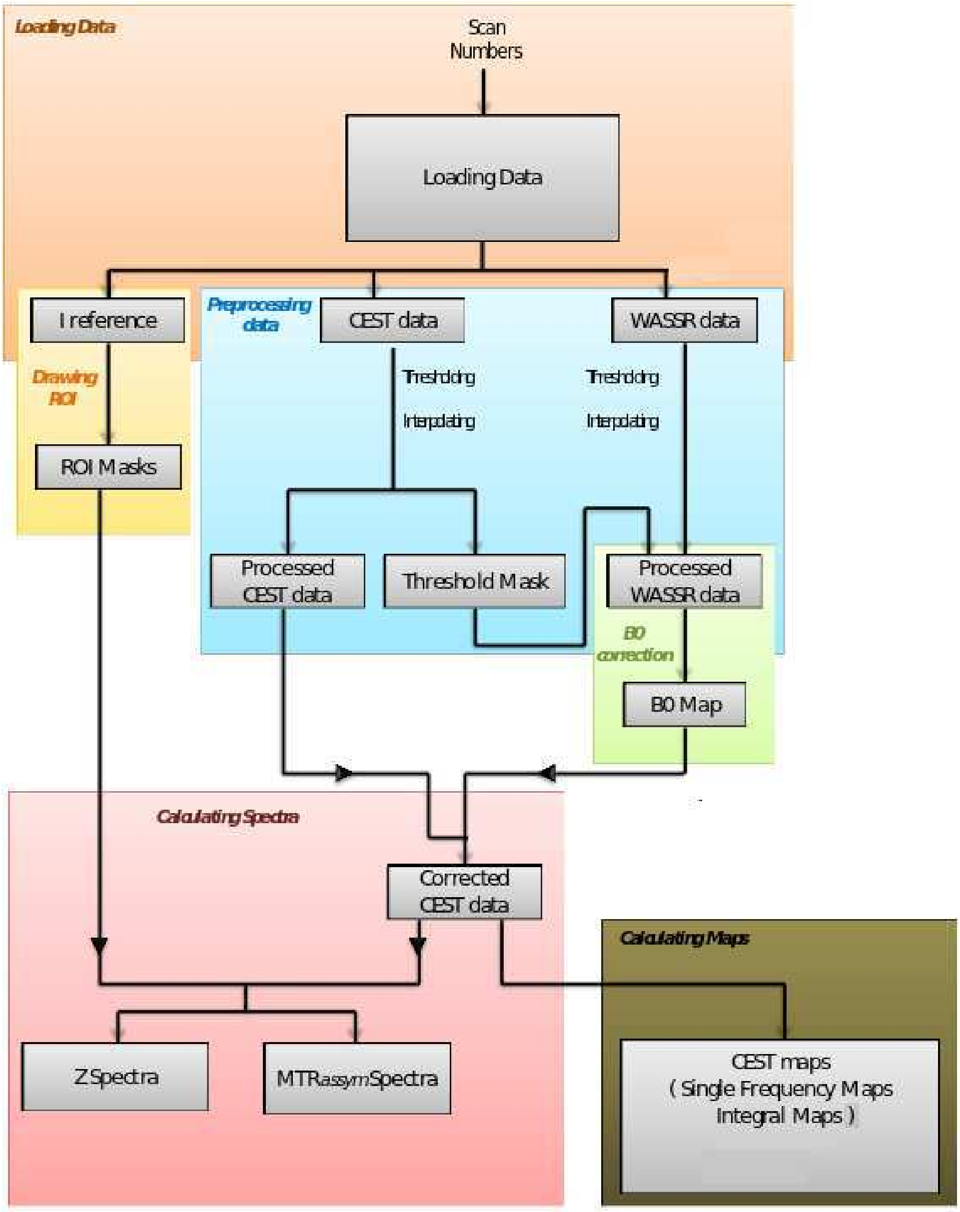

Figure 5.8: Matlab CEST tool diagram, illustrating the analysis process. The analysis tool was developed by Ryan Bendell [315] and optimised by Gaelle Ardito [316].

The images were thresholded and the CEST and WASSR spectra were interpolated using a spline method. WASSR frequency shift maps were derived with the maximum symmetry algorithm and CEST maps were corrected accordingly. Single frequency maps at 0.6 ppm and integral maps at 0.5-1 ppm were calculated. Two ROIs were drawn in both sides of the hippocampus and Z spectra and MTRasym spectra from those areas were obtained. CEST MTRasym values are expressed as the average contrast in a region of interest drawn on a CEST map ± standard error of the mean.

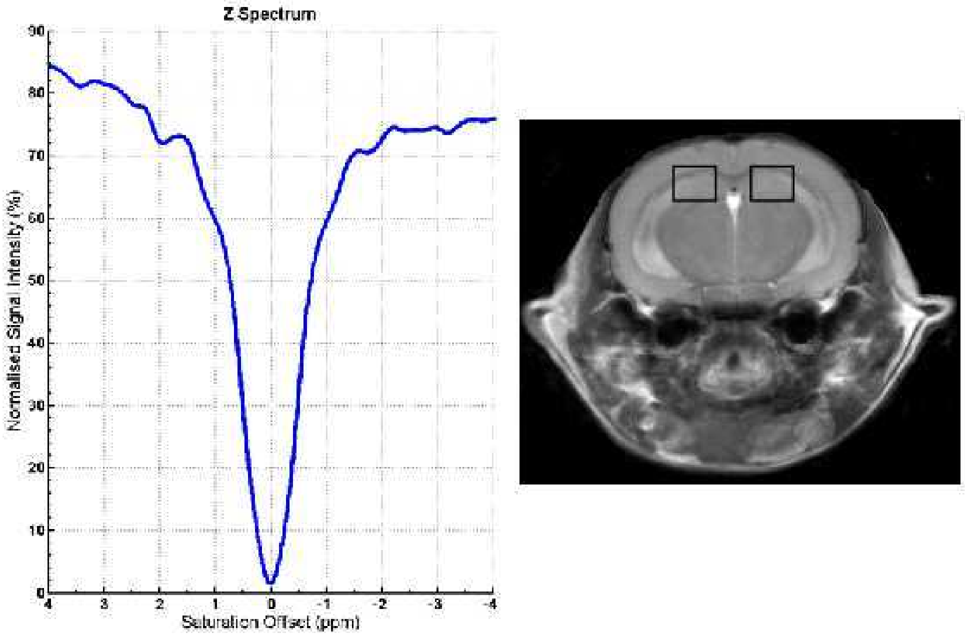

Figure 5.9: A representative anatomical image, showing two ROIs on both sides of the hippocampus (drug and saline) and a representative Z spectrum from one ROI.

T2 map

T_2 quantitative maps were obtained from a series of 16 spin echoes acquired after a single excitation (multiple echo protocol). TE array values (in ms) were: 9, 18, 27, 36, 45, 54, 64, 73, 82, 91, 100, 109, 119, 128, 137 and 146. TR was 15 s, so that all spins could return to equilibrium, and the acquisition time was 30 min. T_2 maps were analysed using Matlab.

MRS

The sequence used for MRS was LASER (localization by adiabatic selective refocusing). This method is insensitive to B_1 variations, minimises artifacts for J-coupled resonances and produces defined excitation profiles at high fields, since refocusing adiabatic pulses have much higher bandwidth compared to the pulses used in PRESS or STEAM [9]. More details can be found in section 1.3.6. The MRS voxel size was 2x2x2 mm, placed over the right or left side of the hippocampus. Once the voxel was selected, the linewidth was measured and if it exceeded 17 Hz, FASTMAP was used for further shimming. The FASTMAP shim was performed in a larger voxel to maximise SNR. LASER sequence parameters were: 24 ms TE, 2500 ms TR, 4006 Hz spectral width, 4096 real data points, 512 averages, 8 dummy scans. A VAPOR scheme (see section 1.3.5 for details) was used for the water suppression, the duration of the 90° pulse (at60.n29) was 4000 μs and the duration of the 180° pulse was 2000 μs. Before the acquisition of a spectrum, the 180° pulse was calibrated (starting from the automatic values coming from the initial global calibration), to check that it was behaving as an adiabatic pulse (that is, that it had reached its maximum power, and not started to drop). TE was reduced from its default value by shortening the initial width of the 180° pulse and the duration of the gradient crushers. This was done in order to obtain as many metabolite information in the spectrum as possible. The final echo time was 24 ms, since a shorter TE produced an uneven baseline *in vivo*. However, the minimum TE achievable with LASER is higher than with PRESS or STEAM, due to the six localization pulses and twelve gradient crushers.

To minimise motion artifacts and frequency drift, the 512 averages were acquired in groups of two, so that in postprocessing they could all be aligned and summed up (the water peak was used as reference for the alignment). Finally, a reference scan without water suppression was acquired together with the LASER spectrum, for subsequent eddy current correction. All postprocessing (fid frequency and phase alignment, sum of the fids, eddy current correction) was done in Vnmrj 4.0.

MRS analysis

MRS data was analysed using LCmodel [10] with a simulated PRESS basis set (provided by Provencher) with TE = 0 ms, without any data postprocessing other than eddy current correction. As mentioned by Kaiser et al. although LASER localization cannot be performed at very short echo times (due to the three pairs of refocusing pulses), J-coupled resonances yield signal intensities and phases closer to short TE spectra (shown with simulations [9]). Another study, by Oz and Tkac demonstrated close similarity of spectral patterns between LASER and ultra-short TE spectra (human subjects [317]). Individual spectra with line widths larger than 15 Hz were excluded.

Metabolites consistently within Cramér-Rao bounds < 10% were included in further analysis, i.e. glutamate (Glu), myo-Inositol (Ins), N-acetyl-aspartate (NAA), taurine (Tau), total choline (tCho), total creatine and Glx (Glu + Gln). Metabolite concentration was expressed as a ratio to the sum of those selected metabolites. Expressing metabolites ratios to total creatine or to the sum of selected metabolites give very similar results, with a smaller standard error in the second case, which is how all data is presented. The ratios are expressed as percentage change from the control side (mean ± standard error of the mean).

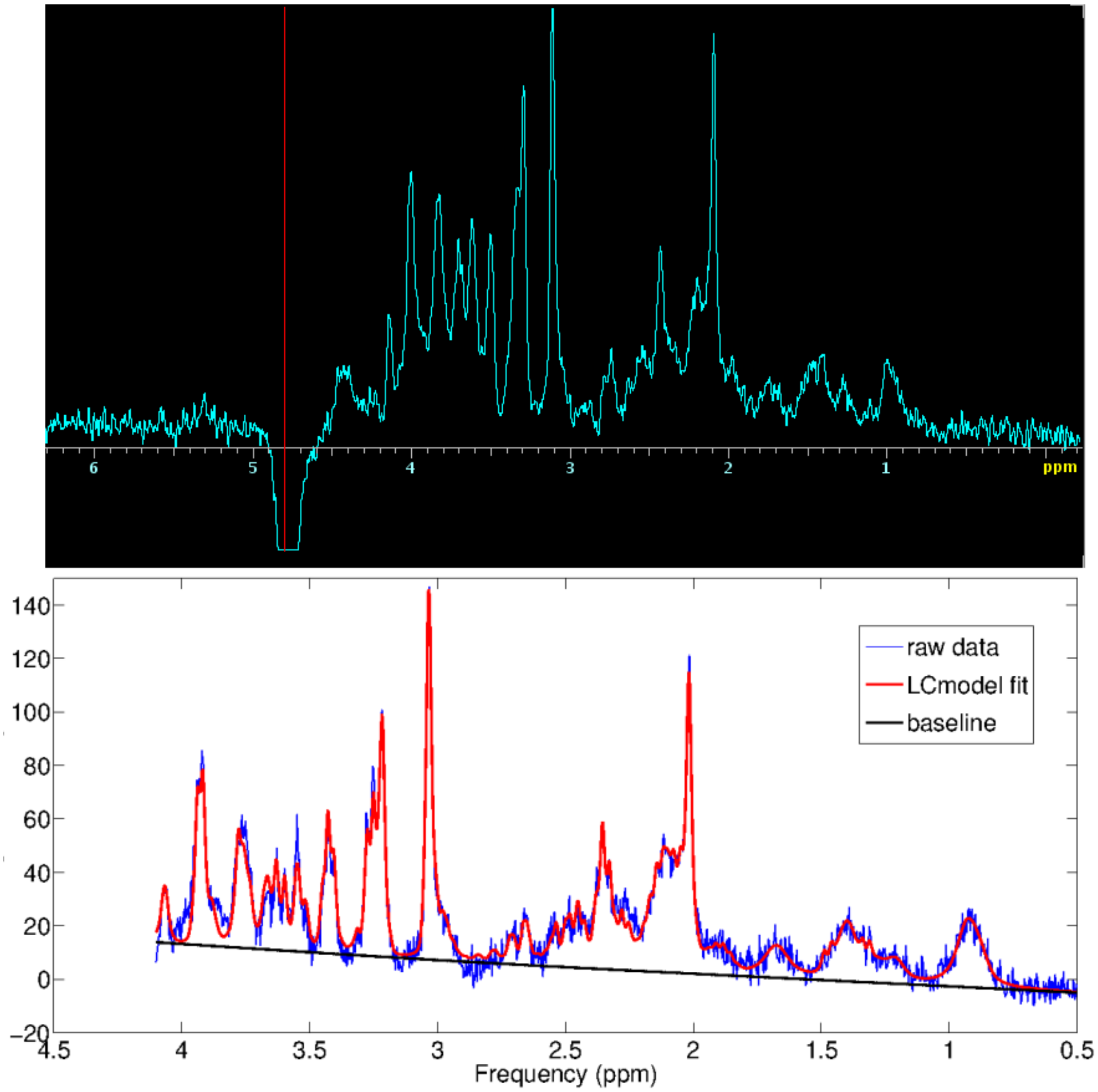

Figure 5.10: A representative LASER spectrum

Top: LASER MRS spectrum, displayed in Vnmrj 4.0, with line broadening applied only for viewing purposes (apodization line broadening factor, lb = 10). **Bottom:** LASER MRS spectrum, after LCmodel analysis. The raw data (no postprocessing other than eddy current correction) is in blue, the calculated baseline in black and the fitted spectrum in red. Notice how the raw data is much noisier than above, due to the absence of exponential apodization. The relative metabolite concentrations are calculated from the fitted data.

5.3.2.5 Histology

Mice were humanely killed using an approved (Schedule 1) method (neck dislocation) at approximately three hours after injection, and the brains extracted. Brains were post-fixed in 4% perfluroaldehyde (PFA) and refrigerated for a minimum of 48 hours, then dehydrated by an ascending alcohol series and embedded in paraffin. The paraffin blocks were cut into coronal microtome sections (thickness 7 μm) and those corresponding to a coronal plane around 2 mm posterior to Bregma were drawn up on microscope slides.

These slides were then deparaffined in xylene until cleaned, rehydrated with concentration-decreasing ethanol solutions and boiled in 10 mM citrate buffer (pH 6, to improve the accessibility of antibodies to tissue antigens), before the staining procedure. H_2O_2 was used to block endogenous peroxidase and NGS (normal goat serum) to reduce non-specific background and cross linking. For the staining, primary antibody Iba1 was used for microglia, followed by secondary antibody (anti rabbit) for colour, ABC (in PBSt) for bond enhancement and DAB (prepared in distilled water).

The counterstain involved submerging the slides in Harris Haematoxylin for 1 min, then a wash of warm water, followed by a dip into lithium carbonate (Scott's tap water) for 10-15 s and another bath. The slides were then submerged in Eosin (1%) for a few seconds and after another wash, they were dehydrated by exposure to various alcohol solutions (50%, 70%, 90% and 100%). Finally, they were dipped into xylene and slipcovered with a few drops of DPX, avoiding any bubble formation. 20x images were taken with a NanoZoomer 2.0-RS C10730 digital slide scanner (Hamamatsu Photonics K.K. Systems, Japan).

The histology slides were visualized using NDP view 2 software, where regions of interests (ROIs) were selected at 15x zoom in the hippocampus, in the areas of injection (LPS and PBS). A semi-automatic thresholding was performed using ImageJ and the percentage of stained area for every ROI was calculated. The difference in the percentage of stained area between LPS and PBS side was calculated per brain slide and averaged for every mouse (at least three slides per mouse).

5.3.2.6 Data exclusions

N=28 female mice were used in total for this experiments: n=11 in the pilot and n=17 in the subsequent study. N=5 mice died before the end of the experiment due to anaesthesia complications and were excluded from the dataset.

N=8 CEST datasets had to be rejected due to insufficient quality: some of these images showed too many motion artifacts in the scanner and could not be repositioned satisfactorily (so the full dataset could not be taken), while others had poor shimming (artifacts in B_0 map being reflected in the 0-1 ppm range CEST maps). Therefore, only n=15 (9 WT, 6 AD) CEST datasets were included in the analysis in total: n=6 (5 WT, 1 AD) from the pilot and n=9 (4 WT, 5 AD) in the following study.

N=12 Iba1 datasets were included in the histology analysis in total, while N=13 were included in the MRS analysis.

5.3.3 Results

5.3.3.1 CEST imaging of neuroinflammation, pilot study

Iba1 staining reveals lipopolysaccharide-induced microglial activation

An example of an Iba1 stained brain slice presenting reactivity can be seen in Figure 5.11. All mice from the pilot experiment showed a significant microglia activation, with a 50% average increase in the LPS stained for Iba1 area compared with controls (see Figure 5.12A). This difference in contrast between the two sides was clearly visible, allowing an observer to predict the area of LPS injection. Inside the groups, there are no genotype differences, most likely due to low numbers.

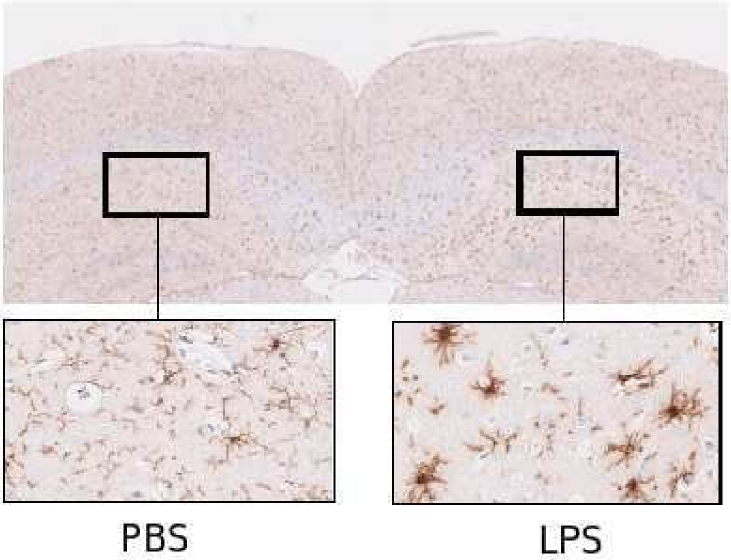

Figure 5.11: Iba1 staining: Example of a Iba1 stained brain slice, with two areas chosen in the CA1 (*cornus ammonis* 1) part of the right and left hemisphere hippocampus. At the bottom of the figure, 20x detail of the selected areas. On the right side, where the LPS drug was injected, the stained microglia show less ramifications and much bigger cell bodies compared with the control side, both characteristics of an activated state.

Myo-inositol levels experience a significant increase in the area of LPS administration

The results showed a significant increase in the myo-inositol ratio values in the LPS side of the hippocampus voxel compared with the control voxel (see Figure 5.12B). No other MRS metabolites exhibited significant changes with the LPS neuroinflammatory stimulus and there were no genotype differences (but there was only one AD mouse in the pilot).

Positive CEST contrast in the 0.5-1 ppm range on the LPS injection area

The images reflect visible CEST changes occurring in the 0-1 ppm region (arising from CEST hydroxyl groups), manifesting as a positive contrast on the side of the brain corresponding to the LPS injection. The average CEST effect in the 0.5-1 ppm range from the right hippocampus ROI (LPS site) was significantly higher compared with the equivalent average signal from the control side, see Figure 5.12C. Individual maps from all six mice included in the analysis can be seen in Figure 5.13.

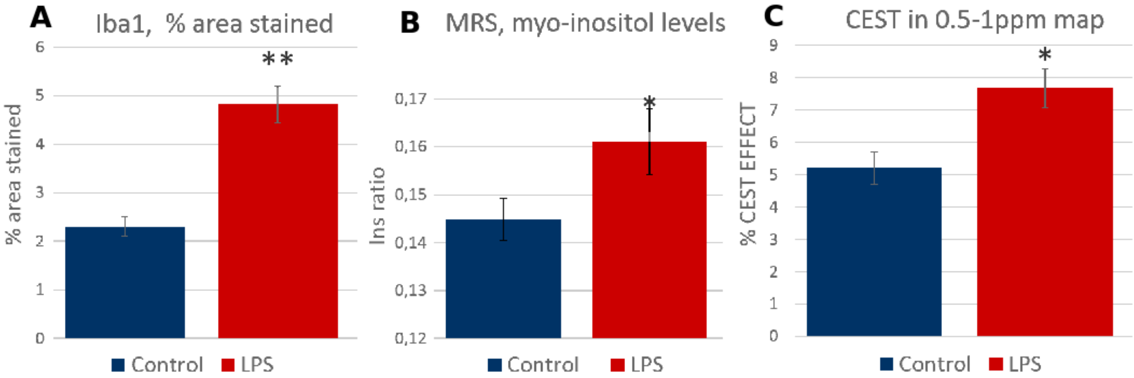

Figure 5.12: Pilot study results: **A Microglia staining:** All mice had a significant increase (around 50%) in the percentage of area stained from the LPS injected side of the hippocampus, compared to the control side. **B Myo-inositol MRS levels:** Percentage change of the myo-inositol ratio from the LPS voxel to the control voxel, measured by LASER MRS. There is a significant increase (around 9%) in the percentage of LPS area stained compared to the control side. **C CEST 0.5-1 ppm:** There is an increase of the CEST effect where LPS was administered. *p<0.05

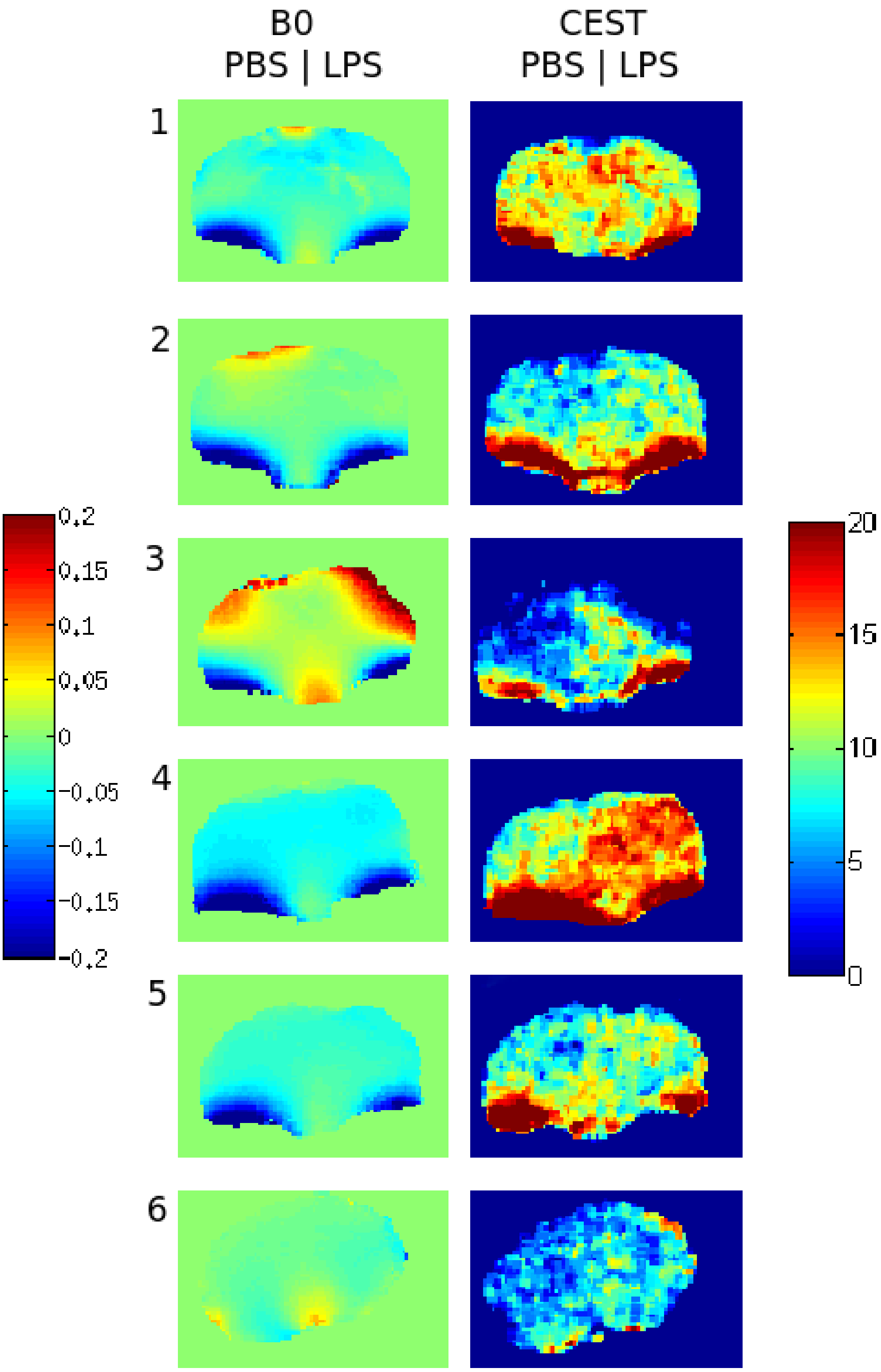

Figure 5.13: Individual data from the pilot study, CEST contrast with LPS (n=6). **Left**: B_0 maps. **Right**: Correspondent CEST 0.5-1 ppm maps. The LPS was injected on the right hippocampus. An increase in CEST contrast can be seen on the LPS injection side. All these animals are wild type, except for number 3 (AD).

5.3.3.2 CEST imaging of neuroinflammation

No significant differences between LPS and control sides for all measurements

Iba1 staining did not present significant differences between both sides of the hippocampus (LPS and control injection sites) or with genotype, see Figure 5.14A. The microglial cells presented small cell bodies with long ramifications, characteristics of a resting state.

There were no significant differences in any metabolite levels measured with MRS, including myo-inositol, either with genotype or area of treatment (Figure 5.14B).

The CEST results displayed no significant differences in any area of the spectrum, either with genotype or region of treatment. Mice from this group (n=9, 4 WT, 5 AD) showed an equal contrast or even a small decrease in the LPS side of the hippocampus, compared with the control region, see Figure 5.14C. Individual maps from all mice included in the analysis can be seen in Figure 5.15.

The injections (both LPS and PBS) produced a visible effect on the T_2 maps, as seen in Figure 5.16A and B, although there was no significant difference between the two sides of the hippocampus (LPS/PBS) in the T_2 values extracted from the map (Figure 5.16C). However, taking into account the mouse genotype, AD mice had significantly longer T_2 values than WT mice in the hippocampus: average $T_{2WT} = 41.10 \pm 0.09$ ms vs average $T_{2AD} = 44.20 \pm 0.13$ ms.

A comparison between the CEST, MRS and microglia staining results from the pilot and the subsequent study can be found in Figure 5.17, including details of the MTRasym spectra.

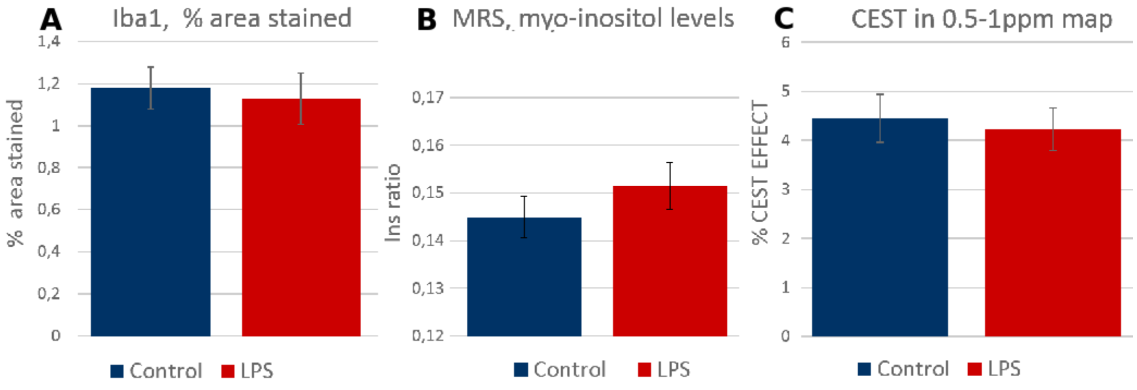

Figure 5.14: Study results: **A Microglia staining:** The difference between the two sides of the hippocampus (LPS and control) was negligible. **B Myo-inositol MRS levels:** Percentage change of the myo-inositol ratio from the LPS voxel to the control voxel, measured by LASER MRS. Negligible difference LPS/control side. **C CEST 0.5-1 ppm:** There are no significant differences LPS/control in the CEST contrast.

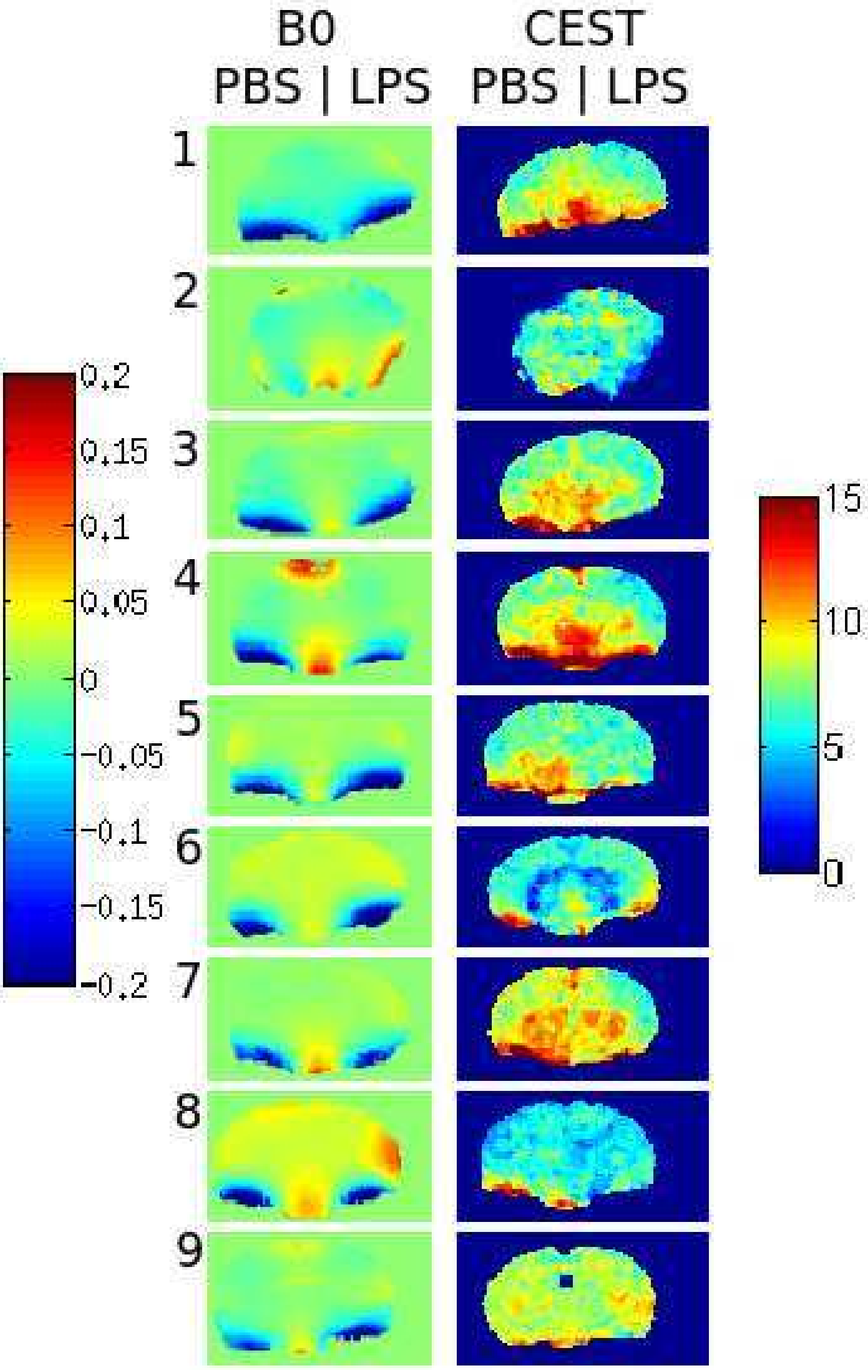

Figure 5.15: Individual data from the study, no CEST effect of the drug (n=9). **Left**: B_0 maps. **Right**: Correspondent CEST 0.5-1 ppm maps. The LPS was injected on the right hippocampus. There is no clear difference in CEST contrast for any of these animals (4 WT and 5 AD).

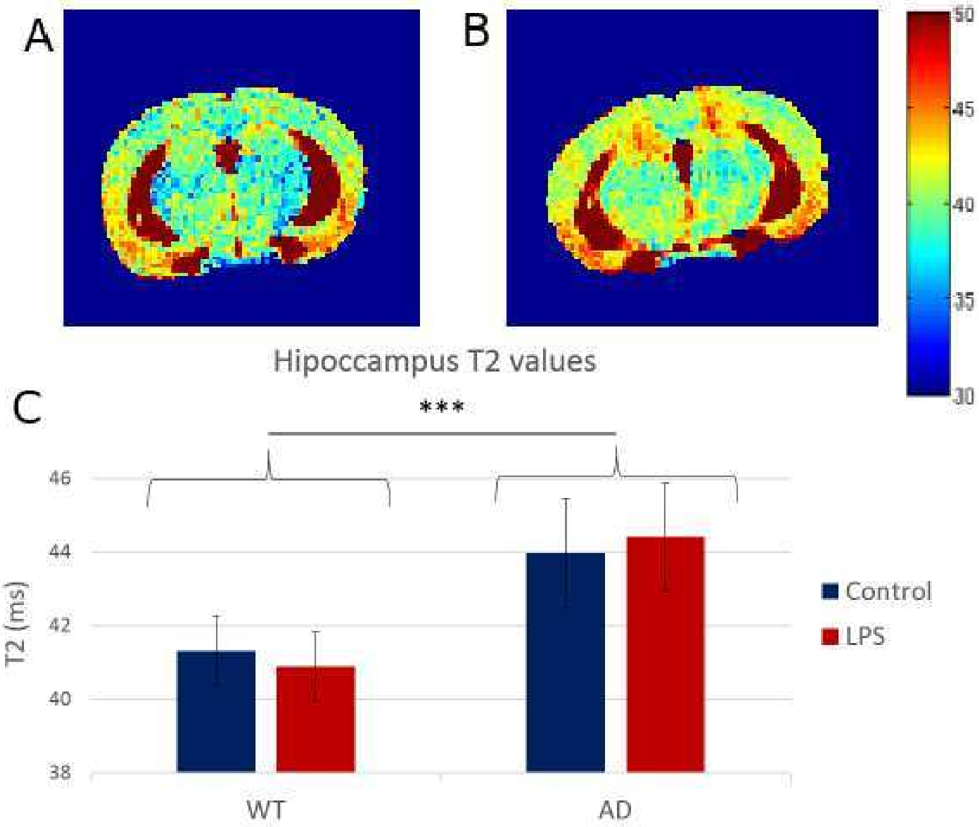

Figure 5.16: **T_2 results:**

A: T_2 map from a control mouse (no solutions injected). **B:** T_2 map from one of the mice from the experiment (LPS injected on the right hippocampus, PBS on the left). Both injections are visible in the map. The colours represent T_2 values in ms. **C:** T_2 values from regions of interest in the right hippocampus (LPS, red) and left hippocampus (control, blue). The first two columns are WT mice (n=6), and the last two belong to the AD mice (n=5). On average, AD mice have significantly longer T_2 values than WT mice: average $T_{2WT} = 41.10 \pm 0.09$ ms vs average $T_{2AD} = 44.20 \pm 0.13$ ms. However, there is no significant difference between the LPS and PBS sides of the hippocampus, which ensures that the CEST contrast is not affected by T_2.

**p<0.0001.

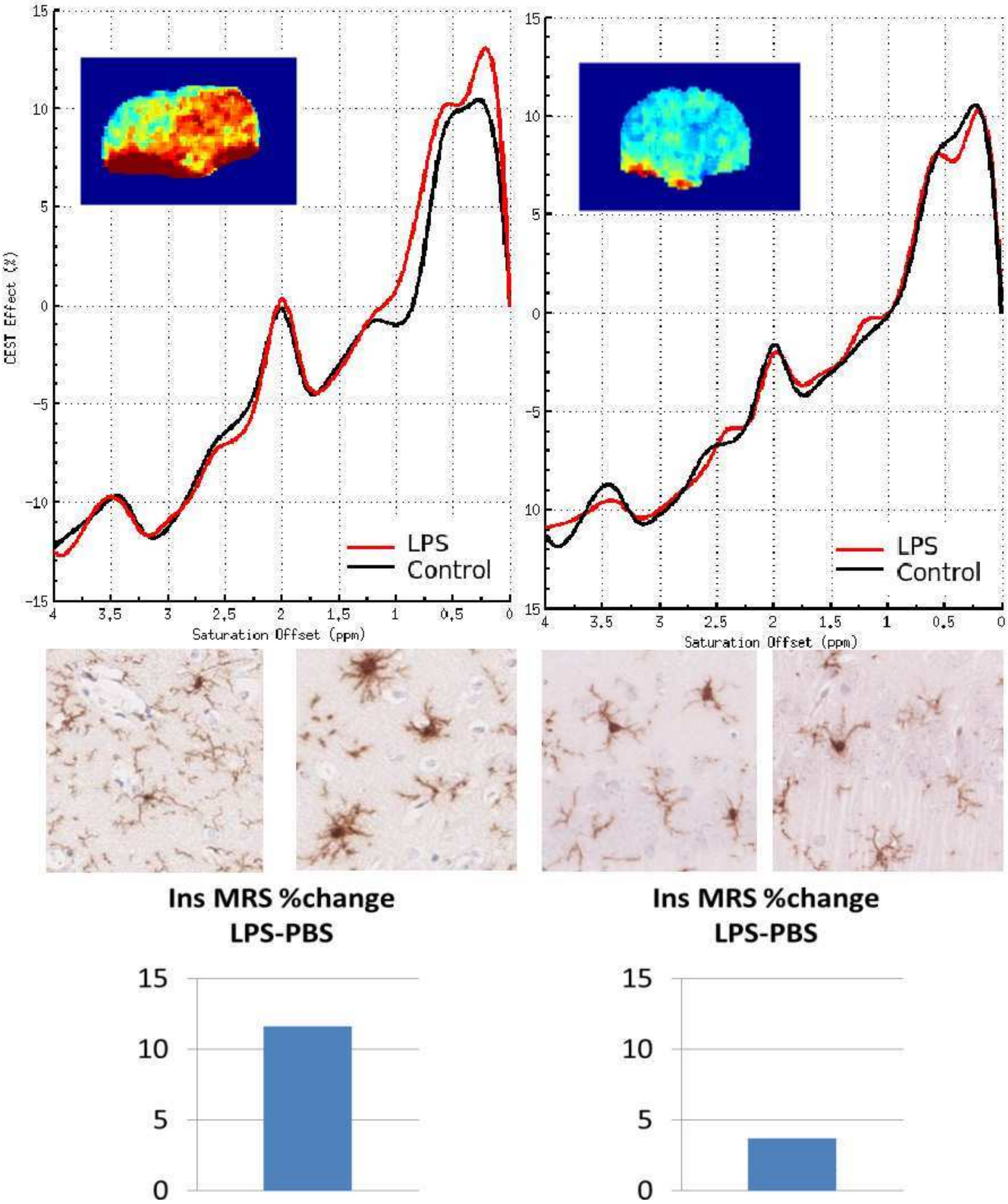

Figure 5.17: Measurement comparison between two representative animals from the pilot and the study (CEST, MRS, histology)
Left: MTRasym spectrum from a mouse from the pilot study (experiments performed 0-3 months after LPS preparation), with an increase in LPS signal (red) over control (black) in the 0-1 ppm range and the correspondent 0.5-1 ppm CEST map. Below, Iba1 staining from left and right hippocampus from the same mouse and at the bottom, myo-inositol MRS ratio percentage difference LPS/control. The immunohistochemistry shows activation on the right side and the MRS levels are higher in that side compared with the contralateral area. **Right**: MTRasym spectrum from a mouse from the subsequent study (>5 months after LPS preparation), with similar signals coming from LPS and control ROIs and the correspondent 0.5-1 ppm CEST map. Below, Iba1 staining from left and right hippocampus from the same mouse and at the bottom, myo-inositol MRS ratio percentage difference LPS/control. There are no significant differences in the Iba1 staining or MRS myo-inositol levels between the two sides of the hippocampus.

5.3.3.3 The CEST contrast is correlated with MRS myo-inositol levels and Iba1 immunostaining.

There was a correlation ($R^2 = 0.67$) between CEST (0.6 ppm maps) and myo-inositol levels measured by MRS (ratio to sum of metabolites), see Figure 5.18A. Furthermore, a correlation could also be established ($R^2 = 0.7$) between CEST (0.6 ppm maps) and histology (Iba1 percentage of area stained), Figure 5.18B. Iba1 identifies all microglial cells, both activated and not activated. However, an increase in microglia concentration is one of the characteristics associated with the activation process.

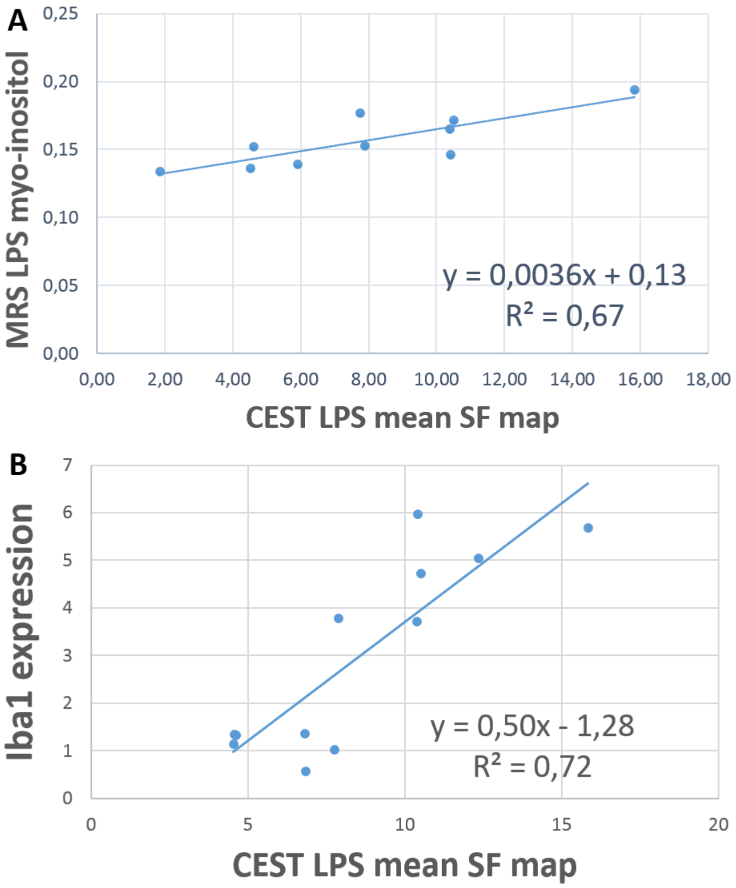

Figure 5.18: CEST is correlated with MRS myo-inositol levels and Iba1 immunostaining. **A**: X axis: Average CEST contrast (0.6 ppm map) from a region of interest over the LPS injection site (right hippocampus). Y axis: MRS myo-inositol ratios from the right hippocampus voxel. The linear correlation coefficient, R^2, is 0.67. **B**: Y axis: Percentage of area stained (Iba1) in the LPS injection area. X axis: Average CEST contrast (0.6 ppm map) from a region of interest over the LPS injection site. The linear correlation coefficient, R^2, is 0.7.
Data from both the pilot and the following study are included in these graphs, which suggest that CEST can reflect myo-inositol levels and microglia concentration, associated with the activation process.

5.3.4 Discussion

Building on the LPS MRS study results in chapter 3, the aim for this study was to evaluate if an increase in myo-inositol levels following LPS administration would lead to an observable CEST contrast, and if the CEST effect could be associated to myo-inositol (validation with spectroscopy and Iba1 histology).

The mice in the pilot study (n=6) displayed a significantly increased CEST contrast in the 0.5-1 ppm range (hydroxyl) compared with the control side. This was accompanied by significantly elevated myo-inositol levels (measured with MRS) in a voxel over the LPS injection area (right hippocampus), compared with the contralateral PBS region. Finally, these animals showed microglial proliferation on the right side of the hippocampus, with Iba1 staining revealing lipopolysaccharide-induced microglial activation. The percentage of area stained was significantly higher compared with the control side (left side of the hippocampus).

These results could not be confirmed in a subsequent study (n=9 animals), in which the mice showed no significant differences in CEST, histology or spectroscopy. Since the LPS solution was prepared at the same time the pilot started, the mice from that group were injected up to three months later (duration of the pilot) and in the case of the mice from the subsequent study, from five to six months after the solution was mixed. The LPS solution was stored in the freezer in plastic containers during those six months, and it is possible that some degradation has occurred, with the drug binding to the plastic, that could explain the apparent lack of response in the last group of animals.

There were no significant genotype differences in the LPS response for CEST, histology or spectroscopy, a fact most likely related to the low number of animals in both groups (13 WT, 11 AD in total). T_2 maps were acquired to assess whether a hypothetical T_2 contrast due to inflammation could be a contribution to the CEST effect (a longer T_2 can increase the CEST contrast and a shorter T_2 reduce it, see chapter 4). There was no apparent effect of the LPS drug in the T_2 maps, except that the LPS drug might have been no longer active by then and T_2 maps were not acquired during the pilot. There was however a difference in the T_2 values in the hippocampus between the transgenic AD mice and the wild types, with AD mice showing slightly longer T_2 values. This change in T_2 contradicts the results from Falangola et al., who found reduced T_2 values in the hippocampus and cortex of young transgenic AD mice (PS/APP) compared with age matched [318], and so it could be a type I error.

Motion artifacts were one the main experimental difficulties for this project. Due to the nature of the animal setup (which did not allow for ear bars, see 5.2.1), the breathing of the animal was an issue for several datasets, which had to be discarded, directly due to the effect it had on the CEST images or indirectly, through the shimming process. Possible alternatives for improvement could be a different holder design/coil size, triggering during shimming/acquisition, or paralysing the animal for the duration of the experiment (pancuronium bromide has been used for several CEST studies [26, 319, 320]).

The use of a fast spin echo sequence (RARE) instead of a segmented gradient echo for CEST could have reduced B_0 inhomogeneity artifacts at 9.4 T. However, the linewidth achieved after shimming was consistently under 30 Hz across the brain (in a 2 mm thickness slice) during the *ex vivo* testing of the protocol, which indicates that movement is a bigger issue in order to improve *in vivo* reproducibility.

By taking all the data points from the pilot and subsequent study, a correlation is established ($R^2 = 0.67$) between CEST at 0.6 ppm and MRS myo-inositol levels, accompanied by another correlation between CEST at 0.6 ppm and Iba1 staining ($R^2 = 0.7$), both in the area of LPS administration (right hippocampus). Therefore, this CEST effect may be linked to myo-inositol and microglia concentration. Indeed, MICEST [123] has been proposed as a novel contrast method for glial cells proliferation, with increased MICEST contrast having been described in 20 month old transgenic AD mice compared with age matched controls, in addition to elevated myo-inositol MRS levels and GFAP immunostaining, although correlations could not described in this case. Astrocyte reactivity has also been studied with CEST in recently published study by Carrillo-de Sauvage et al. [273]. In this case the signal at 3 ppm was associated to the metabolite glutamate and verified with histology and MRS in a rat model (overexpression of the cytokine ciliary neurotrophic factor CTNTF [321]).

5.3.5 Conclusion

A model of microglial activation, as used in this project, would be extremely useful towards getting an understanding of the early stages of many neurological disorders, while CEST as a biomarker or inflammation has a lot of potential due to its non-invasive nature, high spatial resolution and clinical translation. Correlations have been established between the CEST contrast at 0.6 ppm and MRS myo-inositol levels/microglial concentration (Iba1). Nevertheless, the complex CEST readout with many metabolites contributing to the signal and its sensitivity to B_0 inhomogeneity artifacts, in particular at high fields, which are required for myo-inositol, complicate the robustness and reproducibility of the technique.

CHAPTER 6

Discussion and conclusion

6.1 Summary of main findings

The work undertaken in this thesis is focused on the study of neuroinflammation with molecular MRI methods. Neuroinflammation is present in a vast array of neurological disorders, such as neurodegeneration, where chronic inflammatory responses may play an important part in the onset and progress of the disorders. Molecular MR methods used are magnetic resonance spetroscopy (MRS) and chemical exchange saturation transfer (CEST).

The investigation of the neuroinflammatory response was carried out with lipopolysaccharide (LPS) as an inflammatory stimulus. In order to find a quantitative molecular biomarker, a pilot study was performed on wild type animals using serial MR Spectroscopy (MRS) and peripheral LPS administration. The results showed a myo-inositol (considered a glial marker) increase in a cohort of the animals, peaking at four hours after injection. Based on this pilot, a full MRS study was carried out, including a mouse model of Alzheimer's disease (AD) together with wild type controls and histology as validation, to evaluate the degree of microglia (Iba1) and astrocyte activation (GFAP). MRS myo-inositol changes indicated a mild neuroinflammatory transient state in AD mice, induced by a low dose of LPS, as seen in the histology results. This neuroinflammatory state is still present in the wild type, according to microglia staining, but it is stronger in AD mice, which supports the existence of a primed microglial state in the mice with a chronic disease condition compared with wild types.

Since MRS is limited by low spatial resolution, the aim of this thesis was to develop a molecular MRI method to monitor neuroinflammation, chemical exchange saturation transfer (CEST). The CEST signal was modelled in Matlab, using two and three compartment simulations developed and optimized for myo-inositol contrast. A robust *in vitro* CEST protocol was established and tested with the simulations, providing insights into the complex CEST signal, where several metabolites (glucose, glutamate, creatine, etc) overlap with myo-inositol.

Following the basis from the simulations, from where a set of optimal sequence parameters was obtained, a reproducible *in vivo* CEST protocol with a running time of 10 minutes was developed, suitable for preclinical experiments. CEST and MRS measurements were taken after a LPS injection (10 ng) in the right hippocampus and a control PBS injection on the other side, with histology as validation. A correlation was found between CEST at 0.6 ppm and MRS myo-inositol levels, as well as between CEST and microglia concentration (Iba1 immunostaining).

6.2 APPswe/PS1dE9 as an AD animal model

Alzheimer's disease (AD) neuropathology is characterised by the accumulation of amyloid-β (Aβ) plaques and neurofibrillary tangles, together with widespread loss of synapses, inflammation and and neuronal death. Less than 1% of AD cases are caused by autosomal (not sex-linked) dominant inheritance, known as early onset familial Alzheimer's disease (onset before age 65). However, the vast majority of the AD cases (sporadic AD) do not appear to have a certain genetic cause, although environmental and genetic differences can act as risk factors [322].

In neurodegenerative diseases, such as AD, the concentration of microglial cells increases and they adopt an activated state ("priming" process [289]). "Priming" makes microglia susceptible to a secondary inflammatory stimulus, and is considered to exacerbate disease progression. Neuroinflammation in AD is not a passive system activated by plaques and neurofibrillar tangles, but instead it contributes to pathogenesis as much as plaques and tangles do. Several genetic risk factors in AD have been associated to microglial function, compromising phagocytic efficiency and clearance of amyloid deposits as well as enhancing neuroinflammation. Glial activation, as a pathological mechanism in AD, is a potential mechanistic biomarker for the development of new treatments targeting neuroinflammation or a dysfunctional amyloid metabolism [323].

Intensive research over the years, centered on the genes and proteins involved in the pathology has permitted the development of genetically altered mouse models. The neuropathology and clinical phenotype are usually indistinguishable between early-onset familial and sporadic AD, with the main difference being the earlier onset in the first type. Since the etiology of sporadic AD is still unknown, the animal models developed are based on genetic mutations present in familial AD. This can be justified by the fact that the course of the disease is quite similar after the initial trigger for both cases [324].

APPswe/PS1dE9 mice express two different transgenes: the human gene APP695 containing the Swedish mutation K594N/M595L (Amyloid Precursor Protein, APPswe) and presenilin 1 without exon 9 (PS1dE9) [278]. These mutations lead to a progressive, age-related Aβ neuropathology with amyloid plaques and elevated levels of Aβ [278], which are linked to familial forms of Alzheimer's disease (AD) [279]. The mice develop behavioural phenotypic and pathological features which make them useful as an AD model, such as Aβ plaques (as early as 4 months [280]), surrounded by activated microglia and astrocytes and significant memory deficits at 6 months compared with wild type controls [281].

One of the limitations of the animal model is related to age considerations. Microglial density was not significantly increased in AD mice compared to wild types in the PBS side of the hippocampus (control region) in the direct injection experiment, which can be a factor towards explaining the lack of genotype differences in the results. The animals used were three months old, and older animals could not be used due to restrictions on the animal size caused by the coil diameter (22 mm).

6.3 Lipopolysaccharide as a neuroinflammatory model

Lipopolysaccharide (LPS) is a bacterial endotoxin. Inside the brain, LPS binds to the Toll-like receptor 4 (TLR4), predominantly expressed by microglia in the CNS, as an agonist [175], stimulating cytokines (IL-1β and TNFα) and chemokines expression and release and inducing an acute neuroinflammatory response, with microglia and astrocyte activation. LPS administration, central or peripheral, is considered a neuroinflammatory challenge and has been widely used as a neuroinflammatory stimulus [176].

The main advantages of such a model is the possibility of inducing a transient inflammatory response in a well-controlled experimental environment. However, the dose of LPS as well as the source and route of the application are likely critical factors differently affecting the timing and intensity of the effects. Moreover, from a clinical point of view, it has to be noted that LPS administration creates a transient response with normalization of the cytokine levels within hours. Therefore, it cannot be considered as a model of chronic inflammation, frequently encountered in many neurological disorders. In particular, the levels of proinflammatory cytokines induced in chronic disease are usually lower than those induced by LPS [325].

In the experiments presented in this work, the aim was to investigate the early metabolic effects to a mild inflammatory stimulus, so the hurdles of the LPS model were related to finding an appropriate dosage which would induce metabolic changes but did not produce sickness syndrome, as well as finding the time course to guide the measurements post-injection. The possible anaesthesia/experimental setup effects that could be present together with the drug effects are another possible limitation.

6.4 Potential for future experimental work of this nature

Animal work allows for a mechanistic approach and it has the capability of defining critical disease-related mechanisms. It can help to predict outcomes from pharmacological interventions, with many treatments currently in clinical trial owing their origins to studies initially performed in mice. In this case, glial activation is of great interest as a potentially key modifiable pathological mechanism in AD and other neurodegenerative disorders.

Another advantage of working with mice are ethical considerations, since experiments of the nature of the ones performed in this work would not be readily possible or ethical with human patients (and would not produce the desired information with samples). In addition, animal work permits an in depth study of a single process, while human diseases often contain multiple underlying conditions that complicate our understanding of the disorder. Nevertheless, it should be mentioned that this advantage can also be a disadvantage, which can cause significant translational issues between preclinical drug studies and human clinical trials [324].

6.5 Clinical potential of CEST and MRS in neuroinflammation

There is evidence suggesting that neuroinflammation has a causal role in Alzheimer's disease, with analysis of clinical manifestations that precede the dementia stage of AD, such as mild cognitive impairment, supporting an early and crucial involvement of inflammation in disease pathogenesis. The initial acute inflammatory response is thought to help clearance and restore tissue homoeostasis. Triggers and aggravators stimulate prolonged exposure and immune activation, ultimately leading to chronic neuroinflammation. Perpetuation of microglia activation and continuous exposure to proinflammatory cytokines induce functional and structural changes that result in neuronal degeneration [323].

Microglia are key players in the neuroinflammatory response: changes in microglia are evident in the post-mortem brains of AD patients and in AD animal models. Glial activation is of great interest as a potentially key modifiable pathological mechanism in AD and other neurodegenerative disorders. Microglia activation (and potentially myo-inositol levels, measured through MRS or CEST) could be used as predictive biomarkers for the development of new treatment options targeting neuroinflammation or a dysfunctional amyloid metabolism. These biomarkers could help identifying patients that are more likely to respond favourably to a given therapy, in order to stratify different patient groups in terms of clinical response, so as to develop personalised, preventive or therapeutic strategies. For example, non-steroidal anti-inflammatory drugs (NSAIDs) could be used to block incipient inflammation-driven AD pathogenesis at early stages [323].

6.6 Prospects and difficulties in the translation of this approach to clinical use

Nuclear imaging methods such as positron emission tomography (PET) have a very high sensitivity, but they are hindered by the use of radioactive isotopes and suboptimal spatial resolution. Optical imaging is restricted in terms of clinical applications due to poor depth of penetration. MRS has been extensively used for *in vivo* quantifications of concentrations of a large range of metabolites, whose concentrations are high enough for MR detection. However, low spatial resolution and long acquisition times make widespread clinical applications challenging. On the other hand, MRI is a high resolution non-ionizing imaging technique, widely utilized clinically. Molecular MRI imaging techniques have relied traditionally on exogenous contrast agents (fluorine MRI, manganese enhanced MRI, superparamagnetic iron oxide nanoparticles) and therefore, there is a need to develop non-invasive quantitative methods to measure *in vivo* molecular changes.

Endogenous CEST MRI does not usually require any external agents and CEST imaging can be performed using modifications of existing MRI pulse programs. Consequently, endogenous CEST MRI has a great potential to reach clinical applications. However, many difficulties are associated to any attempt to translate myo-inositol CEST into a clinical setting, which are described here, together with more generic CEST difficulties:

6.6.1 Clinical translation of CEST

Endogenous CEST MRI applications are a promising non-invasive, non-ionizing tool for molecular imaging. Several endogenous metabolites with exchangeable protons have recently been identified and imaged *in vivo* and the feasibility of implementing these methods both in preclinical models and in human studies has been demonstrated [37, 110]. These endogenous molecules can be exploited as biomarkers for characterization of diseases such as cancer [125], neurological diseases [93], stroke [66] or osteoarthritis [326]. Several obstacles need to be addressed when translating a CEST protocol into the clinic:

6.6.1.1 SAR

Ideally, standard CEST should use prolonged irradiation (long enough so that the system can reach steady-state). Long rectangular CW pulses are widely used in CEST imaging, but specific absorption rate (SAR) concerns can make the CEST imaging clinical translation problematic. The field strength of the saturation pulses (B_1) will be limited, which will particularly affect those exchanging groups with faster exchange rates. Scanner hardware constraints can also play a part in limiting maximum pulse durations (in contrast to the preclinical scanners, the RF amplifiers from clinical scanners cannot produce irradiation with a high duty cycle).

There are several solutions to overcome these limitations: triggering and the type or size of transmit coil can reduce the heat deposition [327], parallel MRI reduces the number of phase encoding steps needed for image reconstruction (using redundant spatial encoding information from arrays of surface coils) and can result in longer repetition times for the same total acquisition time, which will lower SAR (this will also produce a lower signal to noise ratio).

However, if long or strong enough CW pulses are not allowed for saturation, a train of strong and short shaped prepulses is used instead, often called pulsed-CEST MRI. Parallel RF transmission can get around hardware constraints [328]. Two amplifiers can be used in interleaved fashion to create RF with a duty cycle close to 100%. Each of them is allowed to rest for a long enough time between the pulses, without losing overall RF power. This way, a long, high duty cycle, pulsed RF saturation train can be generated. The optimisation of a pulsed-CEST MRI sequence is more involved than a CW CEST sequence, due to the many more parameters involved. The full numerical solutions to the Bloch McConnell solutions can be used for optimisation and several approximations can be applied to make it less computationally intensive [300].

6.6.1.2 Time (3D)

Most CEST applications use a single slice readout. This is because of the necessity for multiple acquisitions at different saturation with long repetition times to allow for relaxation. Therefore, single slice acquisition is the standard approach for pre-clinical studies, although it is not desirable for clinical translation. Development of fast, multi-slice or 3D CEST techniques is crucial to clinical application translations.

In order to acquire volumetric CEST measurements, an RF saturation pulse (CW) or pulse train (pulsed CEST) can be directly inserted in front of a full 3D or a multi-slice acquisition module. However, CEST contrast decays over time with relaxation time T_1, once the presaturation module is finished. Post-processing corrections are needed to account for this effect, based on prior knowledge of T_1 and k-space trajectory [99].

Other alternatives have been studied to obtain fast multi-slice and three dimensional CEST:

One alternative is to apply steady state methods to build up CEST contrast throughout the 3D region. For example, a long initial saturation pulse can be used to create CEST contrast, followed by repetitive short secondary saturation pulses immediately after the first image acquisition, so as to maintain the steady state CEST contrast for multi-slice acquisition [329]. A different approach uses a repetitive module containing a short frequency-selective saturation pulse in front of each slice selective pulse, followed by a fast imaging sequence with a short enough repetition time to allow a build-up in saturation contrast. As the TR of the gradient echo readout pulses is much less than T_1, this leads to a cumulative effect of saturation pulses for slowly exchanging spins and it is therefore appropriate for an interleaved, multi-slice readout. [38].

The combination of parallel imaging hardware with 3D k-space sampling strategies can be used to obtain 3D CEST images. Jones et al. has used a 3D gradient and spin echo (GRASE) readout, combined with a multi-channel coil benefiting from parallel imaging techniques to achieve a z-spectrum of the whole brain in less than 10 minutes [37]. The CEST contrast loss coming from T_1 relaxation was minimised independently of the number of slices, using a centric 3D k-space acquisition scheme. The center of k-space, which determines the contrast, was acquired before T_1 relaxation would occur. The rest of the k-space data was collected at a later time.

These techniques rely on steady state CEST contrast and consequently, may not be optimal for faster exchanging spins.

6.6.1.3 B0 and B1 correction

B_0 correction is essential to obtain reliable and reproducible CEST images. The water saturation shift referencing (WASSR) [141] method is the preferred technique for preclinical studies, since it provides an absolute value for the frequency shift from water for every voxel and it does not require corregistration with the CEST image. It is however a lengthier method than a conventional B_0 map, which can make it less desirable for time-restricted clinical protocols, although the time difference can be made minimal [330]. B_0 correction is of capital relevance for diaCEST agents, with a resonance frequency close to the water peak (in particular, those containing hydroxyl groups).

In addition to B_0 inhomogeneities, B_1 inhomogeneities can produce insufficient saturation of the exchanging pool, especially in the translation of CEST technology to high field clinical scanners. B_1 field maps have been measured in a study by Singh et al. using a double angle method. The maps were then used to correct the CEST asymmetry maps in the presence of severe B_1 inhomogeneity, using a calibration curve (empirical approach). However, accurate determination of the calibration coefficients depends on the presaturation and acquisition parameters and the type of tissue [331]. Parallel RF transmit can also be used to minimise B_1 inhomogeneities and thus improve the CEST contrast [332].

For diaCEST agents, B_0 inhomogeneities play a more important role than B_1 inhomogeneities, assuming that B_1 homogeneity is good enough for a relatively uniform saturation [140].

6.6.2 Clinical translation of myo-inositol CEST

The myo-inositol molecule contains six hydroxyl groups. The proton exchange rate and resonance frequency have been reported to be 600 Hz and 0.6 ppm (conventional saturation method), 1250 Hz and 0.93 ppm (spin-lock method) and 1381 Hz and 1.1 ppm (FLEX method), by Haris et al., Jin and Kim and Yadav et al., in 2011, 2012 and 2014 respectively.

CEST techniques require the condition of slow exchange regime, or slow to intermediate regime in order to selectively saturate the solute protons [19]:

$$k_{ba} \leq \Delta\omega \tag{6.6.1}$$

where k_{ba} is the exchange rate from the bound protons to the free water and $\Delta\omega$ is the chemical shift ($\Delta\omega = \omega_{water} - \omega_{bound\ protons}$) [50]. Therefore, CEST benefits from high fields: the frequency separation is increased and there is a reduced interference of direct water saturation.

Table (6.1) shows the myo-inositol values for different magnetic field strengths: Myo-inositol hydroxyl groups resonate at around 1 ppm down field from water and have an exchange rate in the range of 600-1400 Hz. These values do not satisfy the condition of slow to intermediate exchange on the NMR time scale at lower fields, such as 1.5 T and 3 T. Effective saturation of rapidly exchanging labile protons requires high B_1 irradiation powers. However, because the resonance frequencies of endogenous hydroxyl protons are close to that of water, the applicable irradiation power is limited by direct water saturation and therefore, low-powered saturation pulses have to be used instead, producing less than optimal CEST effects. As an example, an important application of hydroxyl CEST imaging is glycosaminoglycans imaging in cartilage (GagCEST), as a potential biomarker for osteoarthritis: a 20% increase in the gagCEST signal was initially reported in cartilage at 3 T. With optimised B_0 correction, the effect was later showed to be negligible instead, due to direct saturation effects from the saturation scheme necessary to saturate faster exchanging spins with a small chemical shift.

B_0	Exchange rate (k_{ba})	Resonance frequency ($\Delta\omega$)	$k_{ba} \leq \Delta\omega$
1.5 T	600/1250/1381 Hz	0.6/0.93/1.1 ppm	600/1250/1381 $\nleq$ 241/374/442
3 T	600/1250/1381 Hz	0.6/0.93/1.1 ppm	600/1250/1381 $\nleq$ 480/745/881
7 T	600/1250/1381 Hz	0.6/0.93/1.1 ppm	600/1250/1381 $\leq$ 1130/1752/2072
9.4 T	600/1250/1381 Hz	0.6/0.93/1.1 ppm	600/1250/1381 $\leq$ 1508/2337/2765

Table 6.1: Myo-inositol hydroxyl proton exchange regime, for different magnetic field strengths.

Conventional myo-inositol CEST can be performed *in vivo* at higher fields ($\geq$ 7 T) with improved sensitivity and all the limitations/difficulties discussed in this chapter. Only one preclinical full study [123] has been published so far, and high field human feasibility studies have yet to be performed.

Alternative technique chemical exchange-sensitive spin-lock (CESL) can suppress direct water saturation, providing a much wider range of available irradiation parameters. In particular, it makes possible the use of high-powered B_1, which can be exploited to improve the sensitivity of exchanging groups in the intermediate exchange regime. Jin and Kim has recently described the theoretical model and compared CEST and CESL approaches in phantoms of several relevant metabolites (including myo-inositol) with promising results [333]. More *in vitro* and simulation efforts have also been recently focused on CESL, with a feasibility study by Roeloffs et al. describing the quantification of proton exchange rates from data obtained in pulsed spin-lock experiments on a clinical 3 T scanner, using an interleaved saturation-relaxation approach [334].

6.7 Methodology used for MR data analysis

6.8 CEST

CEST images were imported into a custom made CEST tool written in Matlab. Postprocessing included image referencing, thresholding and interpolation (spline method). WASSR frequency shift maps were derived with the maximum symmetry algorithm and were used to correct the CEST spectra. CEST single frequency and integral maps were calculated, ROIs were drawn in and Z spectra and MTRasym spectra from ROIs were obtained. The MTR asymmetry metric is still the most widely used in CEST studies. It relies on the assumption that conventional magnetization transfer effects are symmetric around the water peak, which is just an approximation. However, asymmetric MT does not have a significant effect on the CEST contrast for frequency offsets close to the water peak ($<$ 1 ppm, such as myo-inositol).

Other confounders in traditional MTRasym are NOE mediated effects and direct saturation effects. The inverse metric [60, 61] removes direct saturation and MT effects (unwanted T_2 and MT contributions), but it requires the system to have reached steady state or near steady state, which is not the case with the sequence used in this work. Model based analysis methods are frequently used in the CEST literature (z-spectral fitting to the Bloch-McConell equations [64], with varying number of different CEST pools assumed, or Lorentzian fitting [142], decomposing the CEST spectrum into a sum of Lorentzian shapes).

These approaches are particularly difficult in hydroxyl CEST, due to the absence of a clear distinctive CEST peak, separated from the water (intermediate-to-fast exchange regime). These techniques benefit from observable narrow peaks in the z-spectra and thus have limited applicability in small frequency shifted and/or fast exchanging spins. Moreover, while *in vitro* contributions can be readily separated with these methods, it is harder to check their *in vivo* accuracy [139].

6.9 MRS

MRS data was analysed using LCmodel [10]. Different parameters were tested in the LCmodel to try to achieve the best possible fit to the data, which was assumed to be the one producing the lower residuals. The window of frequency-domain data, by default from 0.2 ppm to 4 ppm, excluded one of the myo-inositol resonances (extra peak around 4.1 ppm). A possible downside of extending the range to include this peak was the proximity to the water frequency (around 4.7 ppm). Inhomogeneity in the water suppression results over different spectra could be an argument against including it. To improve baseline reproducibility, other options explored have been to remove some macromolecular resonances from the frequency-domain window (from 0.2 ppm to 0.5 ppm), or to exclude NAA as one of the main metabolites defining the lineshape (since NAA was quite low for several datasets) or even to restrict the baseline and make it quite flat. However, none of these changes made a positive influence in the residual sum of squares (RSS), which was actually bigger with the new set of parameters.

Three different references were used for metabolite quantification: water concentration (value taken from the water reference scan, without water suppression), the total creatine concentration (using the metabolite total creatine as a reference) or a sum of selected metabolites, by choosing a subset of the most accurately fitted metabolites together as reference [284]: total creatine, total choline, taurine, myo-inositol, NAA and the sum of glutamate and glutamine (Glx). The reproducibility of the three references was evaluated: the water content was the most reproducible, followed by the sum of selected metabolites and total creatine. However, due to experimental mistakes, water reference scans were lost for several datasets, and the sum of selected metabolites was chosen as the preferred method.

A custom made MRS tool was written in Matlab, to export LCmodel results, which helped with reliability and speed in data processing.

6.10 Optimisation of pulse sequences

6.10.1 CEST

The CEST effect depends on several factors such as static field strength (B_0), concentration of metabolites with exchanging groups, exchange rate, RF saturation pulse duration and amplitude, T_1 of free water protons, B_0 homogeneities, overlap of different metabolites in the CEST signal, MT and NOE mediated contributions. Therefore, when interpreting a CEST measurement all these factors have to be taken into account.

A CEST pulse sequence has a presaturation module (where the CEST contrast is produced) and a imaging module (where the contrast is acquired). Long low-powered rectangular presaturation pulses (CW CEST), accompanied by single slice acquisitions are commonly employed in phantom and animal model studies, while in a clinical setting, trains of shaped short prepulses separated by short delays are used instead (Pulsed CEST) and multi-slice acquisition is desired. The presaturation module in this work has been optimised using simulations. Hydroxyl resonances are situated very close to the water peak, and therefore their measurement is made harder by the presence of direct water saturation effects, as well as inhomogeneities of the main B_0 field. The aim of the CEST simulations was to optimise myo-inositol CEST parameters, in order to maximize the contrast for *in vivo* experiments. Several models were studied during the simulations: long T_2 (distilled water + myo-inositol) and short T_2 (agar gel + myo-inositol) in a two pool model and a three pool model including conventional MT effects. *In vitro* experiments were performed to check the accuracy of all the simulations. The short T_2 two pool model was proven to be a good approach to calculate optimum myo-inositol CEST parameters, with a very short computing time. Asymmetric magnetization transfer effects did not have a significant effect on the CEST contrast for frequency offsets so close to the water peak ($<$ 1 ppm).

The *in vivo* imaging module chosen was a segmented gradient echo readout (two segments), with a centric encoding, so as to not lose contrast, which is given by the center of k space. Gradient echo sequences have the advantage of low SAR and high speeds (less than 10 min for the full protocol), but they can produce poor quality images because of eddy currents and B_0 inhomogeneity, compared with their spin echo counterparts. Two different schemes were tested for their reproducibility, with the final sequence incorporating both gradient spoiling and RF spoiling in the imaging module. A robust and reproducible CW CEST sequence was thus developed, maximizing the *in vivo* myo-inositol contrast.

6.10.2 LASER MRS

The sequence used for MRS at 9.4 T was LASER (localization by adiabatic selective refocusing). This method is insensitive to B_1 variations, minimises artifacts for J-coupled resonances and produces defined excitation profiles at high fields, since refocusing adiabatic pulses have much higher bandwidth compared to the pulses used in PRESS or STEAM. The 180 degree pulse power required careful calibration before the protocol was run. At the start, a global power calibration was performed (with a long TR), followed by the voxel positioning and shimming procedures. During the 180 degree calibration, an array of pulses were applied and the adiabatic plateau behaviour could be tested (that is, the power had reached its maximum and it had not started to drop). The default TE value was initially 40 ms and this could be reduced by applying different procedures, for example: reducing the width of the 180 degree pulse (followed by calibration) or reducing the duration of the gradient crushers. This last modification could introduce unwanted coherences on the baseline of the spectrum, which could be compensated by increasing the gradient crusher amplitude (paying attention to the effect this could have on the eddy currents). The final TE achieved was 24 ms and the baseline of the spectrum was routinely checked before any MRS scan was started.

To control movement artifacts and frequency drift, the averages of the LASER sequence (512) were acquired in groups of two, so that in postprocessing they could all be aligned and summed together, with the water peak used as reference for the alignment. The water suppression scheme (VAPOR) was initially optimized automatically but too much suppression caused problems sometimes when using the water peak as a reference and therefore, the optimisation of the water suppression was eliminated from the protocol. Moreover, a reference scan without water suppression was acquired at the beginning, for subsequent eddy current correction.

6.11 Experimental difficulties

Some of the work performed in this thesis is experimental and of high difficulty. This is particularly the case for the *in vivo* work described in Chapter 5. The main technical complications are described here:

6.11.1 Anaesthesia

Respiratory depression is a major adverse effect and the most probable emergency situation of inhalational anaesthetics [335]. Isoflurane is recommended as the first choice anaesthetic in mice and was administered at 3% for induction and 1-2% for maintenance. Hypothermia, which usually occurs under anaesthesia, was prevented by placing the animal on a warmed mat. Moreover, the animals' respiratory pattern and depth of anaesthesia, including testing the responsiveness to manipulations and rear foot reflexes, were monitored throughout the surgery, which was performed following appropriate training and supervision as required.

6.11.2 Shim and movement artifacts

The experimental difficulties of imaging hydroxyl groups using CEST have to be considered. Myo-inositol has six hydroxyl (OH) groups and hydroxyl CEST resonances are affected by direct water saturation effects, due to their proximity to the water peak. High magnetic fields maximise the frequency separation between OH and free water resonances, which is why this study was performed at 9.4 T. There is a trade-off between saturation efficiency of the hydroxyl CEST resonances, with the CEST effect increasing with $\vec{B}_1$ power and spillover effects or direct saturation of the free water pool, which also increases with $\vec{B}_1$ power. Direct saturation effects impose a restriction on the RF pulse power that can be used (0.9 μT was chosen in this case) and therefore on the saturation efficiency of the CEST sequence.

A 22 mm volume coil maximised the homogeneity of the B_1 magnetic field in the experiments. Static magnetic field (B_0) inhomogeneities also present a challenge for CEST imaging. This is particularly relevant for high magnetic fields, where the effects of B_0 inhomogeneities are magnified. B_0 inhomogeneities lead to a shift in the water resonance frequency that results in asymmetric direct water saturation and consequently to artificial CEST effects in the conventional asymmetry analysis. Even small shifts in B_0 inhomogeneity can cause large errors in the measured CEST asymmetry. Accurate correction of field inhomogeneities is essential to obtain precise CEST asymmetry measurements. The WASSR method has been used in this work to obtain an absolute mapping of the water frequency, together with intensive shimming before the CEST and WASSR measurements. However, susceptibility artifacts in regions of tissue interface changes, such as the cortex and the lower parts of the brain complicated the task of shimming. Agar caps in between the top of the animal head and the volume coil were introduced to reduce those susceptibility artifacts. Nevertheless, shimming artifacts can be observed in many datasets, especially in the lower area of the brain (due to the proximity of the ear canal).

Movement has been a major complication. A purposedly built mouse holder was designed for the experiment, without ear bars, due to the small space available inside the volume coil, which also restricted the weight of the animals. Movement effects rendered some datasets unusable (n=8) and were the main factor affecting *in vivo* reproducibility. Of the datasets that had to be discarded due to movement, either a good enough shim could not be achieved or movement artifacts could be seen in the CEST/WASSR images, even after repositioning the animal inside of the scanner.

6.11.3 Specificity

An intrinsic complication is the overlap of different molecules in the CEST signal in the region of the myo-inositol resonance, including metabolites such as glutamate, creatine or any hydroxyl group (i.e. glucose). Therefore, definite relations effect-metabolite are not feasible with this technique. Alternative techniques were used to confirm myo-inositol changes (MRS) and correlations were established instead (with myo-inositol MRS and with Iba staining), but the limitation remains that if more than one CEST metabolite were affected, changes in overlapping metabolites could interfere with each other, complicating the interpretation of the CEST contrast.

A further constraint in specificity is the potentially confounding effect of prolonged anaesthesia on some metabolites. As an inhalatory anaesthetic, isofluorane permits accurate control of the depth of anaesthesia, however, AD mouse models were reported to be more susceptible to repeated anaesthesia with isofluorane than controls [336].

6.12 Future work arising from this thesis

The main challenges in this project were to find the right quantitative molecular biomarker, a robust neuroinflammatory model with which to test the hypothesis and finally, the difficulties associated with a reproducible *in vivo* myo-inositol CEST protocol.

Future work on this project could be centered around refining myo-inositol CEST quality. Motion of the animal caused artifacts in some datasets and problems with shimming. Possible improvements could include upgrading the animal holder design, to achieve a better restraint of the animal body. Breathing effects are the cause of the movement and therefore, potential improvements could be evaluated, such as experimenting with alternative anaesthetic agents (i.e. injectable), or paralysing the animal for the duration of the experiment. *In vivo* reproducibility could possibly benefit from the use of other analysis methods, such as multiple Lorentz pool fitting or model based analysis based on the full solution of the Bloch-McConnell equations, with a finite number of pools.

Specificity is a inherent limitation of conventional CEST. Diverse alternative methods to improve this could be investigated, such as frequency-labelled exchange (FLEX [20]) transfer or chemical exchange-sensitive spin-lock (CESL). FLEX labels exchangeable protons by their chemical shift evolution instead of the usual saturation method. This has several advantages for specificity: it can separate different magnetization transfer effects using time domain analysis and exchange rate filtering, and direct saturation effects on water can be removed without the need for asymmetry analysis. This method has been proven to be successful *in vivo* for paraCEST [337] and diaCEST [338]. CESL can suppress direct water saturation, improving the sensitivity and specificity of molecules containing fast exchanging protons (such as hydroxyls). This approach has been recently used *in vivo* to measure cerebral glucose uptake by Zu et al.. Better sensitivity than CEST and more specificity to the exchange effects of interest have been reported [339].

Microglia activation is a well established characteristic of neuroinflammation and myo-inositol is considered to be a glial marker. However, the physiological mechanism has not been properly described and evidence is usually limited to myo-inositol levels increasing in many neuroinflammatory disorders. Therefore, myo-inositol, although a promising quantitative biomarker for neuroinflammation needs to be further researched and tested. In the search for robust neuroinflammatory challenges, alternative LPS dosages could be evaluated. At the time this work was performed, the LPS dose was limited by the Home Office license (hard constraint), but the license can be amended for future experiments. A too strong LPS dose injected in one of the sides of the hippocampus will spread across the whole brain and invalidate the use of the contralateral region as control, but intermediate dosages could be tested. Additionally, different neuroinflammatory challenges could be used: Carrillo-de Sauvage et al. has recently reported GluCEST changes in a model of selective astrocyte activation (overexpression of the cytokine ciliary neurotrophic factor, CNTF). This rat animal model, as characterised by LASER MRS shows a 61% increase in myo-inositol, accompanied by other metabolic changes (total choline (33%), glutamine (-14%), total NAA (-19%), taurine (-9%) and glutamate (-18%) [273]. A robust neuroinflammatory model would provide further validation for myo-inositol as a glial marker and CEST as an imaging biomarker for neuroinflammation.

References

[1] M. H. Leavitt. *Spin Dynamics: Basics of Nuclear Magnetic Resonance*. Wiley, 2nd edition, 2008.

[2] K. S. Krane. *Introductory Nuclear Physics*. 1988.

[3] R. Garstang. Atoms in high magnetic fields. *Rep. Prog. Phys.*, 40:105–154, 1977.

[4] G. W. Morley. Wikimedia commons image: The spin echo sequence, May 2011.

[5] M. A. Bernstein. *Handbook of MRI Pulse Sequences*. Elsevier, Academic Press, 2004.

[6] T. C. Farrar. *Pulse and Fourier Transform NMR, Introduction to theory and methods*. Academic Press Inc, 1971.

[7] R. R. Ernst and W. A. Anderson. Application of fourier transform spectroscopy to magnetic resonance. *Rev Sci Instrum*, 37(1):93–102, 1966.

[8] R. A. de Graaf. *In vivo NMR Spectroscopy*. Wiley, 2nd edition, 2007.

[9] L. G. Kaiser, K. Young, and G. B. Matson. Numerical simulations of localized high field ^1HMR spectroscopy. *J Magn Reson*, 195(1):67 – 75, 2008.

[10] S. W. Provencher. Estimation of metabolite concentrations from localized in vivo proton NMR spectra. *Magn Reson Med*, 30(6):672–679, 1993.

[11] M. Wilson, G. Reynolds, R. Kauppinen, T. Arvanitis, and A. Peet. A constrained least-squares approach to the automated quantitation of in vivo ^1H magnetic resonance spectroscopy data. *Magn Reson Med*, 65(1):1–12, 2011.

[12] J. F. A. Jansen, W. H. Backes, K. Nicolay, and M. E. Kooi. ^1H MR spectroscopy of the brain: Absolute quantification of metabolites. *Radiology*, 240(2):318–332, 2006.

[13] T. Ernst, R. Kreis, and B. Ross. Absolute quantitation of water and metabolites in the human brain. I: Compartments and water. *J Magn Reson Ser B*, 102(1):1 – 8, 1993.

[14] P. Tofts. *Quantitative MRI of the brain, measuring changes caused by disease*. Wiley, 2003.

[15] H. Friebolin. *Basic One and Two-Dimensional NMR Spectroscopy*. Wiley-VCH, 1998.

[16] K. M. Ward, A. H. Aletras, and R. S. Balaban. A new class of contrast agents for MRI based on proton chemical exchange dependent saturation transfer (CEST). *J Magn Reson*, 143(1):79–87, 2000.

[17] T. Jin, J. Autio, T. Obata, and S.-G. Kim. Spin-locking versus chemical exchange saturation transfer MRI for investigating chemical exchange process between water and labile metabolite protons. *Magn Reson Med*, 65(5):1448–1460, May 2011.

[18] A. D. Sherry and M. Woods. Chemical exchange saturation transfer contrast agents for magnetic resonance imaging. *Annu Rev Biomed Eng*, 10:391–411, 2008.

[19] P. C. M. van Zijl and N. N. Yadav. Chemical exchange saturation transfer (CEST): what is in a name and what isn't?. *Magn Reson Med*, 65(4):927–48, 2011.

[20] J. I. Friedman, M. T. McMahon, J. T. Stivers, and P. C. M. Van Zijl. Indirect detection of labile solute proton spectra via the water signal using frequency-labeled exchange (FLEX) transfer. *J Am Chem Soc*, 132(6):1813–1815, Feb 2010.

[21] P. D. Johnston and A. G. Redfield. Pulsed FT-NMR double resonance studies of yeast tRNA(phe): Specific nuclear overhauser effects and reinterpretation of low temperature relaxation data. *Nucleic Acids Res*, 5(10):3913–3927, 1978.

[22] K. L. Desmond and G. J. Stanisz. Understanding quantitative pulsed CEST in the presence of MT. *Magn Reson Med*, 67(4):979–990, 2012.

[23] R. M. Henkelman, G. J. Stanisz, and S. J. Graham. Magnetization transfer in MRI: a review. *NMR Biomed*, 14(2):57–64, 2001.

[24] V. Guivel-Scharen, T. Sinnwell, S. Wolff, and R. Balaban. Detection of proton chemical exchange between metabolites and water in biological tissues. *J Magn Reson*, 133(1):36 – 45, 1998.

[25] J. Pekar, P. Jezzard, D. A. Roberts, J. S. Leigh, J. A. Frank, and A. C. McLaughlin. Perfusion imaging with compensation for asymmetric magnetization transfer effects. *Magn Reson Med*, 35(1):70–79, 1996.

[26] J. Zhou, J.-F. Payen, D. A. Wilson, R. J. Traystman, and P. C. M. van Zijl. Using the amide proton signals of intracellular proteins and peptides to detect pH effects in MRI. *Nat Med*, 9(8):1085–1090, Aug 2003.

[27] S. Swanson and Y. Pang. MT is symmetric but shifted with respect to water. In *Proceedings of the 11th Annual Meeting of ISMRM, Ontario, Canada*, page 660, 2003.

[28] A. Overhauser. Polarization of nuclei in metals. *Phys. Rev.*, 92:411, 1953.

[29] I. Solomon. Relaxation processes in a system of two spins. *Phys. Rev.*, 99:559, 1955.

[30] J. Lu, J. Zhou, C. Cai, S. Cai, and Z. Chen. Observation of true and pseudo NOE signals using CEST-MRI and CEST-MRS sequences with and without lipid suppression. *Magn Reson Med*, 73(4):1615–22, 2015.

[31] W. Ling, R. R. Regatte, G. Navon, and A. Jerschow. Assessment of glycosaminoglycan concentration in vivo by chemical exchange-dependent saturation transfer (gagCEST). *Proc Natl Acad Sci USA*, 105(7):2266–2270, Feb 2008.

[32] T. Jin, P. Wang, X. Zong, and S.-G. Kim. Magnetic resonance imaging of the amine-proton exchange (APEX) dependent contrast. *Neuroimage*, 59(2):1218–1227, Jan 2012.

[33] P. Z. Sun, T. Benner, A. Kumar, and A. G. Sorensen. Investigation of optimizing and translating pH-sensitive pulsed-chemical exchange saturation transfer (CEST) imaging to a 3T clinical scanner. *Magn Reson Med*, 60(4):834–41, 2008.

[34] Z. Zu, K. Li, V. A. Janve, M. D. Does, and D. F. Gochberg. Optimizing pulsed-chemical exchange saturation transfer imaging sequences. *Magn Reson Med*, 66(4):1100–8, 2011.

[35] B. Schmitt, M. Zaiss, J. Zhou, and P. Bachert. Optimization of pulse train presaturation for CEST imaging in clinical scanners. *Magn Reson Med*, 65(6):1620–9, 2011.

[36] P. Z. Sun, E. Wang, J. S. Cheung, X. Zhang, T. Benner, and A. G. Sorensen. Simulation and optimization of pulsed radio frequency irradiation scheme for chemical exchange saturation transfer (CEST) MRI-demonstration of pH-weighted pulsed-amide proton CEST MRI in an animal model of acute cerebral ischemia. *Magn Reson Med*, 66(4):1042–8, 2011.

[37] C. K. Jones, D. Polders, J. Hua, H. Zhu, H. J. Hoogduin, J. Zhou, P. Luijten, and P. C. van Zijl. In vivo three-dimensional whole-brain pulsed steady-state chemical exchange saturation transfer at 7T. *Magn Reson Med*, 67(6):1579–1589, 2012.

[38] W. T. Dixon, I. Hancu, S. J. Ratnakar, A. D. Sherry, R. E. Lenkinski, and D. C. Alsop. A multislice gradient echo pulse sequence for CEST imaging. *Magn Reson Med*, 63(1): 253–6, 2010.

[39] P. Z. Sun, J. Lu, Y. Wu, G. Xiao, and R. Wu. Evaluation of the dependence of CEST-EPI measurement on repetition time, RF irradiation duty cycle and imaging flip angle for enhanced pH sensitivity. *Phys Med Biol*, 58(17):229–240, Sep 2013.

[40] P. Z. Sun, P. C. van Zijl, and J. Zhou. Optimization of the irradiation power in chemical exchange dependent saturation transfer experiments. *J Magn Reson*, 175(2):193–200, Aug 2005.

[41] M.-C. Ng, J. Hua, Y. Hu, K. D. Luk, and E. Y. Lam. Magnetization transfer (MT) asymmetry around the water resonance in human cervical spinal cord. *J J Magn Reson Im*, 29 (3):523–528, Mar 2009.

[42] P. Z. Sun, Y. Wang, and J. Lu. Sensitivity-enhanced chemical exchange saturation transfer (CEST) MRI with least squares optimization of Carr Purcell Meiboom Gill multi-echo echo planar imaging. *Contrast Media Mol I*, 9(2):177–181, 2014.

[43] K. W. Y. Chan, M. T. McMahon, Y. Kato, G. Liu, J. W. M. Bulte, Z. M. Bhujwalla, D. Artemov, and P. C. M. van Zijl. Natural D-glucose as a biodegradable MRI contrast agent for detecting cancer. *Magn Reson Med*, 68(6):1764–1773, 2012.

[44] J.-S. Lee, R. R. Regatte, and A. Jerschow. Isolating chemical exchange saturation transfer contrast from magnetization transfer asymmetry under two-frequency rf irradiation. *J Magn Reson*, 215:56–63, Feb 2012.

[45] G. Liu, M. M. Ali, B. Yoo, M. A. Griswold, J. A. Tkach, and M. D. Pagel. PARACEST MRI with improved temporal resolution. *Magn Reson Med*, 61(2):399–408, 2009.

[46] T. Shah, L. Lu, K. M. Dell, M. D. Pagel, M. A. Griswold, and C. A. Flask. CEST-FISP: a novel technique for rapid chemical exchange saturation transfer MRI at 7T. *Magn Reson Med*, 65(2):432–7, 2011.

[47] B. Yoo, V. R. Sheth, C. M. Howison, M. J. K. Douglas, C. T. Pineda, E. A. Maine, A. F. Baker, and M. D. Pagel. Detection of in vivo enzyme activity with CatalyCEST MRI. *Magn Reson Med*, 71(3):1221–1230, May 2013.

[48] L. Q. Chen, C. M. Howison, J. J. Jeffery, I. F. Robey, P. H. Kuo, and M. D. Pagel. Evaluations of extracellular pH within in vivo tumors using acidoCEST MRI. *Magn Reson Med*, 72(5):1408–1417, Nov 2013.

[49] V. R. Sheth, Y. Li, L. Q. Chen, C. M. Howison, C. A. Flask, and M. D. Pagel. Measuring in vivo tumor pHe with CEST-FISP MRI. *Magn Reson Med*, 67(3):760–768, Mar 2012.

[50] E. Terreno, D. D. Castelli, and S. Aime. Encoding the frequency dependence in MRI contrast media: the emerging class of CEST agents. *Contrast Media Mol I*, 5(2):78–98, 2010.

[51] T. Jin and S.-G. Kim. Quantitative chemical exchange sensitive MRI using irradiation with toggling inversion preparation. *Magn Reson Med*, 68(4):1056–64, 2012.

[52] M. Zaiss and P. Bachert. Chemical exchange saturation transfer (CEST) and MR Z-spectroscopy in vivo: a review of theoretical approaches and methods. *Phys Med Biol*, 58(22):221–269, Nov 2013.

[53] M. Haris, K. Cai, A. Singh, H. Hariharan, and R. Reddy. In vivo mapping of brain myo-inositol. *NeuroImage*, 54(3):2079 – 2085, 2011.

[54] P. C. M. van Zijl, C. K. Jones, J. Ren, C. R. Malloy, and A. D. Sherry. MRI detection of glycogen in vivo by using chemical exchange saturation transfer imaging (glycoCEST). *Proc Natl Acad Sci USA*, 104(11):4359–64, 2007.

[55] R. Scheidegger, E. Vinogradov, and D. C. Alsop. Amide proton transfer imaging with improved robustness to magnetic field inhomogeneity and magnetization transfer asymmetry using saturation with frequency alternating RF irradiation (SAFARI). *Magn Reson Med*, 66:1275–1285, 2011.

[56] J.-S. Lee, D. Xia, Y. Ge, A. Jerschow, and R. R. Regatte. Concurrent saturation transfer contrast in in vivo brain by a uniform magnetization transfer MRI. *Neuroimage*, 95: 22–28, Jul 2014.

[57] X. Song, A. A. Gilad, S. Joel, G. Liu, A. Bar-Shir, Y. Liang, M. Gorelik, J. J. Pekar, P. C. M. van Zijl, J. W. M. Bulte, and M. T. McMahon. CEST phase mapping using a length and offset varied saturation (LOVARS) scheme. *Magn Reson Med*, 68(4):1074–1086, 2012.

[58] Z. Zu, V. A. Janve, K. Li, M. D. Does, J. C. Gore, and D. F. Gochberg. Multi-angle ratiometric approach to measure chemical exchange in amide proton transfer imaging. *Magn Reson Med*, 68(3):711–719, Sep 2012.

[59] Z. Zu, J. Xu, H. Li, E. Y. Chekmenev, C. C. Quarles, M. D. Does, J. C. Gore, and D. F. Gochberg. Imaging amide proton transfer and nuclear overhauser enhancement using chemical exchange rotation transfer (CERT). *Magn Reson Med*, 72(2):471–476, Aug 2014.

[60] M. Zaiss, J. Xu, S. Goerke, I. S. Khan, R. J. Singer, J. C. Gore, D. F. Gochberg, and P. Bachert. Inverse Z-spectrum analysis for spillover, MT, and T1 -corrected steady-state

pulsed CEST-MRI: application to pH-weighted MRI of acute stroke. *NMR Biomed*, 27 (3):240–252, Mar 2014.

[61] J. Xu, M. Zaiss, Z. Zu, H. Li, J. Xie, D. F. Gochberg, P. Bachert, and J. C. Gore. On the origins of chemical exchange saturation transfer (CEST) contrast in tumors at 9.4T. *NMR Biomed*, 27(4):406–416, Apr 2014.

[62] M. Zaiss, B. Schmitt, and P. Bachert. Quantitative separation of CEST effect from magnetization transfer and spillover effects by lorentzian-line-fit analysis of z-spectra. *J Magn Reson*, 211(2):149–155, Aug 2011.

[63] K. L. Desmond, F. Moosvi, and G. J. Stanisz. Mapping of amide, amine, and aliphatic peaks in the CEST spectra of murine xenografts at 7T. *Magn Reson Med*, 71(5):1841–53, Jun 2013.

[64] A. X. Li, R. H. E. Hudson, J. W. Barrett, C. K. Jones, S. H. Pasternak, and R. Bartha. Four-pool modeling of proton exchange processes in biological systems in the presence of MRI-paramagnetic chemical exchange saturation transfer (PARACEST) agents. *Magn Reson Med*, 60(5):1197–206, 2008.

[65] D. E. Woessner, S. Zhang, M. E. Merritt, and A. D. Sherry. Numerical solution of the Bloch equations provides insights into the optimum design of PARACEST agents for MRI. *Magn Reson Med*, 53(4):790–9, 2005.

[66] Y. K. Tee, G. W. J. Harston, N. Blockley, T. W. Okell, J. Levman, F. Sheerin, M. Cellerini, P. Jezzard, J. Kennedy, S. J. Payne, and M. A. Chappell. Comparing different analysis methods for quantifying the MRI amide proton transfer (APT) effect in hyperacute stroke patients. *NMR Biomed*, 27(9):1019–29, Jun 2014.

[67] M. Zaiss, M. Schnurr, and P. Bachert. Analytical solution for the depolarization of hyperpolarized nuclei by chemical exchange saturation transfer between free and encapsulated xenon (HyperCEST). *J Chem Phys*, 136(14):144106, Apr 2012.

[68] L. Schröder, T. J. Lowery, C. Hilty, D. E. Wemmer, and A. Pines. Molecular imaging using a targeted magnetic resonance hyperpolarized biosensor. *Science*, 314(5798):446–449, Oct 2006.

[69] T. Meldrum, L. Schröder, P. Denger, D. E. Wemmer, and A. Pines. Xenon-based molecular sensors in lipid suspensions. *J Magn Reson*, 205(2):242–246, Aug 2010.

[70] F. Schilling, L. Schröder, K. K. Palaniappan, S. Zapf, D. E. Wemmer, and A. Pines. MRI thermometry based on encapsulated hyperpolarized xenon. *ChemPhysChem*, 11 (16):3529–3533, Nov 2010.

[71] T. Meldrum, V. S. Bajaj, D. E. Wemmer, and A. Pines. Band-selective chemical exchange saturation transfer imaging with hyperpolarized xenon-based molecular sensors. *J Magn Reson*, 213(1):14–21, Dec 2011.

[72] Y. Bai, P. A. Hill, and I. J. Dmochowski. Utilizing a water-soluble cryptophane with fast xenon exchange rates for picomolar sensitivity NMR measurements. *Anal Chem*, 84(22): 9935–9941, Nov 2012.

[73] C. Boutin, E. Léonce, T. Brotin, A. Jerschow, and P. Berthault. Ultrafast Z-spectroscopy for ^{129}Xe NMR-based sensors. *J Phys Chem Lett*, 4(23):4172–4176, Dec 2013.

[74] M. Schnurr, C. Witte, and L. Schröder. Functionalized ^{129}Xe as a potential biosensor for membrane fluidity. *Phys Chem Chem Phys*, 15(34):14178–14181, Sep 2013.

[75] J. Sloniec, M. Schnurr, C. Witte, U. Resch-Genger, L. Schröder, and A. Hennig. Biomembrane interactions of functionalized cryptophane-A: combined fluorescence and ^{129}Xe NMR studies of a bimodal contrast agent. *Chemistry*, 19(9):3110–3118, Feb 2013.

[76] T. K. Stevens, R. M. Ramirez, and A. Pines. Nanoemulsion contrast agents with sub-picomolar sensitivity for xenon NMR. *J Am Chem Soc*, 135(26):9576–9579, Jul 2013.

[77] Y. Bai, Y. Wang, M. Goulian, A. Driks, and I. J. Dmochowski. Bacterial spore detection and analysis using hyperpolarized ^{129}Xe chemical exchange saturation transfer (hyper-CEST) NMR. *Chem Sci*, 5(8):3197–3203, Aug 2014.

[78] J. Döpfert, C. Witte, M. Kunth, and L. Schröder. Sensitivity enhancement of hyper-CEST image series by exploiting redundancies in the spectral domain. *Contrast Media Mol I*, 9 (1):100–107, 2014.

[79] J. Döpfert, C. Witte, and L. Schröder. Fast gradient-encoded CEST spectroscopy of hyperpolarized xenon. *ChemPhysChem*, 15(2):261–264, Feb 2014.

[80] S. Klippel, J. Döpfert, J. Jayapaul, M. Kunth, F. Rossella, M. Schnurr, C. Witte, C. Freund, and L. Schröder. Cell tracking with caged xenon: using cryptophanes as MRI reporters upon cellular internalization. *Angew Chem Int Ed Engl*, 53(2):493–496, Jan 2014.

[81] M. Schnurr, K. Sydow, H. M. Rose, M. Dathe, and L. Schröder. Brain endothelial cell targeting via a peptide-functionalized liposomal carrier for xenon hyper-CEST MRI. *Adv Healthc Mater*, Jul 2014.

[82] M. Schnurr, C. Witte, and L. Schröder. Depolarization laplace transform analysis of exchangeable hyperpolarized ^{129}Xe for detecting ordering phases and cholesterol content of biomembrane models. *Biophys J*, 106(6):1301–1308, Mar 2014.

[83] M. G. Shapiro, R. M. Ramirez, L. J. Sperling, G. Sun, J. Sun, A. Pines, D. V. Schaffer, and V. S. Bajaj. Genetically encoded reporters for hyperpolarized xenon magnetic resonance imaging. *Nat Chem*, 6(7):629–634, Jul 2014.

[84] C. Witte, M. Kunth, F. Rossella, and L. Schröder. Observing and preventing rubidium runaway in a direct-infusion xenon-spin hyperpolarizer optimized for high-resolution hyper-CEST (chemical exchange saturation transfer using hyperpolarized nuclei) NMR. *J Chem Phys*, 140(8):084203, Feb 2014.

[85] S. Zhang, M. Merritt, D. E. Woessner, R. E. Lenkinski, and A. D. Sherry. PARACEST agents: modulating MRI contrast via water proton exchange. *Acc Chem Res*, 36(10): 783–90, 2003.

[86] M. Woods, E. W. C. Donald, and A. D. Sherry. Paramagnetic lanthanide complexes as PARACEST agents for medical imaging. *Chem Soc Rev*, 35(6):500–511, 2006.

[87] T. C. Soesbe, Y. Wu, and A. Dean Sherry. Advantages of paramagnetic chemical exchange saturation transfer (CEST) complexes having slow to intermediate water exchange properties as responsive MRI agents. *NMR Biomed*, 26(7):829–38, Oct 2012.

[88] M. Haris, R. P. R. Nanga, A. Singh, K. Cai, F. Kogan, H. Hariharan, and R. Reddy. Exchange rates of creatine kinase metabolites: feasibility of imaging creatine by chemical exchange saturation transfer MRI. *NMR Biomed*, 25(11):1305–9, 2012.

[89] F. Kogan, M. Haris, C. Debrosse, A. Singh, R. P. Nanga, K. Cai, H. Hariharan, and R. Reddy. In vivo chemical exchange saturation transfer imaging of creatine (CrCEST) in skeletal muscle at 3T. *J J Magn Reson Im*, 40(3):596–602, Oct 2013.

[90] F. Kogan, M. Haris, A. Singh, K. Cai, C. Debrosse, R. P. R. Nanga, H. Hariharan, and R. Reddy. Method for high-resolution imaging of creatine in vivo using chemical exchange saturation transfer. *Magn Reson Med*, 71(1):164–72, 2013.

[91] M. Haris, A. Singh, K. Cai, F. Kogan, J. McGarvey, C. Debrosse, G. A. Zsido, W. R. T. Witschey, K. Koomalsingh, J. J. Pilla, J. A. Chirinos, V. A. Ferrari, J. H. Gorman, H. Hariharan, R. C. Gorman, and R. Reddy. A technique for in vivo mapping of myocardial creatine kinase metabolism. *Nat Med*, 20(2):209–214, Feb 2014.

[92] X. Zong, P. Wang, S.-G. Kim, and T. Jin. Sensitivity and source of amine-proton exchange and amide-proton transfer magnetic resonance imaging in cerebral ischemia. *Magn Reson Med*, 71(1):118–132, Jan 2014.

[93] K. Cai, M. Haris, A. Singh, F. Kogan, J. H. Greenberg, H. Hariharan, J. A. Detre, and R. Reddy. Magnetic resonance imaging of glutamate. *Nat Med*, 18(2):302–306, Feb 2012.

[94] M. Haris, K. Nath, K. Cai, A. Singh, R. Crescenzi, F. Kogan, G. Verma, S. Reddy, H. Hariharan, E. R. Melhem, and R. Reddy. Imaging of glutamate neurotransmitter alterations in Alzheimer's disease. *NMR Biomed*, 26(4):386–91, 2012.

[95] K. Cai, A. Singh, D. R. Roalf, R. P. R. Nanga, M. Haris, H. Hariharan, R. Gur, and R. Reddy. Mapping glutamate in subcortical brain structures using high-resolution gluCEST MRI. *NMR Biomed*, 26(10):1278–1284, Oct 2013.

[96] F. Kogan, A. Singh, C. Debrosse, M. Haris, K. Cai, R. P. Nanga, M. Elliott, H. Hariharan, and R. Reddy. Imaging of glutamate in the spinal cord using gluCEST. *Neuroimage*, 77: 262–267, Aug 2013.

[97] R. Crescenzi, C. DeBrosse, R. P. R. Nanga, S. Reddy, M. Haris, H. Hariharan, M. Iba, V. M. Y. Lee, J. A. Detre, A. Borthakur, and R. Reddy. In vivo measurement of glutamate loss is associated with synapse loss in a mouse model of tauopathy. *Neuroimage*, 101C: 185–192, Jul 2014.

[98] M. Haris, A. Singh, K. Cai, K. Nath, G. Verma, R. P. R. Nanga, H. Hariharan, J. A. Detre, N. Epperson, and R. Reddy. High resolution mapping of modafinil induced changes in glutamate level in rat brain. *PLoS One*, 9(7):e103154, 2014.

[99] P. Z. Sun, Y. Murata, J. Lu, X. Wang, E. H. Lo, and A. G. Sorensen. Relaxation-compensated fast multislice amide proton transfer (APT) imaging of acute ischemic stroke. *Magn Reson Med*, 59(5):1175–82, 2008.

[100] Y. K. Tee, M. J. Donahue, G. W. J. Harston, S. J. Payne, and M. A. Chappell. Quantification of amide proton transfer effect pre- and post-gadolinium contrast agent administration. *J J Magn Reson Im*, 40(4):832–838, Nov 2013.

[101] J. Yuan, Q. Zhang, Y.-X. Wang, J. Wei, and J. Zhou. Accuracy and uncertainty of asymmetric magnetization transfer ratio quantification for amide proton transfer (APT) imaging at 3T: A monte carlo study. *Conf Proc IEEE Eng Med Biol Soc*, 2013:5139–5142, Jul 2013.

[102] J. Zhou, D. A. Wilson, P. Z. Sun, J. A. Klaus, and P. C. van Zijl. Quantitative description of proton exchange processes between water and endogenous and exogenous agents for WEX, CEST, and APT experiments. *Magn Reson Med*, 51(5):945–952, 2004.

[103] P. Z. Sun, J. Zhou, W. Sun, J. Huang, and P. C. M. van Zijl. Suppression of lipid artifacts in amide proton transfer imaging. *Magn Reson Med*, 54(1):222–5, 2005.

[104] P. Z. Sun, J. Zhou, J. Huang, and P. van Zijl. Simplified quantitative description of amide proton transfer (APT) imaging during acute ischemia. *Magn Reson Med*, 57(2):405–10, 2007.

[105] J. Zhou, J. O. Blakeley, J. Hua, M. Kim, J. Laterra, M. G. Pomper, and P. C. M. van Zijl. Practical data acquisition method for human brain tumor amide proton transfer (APT) imaging. *Magn Reson Med*, 60(4):842–849, Oct 2008.

[106] O. Mougin, R. Coxon, A. Pitiot, and P. Gowland. Magnetization transfer phenomenon in the human brain at 7T. *NeuroImage*, 49(1):272–281, Jan 2010.

[107] A. N. Dula, E. M. Asche, B. A. Landman, E. B. Welch, S. Pawate, S. Sriram, J. C. Gore, and S. A. Smith. Development of chemical exchange saturation transfer at 7T. *Magn Reson Med*, 66(3):831–838, Sep 2011.

[108] P. Z. Sun, E. Wang, and J. S. Cheung. Imaging acute ischemic tissue acidosis with pH-sensitive endogenous amide proton transfer (APT) MRI: Correction of tissue relaxation and concomitant RF irradiation effects toward mapping quantitative cerebral tissue pH. *NeuroImage*, 60(1):1–6, Mar 2012.

[109] S. Walker-Samuel, S. P. Johnson, B. Pedley, M. F. Lythgoe, and X. Golay. Extracranial measurements of amide proton transfer using exchange-modulated point-resolved spectroscopy (EXPRESS). *NMR Biomed*, 25(6):829–834, Jun 2012.

[110] A. N. Dula, L. R. Arlinghaus, R. D. Dortch, B. E. Dewey, J. G. Whisenant, G. D. Ayers, T. E. Yankeelov, and S. A. Smith. Amide proton transfer imaging of the breast at 3 T: establishing reproducibility and possible feasibility assessing chemotherapy response. *Magn Reson Med*, 70(1):216–224, Jul 2013.

[111] C. K. Jones, A. Huang, J. Xu, R. A. E. Edden, M. Schär, J. Hua, N. Oskolkov, D. Zacà, J. Zhou, M. T. McMahon, J. J. Pillai, and P. C. M. van Zijl. Nuclear overhauser enhancement (NOE) imaging in the human brain at 7T. *Neuroimage*, 77:114–124, Aug 2013.

[112] D. W. J. Klomp, A. N. Dula, L. R. Arlinghaus, M. Italiaander, R. D. Dortch, Z. Zu, J. M. Williams, D. F. Gochberg, P. R. Luijten, J. C. Gore, T. E. Yankeelov, and S. A. Smith. Amide proton transfer imaging of the human breast at 7T: development and reproducibility. *NMR Biomed*, 26(10):1271–1277, Oct 2013.

[113] O. Togao, C. W. Kessinger, G. Huang, T. C. Soesbe, K. Sagiyama, I. Dimitrov, A. D. Sherry, J. Gao, and M. Takahashi. Characterization of lung cancer by amide proton

transfer (APT) imaging: An in-vivo study in an orthotopic mouse model. *PLoS One*, 8 (10):e77019, 2013.

[114] J. Zhou, X. Hong, X. Zhao, J.-H. Gao, and J. Yuan. APT-weighted and NOE-weighted image contrasts in glioma with different RF saturation powers based on magnetization transfer ratio asymmetry analyses. *Magn Reson Med*, 70(2):320–327, Aug 2013.

[115] J. Zhou, H. Zhu, M. Lim, L. Blair, A. Quinones-Hinojosa, S. A. Messina, C. G. Eberhart, M. G. Pomper, J. Laterra, P. B. Barker, P. C. M. van Zijl, and J. O. Blakeley. Three-dimensional amide proton transfer MR imaging of gliomas: Initial experience and comparison with gadolinium enhancement. *J J Magn Reson Im*, 38(5):1119–1128, Nov 2013.

[116] K. Sagiyama, T. Mashimo, O. Togao, V. Vemireddy, K. J. Hatanpaa, E. A. Maher, B. E. Mickey, E. Pan, A. D. Sherry, R. M. Bachoo, and M. Takahashi. In vivo chemical exchange saturation transfer imaging allows early detection of a therapeutic response in glioblastoma. *Proc Natl Acad Sci USA*, 111(12):4542–4547, Mar 2014.

[117] A. Tietze, J. Blicher, I. K. Mikkelsen, L. Østergaard, M. K. Strother, S. A. Smith, and M. J. Donahue. Assessment of ischemic penumbra in patients with hyperacute stroke using amide proton transfer (APT) chemical exchange saturation transfer (CEST) MRI. *NMR Biomed*, 27(2):163–174, Feb 2014.

[118] O. Togao, T. Yoshiura, J. Keupp, A. Hiwatashi, K. Yamashita, K. Kikuchi, Y. Suzuki, S. O. Suzuki, T. Iwaki, N. Hata, M. Mizoguchi, K. Yoshimoto, K. Sagiyama, M. Takahashi, and H. Honda. Amide proton transfer imaging of adult diffuse gliomas: correlation with histopathological grades. *Neuro Oncol*, 16(3):441–448, Mar 2014.

[119] A. Singh, M. Haris, K. Cai, V. B. Kassey, F. Kogan, D. Reddy, H. Hariharan, and R. Reddy. Chemical exchange saturation transfer magnetic resonance imaging of human knee cartilage at 3 T and 7 T. *Magn Reson Med*, 68(2):588–594, Aug 2012.

[120] S. Haneder, S. R. Apprich, B. Schmitt, H. J. Michaely, S. O. Schoenberg, K. M. Friedrich, and S. Trattnig. Assessment of glycosaminoglycan content in intervertebral discs using chemical exchange saturation transfer at 3.0 tesla: preliminary results in patients with low-back pain. *Eur Radiol*, 23(3):861–868, Mar 2013.

[121] B. Schmitt, S. Zbyn, D. Stelzeneder, V. Jellus, D. Paul, L. Lauer, P. Bachert, and S. Trattnig. Cartilage quality assessment by using glycosaminoglycan chemical exchange saturation transfer and ^{23}Na MR imaging at 7 T. *Radiology*, 260(1):257–64, 2011.

[122] G. Varma, R. E. Lenkinski, and E. Vinogradov. Keyhole chemical exchange saturation transfer. *Magn Reson Med*, 68(4):1228–1233, Oct 2012.

[123] M. Haris, A. Singh, K. Cai, K. Nath, R. Crescenzi, F. Kogan, H. Hariharan, and R. Reddy. MICEST: A potential tool for non-invasive detection of molecular changes in Alzheimer's disease. *J Neurosci Meth*, 212(1):87 – 93, 2013.

[124] F. A. Nasrallah, G. Pagès, P. W. Kuchel, X. Golay, and K.-H. Chuang. Imaging brain deoxyglucose uptake and metabolism by glucoCEST MRI. *J Cereb Blood Flow Metab*, 33(8):1270–1278, Aug 2013.

[125] S. Walker-Samuel, R. Ramasawmy, F. Torrealdea, M. Rega, V. Rajkumar, S. P. Johnson, S. Richardson, M. Gonçalves, H. G. Parkes, E. Arstad, D. L. Thomas, R. B. Pedley, M. F. Lythgoe, and X. Golay. In vivo imaging of glucose uptake and metabolism in tumors. *Nat Med*, 19(8):1067–1072, Aug 2013.

[126] S. Goerke, M. Zaiss, and P. Bachert. Characterization of creatine guanidinium proton exchange by water-exchange (WEX) spectroscopy for absolute-pH CEST imaging in vitro. *NMR Biomed*, 27(5):507–518, May 2014.

[127] J.-S. Lee, P. Parasoglou, D. Xia, A. Jerschow, and R. R. Regatte. Uniform magnetization transfer in chemical exchange saturation transfer magnetic resonance imaging. *Sci Rep*, 3:1707, 2013.

[128] Q. Liu, N. Jin, Z. Fan, Y. Natsuaki, W. Tawackoli, G. Pelled, H. Bae, D. Gazit, and D. Li. Reliable chemical exchange saturation transfer imaging of human lumbar intervertebral discs using reduced-field-of-view turbo spin echo at 3 T. *NMR Biomed*, 26(12):1672–9, Jul 2013.

[129] G. Melkus, M. Grabau, D. C. Karampinos, and S. Majumdar. Ex vivo porcine model to measure pH dependence of chemical exchange saturation transfer effect of glycosaminoglycan in the intervertebral disc. *Magn Reson Med*, 71(5):1743–9, Jul 2013.

[130] W. Wei, G. Jia, D. Flanigan, J. Zhou, and M. V. Knopp. Chemical exchange saturation transfer MR imaging of articular cartilage glycosaminoglycans at 3T: Accuracy of B0 field inhomogeneity corrections with gradient echo method. *J Magn Reson Im*, 32(1): 41–7, Oct 2013.

[131] I. Krusche-Mandl, B. Schmitt, L. Zak, S. Apprich, S. Aldrian, V. Juras, K. M. Friedrich, S. Marlovits, M. Weber, and S. Trattnig. Long-term results 8 years after autologous osteochondral transplantation: 7 T gagCEST and sodium magnetic resonance imaging with morphological and clinical correlation. *Osteoarthr cartilage*, 20(5):357–363, May 2012.

[132] G. Saar, B. Zhang, W. Ling, R. R. Regatte, G. Navon, and A. Jerschow. Assessment of glycosaminoglycan concentration changes in the intervertebral disc via chemical exchange saturation transfer. *NMR Biomed*, 25(2):255–261, Feb 2012.

[133] M. Kim, Q. Chan, M.-P. Anthony, K. M. C. Cheung, D. Samartzis, and P.-L. Khong. Assessment of glycosaminoglycan distribution in human lumbar intervertebral discs using chemical exchange saturation transfer at 3 T: feasibility and initial experience. *NMR Biomed*, 24(9):1137–1144, Nov 2011.

[134] D. Liu, J. Zhou, R. Xue, Z. Zuo, J. An, and D. J. J. Wang. Quantitative characterization of nuclear overhauser enhancement and amide proton transfer effects in the human brain at 7 tesla. *Magn Reson Med*, 70(4):1070–1081, Oct 2013.

[135] W. Ling, U. Eliav, G. Navon, and A. Jerschow. Chemical exchange saturation transfer by intermolecular double-quantum coherence. *J Magn Reson*, 194(1):29 – 32, 2008.

[136] M. Zaiss, P. Kunz, S. Goerke, A. Radbruch, and P. Bachert. MR imaging of protein folding in vitro employing nuclear-overhauser-mediated saturation transfer. *NMR Biomed*, 26(12):1815–22, Sep 2013.

[137] J. Lu, C. Cai, S. Cai, Z. Chen, and J. Zhou. Chemical exchange saturation transfer MRI using intermolecular double-quantum coherences with multiple refocusing pulses. *J Magn Reson Im*, 32(6):759–765, Jul 2014.

[138] J. Lu, J. Zhou, C. Cai, S. Cai, and Z. Chen. Observation of true and pseudo NOE signals using CEST-MRI and CEST-MRS sequences with and without lipid suppression. *Magn Reson Med*, May 2014.

[139] G. Liu, X. Song, K. W. Y. Chan, and M. T. McMahon. Nuts and bolts of chemical exchange saturation transfer MRI. *NMR Biomed*, 26(7):810–28, 2013.

[140] P. Z. Sun, C. T. Farrar, and A. G. Sorensen. Correction for artifacts induced by B(0) and B(1) field inhomogeneities in pH-sensitive chemical exchange saturation transfer (CEST) imaging. *Magn Reson Med*, 58(6):1207–15, 2007.

[141] M. Kim, J. Gillen, B. A. Landman, J. Zhou, and P. C. M. van Zijl. Water saturation shift referencing (WASSR) for chemical exchange saturation transfer (CEST) experiments. *Magn Reson Med*, 61(6):1441–50, 2009.

[142] G. Liu, A. A. Gilad, J. W. M. Bulte, P. C. M. van Zijl, and M. T. McMahon. High-throughput screening of chemical exchange saturation transfer MR contrast agents. *Contrast Media Mol I*, 5(3):162–70, 2010.

[143] J. Stancanello, E. Terreno, D. D. Castelli, C. Cabella, F. Uggeri, and S. Aime. Development and validation of a smoothing-splines-based correction method for improving the analysis of CEST-MR images. *Contrast Media Mol I*, 3(4):136–49, 2008.

[144] G. Liu, M. Moake, Y.-e. Har-el, C. M. Long, K. W. Y. Chan, A. Cardona, M. Jamil, P. Walczak, A. A. Gilad, G. Sgouros, P. C. M. van Zijl, J. W. M. Bulte, and M. T. McMahon. In vivo multicolor molecular MR imaging using diamagnetic chemical exchange saturation transfer liposomes. *Magn Reson Med*, 67(4):1106–1113, Apr 2012.

[145] E. Terreno, J. Stancanello, D. Longo, D. D. Castelli, L. Milone, H. M. H. F. Sanders, M. B. Kok, F. Uggeri, and S. Aime. Methods for an improved detection of the MRI-CEST effect. *Contrast Media Mol I*, 4(5):237–47, 2009.

[146] F. Kogan, H. Hariharan, and R. Reddy. Chemical exchange saturation transfer (CEST) imaging: Description of technique and potential clinical applications. *Curr Radiol Rep*, 1(2):102–114, Jun 2013.

[147] W. Streit, R. Mrak, and W. Griffin. Microglia and neuroinflammation: a pathological perspective. *J Neuroinflamm*, 1:1–4, 2004.

[148] A. Winkeler, A. Boisgard, and B. Tavitian. Radioisotopic imaging of neuroinflammation. *J Nucl Med*, 51(1):1–4, 2010.

[149] A. Wunder, J. Klohs, and U. Dirnagl. Non-invasive visualization of CNS inflammation with nuclear and optical imaging. *Neuroscience*, 158(3):1161 – 1173, 2009.

[150] C. A. Dinarello. Proinflammatory cytokines. *Chest*, 118(2):503–508, 2000.

[151] A. Cagnin, A. Gerhard, and R. B. Banati. In vivo imaging of neuroinflammation. *Eur Neuropsychopharm*, 12(6):581 – 586, 2002.

[152] N. Stence, M. Waite, and M. E. Dailey. Dynamics of microglial activation: A confocal time-lapse analysis in hippocampal slices. *Glia*, 33(3):256–266, 2001.

[153] S. Venneti, C. Wiley, and J. Kofler. Imaging microglial activation during neuroinflammation and Alzheimer's disease. *J Neuroimmune Pharm*, 4:227–243, 2009.

[154] S. Kannan, B. Balakrishnan, O. Muzik, R. Romero, and D. Chugani. Positron emission tomography imaging of neuroinflammation. *Journal of Child Neurol*, 24(9):1190–1199, 2009.

[155] A. D. Kraft. Features of microglia and neuroinflammation relevant to environmental exposure and neurotoxicity. *IJERPH*, 8(7):2980–3018, 2011.

[156] R. M. Ransohoff and V. H. Perry. Microglial physiology: Unique stimuli, specialized responses. *Annu. Rev. Immunol.*, 27:119–45, 2009.

[157] H. A. Arnett, J. Mason, M. Marino, K. Suzuki, G. K. Matsushima, and J. Ting. TNFalpha promotes proliferation of oligodendrocyte progenitors and remyelination. *Nat Neurosci*, 4:1116–1122, 2001.

[158] B. A. Barres. The mystery and magic of glia: A perspective on their roles in health and disease. *Neuron*, 60(3):430–440, 2008.

[159] E. G. Hughes, S. H. Kang, M. Fukaya, and D. E. Bergles. Oligodendrocyte progenitors balance growth with self-repulsion to achieve homeostasis in the adult brain. *Nat Neurosci*, 16:668–676, 2013.

[160] F. Sun, C.-L. Glenn Lin, D. Mctigue, X. Shan, C. A. Tovar, J. C. Bresnahan, and M. S. Beattie. Effects of axon degeneration on oligodendrocyte lineage cells: Dorsal rhizotomy evokes a repair response while axon degeneration rostral to spinal contusion induces both repair and apoptosis. *Glia*, 58(11):1304–1319, 2010.

[161] E. J. Benner, D. Luciano, R. Jo, K. Abdi, P. Paez-Gonzalez, H. Sheng, D. S. Warner, C. Liu, C. Eroglu, and C. T. Kuo. Protective astrogenesis from the SVZ niche after injury is controlled by notch modulator Thbs4. *Nat*, 497:369–373, 2013.

[162] C. Goritz, D. Dias, N. Tomilin, M. Barbacid, O. Shupliakov, and F. ÌĄJ. A pericyte origin of spinal cord scar tissue. *Science*, 333:238–242, 2011.

[163] D. Loy, C. Crawford, J. Darnall, D. Burke, S. Onifer, and S. Whittemore. Temporal progression of angiogenesis and basal lamina deposition after contusive spinal cord injury in the adult rat. *J. Comp. Neurol.*, 445:308–324, 2002.

[164] V. Perry. Contribution of systemic inflammation to chronic neurodegeneration. *Acta Neuropathol*, 120:277–286, 2010.

[165] P. PG and L. EE. Can the immune system be harnessed to repair the cns? *Nat. Rev. Neurosci.*, 9:481–93, 2008.

[166] J. E. Burda and M. V. Sofroniew. Reactive gliosis and the multicellular response to cns damage and disease. *Neuron*, 81:229–248, 2014.

[167] L. Qin, X. Wu, M. L. Block, Y. Liu, G. R. Breese, J.-S. Hong, D. J. Knapp, and F. T. Crews. Systemic LPS causes chronic neuroinflammation and progressive neurodegeneration. *Glia*, 55(5):453–462, 2007.

[168] S. F. Carlo Perego and M.-G. D. Simoni. Temporal pattern of expression and colocalization of microglia/macrophage phenotype markers following brain ischemic injury in mice. *J Neuroinflamm*, 8:174, 2011.

[169] Y. L. L. Lawrence F. Eng, Roopa S. Ghirnikar. Glial fibrillary acidic protein: GFAP-thirty-one years (1969–2000). *Neurochemical Res*, 25 9-10:1439–1451, 2000.

[170] S. Lehnardt. Innate immunity and neuroinflammation in the CNS: The role of microglia in Toll-like receptor-mediated neuronal injury. *Glia*, 28(3):253–256, 2010.

[171] G. Ramesh, A. MacLean, and M. Philipp. Cytokines and chemokines at the crossroads of neuroinflammation, neurodegeneration, and neuropathic pain. *Mediators Inflamm*, 480739, 2013.

[172] B. A., R. C., and D. Leibfritz. Multinuclear NMR studies on the energy-metabolism of glial and neuronal cells. *Dev Neurosci*, 15(3-5):289–298, May 1993.

[173] P. Schneider, W. Weber-Fahr, N. Schweinfurth, Y.-J. Ho, A. Sartorius, R. Spanagel, and C. R. Pawlak. Central metabolite changes and activation of microglia after peripheral interleukin-2 challenge. *Brain, Behavior, and Immunity*, 26(2):277 – 283, 2012.

[174] L. Chang, S. M. Munsaka, S. Kraft-Terry, and T. Ernst. Magnetic resonance spectroscopy to assess neuroinflammation and neuropathic pain. *J Neuroimmune Pharmacol*, 8(3): 576–593, Jun 2013.

[175] S. Lehnardt, C. Lachance, S. Patrizi, S. Lefebvre, P. Follett, F. Jensen, P. Rosenberg, J. Volpe, and T. Vartanian. The toll-like receptor TLR4 is necessary for lipopolysaccharide-induced oligodendrocyte injury in the CNS. *J Neurosci.*, 22(7):2478–86, 2002.

[176] R. Muceniece, L. Zvejniece, O. Kirjanova, E. Liepinsh, L. Krigere, L. Baumane, I. Kalvinsh, J. E. S. Wikberg, and M. Dambrova. Beta- and gamma-melanocortins inhibit lipopolysaccharide induced nitric oxide production in mice brain. *Brain Res*, 995 (1):7–13, Jan 2004.

[177] S. Chakravarty and M. Herkenham. Toll-like receptor 4 on nonhematopoietic cells sustains cns inflammation during endotoxemia, independent of systemic cytokines. *J Neurosci*, 25(7):1788–96, 2005.

[178] H. Romeo, D. Tio, S. Rahman, F. Chiappelli, and A. Taylor. The glossopharyngeal nerve as a novel pathway in immune-to-brain communication: relevance to neuroimmune surveillance of the oral cavity. *J Neuroimmunol*, 115(1-2):91–100, 2001.

[179] L. Qin, X. Wu, M. Block, Y. Liu, G. Breese, J. Hong, D. Knapp, and F. Crews. Systemic lps causes chronic neuroinflammation and progressive neurodegeneration. *Glia*, 55(5): 453–62, 2007.

[180] A. Ulmer, E. Rietschel, U. Zahringer, and H. Heine. Lipopolysaccharide: structure, bioactivity, receptors, and signal transduction. trends in glycoscience and glycotechnology. *Glia*, 14:53–68, 2002.

[181] S. Verma, R. Nakaoke, S. Dohgu, and W. Banks. Release of cytokines by brain endothelial cells: A polarized response to lipopolysaccharide. *Brain Behav Immun.*, 20(5): 449–55, 2006.

[182] W. A. Banks and S. M. Robinson. Minimal penetration of lipopolysaccharide across the murine blood-brain barrier. *Brain Behav Immun.*, 24(1):102–109, 2010.

[183] J. Teeling, L. Felton, R. Deacon, C. Cunningham, J. Rawlins, and V. Perry. Sub-pyrogenic systemic inflammation impacts on brain and behavior, independent of cytokines. *Brain, Behavior, and Immunity*, 21(6):836 – 850, 2007.

[184] C. Cunningham, S. Campion, K. Lunnon, C. L. Murray, J. F. Woods, R. M. Deacon, N. P. Rawlins, and V. H. Perry. Systemic inflammation induces acute behavioral and cognitive changes and accelerates neurodegenerative disease. *Biol Psychiatry*, 65(4): 304–312, 2009.

[185] M. Takashima-Hirano, M. Shukuri, T. Takashima, M. Goto, Y. Wada, Y. Watanabe, H. Onoe, H. Doi, and M. Suzuki. General method for the ^{11}C-labeling of 2-arylpropionic acids and their esters: construction of a PET tracer library for a study of biological events involved in COXs expression. *Chemistry*, 16(14):4250–4258, Apr 2010.

[186] F. Ito, H. Toyama, G. Kudo, H. Suzuki, K. Hatano, M. Ichise, K. Katada, K. Ito, and M. Sawada. Two activated stages of microglia and PET imaging of peripheral benzodiazepine receptors with [^{11}C]PK11195 in rats. *Ann Nucl Med*, 24(3):163–169, Apr 2010.

[187] A. G. Horti, Y. Gao, H. T. Ravert, P. Finley, H. Valentine, D. F. Wong, C. J. Endres, A. V. Savonenko, and R. F. Dannals. Synthesis and biodistribution of [^{11}C]A-836339, a new potential radioligand for PET imaging of cannabinoid type 2 receptors (CB2). *Bioorg Med Chem*, 18(14):5202–5207, Jul 2010.

[188] A. M. Dickens, S. Vainio, P. Marjamäki, J. Johansson, P. Lehtiniemi, J. Rokka, J. Rinne, O. Solin, M. Haaparanta-Solin, P. A. Jones, W. Trigg, D. C. Anthony, and L. Airas. Detection of microglial activation in an acute model of neuroinflammation using PET and radiotracers ^{11}C-(R)-PK11195 and ^{18}F-GE-180. *J Nucl Med*, 55(3):466–72, 2014.

[189] L. Lopez de Heredia, A. Gengatharan, J. Foster, S. Mather, and C. Magoulas. Bioluminescence imaging of the brain response to acute inflammation in living C/EBP reporter mice. *Neurosci Lett*, 497(2):134–138, Jun 2011.

[190] H. Akimoto, H. J. Kwon, M. Ozaki, K. Yasuda, K.-i. Honma, and Y. Ohmiya. In vivo bioluminescence imaging of bone marrow-derived cells in brain inflammation. *Biochem Biophys Res Commun*, 380(4):844–849, Mar 2009.

[191] M. Gorelik, I. Orukari, J. Wang, S. Galpoththawela, H. Kim, M. Levy, A. A. Gilad, A. Bar-Shir, D. A. Kerr, A. Levchenko, J. W. M. Bulte, and P. Walczak. Use of MR cell tracking to evaluate targeting of glial precursor cells to inflammatory tissue by exploiting the very late antigen-4 docking receptor. *Radiology*, 265(1):175–185, Oct 2012.

[192] H.-Y. Wu, M.-C. Chung, C.-C. Wang, C.-H. Huang, H.-J. Liang, and T.-R. Jan. Iron oxide nanoparticles suppress the production of IL-1beta via the secretory lysosomal pathway in murine microglial cells. *Part Fibre Toxicol*, 10:46, 2013.

[193] H. R. Herschman. Molecular imaging: Looking at problems, seeing solutions. *Science*, 302(5645):605–608, 2003.

[194] R. Weissleder and U. Mahmood. Molecular imaging. *Radiology*, 219(2):316–333, 2001.

[195] C. Wu, F. Li, G. Niu, and X. Chen. PET imaging of inflammation biomarkers. *Theranostics*, 3(7):448–66, 2013.

[196] A. Cagnin, A. Gerhard, and R. B. Banati. The concept of in vivo imaging of neuroinflammation with [^{11}C](R)-PK11195 PET. *Ernst Schering Research Foundation Workshop*, (39):179–191, 2002.

[197] P. Edison, H. A. Archer, A. Gerhard, R. Hinz, N. Pavese, F. E. Turkheimer, A. Hammers, Y. F. Tai, N. Fox, A. Kennedy, M. Rossor, and D. J. Brooks. Microglia, amyloid, and cognition in Alzheimer's disease: An [^{11}C](R)PK11195-PET and [^{11}C]PIB-PET study. *Neurobiol Dis*, 32(3):412–419, Dec 2008.

[198] A. Cagnin, D. J. Brooks, A. M. Kennedy, R. N. Gunn, R. Myers, F. E. Turkheimer, T. Jones, and R. B. Banati. In-vivo measurement of activated microglia in dementia. *The Lancet*, 358(9280):461–467, Aug 2001.

[199] A. Cagnin, M. Rossor, E. L. Sampson, T. MacKinnon, and R. B. Banati. In vivo detection of microglial activation in frontotemporal dementia. *Ann Neurol.*, 56(6):894–897, Dec 2004.

[200] A. J. Stoessl. Developments in neuroimaging: positron emission tomography. *Parkinsonism Relat Disord*, 20 (Suppl 1):180–183, Jan 2014.

[201] Y. Ouchi, E. Yoshikawa, Y. Sekine, M. Futatsubashi, T. Kanno, T. Ogusu, and T. Torizuka. Microglial activation and dopamine terminal loss in early Parkinson's disease. *Ann Neurol.*, 57(2):168–175, Feb 2005.

[202] D. J. Brooks. Imaging approaches to Parkinson disease. *J Nucl Med*, 51(4):596–609, Apr 2010.

[203] R. B. Banati, J. Newcombe, R. N. Gunn, A. Cagnin, F. Turkheimer, F. Heppner, G. Price, F. Wegner, G. Giovannoni, D. H. Miller, G. D. Perkin, T. Smith, A. K. Hewson, G. Bydder, G. W. Kreutzberg, T. Jones, M. L. Cuzner, and R. Myers. The peripheral benzodiazepine binding site in the brain in multiple sclerosis: quantitative in vivo imaging of microglia as a measure of disease activity. *Brain*, 123 (11):2321–37, 2000.

[204] A. Thiel, B. A. Radlinska, C. Paquette, M. Sidel, J.-P. Soucy, R. Schirrmacher, and J. Minuk. The temporal dynamics of poststroke neuroinflammation: a longitudinal diffusion tensor imaging-guided PET study with ^{11}C-PK11195 in acute subcortical stroke. *J Nucl Med*, 51(9):1404–12, 2010.

[205] F. Chauveau, H. Boutin, N. Van Camp, F. Dollé, and B. Tavitian. Nuclear imaging of neuroinflammation: a comprehensive review of [^{11}C]PK11195 challengers. *Eur J Nucl Med Mol Imaging*, 35(12):2304–2319, Dec 2008.

[206] R. Ahmad, M. Koole, N. Evens, K. Serdons, A. Verbruggen, G. Bormans, and K. Laere. Whole-body biodistribution and radiation dosimetry of the cannabinoid type 2 receptor ligand [^{11}C]-NE40 in healthy subjects. *Mol Imaging Biol*, 15(4):384–390–, 2013.

[207] L. Minghetti. Cyclooxygenase-2 (COX-2) in inflammatory and degenerative brain diseases. *J Neuropathol Exp Neurol.*, 63(9):63(9), 2004.

[208] E. F. de Vries, J. Doorduin, R. A. Dierckx, and A. van Waarde. Evaluation of [^{11}C]rofecoxib as PET tracer for cyclooxygenase 2 overexpression in rat models of inflammation. *Nucl Med Biol*, 35(1):35–42, Jan 2008.

[209] A. R. Jalilian, M. Bineshmarvasti, and S. Sardari. Application of radioisotopes in inflammation. *Curr Med Chem*, 13(8):959–965, 2006.

[210] K. Herholz. PET studies in dementia. *Ann Nucl Med*, 17(2):79–89, 2003.

[211] V. Berti, A. Pupi, and L. Mosconi. PET/CT in diagnosis of dementia. *Ann NY Acad Sci*, 1228:81–92, Jun 2011.

[212] N. L. Foster, J. L. Heidebrink, C. M. Clark, W. J. Jagust, S. E. Arnold, N. R. Barbas, C. S. DeCarli, R. Scott Turner, R. A. Koeppe, R. Higdon, and S. Minoshima. FDG-PET improves accuracy in distinguishing frontotemporal dementia and Alzheimer's disease. *Brain*, 130(10):2616–2635, Oct 2007.

[213] G. Stoll and M. Bendszus. New approaches to neuroimaging of central nervous system inflammation. *Curr Opin Neurol*, 23(3):282–286, Jun 2010.

[214] M. Rausch, P. Hiestand, D. Baumann, C. Cannet, and M. Rudin. MRI-based monitoring of inflammation and tissue damage in acute and chronic relapsing EAE. *Magn Reson Med*, 50(2):309–314, 2003.

[215] P. J. Schweitzer, B. A. Fallon, J. J. Mann, and J. D. Kumar. PET tracers for the peripheral benzodiazepine receptor and uses thereof. *Drug Discov Today*, 15(21–22):933 – 942, 2010.

[216] G. Brix, E. Nekolla, D. Nosske, and Griebel. Risks and safety aspects related to PET/MR examinations. *Eur J Nucl Med Mol I*, 36:131–138, 2009.

[217] N. Braakman, T. Oerther, H. J. de Groot, and A. Alia. High resolution localized two-dimensional MR spectroscopy in mouse brain in vivo. *Magn Reson Med*, 60(2):449–456, 2008.

[218] B. L. Miller, R. A. Moats, T. Shonk, T. Ernst, S. Wooley, and B. D. Ross. Alzheimer disease: Depiction of increased cerebral myoinositol with proton MR spectroscopy. *Radiology*, 187(2):433–437, May 1993.

[219] M. J. Firbank, R. M. Harrison, and J. T. O'Brien. A comprehensive review of proton magnetic resonance spectroscopy studies in dementia and Parkinson's disease. *Dement Geriatr Cogn Disord*, 14(2):64–76, 2002.

[220] D. Rigotti, M. Inglese, I. I. Kirov, E. Gorynski, N. N. Perry, J. S. Babb, J. Herbert, R. I. Grossman, and O. Gonen. Two-year serial whole-brain N-acetyl-L-aspartate in patients with relapsing-remitting multiple sclerosis. *Neurology*, 78(18):1383–9, 2012.

[221] B. Schweinsburg, M. Taylor, O. Alhassoon, R. Gonzalez, G. Brown, R. Ellis, S. Letendre, J. Videen, J. McCutchan, T. Patterson, and I. Grant. Brain mitochondrial injury in human immunodeficiency virus-seropositive (HIV+) individuals taking nucleoside reverse transcriptase inhibitors. *J NeuroVirol*, 11(4):356–364, 2005.

[222] V. P. B. Grover, N. Pavese, S.-B. Koh, M. Wylezinska, B. K. Saxby, A. Gerhard, D. M. Forton, D. J. Brooks, H. C. Thomas, and S. D. Taylor-Robinson. Cerebral microglial

activation in patients with hepatitis C: in vivo evidence of neuroinflammation. *J Viral Hepat*, 19(2):89–96, 2012.

[223] J. J. G. Geurts, I. E. W. Reuling, H. Vrenken, B. M. J. Uitdehaag, C. H. Polman, J. A. Castelijns, F. Barkhof, and P. J. W. Pouwels. MR spectroscopic evidence for thalamic and hippocampal, but not cortical, damage in multiple sclerosis. *Magn Reson Med*, 55 (3):478–483, Mar 2006.

[224] S. Letendre, J. Zheng, M. Kaul, C. Yiannoutsos, R. Ellis, M. Taylor, J. Marquie-Beck, and B. Navia. Chemokines in cerebrospinal fluid correlate with cerebral metabolite patterns in HIV-infected individuals. *J NeuroVirol*, 17(1):63–69, 2011.

[225] T. K. Shonk, R. A. Moats, P. Gifford, T. Michaelis, J. C. Mandigo, J. Izumi, and B. D. Ross. Probable alzheimer-disease - diagnosis with proton mr spectroscopy. *Radiology*, 195(1):65–72, Apr 1995.

[226] K. Kantarci, Jack, C. Jr, Y. Xu, N. Campeau, P. O'Brien, G. Smith, R. Ivnik, B. Boeve, E. Kokmen, E. Tangalos, and R. Petersen. Regional metabolic patterns in mild cognitive impairment and Alzheimer's disease: A 1H MRS study. *Neurology*, 55(2):210–7, 2000.

[227] B. Ross, S. Bluml, R. Cowan, E. Danielsen, N. Farrow, and J. Tan. In vivo MR spectroscopy of human dementia. *Neuroimaging Clin N Am*, 8(4):809–22, 1998.

[228] W. Huang, G. Alexander, E. Daly, H. Shetty, J. Krasuski, S. Rapoport, and M. Schapiro. High brain myo-inositol levels in the predementia phase of Alzheimer's disease in adults with Down's syndrome: a 1H MRS study,. *American Journal of Psychiatry*, 156(12): 1879–1886, 1999.

[229] S. Chantal, M. Labelle, R. W. Bouchard, C. M. J. Braun, and Y. Boulanger. Correlation of regional proton magnetic resonance spectroscopic metabolic changes with cognitive deficits in mild Alzheimer disease. *Archives of Neurology*, 59(6):955–962, 2002.

[230] C. C. Cloak, L. Chang, and T. Ernst. Increased frontal white matter diffusion is associated with glial metabolites and psychomotor slowing in HIV. *Journal of Neuroimmunology*, 157(1-2):147–152, 2004.

[231] D. H. Miller. Brain atrophy, interferon beta, and treatment trials in multiple sclerosis. *Lancet*, 364(9444):1463–1464, 2004.

[232] M. Marjanska, G. Curran, T. Wengenack, P. Henry, R. Bliss, J. Poduslo, C. Jack, K. Ugurbil, and M. Garwood. Monitoring disease progression in transgenic mouse models of Alzheimer's disease with proton magnetic resonance spectroscopy. *Proc Natl Acad Sci USA*, 102(33):11906–11910, Aug 2005.

[233] D. Piani and A. Fontana. Involvement of the cystine transport system xc- in the macrophage-induced glutamate-dependent cytotoxicity to neurons. *J Immunol.*, 152(7): 3578–85, 1994.

[234] I. El Ghazi. Changes in the NMR metabolic profile of human microglial cells exposed to lipopolysaccharide or morphine. *J Neuroimmune Pharm*, 5:574–581, 2010.

[235] I. Yawata, H. Takeuchi, Y. Doi, J. Liang, T. Mizuno, and A. Suzumura. Macrophage-induced neurotoxicity is mediated by glutamate and attenuated by glutaminase inhibitors and gap junction inhibitors. *Life Sci*, 82:1111–1116, 2008.

[236] M. A. Mohamed, P. B. Barker, R. L. Skolasky, O. A. Selnes, R. T. Moxley, M. G. Pomper, and N. C. Sacktor. Brain metabolism and cognitive impairment in HIV infection: a 3 T magnetic resonance spectroscopy study. *Magnetic Resonance Imaging*, 28(9):1251–1257, 2010.

[237] E. Pioro, A. Majors, H. Mitsumoto, D. Nelson, and T. Ng. H-1-MRS evidence of neurodegeneration and excess glutamate plus glutamine in ALS medulla. *Neurology*, 53(1): 71–79, Jul 1999.

[238] N. A. Puts and R. A. Edden. In vivo magnetic resonance spectroscopy of GABA: A methodological review. *Prog Nucl Magn Reson Spectrosc.*, 60:29–41, Jan 2012.

[239] U. E. Emir, P. J. Tuite, and G. Öz. Elevated pontine and putamenal GABA levels in mild-moderate Parkinson disease detected by 7 tesla proton MRS. *PLoS ONE*, 7(1):e30918, 01 2012.

[240] A. H. Jacobs, B. Tavitian, and the INMIND consortium. Noninvasive molecular imaging of neuroinflammation. *J Cereb Blood Flow Metab*, 32(7):1393–1415, Jul 2012.

[241] S. J. Nelson, D. B. Vigneron, J. Star-Lack, and J. Kurhanewicz. High spatial resolution and speed in MRSI. *NMR Biomed*, 10(8):411–422, 1997.

[242] G. D. Luker and K. E. Luker. Optical imaging: Current applications and future directions. *J Nucl Med.*, 49:1:4, 2008.

[243] D. Davalos, J. Grutzendler, G. Yang, J. V. Kim, Y. Zuo, S. Jung, D. R. Littman, M. L. Dustin, and W.-B. Gan. ATP mediates rapid microglial response to local brain injury in vivo. *Nat Neurosci*, 8(6):752–758, Jun 2005.

[244] C. Berger, H.-U. Gremlich, P. Schmidt, C. Cannet, R. Kneuer, P. Hiestand, M. Rausch, and M. Rudin. In vivo monitoring the fate of Cy5.5-Tat labeled T lymphocytes by quantitative near-infrared fluorescence imaging during acute brain inflammation in a rat model

of experimental autoimmune encephalomyelitis. *J Immunol Methods*, 323(1):65–77, May 2007.

[245] J. Klohs, M. Gräfe, K. Graf, J. Steinbrink, T. Dietrich, D. Stibenz, P. Bahmani, G. Kronenberg, C. Harms, M. Endres, U. Lindauer, K. Greger, E. H. K. Stelzer, U. Dirnagl, and A. Wunder. In vivo imaging of the inflammatory receptor CD40 after cerebral ischemia using a fluorescent antibody. *Stroke*, 39(10):2845–2852, Oct 2008.

[246] B. T. R. Sato, Akiko; Klaunberg. In vivo bioluminescence imaging. *J Am Assoc Lab Anim Sci.*, 54(6):631–634, 2004.

[247] P. Cordeau, Jr, M. Lalancette-Hébert, Y. C. Weng, and J. Kriz. Live imaging of neuroinflammation reveals sex and estrogen effects on astrocyte response to ischemic injury. *Stroke*, 39(3):935–942, Mar 2008.

[248] J. Luo, P. Ho, L. Steinman, and T. Wyss-Coray. Bioluminescence in vivo imaging of autoimmune encephalomyelitis predicts disease. *J Neuroinflammation*, 5:6, 2008.

[249] L. Zhu, S. Ramboz, D. Hewitt, L. Boring, D. S. Grass, and A. F. Purchio. Non-invasive imaging of GFAP expression after neuronal damage in mice. *Neurosci Lett*, 367(2):210 – 212, 2004.

[250] M. Lalancette-Hébert, C. Julien, P. Cordeau, I. Bohacek, Y.-C. Weng, F. Calon, and J. Kriz. Accumulation of dietary docosahexaenoic acid in the brain attenuates acute immune response and development of postischemic neuronal damage. *Stroke*, 42(10): 2903–2909, Oct 2011.

[251] L. M. De Leon-Rodriguez, A. J. M. Lubag, C. R. Malloy, G. V. Martinez, R. J. Gillies, and A. D. Sherry. Responsive MRI agents for sensing metabolism in vivo. *Acc Chem Res*, 42(7):948–57, 2009.

[252] M. Rudin, T. Mueggler, P. R. Allegrini, D. Baumann, and M. Rausch. Characterization of CNS disorders and evaluation of therapy using structural and functional MRI. *Anal Bioanal Chem*, 377(6):973–981, Nov 2003.

[253] A. Giorgio, M. Battaglini, S. Smith, and N. De Stefano. Brain atrophy assessment in multiple sclerosis: importance and limitations. *Neuroimaging Clin N Am*, 18(4):675–86, 2008.

[254] J. S. Weinstein, C. G. Varallyay, E. Dosa, S. Gahramanov, B. Hamilton, W. D. Rooney, L. L. Muldoon, and E. A. Neuwelt. Superparamagnetic iron oxide nanoparticles: diagnostic magnetic resonance imaging and potential therapeutic applications in neurooncol-

ogy and central nervous system inflammatory pathologies, a review. *J Cereb Blood Flow Metab*, 30(1):15–35, 2010.

[255] E. Lavi and C. Constantinescu. *Experimental models of multiple esclerosis*. Springer Science, 2005.

[256] C.-L. Chin, M. Pai, P. F. Bousquet, A. J. Schwartz, E. M. O'Connor, C. M. Nelson, V. P. Hradil, B. F. Cox, B. L. McRae, and G. B. Fox. Distinct spatiotemporal pattern of CNS lesions revealed by USPIO-enhanced MRI in MOG-induced EAE rats implicates the involvement of spino-olivocerebellar pathways. *J Neuroimmunol*, 211(1–2):49 – 55, 2009.

[257] V. Dousset, L. Ballarino, C. Delalande, M. Coussemacq, P. Canioni, K. G. Petry, and J.-M. Caillé. Comparison of ultrasmall particles of iron oxide USPIO-enhanced T2-weighted, conventional T2-weighted, and gadolinium-enhanced T1-weighted MR images in rats with experimental autoimmune encephalomyelitis. *Am J Neuroradiol*, 20(2):223–227, Feb 1999.

[258] G. Fleige, C. Nolte, M. Synowitz, F. Seeberger, H. Kettenmann, and C. Zimmer. Magnetic labeling of activated microglia in experimental gliomas. *Neoplasia*, 3(6):489–99, 2001.

[259] M. M. Vellinga, H. Vrenken, H. E. Hulst, C. H. Polman, B. M. Uitdehaag, P. J. Pouwels, F. Barkhof, and J. J. Geurts. Use of ultrasmall superparamagnetic particles of iron oxide USPIO-enhanced MRI to demonstrate diffuse inflammation in the normal-appearing white matter (NAWM) of multiple sclerosis (MS) patients: An exploratory study. *J Magn Reson Im*, 29(4):774–779, 2009.

[260] G. Weise, T. C. Basse-Lüsebrink, C. Kleinschnitz, T. Kampf, P. M. Jakob, and G. Stoll. In vivo imaging of stepwise vessel occlusion in cerebral photothrombosis of mice by ^{19}F MRI. *PLoS ONE*, 6(12):e28143, 12 2011.

[261] A. P. Koretsky and A. C. Silva. Manganese-enhanced magnetic resonance imaging (MEMRI). *NMR Biomed*, 17(8):527–531, 2004.

[262] M. Wideroe, O. Olsen, T. B. Pedersen, P. E. Goa, A. Kavelaars, C. Heijnen, J. Skranes, A.-M. Brubakk, and C. Brekken. Manganese-enhanced magnetic resonance imaging of hypoxic-ischemic brain injury in the neonatal rat. *Neuroimage*, 45(3):880–90, 2009.

[263] A. Haapanen, U. A. Ramadan, T. Autti, R. Joensuu, and J. Tyynela. In vivo MRI reveals the dynamics of pathological changes in the brains of cathepsin D-deficient mice and correlates changes in manganese-enhanced MRI with microglial activation. *J Magn Reson Im*, 25(7):1024–31, 2007.

[264] A. N. Bade, B. Zhou, A. A. Epstein, S. Gorantla, L. Y. Poluektova, J. Luo, H. E. Gendelman, M. D. Boska, and Y. Liu. Improved visualization of neuronal injury following glial activation by manganese enhanced MRI. *J Neuroimmune Pharmacol*, 8(4):1027–1036, Sep 2013.

[265] J. Ruiz-Cabello, B. P. Barnett, P. A. Bottomley, and J. W. Bulte. Fluorine (^{19}F) MRS and MRI in biomedicine. *NMR Biomed*, 24(2):114–129, 2011.

[266] G. Weise, T. Basse-Luesebrink, C. Wessig, P. Jakob, and G. Stoll. In vivo imaging of inflammation in the peripheral nervous system by ^{19}F MRI. *Exp Neurol*, 229(2):494 – 501, 2011.

[267] U. Flogel, Z. Ding, H. Hardung, S. Jander, G. Reichmann, C. Jacoby, R. Schubert, and J. Schrader. In vivo monitoring of inflammation after cardiac and cerebral ischemia by fluorine magnetic resonance imaging. *Circulation*, 118(2):140–148, Jul 2008.

[268] H. Waiczies, S. Lepore, S. Drechsler, F. Qadri, B. Purfürst, K. Sydow, M. Dathe, A. Kühne, T. Lindel, W. Hoffmann, A. Pohlmann, T. Niendorf, and S. Waiczies. Visualizing brain inflammation with a shingled-leg radio-frequency head probe for $^{19}F/^{1}H$ MRI. *Sci Rep*, 3:1280, 2013.

[269] G. Liu, C. Bettegowda, Y. Qiao, V. Staedtke, K. W. Y. Chan, R. Bai, Y. Li, G. J. Riggins, K. W. Kinzler, J. W. M. Bulte, M. T. McMahon, A. A. Gilad, B. Vogelstein, S. Zhou, and P. C. M. van Zijl. Noninvasive imaging of infection after treatment with tumor-homing bacteria using chemical exchange saturation transfer (CEST) MRI. *Magn Reson Med*, Oct 2013.

[270] N. Rupp, B. M. Wegenast-Braun, R. Radde, M. E. Calhoun, and M. Jucker. Early onset amyloid lesions lead to severe neuritic abnormalities and local, but not global neuron loss in APPPS1 transgenic mice. *Neurobiology of Aging*, 32(12):2324.e1–2324.e6, 2011.

[271] Crescenzia, C. DeBrossea, R. Prakash, R. Nanga, S. Reddy, M. Haris, H. Hariharan, M. Iba, V. Lee, J. Detre, A. Borthakur, and R. Reddy. In vivo measurement of glutamate loss is associated with synapse loss in a mouse model of tauopathy. *Neuroimage*, 101: 185–192, 2015.

[272] J. Wells, J. O'Callaghan, H. Holmes, N. Powell, R. Johnson, B. Siow, F. Torrealdea, O. Ismail, S. Walker-Samuel, X. Golay, M. Rega, S. Richardson, M. Modat, M. Cardoso, S. Ourselin, A. Schwarz, Z. Ahmed, T. Murray, M. O'Neill, E. Collins, N. Colgan, and M. Lythgoe. In vivo imaging of tau pathology using multi-parametric quantitative mri. *Neuroimage*, 111:369–78, 2015.

[273] M. Carrillo-de Sauvage, J. Flament, Y. Bramoulle, L. Ben Haim, M. Guillermier, A. Berniard, G. Aurégan, D. Houitte, E. Brouillet, G. Bonvento, P. Hantraye, J. Valette, and C. Escartin. The neuroprotective agent CNTF decreases neuronal metabolites in the rat striatum: an in vivo multimodal magnetic resonance imaging study. *Journal of Cerebral Blood Flow and Metabolism*, Epub ahead of print, 2015.

[274] A. Martin-Recuero, A. Krzyzanowska, P. Lopez-Larrubia, C. Avendaño, and S. Cerdan. Early increases in Glu/Gln, Tau and tCho ^1H MRS resonances in vivo, anticipate later imaging repercussions of the cerebral inflammatory response in a mouse model of LPS-induced endotoxemia. In *Proc. Intl. Soc. Mag. Reson. Med. 21 (2013)*, 2013.

[275] M. Moshkin, A. Akulov, D. Petrovski, O. Saik, E. Petrovskiy, A. Savelov, and I. Koptyug. Proton magnetic resonance spectroscopy of brain metabolic shifts induced by acute administration of 2-deoxy-d-glucose and lipopolysaccharides. *NMR Biomed*, 27(4):399–405, 2014.

[276] G. Lodygensky, N. Kunz, E. Perroud, E. Somm, V. Mlynarik, P. Huppi, R. Gruetter, and S. Sizonenko. Definition and quantification of acute inflammatory white matter injury in the immature brain by MRI/MRS at high magnetic field. *Pediatr Res*, 75:415–423, 2014.

[277] R. Johnson. The concept of sickness behavior: a brief chronological account of four key discoveries. *Vet Immunol Immunop*, 87:443–450, 2002.

[278] D. R. Borchelt, T. Ratovitski, J. van Lare, M. K. Lee, V. Gonzales, N. A. Jenkins, N. G. Copeland, D. L. Price, and S. S. Sisodia. Accelerated amyloid deposition in the brains of transgenic mice coexpressing mutant presenilin 1 and amyloid precursor proteins. *Neuron*, 19(4):939 – 945, 1997.

[279] G. S. Price DL, Sisodia SS. Amyloid beta amyloidosis in Alzheimer's disease. *Curr Opin Neurol*, 8(4):268–74, 1995.

[280] T. Malm, J. Koistinaho, and K. Kanninen. Utilization of APPswe/PS1dE9 transgenic mice in research of alzheimer's disease: Focus on gene therapy and cell-based therapy applications. *International Journal of Alzheimer's Disease*, 2011.

[281] H. Xiong, D. Callaghan, J. Wodzinska, J. Xu, M. Premyslova, Q. Liu, and W. Connelly, Jand Zhang. Biochemical and behavioral characterization of the double transgenic mouse model (APPswe/PS1dE9) of Alzheimer's disease. *Neurosci Bull*, 27(4):221–32, 2011.

[282] L. Lawson, V. Perry, P. Dri, and S. Gordon. Heterogeneity in the distribution and morphology of microglia in the normal adult mouse brain. *Neuroscience*, 39(1):151 – 170, 1990.

[283] R. Deacon. Burrowing in rodents: a sensitive method for detecting behavioral dysfunction. *Nat Protoc*, 1(1):118–121, 2006.

[284] K. D. Duncan Forster and S. Williams. Magnetic resonance spectroscopy in vivo of neurochemicals in a transgenic model of Alzheimer's disease: A longitudinal study of metabolites, relaxation time, and behavioral analysis in TASTPM and wild-type mice. *Magn Reson Med*, 69(4):944–55, 2013.

[285] R. Clark, M. Shoaib, K. Hewitt, S. Stanford, and S. Bate. A comparison of InVivoStat with other statistical software packages for analysis of data generated from animal experiments. *J Psychopharmacol*, 26(8):1136–1142, 2012.

[286] F. Easton. Imaging microglial activation as an in-vivo biomarker for neuroinflammation. Master's thesis, School of Medicine, University of Nottingham, 2014.

[287] P.-G. H. Uzay E. Emir, Dinesh Deelchand and M. Terpstra. Noninvasive quantification of T2 and concentrations of ascorbate and glutathione in the human brain from the same double-edited spectra. *NMR Biomed*, 24(3):263–269, 2011.

[288] R. Goodacre, D. Broadhurst, A. Smilde, B. Kristal, J. Baker, R. Beger, C. Bessant, S. Connor, G. Calmani, A. Craig, T. Ebbels, D. Kell, C. Manetti, J. Newton, G. Paternostro, R. Somorjai, M. Sjostrom, J. Trygg, and F. Wulfert. Proposed minimum reporting standards for data analysis in metabolomics. *Metabolomics*, 3:231–241, 2007.

[289] V. H. Perry and C. Holmes. Microglial priming in neurodegenerative disease. *Nat Rev Neurol*, 10:217–224, 2014.

[290] P. Saransaari and S. S. Oja. Taurine and neural cell damage. *Amino Acids*, 19:509–526, 2000.

[291] R. A. Ferihan Cetin, Sibel Dincer and S. Guney. Systemic taurine prevents brain from lipopolysaccharide-induced lipid peroxidation in rats. *Afr J Pharm Pharmacol*, 6(15): 1099–1105, 2012.

[292] J. Tukey. Some thoughts on clinical trials, especially problems of multiplicity. *Science*, 198:679–684, 1977.

[293] J. Bland and D. Altman. Multiple significance tests: the bonferroni method. *BMJ*, 310: 170, 1995.

[294] T. V. Perneger. What's wrong with bonferroni adjustments. *BMJ*, 316:1236, 1998.

[295] H. M. McConnell. Reaction rates by nuclear magnetic resonance. *J Chem Phys*, Volume 28 Issue 3:430, 1958.

[296] P. Z. Sun and A. G. Sorensen. Imaging pH using the chemical exchange saturation transfer (CEST) MRI: Correction of concomitant RF irradiation effects to quantify CEST MRI for chemical exchange rate and pH. *Magn Reson Med*, 60(2):390–7, 2008.

[297] E. Baguet and C. Roby. Off-resonance irradiation effect in steady-state NMR saturation transfer. *J Magn Reson*, 128(2):149 – 160, 1997.

[298] K. Murase and N. Tanki. Numerical solutions to the time-dependent Bloch equations revisited. *J Magn Reson Im*, 29(1):126–131, Jan 2011.

[299] C. Moler and C. Van Loan. Nineteen dubious ways to compute the exponential of a matrix, twenty-five years later. *SIAM Rev*, 45(1):3–49, Mar 2003.

[300] Y. Tee, A. Khrapitchev, N. Sibson, S. Payne, and M. Chappell. Evaluating the use of a continuous approximation for model-based quantification of pulsed chemical exchange saturation transfer (CEST). *J Magn Reson*, 222(0):88 – 95, 2012.

[301] D. S. Shampine LF, Watts HA. Solving nonstiff ordinary differential equations: The state of the art. *SIAM Rev.*, 18:376–411, 1976.

[302] J. G. Sled and G. B. Pike. Quantitative imaging of magnetization transfer exchange and relaxation properties in vivo using MRI. *Magn Reson Med*, 46(5):923–931, 2001.

[303] R. M. Henkelman, X. Huang, Q.-S. Xiang, G. J. Stanisz, S. D. Swanson, and M. J. Bronskill. Quantitative interpretation of magnetization transfer. *Magn Reson Med*, 29(6): 759–766, 1993.

[304] S. Phillip Zhe. Simultaneous determination of labile proton concentration and exchange rate utilizing optimal RF power: Radio frequency power (RFP) dependence of chemical exchange saturation transfer (CEST) MRI. *J Magn Reson*, 202(2):155–161, Feb 2010.

[305] R. A. de Graaf, P. B. Brown, S. McIntyre, T. W. Nixon, K. L. Behar, and D. L. Rothman. High magnetic field water and metabolite proton T1 and T2 relaxation in rat brain in vivo. *Magn Reson Med*, 56(2):386–394, 2006.

[306] A. X. Li, M. Suchy, C. K. Jones, R. H. E. Hudson, R. S. Menon, and R. Bartha. Optimized MRI contrast for on-resonance proton exchange processes of PARACEST agents in biological systems. *Magn Reson Med*, 62(5):1282–91, 2009.

[307] J. Hua, C. Jones, J. Blakeley, S. Smith, P. van Zijl, and J. Zhou. Quantitative description of the asymmetry in magnetization transfer effects around the water resonance in the human brain. *Magn Reson Med*, 58(4):786–93., 2007.

[308] M. N. Kassem and R. Bartha. Quantitative proton short-echo-time LASER spectroscopy of normal human white matter and hippocampus at 4 tesla incorporating macromolecule subtraction. *Magn Reson Med*, 49:918–927, 2003.

[309] N. Goffeney, J. Bulte, J. Duyn, L. J. Bryant, and P. van Zijl. Sensitive NMR detection of cationic-polymer-based gene delivery systems using saturation transfer via proton exchange. *J Am Chem Soc.*, 123(35):8628–9, 2001.

[310] J.-S. Lee, D. Xia, Y. Ge, A. Jershow, and R. Regatte. Isolation of CEST contrasts from asymmetric MT effects in a human brain. In *Proceedings of the Joint Annual Meeting ISMRM-ESMRMB 2014*, 2014.

[311] N. N. Yadav, J. Xu1, X. Xu1, M. T. McMahon, and P. C. M. van Zijl. Hybrid frequency encoding/water relaxation method for detecting exchangeable solute protons with increased sensitivity and specificity. In *Proceedings of the Joint Annual Meeting ISMRM-ESMRMB 2014*, 2014.

[312] G. B. Pike. Pulsed magnetization transfer contrast in gradient echo imaging: A two-pool analytic description of signal response. *Magn Reson Med*, 36(1):95–103, 1996.

[313] G. Nair and T. Q. Duong. Echo-planar bold fMRI of mice on a narrow-bore 9.4 T magnet. *Magn Reson Med*, 52(2):430–434, 2004.

[314] J. M. Adamczak, T. D. Farr, J. U. Seehafer, D. Kalthoff, and M. Hoehn. High field bold response to forepaw stimulation in the mouse. *NeuroImage*, 51(2):704 – 712, 2010.

[315] R. Bendell. Molecular MRI using chemical exchange saturation transfer (CEST). Master's thesis, School of Medicine, University of Nottingham, 2011.

[316] G. Ardito. Second year internship for the Ecole Centrale Lyon: A Matlab tool for CEST imaging. Technical report, The University of Nottingham, 2013.

[317] G. Oz and I. Tkac. Short-echo, single-shot, full-intensity ^1HMRS for neurochemical profiling at 4T: Validation in the cerebellum and brainstem. *Magn Reson Med*, 65(4): 901–10, 2011.

[318] M. Falangola, V. Dyakin, S. Lee, A. Bogart, J. Babb, K. Duff, R. Nixon, and J. Helpern. Quantitative MRI reveals aging-associated T2 changes in mouse models of Alzheimer's disease. *NMR Biomed*, 20:343:351, 2007.

[319] P. C. van Zijl, J. Zhou, N. Mori, J.-F. Payen, D. Wilson, and S. Mori. Mechanism of magnetization transfer during on-resonance water saturation. a new approach to detect mobile proteins, peptides, and lipids. *Magn Reson Med*, 49:440–449, 2003.

[320] X. Z. Tao Jin, Ping Wang and S.-G. Kim. MR imaging of the amide-proton transfer effect and the pH-insensitive nuclear overhauser effect at 9.4 T. *Magn Reson Med*, 69(3): 760–770, 2013.

[321] C. Escartin, E. Brouillet, P. Gubellini, Y. Trioulier, C. Jacquard, C. Smadja, G. W. Knott, L. Kerkerian-Le Goff, N. Déglon, P. Hantraye, and G. Bonvento. Ciliary neurotrophic factor activates astrocytes, redistributes their glutamate transporters GLAST and GLT-1 to raft microdomains, and improves glutamate handling in vivo. *J Neurosci*, 26(22): 5978–5989, 2006.

[322] S. Webster, A. Bachstetter, P. Nelson, F. Schmitt, and L. VanEldik. Using mice to model Alzheimer's dementia: an overview of the clinical disease and the preclinical behavioral changes in 10 mouse models. *Front Genet*, 5(88), 2014.

[323] M. Heneka, M. Carson, J. ElKhoury, G. Landreth, F. Brosseron, D. Feinstein, A. Jacobs, T. Wyss-Coray, J. Vitorica, R. Ransohoff, K. Herrup, S. Frautschy, B. Finsen, G. Brown, A. Verkhratsky, K. Yamanaka, J. Koistinaho, E. Latz, A. Halle, G. Petzold, T. Town, D. Morgan, M. Shinohara, V. Perry, C. Holmes, N. Bazan, B. DJ, S. Hunot, B. Joseph, N. Deigendesch, O. Garaschuk, E. Boddeke, C. Dinarello, J. Breitner, G. Cole, D. Golenbock, and M. Kummer. Neuroinflammation in Alzheimer's disease. *Lancet Neurol*, 14 (4):388–405, 2015.

[324] F. LaFerla and K. Green. Animal models of Alzheimer disease. *Cold Spring Harb Perspect Med*, 2(11), 2012.

[325] C. Cunningham. Microglia and neurodegeneration: The role of systemic inflammation. *Glia*, 61(1):71–90, 2013.

[326] G. Jia, Y. Takayama, D. C. Flanigan, C. C. Kaeding, J. Zhou, A. Chaudhari, D. Clark, S. Sammet, J. Liang, S. Choi, and M. V. Knopp. Quantitative assessment of mobile protein levels in human knee synovial fluid: feasibility of chemical exchange saturation transfer (proteincest) MRI of osteoarthritis. *J Magn Reson Im*, 29(3):335–41, 2011.

[327] D. Liu, J. Zhou, R. Xue, Z. Zuo, J. An, and W. DJJ. RF power dependence of human brain CEST, NOE and metabolite MT effects at 7T. In *Proceedings of the 20th Annual Meeting of ISMRM, Melbourne, Australia*, 2012.

[328] I. Dimitrov, M. Takahashi, K. Sagiyama, A. Sherry, , and J. Keupp. In vivo human kidney ph mapping at 3t using time-interleaved parallel RF transmission CEST. In *Proceedings of the 20th Annual Meeting of ISMRM, Melbourne, Australia*, 2012.

[329] P. Z. Sun, J. S. Cheung, E. Wang, T. Benner, and A. G. Sorensen. Fast multislice pH-weighted chemical exchange saturation transfer (CEST) MRI with unevenly segmented RF irradiation. *Magn Reson Med*, 65(2):588–94, 2011.

[330] X. Zhao, Z. Wen, G. Zhang, F. Huang, S. Lu, X. Wang, S. Hu, M. Chen, and J. Zhou. Three-dimensional turbo-spin-echo amide proton transfer mr imaging at 3 tesla and its application to high-grade human brain tumors. *Mol Imaging Biol*, 15(1):114–22, 2013.

[331] A. Singh, K. Cai, M. Haris, H. Hariharan, and R. Reddy. On b1 inhomogeneity correction of in vivo human brain glutamate chemical exchange saturation transfer contrast at 7T. *Magn Reson Med*, 69(3):818–824, 2013.

[332] E. Vinogradov, A. D. Sherry, and R. E. Lenkinski. CEST: from basic principles to applications, challenges and opportunities. *J Magn Reson*, 229:155–172, Apr 2013.

[333] T. Jin and S. Kim. Advantages of chemical exchange-sensitive spin-lock (CESL) over chemical exchange saturation transfer (CEST) for hydroxyl and amine water proton exchange studies. *NMR in Biomed*, 27(11):1313–1324, 2014.

[334] V. Roeloffs, C. Meyer, P. Bachert, and M. Zaiss. Towards quantification of pulsed spin-lock and CEST at clinical MR scanners: an analytical interleaved saturation-relaxation (ISAR) approach. *NMR in Biomed*, 28(1):40–53, 2015.

[335] N. Cesarovic, F. Nicholls, A. Rettich, P. Kronen, M. HÃď’ssig, P. Jirkof, and M. Arras. Isoflurane and sevoflurane provide equally effective anaesthesia in laboratory mice. *Lab Anim*, 44(4):329–36, 2010.

[336] J. Perucho, I. Rubio, M. Casarejos, A. Gomez, J. Rodriguez-Navarro, R. Solano, J. De Yebenes, and M. Mena. Anesthesia with isoflurane increases amyloid pathology in mice models of Alzheimer’s disease. *J Alzheimers Dis*, 19(4):1245–57, 2010.

[337] C.-Y. Lin, N. N. Yadav, J. Ratnakar, A. D. Sherry, and P. C. M. van Zijl. In vivo imaging of PARACEST agents using frequency labeled exchange transfer MRI. *Magn Reson Med*, Mar 2013.

[338] N. N. Yadav, C. K. Jones, J. Hua, J. Xu, and P. C. M. van Zijl. Imaging of endogenous exchangeable proton signals in the human brain using frequency labeled exchange transfer imaging. *Magn Reson Med*, 69(4):966–973, Apr 2013.

[339] Z. Zu, J. Spear, H. Li, J. Xu, and J. Gore. Measurement of regional cerebral glucose uptake by magnetic resonance spin-lock imaging. *Magn Reson Imaging*, 32(9):1078–84, 2015.